Order number Year 2009

A thesis submitted

for the degree of Doctor of Philosophy

in Ecole Centrale de Lyon

Specialty: Mechanics

by

Vsevolod KHARYTON

FAULTS DETECTION IN BLADES OF AN AVIATION ENGINE IN OPERATION

Doctoral Committee:

Mr M. ARGHIR, Professor, Université de Poitiers	Reviewer
Mr M. COLLET, Senior Researcher, Université de Besançon	Reviewer
Mr R. DUFOUR, Professor, INSA Lyon	Examiner
Mr M. GILLET, Engineer, Group SAFRAN – SNECMA	Examiner
Mr O. KUCHER, Professor, National Aviation University	Director of thesis
Mr J.-P. LAINE, Associate Professor, Ecole Centrale de Lyon	Co-director of thesis
Mr F. THOUVEREZ, Professor, Ecole Centrale de Lyon	Director of thesis

Abstract

The general aim of the study is to offer mathematical model of the process, which can allow crack identification in the compressor or turbine blade of aircraft gas-turbine engine in operation.

Within the frameworks of this goal cracked blade non-linear dynamic model was elaborated and introduced to the global model of the bladed disk. Crack induced non-linearity was taken into account applying contact analysis elements in conjunction with harmonic balance method. For system size reduction the sub-structuring methodology using fixed-interface method was applied. It supposes the crack location to be considered as interface between two dependent, in this case, sub-structures. Such approach was applied to the both uncoupled cracked blade and bladed disk models. Also considering uncoupled cracked blade the centrifugal forces effect was examined. It was concluded, that depending on crack properties (location and size), it will be enough to use the linear crack presence formulation supposing crack to be always open (initial gap).

During simulation of the bladed disk forced response containing cracked blade the effect of blade mistuning was simulated. Simulation results shown that at certain level of mistuning it becomes impossible to separate cracked blade response. Furthermore such crack detectability decreases with absence of cracked blade frequency localization. The last one phenomenon is very important diagnostic sign, which simplifies cracked blade detection at almost all cases.

The last phase of the work was devoted to simulation of blade tip-timing method application for cracked blade identification. It consisted in blade arriving time generation, blade tip amplitudes reconstruction and bladed disk frequency response calculation on the base of measured (simulated) time data. Such approach allowed us to identify cracked blade in the same way as in frequency response analysis. Generally speaking, blade tip-timing method can be used as the part of engine health monitoring system for compressor or turbine blades dynamic performances monitoring.

Keywords:

cracked blade, bladed disk, harmonic balance method,
mistuning, cracked blade dynamic localization,
blade tip-timing method

Résume

Ce travail porte sur le développent de modèle mathématique du processus d'identification de la fissure dans une aube de compresseur ou de turbine d'un moteur d'avion en fonctionnement.

Dans le cadre de cette problématique, le modèle non-linaire d'aube fissurée a été développé et introduit dans la modèle globale de roue aubagée. La non-linéarité causée par la présence de fissure a été prise en considération par application des éléments d'analyse de contact conjointement avec la méthode de balance harmonique. Nous avons utilisé l'approche de sous-structuration pour la réduction de la taille du système. Cette approche se base sur la méthode à interface fixe en supposant que la fissure forme l'interface entre deux sus-structures dépendants. Elle a été appliquée aux modèles d'aube isolée et roue aubagée. L'effet de forces centrifuges a aussi été étudié en utilisant le modèle d'aube pas couplée. On peut déduire de cette étude qu'il suffit de simuler le comportement vibratoire d'une aube fissurée par l'approche linaire, mais cela dépend de la position et de la taille de la fissure. La formulation linéaire de comportement dynamique d'aube fissurée consiste à supposer que la fissure est toujours ouverte.

L'effet de désaccordage a été examiné avec la simulation de réponse forcée de la roue aubagée contenant une aube fissurée. Les résultats de simulations montrent qu'un certain niveau de désaccordage peut cacher la réponse de l'aube fissurée. De plus, la capacité de détecter cette aube se dégrade avec l'absence de sa localisation dynamique fréquentielle.

La dernière phase du travail a été consacrée à la simulation d'application de la méthode de tip-timing à l'identification d'aube fissurée. Elle se constitue de la génération du temps d'arrivé, la reconstruction d'amplitude de réponse en tète d'aube et le calcul de la réponse forcée du disque à partir des données mesurées (générées). Cela nous donne la possibilité d'identifier l'aube fissurée de manière analogue à l'analyse de la réponse forcée. On peut conclure qu'il sera possible d'utiliser la méthode de tip-timing comme une partie d'un système global de health monitoring de moteurs d'avion pour contrôler le comportement dynamique d'aubes de compresseur ou de turbine.

Mot clés:

aube fissurée, roue aubagée, méthode de balance harmonique,
désaccordage, localisation dynamique d'aube fissurée,
méthode de tip-timing

Table of contents

Abstract i

Résume iii

Table of contents v

Introduction 1

1. Some aspects of gas-turbine engines structural dynamics 5

1.1 Aviation engine in the scope of health monitoring 5

1.1.1 Overview of an aircraft gas-turbine engine 5

1.1.2 Bases of aviation technique health monitoring 7

1.1.3 Aircraft gas-turbine engine health monitoring system 8

1.1.4 Methods of parametric diagnostic of aircraft gas-turbine engine 11

1.1.5 Physics of aircraft gas-turbine engine parameters modification 12

1.2 Dynamics of deformable solid bodies in rotation 13

1.3 Forced response of tuned bladed disk 17

1.3.1 Cyclic analysis of tuned bladed disks 17

1.3.2 Engine order excitation 19

1.3.3 Zig-zag diagram application to periodic structures 21

1.4 Mistuning and vibration localization in bladed disk structures 22

1.4.1 Mistuning influence on dynamics of bladed disk 23

1.4.2 Vibration localization in mistuned bladed disks 26

1.5 Dynamics of bladed disk with a crack presence in the blade 30

Conclusions 35

2. Contact analysis and crack propagation 37

2.1. Contact analysis elements for crack inside interaction modelling 37

2.1.1 Taking into account friction in contact analysis 39

2.1.2 Stress-deformed state in contact zone 41

2.1.3 Virtual work principle 43

2.1.4 Variational inequality 44

2.1.5 Variational equality 46

2.1.6 Solution of the contact problem 47

2.2 Fatigue and endurance calculation of structures elements 51

2.2.1 Alternating loads 52

2.2.2 Fatigue curve and limit stresses diagram 54
2.2.3 Distribution curve of cyclical durability 56
2.2.4 Damage accumulation. Durability estimation 57
2.3 Structure crack resistance calculation 59
2.3.1 Stress intensity coefficient 59
2.3.2 Force criterion of cracked structures strength 64
2.3.3 Critical stress and critical length of crack. Safety factor 66
2.3.4 Example of residual strength calculation of the cracked structure 69
2.4 Residual durability of structure with crack 73
2.4.1 Diagram of material cyclical crack resistance 74
2.4.2 Definition of residual durability of structure with crack 76
2.4.3 Example of cracked structure residual durability calculation 77
Conclusions 80
3. Nonlinear analysis of the cracked structures in dynamics 81
3.1 A solution to a non-linear dynamic problem 82
3.1.1 Time domain methods for a solution to the non-linear problems 83
3.1.2 Frequency domain methods for a solution to the non-linear problems 86
3.1.3 Methods for reduced order modelling 89
3.2 Cracked blade model dynamic 92
3.2.1 Reduction of cracked blade model 94
3.2.2 Application of penalty method for non-linear force representation 97
3.2.3 Non-linear solution of the problem 98
3.2.4 Validation of harmonic balance method results by direct time integration 102
3.2.5 Frequency response of the non-linear cracked blade model 104
3.2.6 Centrifugal forces effect on cracked blade non-linearity 109
3.2.7 Fracture mechanics elements application to cracked blade model 112
3.3 Dynamic model of bladed disk with a cracked blade 114
3.3.1 Bladed disk model reduction 117
3.3.2 Choosing the number of retained harmonics in the case of bladed disk model 120
3.3.3 Effect of the phase lag of excitation forces on the bladed disk forced response 121
3.3.4 Mistuning effect on the bladed disk forced response 122
3.3.5 Prediction of mistuned bladed disk frequency response 127
Conclusions 131

4. Tip-timing method application for cracked blade detection 133

4.1 Blade amplitude reconstruction from multi-probe measurements data 135

4.2 Blade tip-timing method application to the bladed disk model 139

4.2.1 Simulation of tip-timing measurements 140

4.2.2 Comparison of frequency response reconstructed by tip-timing method data with harmonic balance method results 154

4.3 Tip-timing measurements simulation at different mistuning levels 155

4.3.1 Presence of cracked blade frequency localization 155

4.3.2 Absence of cracked blade frequency localization 160

4.4 Measurement performances influence on cracked blade detectability 161

Conclusions 167

Conclusions and perspectives 169

Personal publications 173

References 174

Nomenclature 183

List of figures 187

List of tables 193

Annex 1 195

Introduction

The research study presented in this dissertation aims to provide computational methodologies and understanding of the physical phenomena that will aid to control bladed disk dynamic behaviour containing one or several cracked blades.

Bladed disk structures are found in a wide array of applications from small impeller pumps via automotive turbosystems up to large turbines for power generation and aviation gas-turbine engines for military and commercial aircrafts. Up-to-date aviation engines are complex products therefore requiring much attention to them. They are elaborated in the conditions of the extremely high concurrence level, within the frameworks of very strict requirements to their performances: technical, economical and environmental. Due to this, entire aviation gas-turbine engine health monitoring through on-line damage detection is increasingly gaining the interest of manufacturers.

The various today's on-wing health monitoring systems are a collection of separate, unrelated technologies providing a basic monitoring level. Their capabilities are relatively limited and the information they provide is used, normally, to initiate maintenance actions. And they are not applicable for real-time controlled objects tracing and decision-making.

As far as turbines and compressor blades are among the most critical engine elements, special measures should be applied to include them in an accurate way to the engine health monitoring system. Their behaviour characteristic parameters should be traced continuously during engine operation because damages, like fatigue induced cracks, have features to propagate. So that. crack initiation and attainment of the limit working cycles number could happen between engine checks. Also blade monitoring can be carried out on the base of blade forced response at different excitation frequencies or engine rotation speed, alias during engine operation only. This can give us much more diagnostic information and that is more important – such information will be updated in each measurement (time point) and initiated ruinous defects could be revealed. Thus, the problem of knowledge necessity about dynamic behaviour of cracked blades becomes more and more important.

Some difficulties are brought by probabilistic character of crack characteristic parameters. But they are not alone. Problems of mistuning, vibration localization caused by cracked blade presence should be studied because they will have effect on the process of crack presence

detection. In the study we will deal with model of the bladed disk, which has properties of the blisk structure. So that, the questions of blade to disk connection will be omitted. With the advent of blisks, single part bladed disks, the interest about blade mistuning as an objectionable phenomenon has increased. In the blisk blades are permanently attached to the disk and it is not possible to discard the blades that fall outside acceptable manufacturing tolerances.

Also the question of proper modelling of crack behaviour becomes one of the most important. It will influence on dynamic structure response ability to give to the maintenance engineer certain information, which is sufficient or not for cracked blade identification. Generally, the crack is modelled by linear approach supposing it to be always open and such model can be easily introduced by perturbation of blade partition of global bladed disk stiffness matrix. But in reality due to inside crack contact such approach may be not realistic enough. Contact induced non-linear cracked blade behaviour could hide the crack presence effect on overall bladed disk forced response, if mistuning is taken into account. Such considerations are also true for cracked blade frequency localization case.

After it the main attention is focused on application of the non-invasive method able to map out bladed disk dynamics during engine operation. In such way we will transfer to investigate the possibility to apply a method of cracked blade identification based on measurements of blade tip deflections. For this purposes blade tip arriving times, when blade tip passes through stationary installed on engine casing probe, are used. Methods using such methodology are known as blade tip-timing methods. Vibration characteristics of the investigated object are analyzed according to acquisition of arriving times data. Further, the related blade fatigue life or/and its health conditions are evaluated. Blade tip-timing method can be used to create on-line system of blade health monitoring. This system should be able to solve the following tasks:

- initial data measurements;
- calculation of characteristic parameters by measured data;
- processing of characteristic parameters to describe chosen blade dynamic behaviour.

In such on-line blade monitoring system, non-contact displacement sensors play an important role. Several physical principles are used for non-contact measurements. Among these, eddy current, optical reflection and capacitive sensors have good properties.

The analysis and applicability of the non-linear bladed disk dynamic model to tip-timing method should be fulfilled with investigation of the method’s ability to detect cracked blade using only measurement data.

Obtained results should provide solid ground for deeper understanding of cracked blade identification problem on the base of its dynamic behaviour and show effective ways of preventing of disastrous effects. They are believed to be beneficial for the industry.

In order to accomplish all required tasks the presented study is structured in the following way. As far as it deals with faults detection in blades of an aviation engine in operation, firstly, the engine should have been considered as a complex dynamic object. Therefore, c*hapter 1* deals with questions of aviation gas-turbine engines diagnostics, dynamics of solid bodies and simulation approaches of crack presence in a blade. The special attention is paid to bladed disks in the scope of mistuning presence and cyclic symmetry analysis.

The questions of contact analysis fundamentals and theoretical formulation of crack presence in a structure using fracture mechanics theory are considered in *chapter 2*. It serves to go together with proper formulation of crack presence in the blade. Moreover, application of fracture mechanics to estimation of cracked structure residual durability can be integrated as an assessment element of health monitoring system responsible for cracked blade detection. Such system can be based on realistic non-linear model of cracked blade and application of on-line procedure of blade dynamic performances monitoring (e. g., tip-timing method).

Accordingly, the principal part of the study is contained in *chapter 3,* where development of non-linear cracked blade model is presented. The non-linear approach of crack presence simulation supposes simultaneous application of harmonic balance method and elements of contact analysis (penalty method). The model of bladed disk with cracked blade is then investigated. It is subjected to mistuning influence that, in most of cases, affect cracked blade detectability. An example is devoted to zig-zag diagram application, which is shown to be applicable even in the case of disrupted symmetry (by influence of both mistuning and cracked blade).

Finally, the study is concluded by tip-timing method application to the bladed disk model (*chapter 4*). It is aimed on simulation of real measurements, which can be performed during engine operation or maintenance. Simulations supposing different crack cases (size, location) are performed to show the method ability to trace bladed disk frequency response and, consequently, to detect cracked blade.

Chapter 1
Some aspects of gas-turbine engines structural dynamics

The aim of this chapter is to present main outlines in aviation gas-turbine engine structural dynamics in connection with engine health monitoring. Parameters of dynamic behaviour of engine components will be considered as their probable diagnostic signs.

Firstly, main aspects of the engine design are presented and principles of its operation are explained. The attention is paid to engine operational modes, engine operational loads, sources and signs of vibrations. Main engine critical parts are singled out and their influence on engine availability and performances is summarized.

Theoretical aspects of solid body dynamics in rotation are considered to form the background for all following developments. Crack modelling approaches are considered to choose the most appropriate one to simulate non-linear behaviour of cracked blade.

Also mistuned bladed disk dynamics, cyclic modelling and vibration localization are presented in the form of bibliographical review. Frequency localization phenomenon of mistuned structures is considered as one of the most important aspects that can be used in engine health monitoring for cracked blade identification.

1.1 Aircraft engine in the scope of health monitoring

1.1.1 Overview of an aircraft gas-turbine engine

Now, aircraft gas-turbine engines gain wide application in all spheres of civil aviation and they are under continuous development. The social and economical factors play the main role in their perspective development [66].

Social factors mean such requirements as safety guarantee, flight time reduction and effect on environment. Economical factors are the increased requirements to engine efficiency and reduction of maintenance costs. All these factors make demands to the engines and denote main directions of their perspective development:

– intensification of the working process by effective control using diagnostic systems;

– optimization of engine design (weight and durability parameters).

In all following studies we will deal with turbofan engine, as soon as its structural parts and assemblies will be the objects of all simulations.

A turbofan engine gas path consists of several components arranged from front to back (Fig. 1.1). The first component is the fan, which is open to the outside, and, in a civil aircraft engine, provides most of the thrust by propulsion of a huge quantity of air through the engine core. The first of these remaining components is the booster, also known as the low pressure compressor (LPC), which is followed by the high pressure compressor (HPC). This opens into the combustor where fuel is injected and burned. The resulting hot gas drives the high pressure turbine (HPT) and the low pressure turbine (LPT). Each of these components affects the engine's operation, and algorithms for improved control and knowledge about component health will enable a higher level of performance to be obtained.

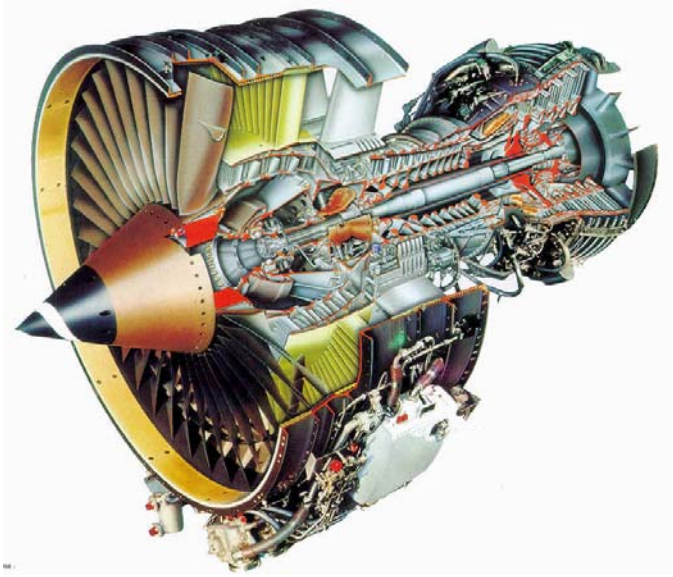

Fig. 1.1. Aircraft turbofan engine

The state of component health involves characteristics that degrade over time: such features as efficiency, flow capacity, and seal leakage. These tend to change slowly over many flights, but abrupt changes might indicate the occurrence of a sudden fault. From a structural point of view, the engine is made up of rotating and non-rotating parts. The non-rotating outer portion consists of, among other things, the ducts for bypass airflow, and stator vanes which project into the airflow through the components. It also contains the bearings outer races that hold the rolling elements that support the shafts. The shafts, in turn, support the fan, compressor and turbine disks – these are the rotating components. The low pressure shaft supports the fan, LPC, and LPT. The hollow high pressure shaft fits around the low pressure shaft and it is separated from it by bearings. It supports the HPC and HPT. The compressors and turbines each consist of multiple disks attached to the

shaft, and each disk is fitted with multiple blades around its circumference. As these parts rotate, they interact, setting up natural vibrations and resonances. Change in an engine vibration signature may be recognized as a damage sign.

Working blade of aviation gas-turbine engine is one of its most important and highly loaded components (Fig. 1.2). Some aspects of its design are presented here because it will be the main object of the work in all following chapters.

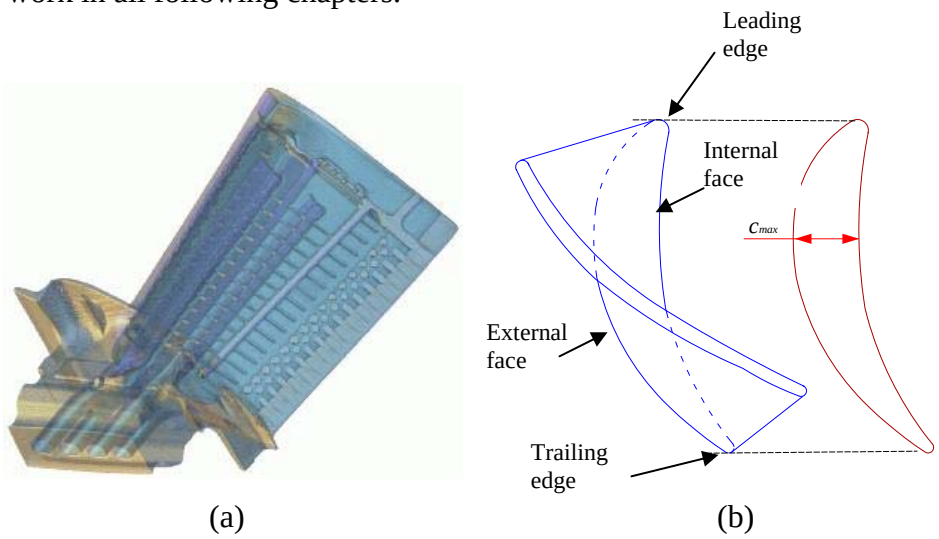

(a) (b)

Fig. 1.2: (a) typical turbine blade design (cooled); (b) turbine blade profiling

Parameters of blades profiling must provide operational gas-dynamic parameters of blade row performances. For simplification of blades manufacturing its body concave (external face) surface is outlined by circle arch and convex (internal face) surface is outlined by parabola or lemniscate segments (Fig. 1.1). Profile mass centres are aligned in order to reduce bending stresses. Maximum relative profile thickness c_{max} is changed from 20-25% at root section to 4-6% at blade tip. Blades with cooling system have higher values of the relative thickness.

Cross-section area of the blade profile is generally decreased from root to tip non-linearly:

$$F(R) = F_r - (F_r - F_p)\left(\frac{R - R_r}{R_p - R_r}\right)^q, \qquad (1.1)$$

where R_r end F_r – radius and area of the root section and R_p end F_p – radius and area of the periphery section, q – power low rate. For turbine blades q=0.5-0.6 and F_p / F_r=0.3-0.4. Profile of chord generally is not changed or changed slightly along blade height. These measures allow reduce stresses in root section on up to 30-35%.

1.1.2 Bases of aviation technique health monitoring

At present, systems using on-board control devices and information accumulation on engine technical condition are widely spread. These systems allow performing of estimates of serviceability, operability and trouble-shooting up to replaceable assembly [51].

Different methods and diagnostic tools were developed for engines health monitoring [8, 52, 99]. They are aimed on improvement of on-board and land-based devices and specialised systems, which are used for flight data acquisition, storage and processing. Also such methods provide engine diagnosing with minimum time and financial expenses. Optimum efficiency can be attained by assembling diagnostic tools in a unified complex integrated system. Creation of the overall health monitoring system requires in-depth study of method capabilities and drawbacks, its optimum application regarding to operation conditions and full use of the acquired information.

Efficiency of diagnostic systems is determined by controllability and accessibility of the engine to diagnosing in the volume ensuring faults detection; presence of powerful and trusty airborne system of parameters control, which allows engine and its functional systems health monitoring; high resolution of diagnostic methods and tools ensuring fault detection at early stage; sophisticated system of decision making about possibility of engine operation; possibility of nondestructive methods utilization.

There are some ways of maintenance and repair cost reduction providing the required reliability level. One way is to make possible engine accessibility for inspections without its removal. Another one way is the use of overall system of in-condition health monitoring with parameters control.

1.1.3 Aircraft gas-turbine engine health monitoring system

The system of parametric control and diagnostics of gas-turbine engine is intended for estimation of its technical condition while in service. It performs in-flight failures detection and prevents faults of the engine and its main functional systems (start, fuel and oil system, compressor control system, thrust reverse system) [98].

The system performs automatic recording of parameters and signals acquired by on-board devices, their express processing after each flight, monitoring and analysis by the methods of parametric diagnostics. It allows yielding operative estimate of current technical condition of the engine and its functional systems. Current estimate of engine technical condition is performed by logical analysis of parameters and signals, proximate analysis of flight and engine runs information, visual observation of parameters and signals. Analysis of parameter trends is used for intermediate term estimate and prediction of serviceability of the engine. Such kind of analysis establishes parameters dependence on operating time. Then, trends of set limits overrun are determined. Complex analysis of flight information in the diagnostic laboratory allows engines classification on "faultless" and "supposed to be defective". Also it allows solution making about engine technical condition, necessity of components substitution, inspections and regulations.

Generalized system of the parametric control and diagnosing performs the following tasks [4]:

- Proximate analysis of engine technical condition by flight information;
- Processing and analysis of engine runs;
- Aviation engine health monitoring by measured parameters;
- Decision making on aviation engine technical condition;
- Monitoring of current and equivalent engine operating times;
- Scanning and visualisation of flight information;
- Data management about failures and measures of their elimination;
- Thermodynamic model of the engine for the engine diagnosing;
- Program of fuel rate monitoring;
- Oil system condition monitoring program;
- Engine thrust calculation program;
- Vibration performances monitoring;
- Official data management on aviation engine.

From the point of view of algorithmization all tasks of parametric control and diagnosing are divided into three groups: operative estimate of technical condition, diagnostics and predictions, trouble-shooting.

Main taks of operative estimate cover monitoring of on-board diagnostic system, proximate analysis of flight information, processing and analysis of the engine runs and visualisation of flight information.

The problems linked with engine monitoring and diagnosing by parameters measured in flight constitute the second group. This group includes tasks of parameter-trend analysis, monitoring of oil system, fuel rate, engine thrust and vibration performances of the engine. This tasks are intended for intermediate term estimate and prediction.

Problems of aircraft engine official data management form group of the information tasks. Data about failures and modes of their elimination, crew and laboratory notes are used for faults search in conjunction with decision making system.

As it can be understood from stated above, the main task of engine health monitoring is the engine investigation as the diagnostics' object and development of methods and tools of its diagnosing. To solve this task there are some stages to be accomplished:

- localization of the engine state multitude subjected to diagnosing;
- selection of the minimum number of parameters required for particular state recognition;
- development of methods of diagnostic parameters determination;

- analysis of processes occurring in the engine at its operational state and defect propagation monitoring;
- methods development of engine state prognosis and defects localization;
- system development of diagnostic information acquisition, storage and analysis;
- definition of engine health monitoring system in the overall maintenance system with the goal to reduce faults number and full utilization of engine service life abilities.

Engineering analysis of the engine deterioration physical process in operation can be classified by:

- process of gas-dynamic flow deterioration of the engine core indicated by thermo and gas-dynamic parameters changing;
- process of engine mechanical state deterioration caused by continuous wear of engine bearing and exhausting of engine critical parts resource abilities by parameters of long-term strength, low and high-cycle fatigue, thermal-fatigue life.

Consequently, engine health monitoring can be performed by:

- diagnostics using thermo and gas-dynamic parameters;
- diagnostics using engine oil conditions;
- diagnostics using visual control and defectoscopy;
- diagnostics using vibration and acoustic parameters.

Cracked blade identification will be performed with the goal to provide engine health monitoring using diagnostics by vibration parameters.

Methods of vibration diagnostics provide engine technical condition estimation using information contained in oscillation processes accompanying engine operation. Dynamic loads induce acoustic waves propagation in the engine flow. Thus, parameters of vibration depend on vibration spectrum and intensity of excitation loads.

Generally, the reasons of faults occurrence in the structural elements are associated with change of acting loads character. Then, it leads to change of eigenfrequencies caused by fault. And it becomes clear that it is possible to detect fault earlier by vibro-acoustic methods then by any other diagnostic approach. The main sources of engine vibration have aerodynamic and mechanical nature. Aerodynamically induced vibration is normally caused by blade vanes. They produce vibration noise and its intensity is increased with increase of flow turbulence. Sometimes additional spectrum components can occur. They are linked with rotating flow stall, vibrating burning, etc. But the main source of vibration is the rotating rotor. It produces vibration caused by inequalities of its manufacturing, wearing and unbalancing. Also mechanically induced vibrations arise due to gear assemblies, bearings and auxiliary units.

Engine vibration state diagnostics is performed in two ways. Firstly, it is performed by analysis of spectrum frequency content with its comparison in faultless and defected states. In the easiest way this approach provides faults detection, which causes new discrete frequency components (aerodynamic stall) and sufficient increase of vibration level (blade defects). Secondly, analysis of main rotor harmonic levels is carried out at the operational modes. This helps to reveal defects leading to rotor unbalancing. Superharmonics are also used to explore elastic support bearings and connecting clutches.

1.1.4 Methods of parametric diagnostic of aircraft gas-turbine engine

Up-to-date approaches of engine technical condition monitoring using parametric methods are grounded on mathematical model of the engine working process [2, 102]. Such model allows determination of faults resulting in change of engine working process parameters.

Parametric information supposes thermo and gas-dynamic and mechanical parameters to be equal during faultless engine operation, if they are measured within the same operation mode and under equal external conditions.

Parametric methods take their special place in engine health monitoring regarding to some advantages [46]:

- diagnostic information can be acquired continuously on running engine that allows tracing a fault origination and development and forecasting of technical condition modification;
- parameters of engine working process are linked among themselves by strict dependences allowing application of mathematic tools.

The analysis of existing methods of diagnostic information processing allows separation of two main approaches of engine technical condition estimate. Accordingly to the first one, the engine parameters (efficiency of compressor and turbine, squares of characteristic sections, etc.) are used as diagnostic parameters. They are obtained using mathematical model of the engine. After that, they are compared with parameters of mathematical model of faultless engine initial state or defective engine model (fault portrait). By results of comparison, the current technical condition of engine is defined. Accordingly to the second approach, measured parameters are accepted as diagnostic parameters. They are reduced to equal conditions and operation mode [51–52]. Finally, the technical condition estimate is yielded using trend analysis of parameters change caused by origination and development of fault.

For technical conditions estimate the method of the matrixes is used. It is grounded on comparison of reduced parameters deviation from standard values previously calculated for various

possible faults of the engine. However, its practical use is complicated by uncertainty of parametric identification of the engine faults.

Also methods of signs separation in space can be applied for diagnostics purposes [78]. They use "compactness hypothesis". According to it, the points representing the same state are clustered in bounded area of sign space. Consequently, engine state can be estimated by the vector of states in *m*-dimensional space. In this space *m* engine parameters are used as co-ordinates. Though, construction of the confidential hypersurface of the limiting states, considering all possible technical states of the engine and their combinations, is quite difficult task.

Probabilistic methods of diagnostics are grounded on stochastic interdependences of states and their signs [8, 83]. The main problem in application of these methods is elaboration of recognition algorithms, which allow decision making on the engine technical condition.

1.1.5 Physics of aircraft gas-turbine engine parameters modification

Physical processes, happening in the engine at fault origination, result in its parameters modification. The coking of high pressure turbine ports of the combustion chamber (partial or full) leads to increase of temperature field nonuniformity. It increases thermal losses in combustion chamber and, hence, reduces efficiency of extension duct, including combustion chamber and high and low pressure turbines.

Automatic control system has to ensure constant high pressure turbine work in order to maintain constant rotational speed of high pressure rotor. Thus, it is possible to compensate efficiency decrease only by increase of turbine gas temperature and consequently of the fuel rate. If efficiencies of both high and low pressure turbines are fixed, gas temperature behind the turbine increases proportionally to the gas temperature. Consequently, combustion chamber details, rotor blades and nozzle vanes of turbines work in the conditions of more and more increased temperatures and, consequently, thermal loadings.

Simultaneously, owing to heightened thermal loading of the engine "hot part", there are material structural modifications with formation of cracks and burn-outs. On heads and sections of combustion chamber the embossing separation with slot formation is observed. These defects cause losses of strength and cracking that leads to engine operation termination. For prevention of dangerous developments of faults in the flight, resulting in failure or even not localised engine damage, it is required, depending on stage of already visible defects development, to decrease periodicity of optical inspections.

Thus, practical value of technical condition monitoring by parameters consists in: firstly, at initial stage of defect development, it is possible to extend an engine service life by modification of

parameters regulations; and, secondly, at detection of the structural modifications origination, the accomplishment of optimum number of inspections should be performed in order to prevent a defect development [100–101].

1.2 Dynamics of deformable solid bodies in rotation

In the previous subchapter some critical engine elements were outlined. Moreover, as soon as gas-turbine engine rotating elements belongs to them, the particular knowledge is required to proper formulate their dynamic behaviour. Therefore some elements of deformable solids dynamics should be considered in the brief manner.

Formulation of the theory of deformable solids in dynamics will be used throughout the study that makes it to be briefly considered [32].

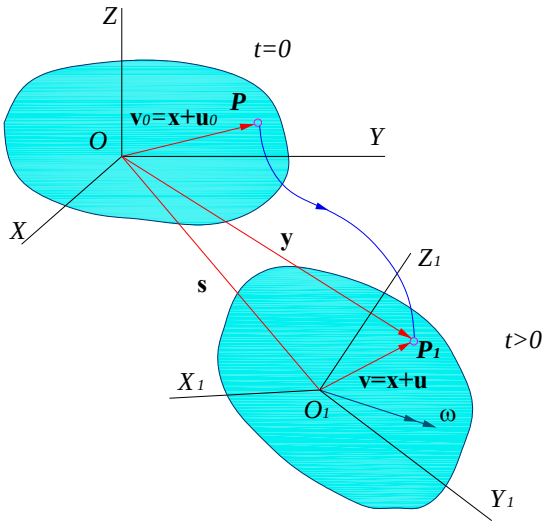

Fig. 1.3. Schematic presentation of deformable solid body

Let's consider the system of the volume Ω with boundary $\partial\Omega$ in its undeformed state located in the origin (Fig. 1.3), which is inertial orthonormal system (*OXYZ*). Each point of the body has co-ordinates expressed by the vector $\mathbf{x} = [x_1, x_2, x_3]^T$. At time *t*=0 the body is in state

$$\mathbf{v}_0(\mathbf{x}) = \mathbf{x} + \mathbf{u}_0(\mathbf{x}), \tag{1.2}$$

where $\mathbf{u}_0(\mathbf{x})$ is the initial displacements vector.

At the time *t*>0 the body state will be described (for example in the point P_1) by the vector

$$\mathbf{v}(\mathbf{x},t) = \mathbf{x} + \mathbf{u}(\mathbf{x},t), \tag{1.3}$$

where $\mathbf{u}(\mathbf{x},t)$ is displacements' vector at the time moment *t*>0 resulting in the body dynamic deformation.

Description of coordinate system transformation requires involving of the translational vector **s** and the matrix of rotation **R**. In the inertial coordinate system point *P* can be described by the vector:

$$\mathbf{y}(\mathbf{x},t) = \mathbf{s}(t) + \mathbf{R}(t)\mathbf{v}(\mathbf{x},t), \tag{1.4}$$

From (1.4) velocity of the solid body points required for dynamic problem formulation will expressed as:

$$\dot{\mathbf{y}} = \dot{\mathbf{s}} + \dot{\mathbf{R}}(\mathbf{x} + \mathbf{u}) + \mathbf{R}\dot{\mathbf{u}} . \tag{1.5}$$

Vector of rotation speed $\boldsymbol{\omega} = [\omega_1, \omega_2, \omega_3]^T$ allows expressing the derivative of rotational matrix, which states the relation between inertial coordinate system and the system of the body in time *t*, will be:

$$\dot{\mathbf{R}} = \mathbf{R}\boldsymbol{\Omega} = \mathbf{R}\begin{bmatrix} 0 & -\omega_3 & \omega_2 \\ \omega_3 & 0 & -\omega_1 \\ -\omega_2 & \omega_1 & 0 \end{bmatrix}. \tag{1.6}$$

Equation of motion of deformable solid is derived on the base of the variation principle of Hamilton. It stipulates that sum of kinetic and potential energy variations and variation of the work performed by nonconservative forces is equal to zero:

$$\delta\int_{t_1}^{t_2}(E_c - E_p)dt + \int_{t_1}^{t_2}\delta W dt = 0 , \tag{1.7}$$

where E_c is kinetic energy, E_p is potential energy and δW is the work performed by nonconservative (dissipative) forces in the interval t_1-t_2. Expression $E_c - E_p + W$ is known as Lagrange function of the system.

Supposing our object movement to be described by *n* generalized co-ordinates $q_i(t)$ (i=1,…,n) the members of equation (1.7) can be presented in the following way:

$$E_c = E_c(\mathbf{q}, \dot{\mathbf{q}}, t),\ E_p = E_p(\mathbf{q}, t),\ \delta W = \delta\mathbf{q}\mathbf{w} , \tag{1.8}$$

where $\mathbf{w}$ – vector of nonconservative forces.

Then utilizing (1.8), equation of Lagrange associated with variation principle can be written:

$$\frac{d}{dt}(\partial E_c / \partial\dot{\mathbf{q}}) - \partial E_c / \partial\mathbf{q} + \partial E_p / \partial\mathbf{q} = \mathbf{w} , \tag{1.9}$$

where $\mathbf{w} = -\partial F_d / \partial\dot{\mathbf{q}}$, F_d – dissipation function of Rayleigh.

Kinetic energy can be expressed as follows:

$$\begin{aligned} E_c = \frac{1}{2}\int_\Omega \rho\mathbf{y}^T\mathbf{y}d\boldsymbol{\Omega} = \frac{1}{2}\int_\Omega \rho\dot{\mathbf{u}}^T\dot{\mathbf{u}}d\boldsymbol{\Omega} + \int_\Omega \rho\dot{\mathbf{u}}^T\boldsymbol{\Omega}\mathbf{u}d\boldsymbol{\Omega} - \frac{1}{2}\int_\Omega \rho\mathbf{u}^T\boldsymbol{\Omega}^2\mathbf{u}d\boldsymbol{\Omega} - \int_\Omega \rho\mathbf{u}^T\boldsymbol{\Omega}(\mathbf{R}^T\dot{\mathbf{s}} + \boldsymbol{\Omega}\mathbf{x})d\boldsymbol{\Omega} + \\ + \int_\Omega \rho\dot{\mathbf{u}}^T(\mathbf{R}^T\dot{\mathbf{s}} + \boldsymbol{\Omega}\mathbf{x})d\boldsymbol{\Omega} + \frac{1}{2}\int_\Omega \rho(\mathbf{s}^T\dot{\mathbf{s}} + 2\dot{\mathbf{s}}^T\mathbf{R}\boldsymbol{\Omega}\,\mathbf{x} - \mathbf{x}^T\boldsymbol{\Omega}^2\mathbf{x})d\boldsymbol{\Omega} \end{aligned} \tag{1.10}$$

Potential energy is derived as:

$$E_p = \frac{1}{2}\int_\Omega \varepsilon^T\mathbf{E}\varepsilon d\Omega = \frac{1}{2}\int_\Omega (\nabla\mathbf{u})^T\mathbf{E}\nabla\mathbf{u}d\Omega . \tag{1.11}$$

Work of nonconservative forces **w** taking into account hypothesis of structural damping is:

$$\mathbf{w} = \frac{1}{2}\int_{\Omega} \xi \dot{\varepsilon}^T \mathbf{E} \dot{\varepsilon} d\Omega , \tag{1.12}$$

where ξ – coefficient of structural damping.

E is the elasticity matrix derived from the expression of elastic deformation low

$$\sigma(\mathbf{x},t) = \mathbf{E}(\varepsilon(\mathbf{x},t) + \xi\dot{\varepsilon}(\mathbf{x},t)) , \tag{1.13}$$

which relies vector σ associated with stress tensor with vector ε associated with deformations tensor.

Finally, applying approach of Rayleigh-Ritz, it is possible to obtain the equation of motion in matrix form. This approach consists in decomposing displacements field in truncated set of functions or generalized coordinates, which describe system motion. In the coordinate system of deformed body it will lead to:

$$\mathbf{u}(\mathbf{x},t) = \mathbf{H}(\mathbf{x})\mathbf{q}(t) , \tag{1.14}$$

where $\mathbf{H}(\mathbf{x})$ is 3 by *n* matrix of system form and $\mathbf{q}(t)$ is the set of *n* generalized displacements.

Substituting (1.14) to (1.9) the equation of motion in matrix form in rotating reference frame will be:

$$\begin{gathered} \mathbf{M}\ddot{\mathbf{q}} + \mathbf{C}\dot{\mathbf{q}} + \mathbf{L}\mathbf{q} + \mathbf{w}(\mathbf{q}) = \mathbf{g}(t) \\ \mathbf{C} = \mathbf{D} + \mathbf{P} \\ \mathbf{L} = \mathbf{K} + \mathbf{N} \end{gathered} \tag{1.15}$$

where **M**, **C**, **L** are the matrices of mass, damping and stiffness respectively, **w** and **g** are the vectors of nonconservative and excitation forces. Matrices **C** and **L** are decomposed in matrices **D** of damping, gyroscopic **P** and stiffness **K** matrices and centrifugal or spin-softening matrix **N**.

All this matrices can be calculated using following expressions:

$$\begin{gathered} \mathbf{K} = \int_{\Omega} (\nabla\mathbf{H})^T \mathbf{E} \nabla\mathbf{H} d\Omega, \\ \mathbf{D} = \int_{\Omega} \xi(\nabla\mathbf{H})^T \mathbf{E} \nabla\mathbf{H} d\Omega, \\ \mathbf{M} = \rho\int_{\Omega} \mathbf{H}^T \mathbf{H} d\Omega, \\ \mathbf{P} = \rho\int_{\Omega} \mathbf{H}^T \mathbf{\Omega} \mathbf{H} d\Omega, \\ \mathbf{N} = \rho\int_{\Omega} \mathbf{H}^T \mathbf{\Omega}^2 \mathbf{H} d\Omega. \end{gathered} \tag{1.16}$$

Using equation (1.15) the system natural frequencies and system deformed states at each eigenmode can be easily obtained. In order to deal with dynamic analysis of compressor or turbine blades, some consideration should be taken into account.

If working wheel disk is sufficiently stiff or coupling ratio between disk and blades is low, blades oscillations can be considered as isolated. From engines operation experience it is known

that fatigue cracks development also can be caused by blades resonant oscillations. In Fig. 1.4 the table of blade natural modes spectrum is shown. Parameter *m* presents number of oscillation nodal lines along blade height and *n* – along its chord. In the first line blade bending modes are placed, in the second – torsional and in the third and following lines – complex or platelet modes.

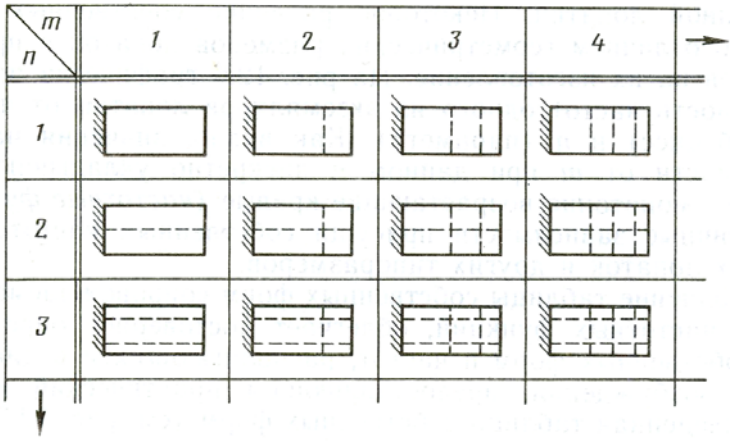

Fig. 1.4. Natural modes spectrum structure of an individual blade

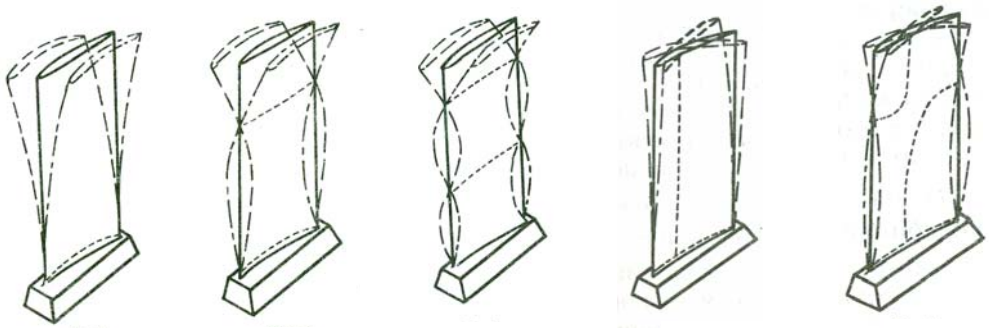

Fig. 1.5. Natural modes of typical turbine blade: (a) flexural, (b) torsional

Reconstruction of full natural modes spectrum of the working blades at required excitation frequency range (Fig. 1.5) gives the possibility to predict dangerous resonance operation modes and to establish reasons of their occurrence, if their have been detected during engine operation [7].

Prestressed effect overview

Questions of stress stiffening effect caused by structure rotation should be considered in more details. This effect is very important for relatively thin structures with bending stiffness comparatively smaller regarding to axial stiffness. In our case, the blade is an example of such structure. The effect arises from the variations in flexible body stiffness induced by inertial internal constraints and external loads.

Theoretically, stress stiffening is the second-order effect, at which structure is subjected to the initial stresses σ_{ij}^0 and displacements field u_{ij}^0. These stresses and displacements are independent on time. The main goal during the analysis is to calculate additional stresses and displacements caused by stress stiffening. Graphically, the stress stiffening effect is shown in Fig. 1.6 [30]. Stress and displacements fields can be represented by equation:

$$\begin{aligned} u_{ij} &= u_{ij}^0 + u_{ij}^* \\ \sigma_{ij} &= \sigma_{ij}^0 + \sigma_{ij}^* \end{aligned}, \tag{1.17}$$

which is system deformed and stressed state measured in its prestressed configuration Ω^*.

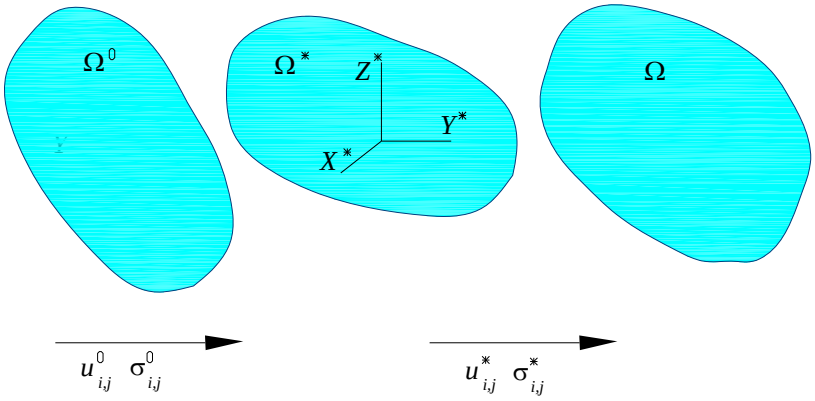

Fig. 1.6. Structure subjected to stress stiffening effect

For the prestressed structure the principle of Hamilton (1.7) can be rewritten in the form of:

$$\delta \int_{t_1}^{t_2} (E_c^* - E_{d\,\mathrm{int}}^* - E_g - E_{d\,\mathrm{ext}}^*) dt = 0, \tag{1.18}$$

where E_c^* is additional kinetic energy, $E_{d\,\mathrm{int}}^*$ is additional energy of linear deformation, $E_{d\,\mathrm{ext}}^*$ is potential of additional external forces, E_g is geometric energy of prestressed state.

It should be underlined that stress stiffening influence becomes notable in the meaning of eigenfrequency increase with increase of rotation frequency. Its effect can be represented by increment of the stiffness matrix and its notation will be omitted. Also gyroscopic **P** and spin-softening **N** matrices can be neglected due blade radial stiffness, which is very high.

1.3 Forced response of tuned bladed disk

1.3.1 Cyclic analysis of tuned bladed disks

Bladed disk assemblies in their undamaged state are an example of a periodic structure. A perfectly periodic structure consists of a chain of interconnected identical elements. If the last

element of the chain is connected to the nearest one, the structure is called cyclically symmetric. All cyclic structures share the same set of modes of vibration. This assumption of perfect cyclic symmetry simplifies the bladed disks vibration analysis. Instead of analyzing the structure as a whole, the equations of motion may be uncoupled and the size of the problem reduced to consideration of blade-disk sector dynamic behaviour.

Tuned turbine and compressor bladed disks belong to the class of periodic structures. Typically the period is one sector of the bladed disk consisting of one blade and corresponding portion of the disk. Cyclic symmetry is valid only for tuned bladed disks. For the degrees of freedom (DOFs) located in the interior of the sector and at its left and right interfaces the following indices will be used: *i*, *l* and *r* (Fig. 1.7).

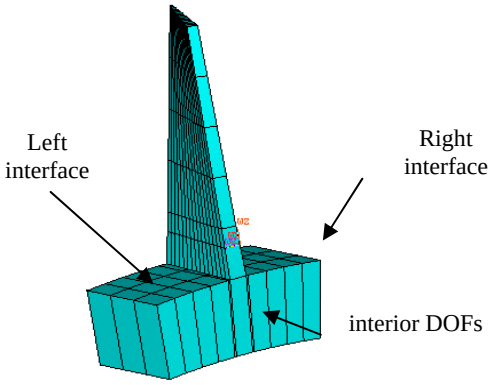

Fig. 1.7. Cyclic structure analysis components

For a wave propagating in the structure the angle of the phase lag is used to describe behaviour of two equivalent points of two adjacent sectors:

$$\beta = \frac{2\pi n}{N}, \tag{1.19}$$

where n is the number of excited diameters and N is the number of sectors (blades).

This allows description of displacements vector of the disk sector:

$$\mathbf{u}_l = e^{i\beta}\mathbf{u}_r. \tag{1.20}$$

Also the forces exercised by the adjacent left and right sectors can be expressed in the analogous way:

$$\mathbf{F}_l = e^{i\beta}\mathbf{F}_r. \tag{1.21}$$

Equation of motion of the discretized sector can be repartitioned between DOFs of left and right interfaces and interior DOFs:

$$\begin{bmatrix} \mathbf{M}_{rr} & \mathbf{M}_{rl} & \mathbf{M}_{ri} \\ \mathbf{M}_{lr} & \mathbf{M}_{ll} & \mathbf{M}_{li} \\ \mathbf{M}_{ir} & \mathbf{M}_{il} & \mathbf{M}_{ii} \end{bmatrix} \begin{bmatrix} \ddot{\mathbf{u}}_r \\ \ddot{\mathbf{u}}_l \\ \ddot{\mathbf{u}}_i \end{bmatrix} + \begin{bmatrix} \mathbf{K}_{rr} & \mathbf{K}_{rl} & \mathbf{K}_{ri} \\ \mathbf{K}_{lr} & \mathbf{K}_{ll} & \mathbf{K}_{li} \\ \mathbf{K}_{ir} & \mathbf{K}_{il} & \mathbf{K}_{ii} \end{bmatrix} \begin{bmatrix} \mathbf{u}_r \\ \mathbf{u}_l \\ \mathbf{u}_l \end{bmatrix} = \begin{bmatrix} \mathbf{F}_r \\ \mathbf{F}_l \\ \mathbf{0} \end{bmatrix}. \tag{1.22}$$

Applying equations (1.19) and (1.20), size of equation (1.22) can be decreased in two times:

$$\begin{bmatrix} \mathbf{M}_{rr}+\mathbf{M}_{ll}+e^{i\beta}\mathbf{M}_{rl}+e^{-i\beta}\mathbf{M}_{lr} & \mathbf{M}_{ri}+e^{i\beta}\mathbf{M}_{li} \\ \mathbf{M}_{ir}+e^{-i\beta}\mathbf{M}_{il} & \mathbf{M}_{ii} \end{bmatrix}\begin{bmatrix} \ddot{\mathbf{u}}_r \\ \ddot{\mathbf{u}}_l \end{bmatrix}+ \\ +\begin{bmatrix} \mathbf{K}_{rr}+\mathbf{K}_{ll}+e^{i\beta}\mathbf{K}_{rl}+e^{-i\beta}\mathbf{K}_{lr} & \mathbf{K}_{ri}+e^{i\beta}\mathbf{K}_{li} \\ \mathbf{K}_{ir}+e^{-i\beta}\mathbf{K}_{il} & \mathbf{K}_{ii} \end{bmatrix}\begin{bmatrix} \mathbf{u}_r \\ \mathbf{u}_l \end{bmatrix}=\begin{bmatrix} \mathbf{0} \\ \mathbf{0} \end{bmatrix}. \tag{1.23}$$

This equation can be represented in the form of the eigenvalues problem, in which mass and stiffness matrices depend on number of excited diameters:

$$\left(\overline{\mathbf{K}}_n-\omega^2\overline{\mathbf{M}}_n\right)\overline{\mathbf{u}}=0. \tag{1.24}$$

Solution to (1.24) will give the eigenfrequencies and deformed shapes, which are calculated using isolated sector for the given number of excited diameters *n*. To obtain deformed modes of the full structure it is enough to use equation (1.19). If to suppose that simulated sector is designated as the reference, then deformation of the *j*-th sector will be:

$$\overline{\mathbf{u}}_j=e^{i\beta}\overline{\mathbf{u}}_{ref}. \tag{1.25}$$

In the case of n=0 ($\beta=0$) and n=N/2 ($\beta=\pi$), $\overline{\mathbf{M}}_n$ and $\overline{\mathbf{K}}_n$ are real symmetric matrices and eigenvalues are also real and simple. In other cases $\overline{\mathbf{M}}_n$ and $\overline{\mathbf{K}}_n$ are complex and eigenvalues are real and double.

To conclude with cyclic symmetry analysis, it makes possible calculation of cyclic structure modes using only one sector. This reduces considerably the size of the problem, which is very critical during bladed disk structures analyses.

1.3.2 Engine order excitation

Generally, excitation during forced response analysis of engine rotating parts is supposed to be an engine order excitation. This excitation condition occurs due to the fact that the rotors are rotating in steady flow, which is non-uniform around the annulus. This non-uniformity is caused by multiple obstacles in the flow channel, e. g. stator blades, fuel nozzles, combustion chamber parts, etc. They represent by themselves spatial variation of the flow and each blade of the disk experiences these spatial variations and, therefore, responds by vibration frequencies, which are directly related to the rotor speed. Due to this the excitation force has a characteristic frequency, which is an integer multiple of the rotor rotation speed. By performing Fourier transformation of the spatial shape of the flow field, it can be decomposed into its spatial harmonics and the response of the assembly to each of these can be analyzed separately.

The forcing function of an engine order *EO* with excitation frequency ω on blade *i* can be expressed as:

$$\mathbf{F}_j=\mathbf{F}_{aj}e^{i\omega t}e^{2i\pi EO(j-1)/N}, \tag{1.26}$$

where N is the number of blades, $\mathbf{F}_j$ is the travelling wave excitation of amplitude $\mathbf{F}_{aj}$ going in the positive j direction (increasing blade number) with wave speed $c = \frac{\omega N}{2\pi EO}$. The positive direction is supposed to be in clockwise relatively to aircraft axis. The blades numeration is also performed in clockwise direction, as well as rotor rotation.

The advantage of examining individually the spatial excitation harmonics consists in the fact that each harmonic excites only modes with the same number of nodal diameters as the excitation. An assembly can have several modes with a given number of nodal diameters, like a circular plate has many modes with a different number of nodal circles for a given number of nodal diameters.

There is a convenient way to present the characteristics of forced response due to engine order excitation. It is known as Campbell or interference diagram (Fig. 1.8). Campbell diagram presents functional dependence of excitation frequency on rotor rotational frequency with indication of the response level on third axis. Also there are horizontal lines showing individual blades natural frequencies. These lines are plotted as horizontal signifying that they are independent of speed. In reality they can change with rotor speed due to centrifugal forces effect causing stiffening of blade modes, bending modes in particular. The diagram also contains engine order lines. When an engine order line crosses a natural frequency curve a resonance condition will occur.

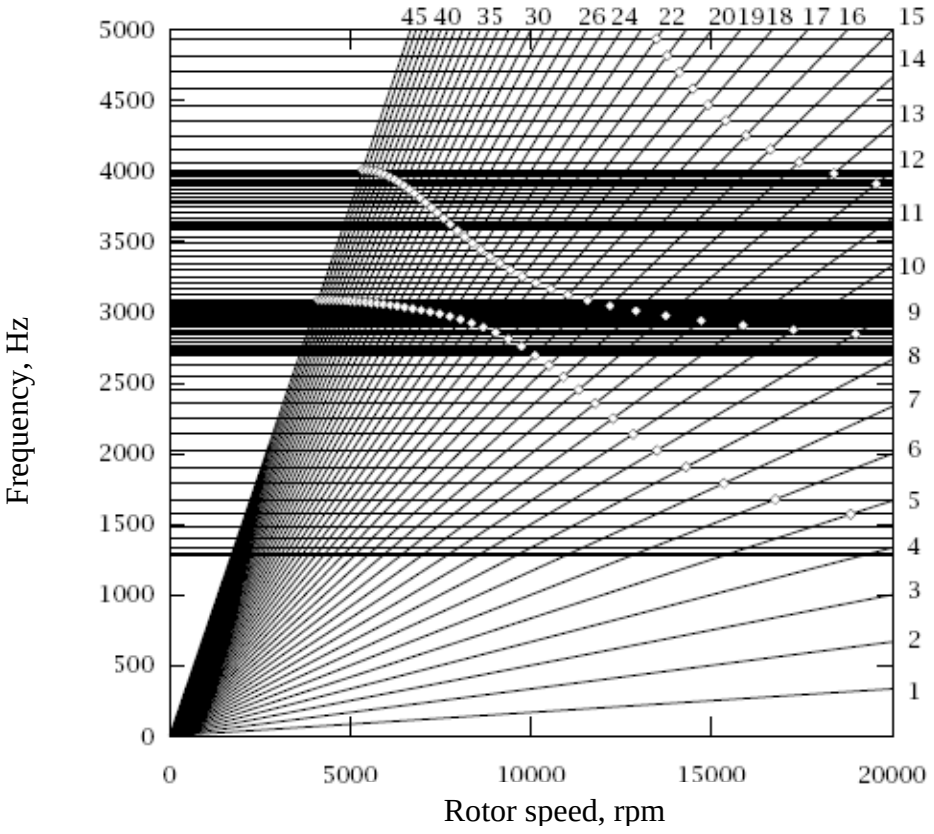

Fig. 1.8. Campbell diagram example

1.3.3 Zig-zag diagram application to periodic structures

In the case of perfect cyclic symmetry of a bladed disk the diagram known as zig-zag takes an important place [104]. It allows to establish the relationship between nodal diameters number of excited mode with excitation order (excitation harmonic multiplied by number of obstacles (stator blades) preceding the considered bladed disk). In order to establish this relationship we can use again one sector formulation as for the perfectly symmetric linear system, applying principle of superposition. The applied forces can be decomposed by spatial Fourier transformation regarding to number of excited diameters *n*. We pass here from force physical values $\mathbf{F}_j$ to their cyclic description $\overline{\mathbf{F}}_n$:

$$\begin{aligned}
\overline{\mathbf{F}}_0 &= \frac{1}{N}\sum_{j=1}^{N}\mathbf{F}_j,\\
\overline{\mathbf{F}}_n^a &= \frac{2}{N}\sum_{j=1}^{N}\mathbf{F}_j\cos\frac{n(j-1)2\pi}{N},\\
\overline{\mathbf{F}}_n^b &= \frac{2}{N}\sum_{j=1}^{N}\mathbf{F}_j\sin\frac{n(j-1)2\pi}{N},\\
\overline{\mathbf{F}}_{N/2} &= \frac{1}{N}\sum_{j=1}^{N}(-1)^{j-1}\mathbf{F}_j, \text{ (exist if } N \text{ is even)}
\end{aligned} \tag{1.27}$$

Generally, excitation force vector can be decomposed and presented in the following form for a reference sector:

$$\mathbf{F}_{ref}(t) = \sum_{k=1}^{K}\mathbf{F}_k^a\cos(kEO\Omega t) - \sum_{k=1}^{K}\mathbf{F}_k^b\sin(kEO\Omega t), \tag{1.28}$$

where *K* is the number of retained harmonics, *k* is the harmonic number, Ω is the rotation speed, rad/sec.

As in our case the external excitation rotates, the forces acting on *j*-th disk sector can be presented by equation:

$$\mathbf{F}_j(t) = \sum_{k=1}^{K}\mathbf{F}_k^a\cos\left[kEO\left(\Omega t + \frac{2\pi(j-1)}{N}\right)\right] - \sum_{k=1}^{K}\mathbf{F}_k^b\sin\left[kEO\left(\Omega t + \frac{2\pi(j-1)}{N}\right)\right]. \tag{1.29}$$

If to consider case of excitation containing a particular harmonic *k* in equation (1.29) and to calculate coefficients from equation (1.27) we will have after applying some transformations [17]:

$$\begin{aligned}
&\overline{\mathbf{F}}_n^a - i\,\overline{\mathbf{F}}_n^b =\\
&= \frac{\mathbf{F}_k^a}{N}\left[\exp(-ikC\Omega t)\sum_{j=1}^{N}\exp\left(\frac{i(kEO-n)(j-1)2\pi}{N}\right) + \exp(ikEO\Omega t)\sum_{j=1}^{N}\exp\left(\frac{-i(kEO+n)(j-1)2\pi}{N}\right)\right] -\\
&-\frac{i\mathbf{F}_k^b}{N}\left[\exp(-ikC\Omega t)\sum_{j=1}^{N}\exp\left(\frac{i(kEO-n)(j-1)2\pi}{N}\right) - \exp(ikEO\Omega t)\sum_{j=1}^{N}\exp\left(\frac{-i(kEO+n)(j-1)2\pi}{N}\right)\right]
\end{aligned} \tag{1.30}$$

It should be noted that harmonic k can excite only determined number of diameters. Equation (1.29) generates different cases supposing presence of number m that $kEO - n = mN$ or. $kEO + n = mN$. The equation relating number of excited diameters and excitation order and excitation harmonics can be written in the following manner:

$$\begin{aligned} n &= mN - kEO, \\ n &= -mN + kEO \end{aligned} \qquad (1.31)$$

One of these equations is chosen in order to respect condition $0 \le m \le N/2$. Also it should be noted that n can not exceed value of $N/2$, if N is even, or $(N\text{-}1)/2$, if N is odd. The example of generalized zig-zag diagram is presented in Fig. 1.9.

It was mentioned that zig-zag diagram is true only for perfectly periodic structures and equation (1.31) can be used only in such cases. For problem with cracked blade or mistuning presence the bladed disk structure is no longer symmetric and such approaches are seemed to be inapplicable.

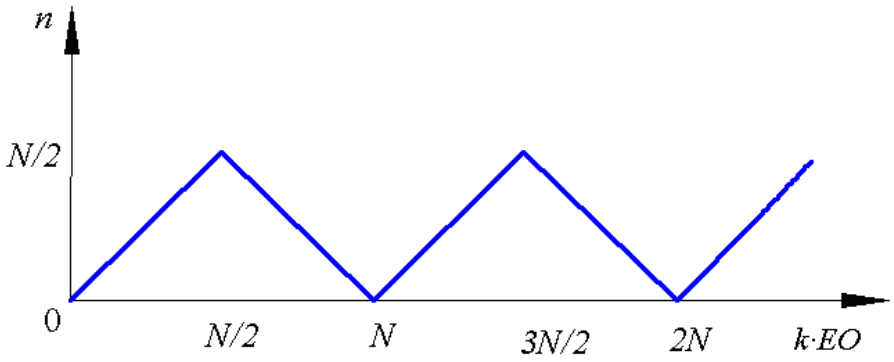

Fig. 1.9. Zig-zag diagram presentation

As example, we take bladed disk with 31 blades excited by engine order 28. In order to use equation (1.30) the input parameters are: k=1, C=28, N=31. This will give us n=3 as the number of excited diameters at m=1. If in excitation the third harmonic will be dominant (k=3), the solution can be reached at only m=3: n=31·3-28·3=9.

1.4 Mistuning and vibration localization in bladed disk structures

Bladed disk is assumed to be tuned, if all blades are strictly identical and also they are identically installed and uniformly spaced. Nowadays, the designers of aircraft gas-turbine engines are aware of inherent differences among rotor blades due to material and manufacturing tolerances as well as in-service degradation, known as mistuning. These events disrupt structure symmetry and lead the structure to be mistuned.

.

1.4.1 Mistuning influence on dynamics of bladed disk

Mistuning is a term adopted to designate the small blade-to-blade variations in geometric and material properties, which are unavoidable in all real bladed disks due to manufacturing and assembly tolerances and non-uniform wear during engine operation. After so many years of research, mistuning is still under consideration as one of the most important events. It is necessary to establish its fundamental role in aviation engine dynamics. A tremendous interest in the mistuning phenomenon can be attributed to its negative influence on bladed disk high-cycle fatigue life and, consequently, to its negative impact on durability and reliability of the engine itself. High-cycle fatigue (HCF) failures result from excessive blade vibration cycles, complicated by mistuning and aeromechanical sources, as thousands of cycles accumulate rapidly due to high rotation speeds of the engines. HCF leads to the early failure of most critical aviation engine components, as turbine or compressor blades, and in rare cases results in the loss of the engine and the entire aircraft. The fundamental blade mistuning problem, shown in Fig. 1.10, comes from the fact that unavoidable (but generally small) blade-to-blade variations produce very large uncertainty in the forced response levels of bladed disks, which, in extreme cases, can lead to a catastrophic HCF failure [87].

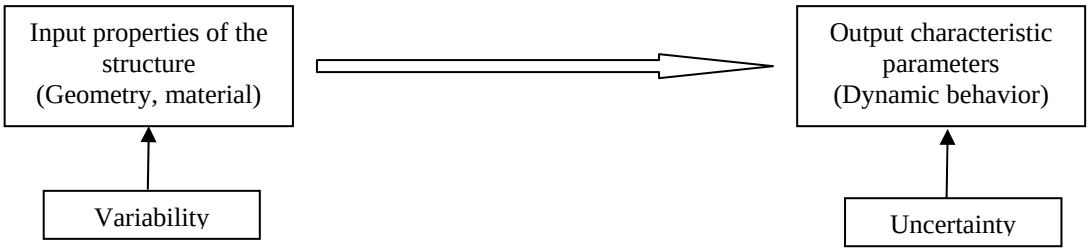

Fig. 1.10. Fundamental presentation of the mistuning problem in bladed disks

Stiffness perturbation approach. Blade mistuning can be modelled by offsets in their modal stiffness Λ or, equivalently, offsets in natural frequencies ω of the blades [9, 37]. The mistuned modal stiffness of *i*-th blade mode for the *j*-th blade may be expressed as

$$\overline{\Lambda}_j^k = (\overline{\omega}_{b,j}^k)^2 = (1+\delta_j^k)\Lambda_j^k, \tag{1.32}$$

where Λ_j^k – modal stiffness of the *j*-th tuned blade mode, δ_j^k – mistuning parameter for the *i*-th blade mode.

Due to simple implementation and validation in most studies on mistuned bladed disks, variations in Young's modulus disks are considered as the main source of blade mistuning. This

leads to uniform rescaling of the stiffness matrix. The mistuning parameter δ_j^k in (1.32) is then replaced by δ_j, which represents the offset of Young's modulus from its nominal value for *j*-th blade. Some methods of mistuning introduction exist, which allow full or partial mistuning implementation to the bladed disk model.

Mistuning projection method. This method is utilized in conjunction with cyclic analysis technique adopted for bladed disks. It is based on the assumption that the mistuned modes of a bladed disk assembly may be realized by a linear combination of its tuned modes. From the work [9] it is confirmed by two observations: the local motion of a blade in mistuned assembly is supposed to be an amplification of its tuned motion and any admissible disk shape may be realized by a linear combination of its harmonic shapes in cyclic coordinates, if all harmonics from 0 to k_{max} are included in the model. To continue with it, global stiffness and analogically mass matrices should be partitioned in the following way:

$$\overline{\mathbf{K}}_{\mathbf{full}} = \begin{bmatrix} \mathbf{I} \otimes \mathbf{K}^{\mathbf{b}} + \mathbf{Bdiag}[\Delta \mathbf{K}_{\mathbf{j}}^{\mathbf{b}}] & \mathbf{0} \\ \mathbf{0} & \mathbf{I} \otimes \mathbf{K}^{\mathbf{d}} \end{bmatrix}, \tag{1.33}$$

where $\mathbf{\Delta K_j^b}$ is a matrix containing the stiffness deviations from the nominal stiffness matrix for the *j*-th blade, $\mathbf{Bdiag}[\Delta \mathbf{K}_{\mathbf{j}}^{\mathbf{b}}]$ denotes a pseudo-block-diagonal matrix. It should be reminded that only blade stiffness mistuning is considered, thus, all other partitions are remained unaffected. Then eigenvalues problem is solved for each harmonics *k*:

$$(\overline{\mathbf{K}}_{\mathbf{full}}^{k} - \omega^2 \overline{\mathbf{M}}_{\mathbf{full}}^{k})\tilde{\mathbf{u}}^{k} = 0. \tag{1.34}$$

In expression (1.34) stiffness and mass matrices are calculated for each harmonic and then cyclic analysis approaches are applied. For constriction of such matrices the global matrices should be repartitioned with relation to: *bb* – blade interior DOF partition, *g* – blade to disk interface DOF partition, *dd* – disk interior DOF partition.

$$\tilde{\mathbf{K}}_{\mathbf{full}}^{h} = \begin{bmatrix} \tilde{\mathbf{K}}_{d,dd}^{k} & \tilde{\mathbf{K}}_{d,dg}^{k} & 0 \\ \tilde{\mathbf{K}}_{d,dg}^{k\,\mathrm{T}} & \tilde{\mathbf{K}}_{d,g}^{k} + \tilde{\mathbf{K}}_{b,g}^{k} & \tilde{\mathbf{K}}_{b,bg}^{k\,\mathrm{T}} \\ 0 & \tilde{\mathbf{K}}_{b,bg}^{k} & \tilde{\mathbf{K}}_{b,bb}^{k} \end{bmatrix}. \tag{1.35}$$

The cyclic representation of the blade matrix partition on the example of its blade to disk partitioning is accomplished as:

$$\tilde{\mathbf{K}}_{b,bg}^{k} = \begin{cases} \mathbf{K}_{b,bb}, k = 0;\ n = N/2 \\ \begin{bmatrix} \mathbf{K}_{b,bb} & 0 \\ 0 & \mathbf{K}_{b,bb} \end{bmatrix}, k \neq 0; k \neq N/2 \end{cases}. \tag{1.36}$$

A fundamental step in this method is to use a small subset of the obtained cyclic modes in order to form a reduced order model by classical modal analysis.

Partial mistuning modelling. Short overview of different mistuning modelling methods was presented in the work [87]. A bladed disk is said to be partially mistuned, if mistuning affects only its small portion. In other words, it affects only limited number of blades. Such analysis is generally motivated by the expectation that at low blade-to-blade coupling the response of a specific blade would be affected by only a few of neighbouring blades. Thus, the remaining blades could be considered as tuned. Partially mistuned bladed disks have been investigated in the work [69] and it has been shown that forced response determination became simpler than at full mistuning consideration. Reduction in complexity is a direct consequence of the limited extent of the mistuning as also was observed in [82]. Let's present our system motion equation as:

$$\mathbf{H}\mathbf{u} = \mathbf{F}, \tag{1.37}$$

where $\mathbf{H} = \mathbf{K} - \omega^2\mathbf{M} + i\omega\mathbf{C}$ is impedance matrix, F is external excitation forces vector.

In the presence of mistuning, **H** can be separated into its tuned partition $\mathbf{H}^*$ and mistuned component $\Delta\mathbf{H}$. It is convenient to partition (1.37) into:

$$\mathbf{u} = \begin{bmatrix} \mathbf{u}_d \\ \mathbf{u}_i \end{bmatrix}; \mathbf{H} = \begin{bmatrix} \mathbf{H}_{dd} & \mathbf{H}_{di} \\ \mathbf{H}_{id} & \mathbf{H}_{dd} \end{bmatrix}; \mathbf{F} = \begin{bmatrix} \mathbf{F}_d \\ \mathbf{F}_i \end{bmatrix}, \tag{1.38}$$

Due to the partial mistuning assumption, the matrices $\mathbf{H}_{di}, \mathbf{H}_{id}$ and $\mathbf{H}_{ii}$ are equal to their tuned equivalents, and $\mathbf{H}_{dd} = \mathbf{H}^*_{dd} + \Delta\mathbf{H}_{dd}$. In order to obtain the equations of motion (1.37) in a form supposing system to be tuned, the mistuning caused force $\mathbf{F}_m = \Delta\mathbf{H}_{dd}\mathbf{u}_d$ is introduced and equation (1.37) becomes:

$$\begin{aligned} \mathbf{H}^*_{dd}\mathbf{u}_d + \mathbf{H}^*_{di}\mathbf{u}_i &= \mathbf{F}_d - \mathbf{F}_m \\ \mathbf{H}^*_{id}\mathbf{u}_d + \mathbf{H}^*_{ii}\mathbf{u}_i &= \mathbf{F}_i \end{aligned}. \tag{1.39}$$

If the vector $\mathbf{F}_m$ is known, (1.39) is equation of motion of tuned system subjected to the combined action of the forces **F** and $\mathbf{F}_m$. Thus, by linearity, the response vector **u** can be rewritten as the sum of the tuned solution (response to the force **F**) and of a mistuned component (response to the force $\mathbf{F}_m$).

Adaptive perturbation method. It is known from [62] that the analysis of disk model given by (1.39) can be achieved not in the physical coordinates $\mathbf{u}(t)$, but rather in terms of a set of variables $\mathbf{q}(t)$ that accurately represent the contributions of the various modes shapes.

These new coordinates would be related to the physical ones by the relation:

$$\mathbf{u}(t) = \mathbf{T}\mathbf{q}(t), \tag{1.40}$$

where **T** is transformation matrix the columns of which are the exact mode shapes of the mistuned bladed disk or their approximation. Then equation of motion will be presented as:

$$\begin{aligned} \tilde{\mathbf{H}}\mathbf{q} &= \tilde{\mathbf{F}} \\ \tilde{\mathbf{H}} = \mathbf{T}^T\tilde{\mathbf{H}}\mathbf{T}, \tilde{\mathbf{F}} &= \mathbf{T}^T\mathbf{F} \end{aligned}. \tag{1.41}$$

Considering the magnitude of the different terms $\tilde{\mathbf{H}}_{jl}$, it was first noted that, if the columns of the matrix **T** are close approximations of the mistuned bladed disk modes, the off-diagonal terms $\tilde{\mathbf{H}}_{jl}$, $j \neq l$ are close to zero. Further, the magnitude of $\tilde{\mathbf{H}}_{jj}$ is "small" when the excitation frequency is close to one of the approximate natural frequencies ω_l associated with **T**, $\omega_l^2 = (\mathbf{T}^T\mathbf{K}\mathbf{T})_{ll} / (\mathbf{T}^T\mathbf{M}\mathbf{T})_{ll}$. On this basis, it was suggested to partition the response vector **q** in terms of the components $\mathbf{q}_S$ and $\mathbf{q}_L$ which are associated with small and large diagonal elements of $\tilde{\mathbf{H}}$ respectively. Proceeding with this partitioning the linear system (1.41) becomes:

$$\begin{bmatrix} \tilde{\mathbf{H}}_{SS} & \tilde{\mathbf{H}}_{SL} \\ \tilde{\mathbf{H}}_{LS} & \tilde{\mathbf{H}}_{LL} \end{bmatrix} \begin{bmatrix} \mathbf{q}_S \\ \mathbf{q}_L \end{bmatrix} = \begin{bmatrix} \tilde{\mathbf{F}}_S \\ \tilde{\mathbf{F}}_L \end{bmatrix}, \tag{1.42}$$

where dimension $S=d$ and dimensions $L=N-d$, d corresponds to the number of retained modes.

The computation of the steady-state components $\mathbf{q}_S$ and $\mathbf{q}_L$ can now be performed.

$$\begin{aligned} \mathbf{q}_S &= \mathbf{G}_{SS}[\tilde{\mathbf{F}}_S - \tilde{\mathbf{H}}_{SL}\tilde{\mathbf{H}}_{LL}^{-1}\tilde{\mathbf{F}}_L] \\ \mathbf{q}_L &= \tilde{\mathbf{H}}_{LL}^{-1}[\tilde{\mathbf{F}}_L - \mathbf{q}_S] \\ \mathbf{G}_{SS} &= [\tilde{\mathbf{H}}_{SS} - \tilde{\mathbf{H}}_{SL}\tilde{\mathbf{H}}_{LL}^{-1}\tilde{\mathbf{H}}_{LS}]^{-1} \end{aligned}. \tag{1.43}$$

Up to this point, the formulation is exact and the results are independent from the selection of the transformation matrix **T**. Relying on the expected large separation between the excitation frequency ω and the approximate natural frequencies ω_l corresponding to Φ_L (matrix **T** is the set of modes Φ_s and Φ_L), it is then proposed [62] that $\tilde{\mathbf{H}}_{LL}^{-1}$ (used for $\mathbf{q}_S$ and $\mathbf{q}_L$ calculation from (1.43) can be approximated by Taylor's series

$$\tilde{\mathbf{H}}_{LL}^{-1} = (\tilde{\mathbf{H}}_{LL}^{*} + \Delta\tilde{\mathbf{H}}_{LL})^{-1} = \tilde{\mathbf{H}}^{*-1}_{LL} - \tilde{\mathbf{H}}^{*-1}_{LL}\Delta\tilde{\mathbf{H}}_{LL}\tilde{\mathbf{H}}^{*-1}_{LL} + \dots, \tag{1.44}$$

where matrices $\tilde{\mathbf{H}}^{*}$ and $\Delta\tilde{\mathbf{H}}$ are the tuned and mistuned components respectively.

Introducing a truncated form of this series leads to the required approximation of the forced response of the mistuned disk. This procedure was called adaptive because its accuracy can be increased or decreased varying the number of retained modes.

1.4.2 Vibration localization in mistuned bladed disks

Having obtained the fundamental mistuning model, a major concern becomes the prediction of the ability to detect cracked blade on the base of the bladed disk forced response. The easiest case at the presence of certain level of mistuning is if we are able to localize cracked blade dynamic

response. Generally the maximum forced vibration response of a subcomponent (blade) of a mistuned structure is often larger than that of a perfectly tuned structure. It comes from that mechanical energy stored in a subcomponent of a mistuned structure is different from those stored in other subcomponents. This is called the vibration localization of a mistuned structure.

The localization phenomenon has recently received wide attention and it has been shown to occur in various types of nearly periodic structures, namely bladed disk assemblies [41, 76]. Localization phenomenon has something similar with damping. It also leads to vibration amplitude decay. But the nature of this decay is different. In the case of damping, energy is dissipated because vibrations are transmitted throughout the system, whereas in the case of localization, the energy is simply absorbed in particular region within the structure. Localization occurs because waves propagating away from the energy source are rejected by the boundary between the slightly different subcomponents constituting the nearly periodic structure. The resulting energy accumulation may lead to higher local amplitudes than it can be predicted, if perfect periodicity has been supposed. This event can possibly have disastrous effect.

The manner, in which the subcomponents making up a nearly periodic structure are interconnected (Fig. 1.11), plays a major role in its dynamics. The vibration energy passes between subcomponents through only these connections. If neighbouring subcomponents are connected through several DOFs, the periodic structure is said to be multi-coupled structure. Localization in multi-coupled systems is much more difficult to analyze, because there are multiple wave pairs and, therefore, the decay rates of all the different wave types must be considered. Next, at any given subcomponent a wave type may not only be partially rejected and transmitted into waves of the same type, but it may be partially rejected and transmitted into other wave types as well.

Usually, for such analyses, in the case of turbine rotor, each subcomponent represents by itself a blade with corresponding partition of the disk. Coupling between blades is due to structural coupling through the disk and aerodynamic coupling through the fluid. Blades may also be connected through a shroud. Hence, a bladed disk is a complex multi-coupled structure. Some methods of vibration localization in mistuned bladed disk exist. Among them are transfer matrix approach and Lyapunov exponents utilization approach.

Transfer matrix approach. The transfer matrix modelling of nearly periodic structures undergoing harmonic motion was discussed in the work [76]. It is supposed that only nearest neighbouring subcomponents are coupled. An interface is the points separating two subcomponents. Transfer matrix corresponds to the state vector for the subcomponents. It relates the states at two consecutive interfaces, or two consecutive subcomponents. The dimension of the state vector must be twice the number of coupling coordinates at each interface. A state vector is most commonly defined as the displacements of the coupling coordinates at the interface and the associated forces.

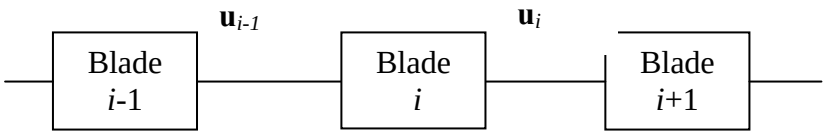

Fig. 1.11. A schematic diagram of nearly periodic system

A transfer matrix that relates the deflections and forces at adjacent interfaces can be presented as:

$$\begin{bmatrix} \mathbf{q} \\ \mathbf{F} \end{bmatrix}_i = \mathbf{T}_o \begin{bmatrix} \mathbf{q} \\ \mathbf{F} \end{bmatrix}_{i-1}, \tag{1.45}$$

where index 0 means a tuned system. For mistuned system the transfer matrix will be different for each subcomponent. Alternatively we could define a state vector for subcomponent as the deflections of the coupling coordinates at both ends of the subcomponent, which rates two adjacent subcomponents:

$$\begin{bmatrix} \mathbf{q}_{i+1} \\ \mathbf{q}_i \end{bmatrix} = \mathbf{T}_o \begin{bmatrix} \mathbf{q}_i \\ \mathbf{q}_{i-1} \end{bmatrix}. \tag{1.46}$$

The representation in equation (1.46) does not take into account external forces acting on the system and hence only the free dynamics is considered. Such formulation requires two equations relating the coupling coordinates $\mathbf{q}_{i\text{-}1}$, $\mathbf{q}_i$ and $\mathbf{q}_{i+1}$. One is the equation of motion taken at interface i:

$$-\mathbf{q}_{i+1} + \beta_0(\omega)\mathbf{q}_i - \mathbf{q}_{i-1} = 0, \tag{1.47}$$

where $\beta_0(\omega)$ is a function defined by the equation of motion of the subcomponent and depends on the frequency of harmonic motion. At the absence of aerodynamic and Coriolis forces equation (1.47) is symmetric. The second equation in (1.47) is identity $\mathbf{q}_i = \mathbf{q}_{i\text{-}1}$. Hence, each subcomponents of tuned structure is described by the same transfer matrix representation:

$$\begin{bmatrix} \mathbf{q}_{i+1} \\ \mathbf{q}_i \end{bmatrix} = \begin{bmatrix} \beta_0(\omega) & -1 \\ 1 & 0 \end{bmatrix} \begin{bmatrix} \mathbf{q}_i \\ \mathbf{q}_{i-1} \end{bmatrix} = \mathbf{T}_o \begin{bmatrix} \mathbf{q}_i \\ \mathbf{q}_{i-1} \end{bmatrix}. \tag{1.48}$$

When mistuning is introduced into the cyclic system, its periodicity is broken. The mistuning may be caused by a parameter which appears in relation to i-th interface - the mistuning of parameters of individual blades. When the symmetry of equation (1.48) is no longer exist and it replaced by

$$\begin{bmatrix} \mathbf{q}_{i+1} \\ \mathbf{q}_i \end{bmatrix} = \begin{bmatrix} \beta(\delta_i) & -1 \\ 1 & 0 \end{bmatrix} \begin{bmatrix} \mathbf{q}_i \\ \mathbf{q}_{i-1} \end{bmatrix} = \mathbf{T}_i \begin{bmatrix} \mathbf{q}_i \\ \mathbf{q}_{i-1} \end{bmatrix}, \tag{1.49}$$

where δ_i is the small deviation of the parameter from its average value, defining the mistuning for the i-th subcomponent. It is commonly accepted as random variable of mean zero.

Alternatively, the mistuning may be caused by a parameter which appears at interfaces, *i* and *i*+1. Then equation (1.48) becomes:

$$\begin{bmatrix} \mathbf{q}_{i+1} \\ \mathbf{q}_i \end{bmatrix} = \begin{bmatrix} \beta(\delta_i, \delta_{i-1}) & -\alpha(\delta_i, \delta_{i-1}) \\ 1 & 0 \end{bmatrix} \begin{bmatrix} \mathbf{q}_i \\ \mathbf{q}_{i-1} \end{bmatrix} = \mathbf{T}_{i,i-1} \begin{bmatrix} \mathbf{q}_i \\ \mathbf{q}_{i-1} \end{bmatrix}. \quad (1.50)$$

When mistuning is introduced, the system is no longer symmetric. This loss of cyclicity results in a splitting of the double natural frequencies, such that the system has *P* clusters of *N* distinct natural frequencies, where *N* is the number of blades and *P* is the number of subcomponent DOFs. The clusters of frequencies correspond, approximately, to the passbands of the system tuned counterpart, although generally they are wider. The corresponding mode shapes are standing waves that no longer possess the cyclic symmetry exhibited by the tuned system, where all blades vibrate with the same amplitude. Instead, the vibration energy may be concentrated in a handful of blades that have significantly larger deflection than the majority of blades. This phenomenon is referred to the mode localization.

Lyapunov exponents utilization approach. Another way that allows analyzing the localization in a multi-coupled system is to find the Lyapunov exponents of global wave transfer matrix [16], which is the matrix that relates the vector of wave amplitudes at one end to the wave amplitude vector at the other end. The Lyapunov exponents provide a measure of the rates of amplitude decay for the various wave types.

The harmonic dynamics of any subcomponent may be represented by 2*m* by 2*m* transfer matrix **T**, which depends on the frequency of motion. If the system is perfectly periodic, then each transfer matrix is identical and adjacent states are related by

$$\mathbf{u}_i = \mathbf{T}_i \mathbf{u}_{i-1}, \quad (1.51)$$

For mistuned system the transfer matrix will be different for each subcomponent. It si possible to use **X**, the matrix of eigenvectors of **T**, to define the transformation from physical to wave coordinates:

$$\mathbf{u} = \mathbf{X}\mathbf{v}, \quad (1.52)$$

where **v** – vector of wave amplitudes.

Equation (1.52) can be rearranged then in the form of:

$$\mathbf{v}_i = \mathbf{W}_i \mathbf{v}_{i-1}, \mathbf{W}_i = \mathbf{X}^{-1}\mathbf{T}_i\mathbf{X}. \quad (1.53)$$

Note, that in tuned system **W** is equal for all subcomponents and it is diagonal, with the diagonal elements equal to the eigenvalues of **T**. Since all off-diagonal elements are zero, this implies that for tuned system there is no wave rejection and any interaction between different wave types., For a mistuned system, however, there will be nonzero off-diagonal terms indicating both wave interactions and rejections.

The goal here is to describe the asymptotic behaviour of the wave vector **v** as it is taken as subsequent subcomponents along the system. If to have an arbitrary initial wave vector $\mathbf{v}_0$ at the left end of a nearly periodic structure, the wave vector after *N* bays is:

$$\mathbf{v}_N = \overline{\mathbf{W}}_N \mathbf{v}_0, \tag{1.54}$$

where $\overline{\mathbf{W}}_N = \mathbf{W}_N \mathbf{W}_{N-1} ... \mathbf{W}_1$ is the global wave transfer matrix for the *N*- subcomponents segment.

Norm of vector **v** is:

$$\begin{aligned} \|\mathbf{v}\| &= [\langle \mathbf{v}, \mathbf{v} \rangle]^{1/2} = [\langle \mathbf{v}^* \mathbf{v} \rangle]^{1/2} \\ \|\mathbf{v}_N\| &= [\langle \mathbf{v}_0^* \overline{\mathbf{W}}_N^* \overline{\mathbf{W}}_N \mathbf{v}_0 \rangle]^{1/2} \end{aligned}, \tag{1.55}$$

where $\langle \cdot, \cdot \rangle$ denotes inner product and asterisk sign -complex conjugate of the transpose.

Evidently, the magnitude of this norm will depend on the eigenvalues of $\overline{\mathbf{W}}_N^* \overline{\mathbf{W}}_N$. It is necessary to introduce the singular values of matrix. The singular values of an arbitrary matrix A are defined as:

$$\sigma_i(\mathbf{A}) = [\lambda_i(\mathbf{A}^* \mathbf{A})]^{1/2}, \tag{1.56}$$

where λ_i – eigenvalues ordered by decreasing magnitude.

Thus, the singular values of $\overline{\mathbf{W}}_N$ dictate the growth or decay of the wave vector after *N* subcomponents. Furthermore, the *N*-th root of the singular values describes the growth per subcomponent of the wave vector. Since $\overline{\mathbf{W}}_N$ is a product of independent and identically distributed random matrices, asymptotically the *N*-th root of the singular values are non-random with probability one. The *N*-th root of an arbitrary *k*-th singular value is of the form.

$$[\sigma_k(\overline{\mathbf{W}}_N)]^{1/N} \to \exp(\gamma_k), N \to \infty, \tag{1.57}$$

where γ_k is the *i*-th Lyapunov exponent. Thus, the Lyapunov exponents are a measure of the asymptotic exponential growth or decay rate of the wave vector. The Wolf algorithm can be used for Lyapunov exponents calculation [105].

1.5 Dynamics of bladed disk with a crack presence in the blade

Vibration-based inspection of structural behaviour offers an effective tool of non-destructive testing. The analysis of the dynamic response of a cracked structure to excitation forces and the monitoring of alterations, which may occur during its lifetime, may be employed as a global integrity-assessment technique to detect the presence of a crack. Indeed it is well known that, in the case of simple structures, crack position and depth can be determined from changes in natural frequencies, modes of vibration or the forced response amplitude level. At the same time for

complex structures or their models, specifying of such dependences is generally unattainable task. In this case only the fact of the crack presence is seemed to be detectable. Reviewing experimental studies we can make common conclusion from them that decrease in the natural frequencies of the beam-like models of cracked blades is the main derived diagnostic sign. Some approaches exist to inspect the vibration response of the structure with non-propagating crack by means of stochastic analysis [14–15], acoustic signals analyzing [29, 108] and using its frequency or modal data [39, 42, 56, 61, 65, 94]. Structure's displacements in time domain also give information about cracked presence in the structure [59, 63, 97]. Majority of authors use open crack model, which also can be modelled by system stiffness reduction [48, 76]. But in reality, it is not sufficient for the cracked blade to be described by a model of open crack. Therefore it must be taken into account that the crack alternately opens and closes, thus giving rise to natural frequencies falling between those corresponding to the open and closed cases. Next, the short overview of different approaches aimed on crack presence simulation is presented.

Perturbation method. This method is very understandably described in the work [24]. A crack in blade, or in its approximation by beam, can cause local stiffness change, and correspondingly, results in changes in structural dynamic properties such as natural frequencies and mode shapes. For simplicity, it is assumed that the crack extends over the entire width of the blade. The *i*-th natural frequency and mode shape of the undamaged beam are ω_i and ϕ_i, respectively. When the crack occurs, the *i*-th natural frequency and mode shape become ω_i^* and ϕ_i^*. Neglecting the mass change and other geometrical changes due to the crack presence, the first-order perturbation method is applied to present numerically the changes in the natural frequencies. It is based on fractional changes in modal strain energy, which can be related to the fractional changes of the eigenvalues (frequencies) in the following way:

$$\frac{\partial \lambda_i}{\lambda_i} = \frac{\partial W_i}{W_i}, \tag{1.58}$$

where W_i and ∂W_i are the *i*-th modal strain energy of the undamaged structure and its change due to the crack, and $\partial \lambda_i / \lambda_i$ is the fractional change of the *i*-th eigenvalue due to the crack.

This approach can be utilized for simple structures like Euler-Bernoulli beams, but for more complex structures it is almost impossible to obtain crack parameters and strain energy release relationships.

Breathing crack model. Such model can be considered as the most representative for crack behaviour simulation [67]. In the work [18] it is dealt with crack alternating behaviour as the response on externally applied varying load. In some studies [1, 23] it was shown that the load-displacement response of a crack can be represented by the curve shown in Fig. 1.12, where P_1, P_2 and P_3 are the points when crack is fully open, partially open and fully closed respectively. Such

type of load-displacement relationship leads to a continuous presentation of crack DOFs stiffness function (DOF describing crack zone geometry) such as

$$k = \frac{dP}{du} = k(t)\,. \tag{1.59}$$

Here, time t is chosen as the independent variable because the crack opening level depends on external load magnitude, which varies with time due to vibration. For mathematical reason, the continuous stiffness in equation (1.59), can be decomposed into Fourier series. Examining the dynamic response of a crack at its first mode, the stiffness may be expressed as

$$k(t) = k_0 + k_{\Delta c}(1+\cos\omega t)\,, \tag{1.60}$$

where ω is the crack breathing frequency, which is equal to the excitation frequency, k_0 is the stiffness of the structure when crack is fully open.

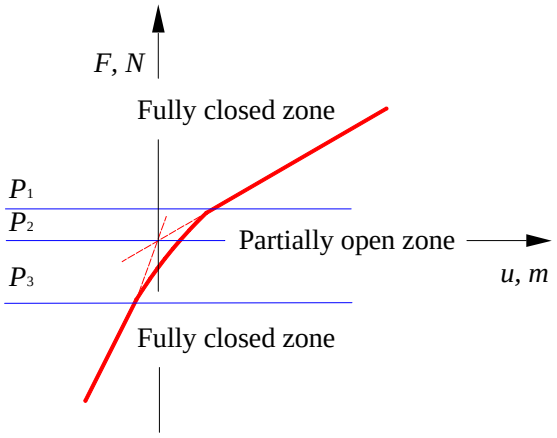

Fig. 1.12. Schematic load-displacement curve for breathing crack behaviour case

The presented above approach is used in many works due to its simplicity of formulation and possibility of accurate crack breathing process simulation using simplified beam-like cracked blade model.

Contact simulation of crack presence in structure. An approach presented in the work [49] with the use of contact analysis elements seems to be very perspective to use throughout our study (Fig. 1.13). In this case the crack presence effect can be simulated by supposing the contact interaction between crack sides. This approach seems to be most realistic as far as it is able to take into account all aspects of inside crack interaction and its effect on cracked structure dynamics. When two or more bodies come into contact, due to externally applied loading, the contact region may increase or decrease, as with crack closing and opening, and these changing boundary conditions result in a non-linear contact problem. In contact analysis often no a priori information concerning the contact conditions is available, which presents considerable difficulties.

When the normal force F_n is compressive, the interface remains in contact and it is assumed that the normal displacements and forces respond as a linear spring. When the normal force F_n is

extension, the contact is broken and no force is transmitted. The change in normal displacement, assuming that there is no gap between bodies, can be given as

$$\Delta u_n = u_{n,B} - u_{n,A}, \tag{1.61}$$

where $u_{n,B}$ and $u_{n,A}$ are the displacements in the normal direction.

The load-displacement curve can now be given as in Fig. 1.13b. Force in the tangent direction is defined only when F_n<0. If $|F_t| < \mu|F_n|$, where μ is the friction coefficient, there is no sliding at the interfaces. Consequently, tangential displacements and forces respond as a linear spring.

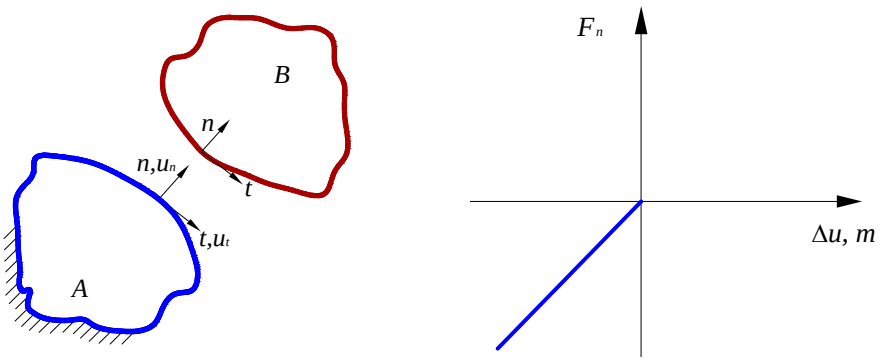

Fig. 1.13. Contact approach for crack behaviour simulation: (a) contact between two bodies, (b) load-displacement curve (normal force)

By using load-displacement relationships the contact stiffness for a nodal point, will be:

$$k = \frac{F_n}{\Delta u_n}. \tag{1.62}$$

This approach was decided to be very representative for crack presence simulation as it can accurately describe crack sides interaction and at the same time it is able to provide crack behaviour simulation, which reflects its breathing nature.

Harmonic balance approach for crack presence simulation. Harmonic balance method has gained a wide spread in the engineering calculation of the complex non-linear problems. And cracked blade is not exclusion, as it was presented in the works [84, 90–91]. Numerical integration of non-linear equation of motion is usually very computer-time consuming. For this reason some researchers have studied techniques capable to obtain the response as steady-state solution avoiding direct integration. In [50] square-wave function $f(t)$ was used to model the beam stiffness, transforming the non-linear equations of motion (1.15) into a linear periodically time-variant equation:

$$\mathbf{M}\ddot{\mathbf{u}} + \mathbf{C}\dot{\mathbf{u}} + (\mathbf{K}_u - \Delta\mathbf{K}f(t))\mathbf{u} = \mathbf{F}. \tag{1.63}$$

In order to apply harmonic balance method the closing crack function $f(t)$ in Fourier series can be expressed as

$$f(t) = \frac{1}{2} + \frac{2}{\pi}\cos(\omega t) - \frac{2}{3\pi}\cos(3\omega t) + \frac{2}{5\pi}\cos(5\omega t) + \ldots, \tag{1.64}$$

where ω represents the angular frequency of harmonic input.

The solution of equation (1.63) was obtained by assuming that

$$\mathbf{F} = \begin{bmatrix} F_1 \\ \vdots \\ F_j \end{bmatrix} \cos(\omega t), \tag{1.65}$$

where F_j is amplitude of external excitation force applied in j-th DOF.

And all DOFs of structure can be expressed as

$$u_j = \sum_{j=1}^{K} a_i \cos(j\omega t) + \sum_{j=1}^{K} b_i \sin(j\omega t), \tag{1.66}$$

where a_i and b_i are the components of vectors of the constant variables. This approach seems to be extremely efficient both in terms of computation time and analytically. Furthermore, this approach enables the higher harmonics of the response to be obtained quickly for any excitation frequency.

All presented above approaches allows simulation of crack presence effect on dynamic properties. But those, which offer parametrical dependence between crack parameters and their influence on dynamic properties, use simplified beam-like blade model. In the case of more or less realistic blade geometry, such functional dependences are almost impossible to derive. As most realistic way for crack presence simulation, the contact approach can be used. But it is very time expensive due to complexity of the problem to solve. So, the best way is application of such methodology with the harmonic balance method, which is able to reduce the computation time and to be very representative for the non-linear problem solution.

Conclusions

The chapter was devoted to the consideration of the main aspects surrounding the problem of cracked blade identification process.

Recently developed approaches of mistuning modelling and its influence on bladed disk dynamic response was overviewed, special attention was paid to vibration localization phenomenon in the presence of mistuning. These events are supposed to have significant effect on cracked blade detectability.

Cracked blade identification process should be developed inside creation of not only realistic model, but also in conjunction with durable and reliable engine health monitoring system. Such system should be able to deliver the data required for cracked blade identification. Different models of crack presence in the blade have been developed and all of them have their own advantages. For future development the approach combining contact interaction inside the crack and harmonic balance method will be used.

In order to continue the following studies it will be necessary to discuss in the next chapters the elements of contact analysis for accurate definition of its application to cracked blade model. Moreover, the fracture mechanics theory should be examined with the goal to consider functional dependences between crack parameters and amplitude of forced response.

Chapter 2

Contact analysis and crack propagation

The present chapter is the preliminary base for the main goal of the research – cracked blade model development. It will cover two very important areas of interest: contact analysis principal fundamentals and theoretical formulation of the crack presence in a structure using fracture mechanics theory.

Necessity to present some basic formulation dealing with contact analysis comes from statement of the crack behavior in the blade. As it was mentioned earlier the contact analysis in conjunction with harmonic balance method is supposed to be the most appropriate to simulate crack breathing process. For clarity and brevity of presentation, the main attention is paid to frictionless contact of an elastic body with a rigid obstacle.

Fracture mechanics element will be shown with the aim to describe process related to crack initiation, propagation and cracked structure failure after certain number of loading cycles has been performed

2.1. Contact analysis elements for crack inside interaction modeling

It is well known that surfaces of the contact interaction in reality do not have planar shape, even if they have been polished. In the microscopic level we can observe presence of bumps and cavities on the contact surfaces. Such irregularities are termed as the surface roughness and depending on their level they can be included or not to the analysis. Different experiments and studies showed that succession of the roughness peaks has height, which vary from $5 \cdot 10^{-7}$m. to $5 \cdot 10^{-5}$m. At the same time the distance between these peaks has bigger spread, varying from $5 \cdot 10^{-7}$m. to $5 \cdot 10^{-3}$m. Inclination of the peaks is estimated to be very small, about 5-12 degrees. Also contact surfaces state will depends on external conditions.

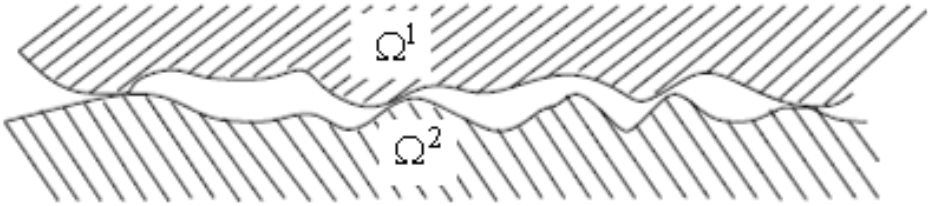

Fig. 2.1. Two solid bodies contact interaction

It means that for two bodies in contact (Fig. 2.1) realistic contact interface will be different from supposed in the analysis due to the roughness of surfaces. It will be lower of the first contact point. Consequently, we can say that stresses appeared in contact points will be comparable with material mechanical properties.

The question of the plastic deformation of the roughness peaks is always under consideration of many researchers [3, 34, 106]. Since materials of the same or comparable hardness are in the contact, a peak can be deformed plastically at the moment of its first contact with opposite surface. At the same time material relaxation will be performed in the elastic way. Then, if new loading will be applied to continue contact interaction, the peak will be under elastic deformation up to the moment when material stress will be equal to that, which induced plastic deformation during previous loading step (Fig. 2.2). Different mathematical models were proposed to try to simulate contact surfaces with the roughness and obtain same results of correlation between normal contact loading and realistic contact surface. They gave the possibility to obtain the law of Coulomb, which was experimentally validated.

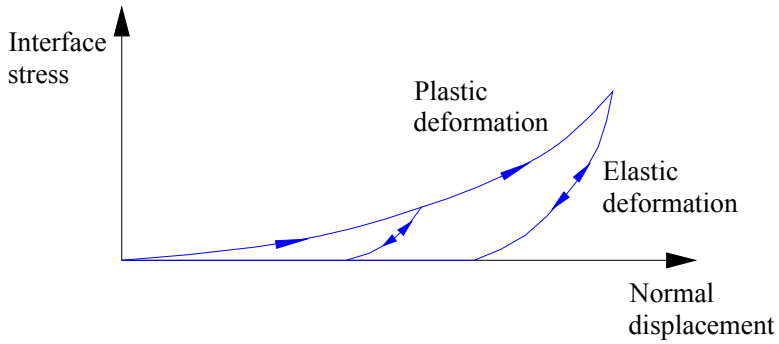

Fig. 2.2. Schematic presentation of metallic contact surface loading with roughness presence

Because in following simulations we will deal with metal surfaces imposed to be in dry contact, it is worth to say some words about such metal surfaces. The scheme of the metal surface is shown in Fig. 2.3. In contact problems with friction performances of metal surface depend on presence of different layers covering metal surface.

Fig. 2.3. Schematic presentation of film covering metal surface

The first covering layer is the layer of oxygenation formed by reaction with oxygen from air. In contact problems with friction the last one strictly depends on presence of different layers covering metal surface. For some materials with low reaction abilities with oxygen such layer can be absent. Then we can find the layer of absorbed gas, which came from the atmosphere and consists of the water and oxygen molecules. Finally, the metal surface is covered by the layer of contaminants, which are generally composed from grease and oil. In these conditions initial dynamic friction coefficient in most of cases varies between 0.1 and 0.3. Thus, friction coefficient will increase gradually with decrease of the layer of contaminants.

2.1.1 Taking into account friction in contact analysis

Firstly, it was discovered that friction force is proportional to the normal loading. Coulomb verified experimentally this fact and stated distinction between static and dynamic frictions supposing contact bodies to be rigid (Fig. 2.4 a).

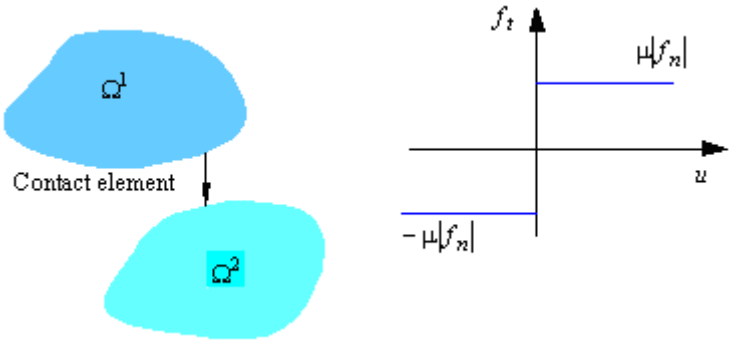

(a) (b)

Fig. 2.4. Schematic presentation of: (a) contact element,
(b) force-displacement curve of Coulomb's model

Classic friction contact problem can be explained using following aspects [75]:

1. Friction force is proportional to the normal contact force:

$$|f_t| \le \mu f_n, \tag{2.1}$$

where μ is the friction coefficient.

Very often two values of the μ coefficient are defined: static friction coefficient μ_s and dynamic friction coefficient μ_d. Static friction coefficient is applied at contact initiation phase, when dynamic friction coefficient is applied during sliding.

2. Friction coefficient is independent on contact process.
3. Static friction coefficient is bigger then dynamic one. Such statement can be confirmed experimentally.
4. Dynamic friction coefficient is independent on sliding velocity. But it is only simplification, because in reality there is dependence between these parameters [85] and such dependence can be stricter in the case of stick-slip movement [103].
5. As soon as tangential movement appears, friction force has same path as relative velocity of two contact bodies, but in opposite direction:

$$f_t \le \mu f_n \frac{v_r}{\|v_r\|}. \tag{2.2}$$

Graphical representation of Coulomb's law is shown in Fig. 2.4b. Also it should be noted that friction coefficient varies with materials properties of contact bodies.

Also Ying [106] defined the bilinear model (Fig. 2.5a) of the contact with friction. This model consists in association of spring with stiffness *k* and one contact element with dry friction, for which Coulomb's law is used.

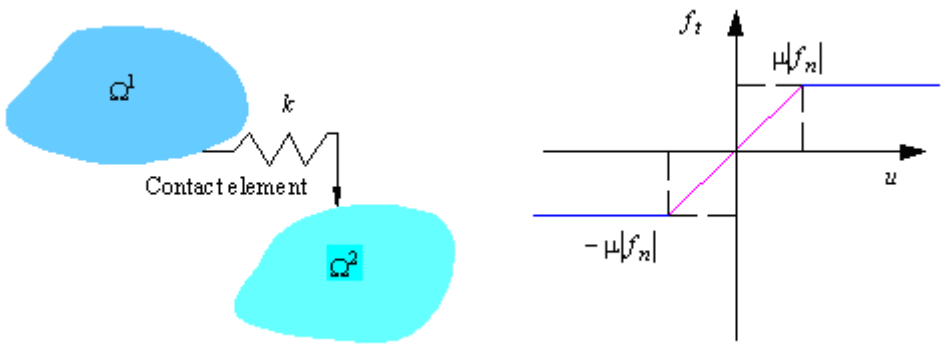

(a) (b)

Fig. 2.5. Schematic presentation of bilinear model (a) and force-displacement curve of bilinear model (b)

Utilization of both spring properties and friction element provides mathematical formulation of the bilinear model in the following form:

$$\begin{cases} f_t = ku, |u| < u_0 \\ f_t = ku_0, |u| > u_0 \end{cases}. \tag{2.3}$$

Bilinear model presents by itself the extension of Coulomb's law by adding a flexibility to the system. Such approach has very important advantage to pass through the singularity in function zero.

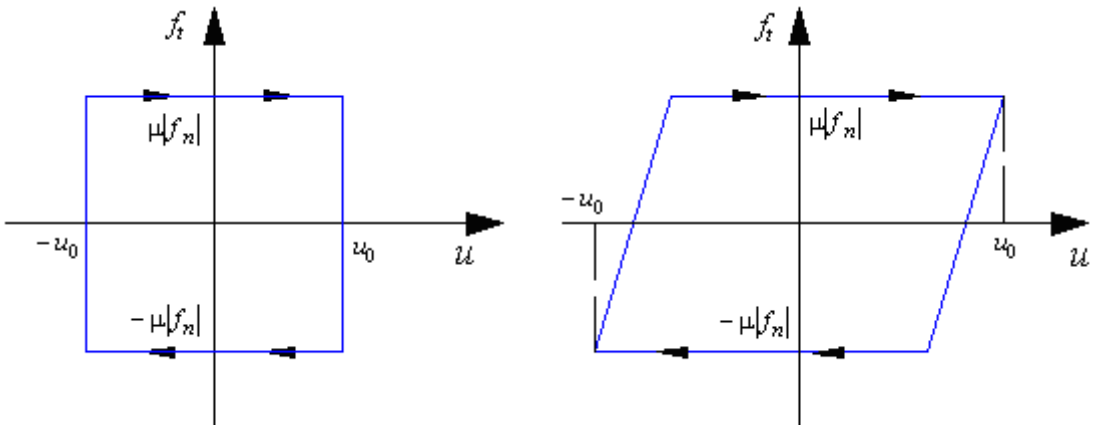

(a) (b)

Fig. 2.6. Schematic presentation of contact models hysteretic properties:
(a) Coulomb's law, (b) bilinear model

2.1.2 Stress-deformed state in contact zone

Let's consider the problem on contact between two deformable solids as it is shown in Fig. 2.7. Deformations are supposed to be small. This supposition also invokes the consideration of the small sliding. The solids occupy two domains Ω^l with boundaries $\Gamma^l, l = 1,2$. They initially come into the contact by boundary $\Gamma_c = \Gamma_c^1 = \Gamma_c^2$. Each solid is subjected to the volumetric forces f^l action and forces T^l acting on Γ_f^l. Consequently, displacement field U^l is imposed on Γ_u^l.

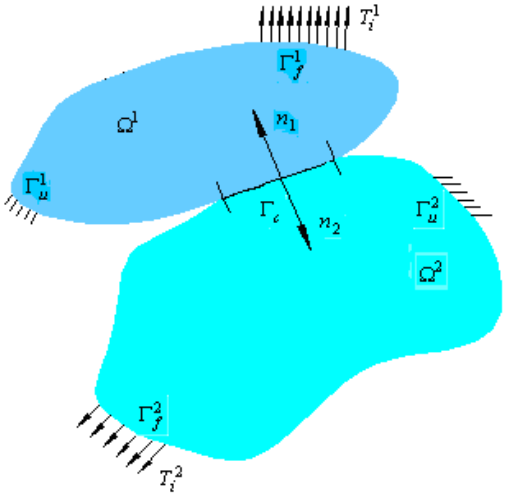

Fig. 2.7. Schematic presentation of contact interaction between two solids

Since deformations supposed to be small, the tensor of deformations can be written:

$$\varepsilon_{ij}(u^l) = \frac{1}{2}(u_{i,j}^l + u_{j,i}^l). \qquad (2.4)$$

Properties of the solids are accepted to be elastic and elasticity tensor a^l_{ijkh} will be used in analysis. Stress tensor will be expressed then as:

$$\sigma^l_{ij} = a^l_{ijkh}\varepsilon_{kh}(u^l), l = 1,2. \tag{2.5}$$

Equation of motion in the local form will be:

$$\sigma^l_{ij,j} + f^l_i = \rho_i \frac{\partial^2 u^l_i}{\partial t^2}, l = 1,2. \tag{2.6}$$

Initial conditions for the presented problem are expressed by:

$$u^l(0) = u^l_0, \dot{u}^l(0) = \dot{u}^l_0, l = 1,2. \tag{2.7}$$

For $l = 1,2$ we will have on Γ^l_u:

$$u^l(0) = U^l_0, \dot{u}^l(0) = \dot{U}^l_0 \tag{2.8}$$

On the boundary Γ_c the stress vector is decomposed in normal and tangential components:

$$T^l = \sigma^l_n n^l + \sigma^l_t, l = 1,2, \tag{2.9}$$

where n^l is normal to the body *l*.

Distance between two bodies is defined on Γ_c:

$$d(u) = -(u^1 n^1 + u^2 n^2), u = (u^1, u^2). \tag{2.10}$$

Finally, conditions of the contact with friction can be presented by following expressions:

$$d \geq 0 \begin{cases} \sigma^1_n = \sigma^2_n = \sigma_n \\ \sigma^1_t = -\sigma^2_t = \sigma_t \end{cases}; \tag{2.11}$$

$$d > 0 \begin{cases} \sigma_n = 0 \\ \sigma_t = 0 \end{cases}; \tag{2.12}$$

$$d = 0 \begin{cases} \dot{d} = 0 \\ \left\|\sigma_t\right\| < \mu\left|\sigma_n\right| \Rightarrow \dot{u}^1_t - \dot{u}^2_t = 0 \\ \left\|\sigma_t\right\| = \mu\left|\sigma_n\right| \Rightarrow \dot{u}^1_t - \dot{u}^2_t = -\lambda\sigma_t \end{cases} \tag{2.13}$$

Equation (2.11) presents by itself Coulomb's law of friction. Locally, two solid bodies are in immovable contact, if condition $\left\|\sigma_t\right\| < \mu\left|\sigma_n\right|$ is provided and sliding occurs at $\left\|\sigma_t\right\| = \mu\left|\sigma_n\right|$. From the formulas (2.9–2.11) it is possible to derive the presence of unilateral contact. Two solids can not penetrate each other in this case.

Classical condition of impenetrability can be expressed in conjunction with condition of compression during the contact and an additional condition:

$$d \geq 0, \sigma_n \leq 0, d\sigma_n = 0 . \tag{2.14}$$

In the case of dynamic contact problem one more condition is added:

$$d\dot{\sigma}_n = 0 . \tag{2.15}$$

2.1.3 Virtual work principle

The objective of this chapter is to derive problem shown in the previous subchapter adapted for following discretization. Let's define fields:

$$\begin{gathered} V(\Omega^l) = \{v^l, v^l = U^l \text{ at } \Gamma_u^l\} \\ K = \{v = (v^1, v^2) \in V(\Omega^1) \times V(\Omega^2), d(v) \geq 0 \text{ at } \Gamma_u^l\} \end{gathered}, \tag{2.16}$$

where K defines admissible displacements field. It should be noted that in this case we do not specify an ensemble, where displacements have been taken. Often, Sobolev's spaces are used for functional representation of the problem.

Since $v \in K$ for each solid body l, $\dot{v}^l$ is the field of compatible virtual velocities. Taking equation of motion (2.6), it is possible to write the balance of virtual works for each solid body in contact:

$$\int_{\Omega^l} \rho^l \ddot{u}_i^l \dot{v}_i^l d\Omega^l = \int_{\Omega^l} \sigma_{ij,j}^l \dot{v}_i^l d\Omega^l + \int_{\Omega^l} f_i^l \dot{v}_i^l d\Omega^l . \tag{2.17}$$

Let's make transformation of the first integral of the second member in (2.17) to the integral by parts and apply the theorem of Ostrogradsky:

$$\int_{\Omega^l} \sigma_{ij,j}^l \dot{v}_i^l d\Omega^l = \int_{\Gamma^l} \sigma_{ij}^l \dot{v}_i^l n_i^l d\Gamma^l - \int_{\Omega^l} \sigma_{ij}^l \dot{v}_{i,j}^l d\Omega^l . \tag{2.18}$$

Then, at $\sigma_{ij}^l = \sigma_{ji}^l$, it can be written:

$$\sum_i \sum_j \sigma_{ij}^l \dot{v}_{i,j}^l = \sum_i \sum_j \sigma_{ij}^l \varepsilon_{ij}(\dot{v}^l) . \tag{2.19}$$

Also the conventional form of the virtual works representation can be expressed as:

$$\int_{\Omega^l} \rho^l \ddot{u}_i^l \dot{v}_i^l d\Omega^l + \int_{\Omega^l} \sigma_{ij}^l \varepsilon_{ij}(\dot{v}^l) d\Omega^l = \int_{\Gamma^l} \sigma_{ij}^l \dot{v}_i^l n_i^l d\Gamma^l + \int_{\Omega^l} f_i^l \dot{v}_i^l d\Omega^l . \tag{2.20}$$

Taking into account boundary conditions of the contact problem shown in the previous subchapter, the work of forces acting on the boundary $\Gamma^l, l = 1,2$ can be derived. These forces work can be decomposed in the following way:

$$\int_{\Gamma^l} \sigma_{ij}^l \dot{v}_i^l n_i^l d\Gamma^l = \int_{\Gamma_f^l} T_i^l \cdot \dot{v}_i^l d\Gamma^l + \int_{\Gamma_u^l} \sigma_{ij}^l \dot{v}_i^l n_j^l d\Gamma^l + \int_{\Gamma_c} \sigma_n^l \dot{v}_n^l d\Gamma^l + \int_{\Gamma_c} \sigma_t^l \dot{v}_t^l d\Gamma^l . \tag{2.21}$$

For two deformable solids in contact it is finally written:

$$\forall v \in K \quad (\rho\ddot{u}, \dot{v}) + a(u, \dot{v}) = L(\dot{v}) + \langle f_u, \dot{v} \rangle + \langle f_{cn}, \dot{v} \rangle + \langle f_{ct}, \dot{v} \rangle . \tag{2.22}$$

where $(\rho\ddot{u}, \dot{v})$ represents the virtual work of inertial forces.

The expression of the virtual work of inertial forces is:

$$(\rho\ddot{u},\dot{v}) = \sum_{l=1}^{2}\int_{\Omega^l}\rho^l\ddot{u}^l\cdot\dot{v}^l d\Omega^l, \tag{2.23}$$

$a(u,\dot{v})$ is the partition of the interior forces virtual work, which can be presented as:

$$a(u,\dot{v}) = \sum_{l=1}^{2}\int_{\Omega^l} a^l_{ijkh}\varepsilon_{kh}(u^l)\varepsilon_{ij}(\dot{v}^l)d\Omega^l, \tag{2.24}$$

Member $L(\dot{v})$ is the representation of the exterior forces virtual work:

$$L(\dot{v}) = \sum_{l=1}^{2}(\int_{\Omega^l} f^l\cdot\dot{v}^l d\Omega^l + \int_{\Gamma^l_f} T^l_i\cdot\dot{v}^l_i d\Gamma^l), \tag{2.25}$$

$\langle f_u,\dot{v}\rangle$ is the virtual work of the forces required to induce displacement on boundaries Γ^1_u and Γ^2_u and it can be written in the following way:

$$\langle f_u,\dot{v}\rangle = \sum_{l=1}^{2}\int_{\Gamma^l_u}\sigma^l_{ij}\dot{v}^l_i n^l_j d\Gamma^l, \tag{2.26}$$

$\langle f_{cn},\dot{v}\rangle$ is the virtual work of the normal contact forces:

$$\langle f_u,\dot{v}\rangle = \sum_{l=1}^{2}\int_{\Gamma_c}\sigma^l_n\dot{v}^l_n d\Gamma^l, \tag{2.27}$$

$\langle f_{ct},\dot{v}\rangle$ is the virtual work of the tangential contact forces:

$$\langle f_u,\dot{v}\rangle = \sum_{l=1}^{2}\int_{\Gamma_c}\sigma^l_t\dot{v}^l_t d\Gamma^l. \tag{2.28}$$

It should be noted that the real virtual work of the normal forces at $v=u$ is equal to zero, $\langle f_{cn},\dot{v}\rangle = 0$.

2.1.4 Variational inequality

It is possible to show that problem from subchapter 2.1.1 can be equal to:

$$\forall v\in K\quad (\rho\ddot{u},\dot{v}-\dot{u}) + a(u,\dot{v}-\dot{u}) + j(u,\dot{v}) - j(u,\dot{u}) \geq L(\dot{v}-\dot{u}) + \langle f_u,\dot{v}\rangle + \langle f_{cn},\dot{v}-\dot{u}\rangle, \tag{2.29}$$

or

$$j(u,\dot{v}) = \sum_{l=1}^{2}\int_{\Gamma_c}\mu\left|\sigma_n(u)\right|\left\|\dot{v}^1_t - \dot{v}^2_t\right\| d\Gamma \quad . \tag{2.30}$$

It should be noted that if u is solution of the problem, then σ^1_t and relative velocity $\dot{u}^1_t - \dot{u}^2_t$ are collinear vectors and they have opposite direction. From this we have:

$$\sigma^1_t\cdot(\dot{u}^1_t - \dot{u}^2_t) = -\left\|\sigma^1_t\right\|\left\|\dot{u}^1_t - \dot{u}^2_t\right\|. \tag{2.31}$$

Consequently for all $v \in K$:

$$\sigma_t^1 \cdot (\dot{u}_t^1 - \dot{u}_t^2) \geq -\left\|\sigma_t^1\right\|\left\|\dot{u}_t^1 - \dot{u}_t^2\right\|, \tag{2.32}$$

and then

$$\sigma_t^1 \cdot (\dot{u}_t^1 - \dot{u}_t^2) - \sigma_t^1 \cdot (\dot{u}_t^1 - \dot{u}_t^2) \geq -\left\|\sigma_t^1\right\|\left(\left\|\dot{u}_t^1 - \dot{u}_t^2\right\| - \left\|\dot{u}_t^1 - \dot{u}_t^2\right\|\right). \tag{2.33}$$

If we have the case of sliding, $\left\|\sigma_t^1\right\| = \mu\left|\sigma_n\right|$, then:

$$\sigma_t^1 \cdot (\dot{u}_t^1 - \dot{u}_t^2) - \sigma_t^1 \cdot (\dot{u}_t^1 - \dot{u}_t^2) \geq \mu\left|\sigma_n\right|\left(\left\|\dot{u}_t^1 - \dot{u}_t^2\right\| - \left\|\dot{u}_t^1 - \dot{u}_t^2\right\|\right). \tag{2.34}$$

If there is sticking, $\left\|\sigma_t^1\right\| \geq -\mu\left|\sigma_n\right|$, then:

$$\sigma_t^1 \cdot (\dot{u}_t^1 - \dot{u}_t^2) \geq -\mu\left|\sigma_n\right|\left\|\dot{u}_t^1 - \dot{u}_t^2\right\|, \tag{2.35}$$

which gives again equation (2.34) with $\dot{u}_t^1 - \dot{u}_t^2 = 0$.

Now it is possible to obtain (2.29) because:

$$\left\langle f_{ct}, \dot{v} - \dot{u} \right\rangle \geq j(u, \dot{u}) - j(u, \dot{v}) . \tag{2.36}$$

We can also remark that:

$$\left\langle f_{ct}, v - u \right\rangle = -\int_{\Gamma_c} \sigma_n(u) d(v) d\Gamma \geq 0 , \tag{2.37}$$

because $d(v) \geq 0$ and $\sigma_n(u) \leq 0$.

This follows to the variational inequality expression in the more compact form:

$$(\rho\ddot{u}, v - u) + a(u, v - u) + j(u, v) - j(u, u) \geq L(v - u) . \tag{2.38}$$

Direct solution of the (2.29) or (2.38) seems to be very challenging problem. Therefore it was proposed [47] to divide such problem into two subproblems: in the first subproblem tangential forces are supposed known and in the second one the normal forces are accepted to be defined. Such approach consists in consequent solution of the subproblems up to the convergence of the global problem will be reached.

Case of the frictionless contact. Such case is most interesting for our work, since frictionless contact will be used through all the study. Solution of the contact problem in this case is easy task because we can follow to the classical constrained optimisation problem. If to consider quasi-static problem, the variational inequality (2.38) will be presented as:

$$a(u, v - u) \geq L(v - u) , \tag{2.39}$$

and our problem will be equivalent to the total potential energy minimisation.

Condition of impenetrability will be used as constrain equation:

$$\min_{v \in K} E_p(v) = \frac{1}{2} a(v, v) - L(v) . \tag{2.40}$$

Also, if $u \in K$ is valid for all v and K in (2.40), then:

$$\frac{1}{2}a(u,u) - L(u) \le L(v) + \frac{1}{2}\big(2a(u,v) - a(u,u)\big). \tag{2.41}$$

Let's suppose that elasticity tensor is symmetric and it verifies ellipticity property:

$$\exists \alpha > 0, a_{ijkh}\varepsilon_{ij}\varepsilon_{ij} \ge \alpha\varepsilon_{ij}\varepsilon_{ij}. \tag{2.42}$$

Consequently, we will have:

$$\begin{gathered} a(v-u,v-u) = a(v,v) + a(u,u) - 2a(u,v) \ge 0, \\ \frac{1}{2}a(u,u) - L(u) \le \frac{1}{2}a(v,v) - L(v) - \frac{1}{2}a(v-u,v-u) \le \frac{1}{2}a(v,v) - L(v). \end{gathered} \tag{2.43}$$

After it, we can see that u minimizes total potential energy. Analogically, if $u \in K$ is valid for all v and K, then:

$$\frac{1}{2}a(u,u) - L(u) \le \frac{1}{2}a(v,v) - L(v). \tag{2.44}$$

Also the symmetry of a will give us:

$$\frac{1}{2}a(v-u,u) + a(v,v-u) - L(v-u) \ge 0. \tag{2.45}$$

In order to pass from the constrained optimisation problem to the unconstrained problem some methods can be applied. They are: penalty method, Lagrange multipliers method and augmented lagrangian method.

Case of the contact with friction. In this the real contact surface Γ_{cr} and normal contact forces are supposed to be known. As a result, the functional corresponding to the contact with friction becomes:

$$j(v) = \int_{\Gamma_{cr}} \mu\left|\sigma_n(u)\right|\left\|\dot{v}_t^1 - \dot{v}_t^2\right\| d\Gamma \quad . \tag{2.46}$$

Analogically to the frictionless contact case, we can show that problem is represented by minimisation of:

$$\pi(v) = \frac{1}{2}a(v,v) - L(v) + j(v). \tag{2.47}$$

Due to the norm of relative displacement $\left\|\dot{v}_t^1 - \dot{v}_t^2\right\|$, $j(v)$ is not differentiable and thus, in this case we do not have standard optimisation problem. In order to overcome such difficulties a kind of function regularization should be applied to j [47].

2.1.5 Variational equality

Taking into consideration (2.22), the problem can be formulated in the following way:

$$\forall v \in K \quad (\rho\ddot{u}, \dot{v} - \dot{u}) + a(u, \dot{v} - \dot{u}) = L(\dot{v} - \dot{u}) + \left\langle f_{cn}, \dot{v}\right\rangle + \left\langle f_{ct}, \dot{v} - \dot{u}\right\rangle. \tag{2.48}$$

Terms corresponding to imposed displacement can be thrown out, because:

$$at\ \ \Gamma_u^1 \times \Gamma_u^2\ \ \dot{u} = \dot{v} = \dot{U} \Rightarrow \left\langle f_u, \dot{v} - \dot{u} \right\rangle = 0\,. \tag{2.49}$$

Majority of the finite elements software utilizes the mentioned above formulation for the solution of the contact problem with friction. Generally, both real contact surfaces and contact forces are unknown. Therefore, some incremental methods of non-linear problems solution must be applied.

2.1.6 Solution of the contact problem

Discretization by finite elements

In the case of application of the variational equality, equation (2.48) can be presented in discretized form as [21]:

$$\mathbf{M}\ddot{\mathbf{U}} + \mathbf{K}\mathbf{U} + \mathbf{F}_c = \mathbf{F}_{ext}\,, \tag{2.50}$$

where **M** is the mass matrix, **K** is the stiffness matrix, $\mathbf{F}_{ct}$ is the vector of contact forces, $\mathbf{F}_{ext}$ is the vector of external forces.

Unilateral contact imposes contact stresses:

$$\forall i \in 1,...,m\ \ (\mathbf{A}_c\mathbf{V})_i \le \mathbf{G}_i\,, \tag{2.51}$$

where m is the number of imposed stresses, equal to the number of contact elements, **A** is the matrix of contact stresses, which depends on discretization of the contact surface and contact element type, **G** is the vector of initial separation distances between contact elements.

Variational inequality described in the sub-chapter 2.1.3 can be represented here using nodal displacements. The problem of the contact will be again divided into two cases: frictionless contact and contact with friction.

In the frictionless contact case the problem returns to minimisation of the total potential energy:

$$\begin{gathered} E_p(\mathbf{V}) = \frac{1}{2}\mathbf{V}^T\mathbf{K}\mathbf{V} - \mathbf{F}_{ext}^T\mathbf{V}, \\ \mathbf{A}_c\mathbf{V} \le \mathbf{G}. \end{gathered} \tag{2.52}$$

For the contact problem with friction it is necessary to perform minimisation of the regularized problem:

$$\Pi(\mathbf{V}) = \frac{1}{2}\mathbf{V}^T\mathbf{K}\mathbf{V} - \mathbf{F}_{ext}^T\mathbf{V} + \mathbf{F}_c^T\Phi(\mathbf{V})\,, \tag{2.53}$$

where $\mathbf{F}_d^T\Phi(\mathbf{V})$ is the discretized form of the regularized functional j, $\mathbf{F}_c$ is the vector of normal contact forces.

During solution procedure it should be verified that there is no lost contact in the zone of imposed normal forces.

It can be performed using equality:

$$\mathbf{A}_c\mathbf{V} = \mathbf{G}\,. \tag{2.54}$$

Lagrange's multipliers method

This approach can be formulated for both variational equality and variational inequality. We start with the method application using variational equality.

Let's take problem formulation (2.53) with friction presence. In order to find the minimum of Π with constraint $\mathbf{A}_c\mathbf{V} = \mathbf{G}$, it is necessary to solve the system of equations:

$$\begin{cases} \mathbf{KV} - \mathbf{F}_{ext}^T\mathbf{V} + \mathbf{F}_d^T\nabla\Phi(\mathbf{V}) + \mathbf{A}_c^T\lambda = \mathbf{F}_{ext} & \text{n equations} \\ \mathbf{A}_c\mathbf{V} = \mathbf{G} & \text{m equations} \end{cases}. \tag{2.55}$$

In the system (2.55), components λ are additional unknowns called as multipliers of Lagrange [45]. Number of these terms is equal to the number of imposed constraints *m*, which is equal to the number of contact elements. $\nabla\Phi$ is the gradient of Φ, which is a function of each contact element. System (2.55) is non-linear system of *n*+*m* equations with *n*+*m* unknowns. The system can be solved by one of Newton-type methods of non-linear systems solution. Functional Π is convex and differentiable. Since the system (2.55) will have solution (U,λ^*), U will be problem global minimum and it will be unique because Π is strictly convex.

The lagrangian of the system is defined by:

$$L(\mathbf{V},\lambda) = \mathbf{V}^T\mathbf{KV} - \mathbf{F}_{ext}^T\mathbf{V} + \mathbf{F}_d^T\Phi(\mathbf{V}) + \lambda^T(\mathbf{A}_c\mathbf{V} - \mathbf{G})\,. \tag{2.56}$$

In the case of variational inequality the problem of contact without friction (2.52) can be formulated in the following manner. It is required to find minimum and U should satisfy to the condition of Karush-Kuhn-Tucker. From this condition vector λ of Lagrange's multipliers should be found that:

$$\begin{cases} \mathbf{KU} + \mathbf{A}_c^T\lambda = \mathbf{F}_{ext} & \text{n equations} \\ (\mathbf{A}_c\mathbf{U} - \mathbf{G})_i \le 0 & \text{m equations} \\ (\lambda)_i \ge 0 & \text{m equations} \\ (\lambda)_i(\mathbf{A}_c\mathbf{U} - \mathbf{G})_i = 0 & \text{m equations (additional conditions)} \end{cases} \tag{2.57}$$

We can see that multipliers of Lagrange correspond to the contact forces in the matrix **A**. If we consider two bodies in the state of initial contact and utilize node to node contact elements, the conditions of Karush-Kuhn-Tucker will be:

$$\begin{cases} \mathbf{KU} + \lambda = \mathbf{F}_{ext} \\ U_{i,n}^1 + U_{i,n}^2 = -d(U_i) \le 0 \\ (\lambda)_i \ge 0 \\ (\lambda)_i\, d(U_i) = 0 \end{cases}. \tag{2.58}$$

Lagrange's multipliers will be exactly in the opposite direction to the contact normal forces. Solution of the conditions of Karush-Kuhn-Tucker is more difficult in the case of their formulation on the base of variational equality.

Penalty method

The penalty method is widely used for solution of the constrained optimisation problems. With its help it is possible to transfer from constrained problem to the unconstrained one. The main advantage consists in omitting of the additional unknowns introduction as in the method of Lagrange's multipliers. But at the same time the penalty method application can lead to the problems of ill-conditioning.

Let's consider again the frictionless contact problem. With node to node elements and without initial separation the problem will be presented as:

$$\begin{cases} \min E_p(\mathbf{V}) = \frac{1}{2}\mathbf{V}^T\mathbf{K}\mathbf{V} - \mathbf{F}_{ext}^T\mathbf{V} \\ g(\mathbf{V}) \le 0 \end{cases} . \tag{2.59}$$

Component $g(\mathbf{V})$ represents the level of penetration for each m-th contact element and they can be calculated using following formula:

$$(g(\mathbf{V}))_i = g(U_i) = U_{i,n}^1 + U_{i,n}^2,\ i = 1,...,m . \tag{2.60}$$

Penalty method, as it was mentioned, consists in replacing of the constrained optimisation problem by the problem without constrains:

$$\min(\frac{1}{2}\mathbf{V}^T\mathbf{K}\mathbf{V}) = \mathbf{F}_{ext}^T\mathbf{V} + \frac{1}{2}\delta\left\|g(\mathbf{V})\right\|^2 . \tag{2.61}$$

In penalty method formulation for the frictionless problem (2.59) parameter δ represents a positive scalar value of the penalty coefficient. It has arbitrary value chosen by the user in dependence on the problem conditions. The ratio $\frac{1}{2}$ is introduced here only with the purpose to give to the parameter δ the meaning of the normal contact stiffness. The problem (2.59) can be solved, for example, by application of the gradient-search method of function optimisation.

Augmented lagrangians method

The method of augmented lagrangians is the modification of penalty method presented previously. The object of the method is always same – seeking of the total potential energy minimum. In this case classic lagrangian is presented as:

$$L(\mathbf{V},\lambda) = \mathbf{V}^T\mathbf{K}\mathbf{V} - \mathbf{F}_{ext}^T\mathbf{V} + \lambda^T g(\mathbf{V}) . \tag{2.62}$$

Then augmented lagrangian will be expressed in the following manner:

$$L(\mathbf{V},\lambda) = \mathbf{V}^T\mathbf{K}\mathbf{V} - \mathbf{F}_{ext}^T\mathbf{V} + \lambda^T g(\mathbf{V}) + \frac{1}{2}\delta\left\|g(\mathbf{V})\right\|^2, \quad (2.63)$$

where δ is the penalty coefficient. In this case, it can be said that such formulation represents by itself the penalisation with use of Lagrange's multipliers.

Augmented lagrangians are generally utilized in the iterative methods developed with the purpose to find exact Lagrange's multipliers. If to suppose λ^k is Lagrange's multipliers vector on *k*-th iteration [58], then the system to be solve will be:

$$\mathbf{K}\mathbf{V} + (\lambda^k + \delta g(\mathbf{V})) = \mathbf{F}_{ext}. \quad (2.64)$$

By the strategy of non-linear problems solution, vector of Lagrange's multipliers is updated by expression:

$$\lambda^{k+1} = \lambda^k + \delta g(\mathbf{V}). \quad (2.65)$$

Penalty coefficient is chosen arbitrary and remained constant through all solution procedure. If to accept as initialization $\lambda^0 = 0$, it will correspond to the penalty method. It should be noted that value of penalty coefficient should not be chosen too big because it will lead to high computation time expenses at required iterations number.

Frequency domain methods of contact problem solution

Separate subchapter will be devoted to such category of methods when cracked blade model will be considered. Here, only short overview will be presented.

Calculation of the steady-state response of the non-linear system can be sufficiently long because all transient responses should be calculated. Frequency domain methods allow direct calculation of the non-linear system steady-state response supposing it to be harmonic and that system response contains same harmonics as the excitation.

The most widely used method representing such approach is harmonic balance method, which proposes projecting equation of system motion on the base of some harmonics. Also it is very close to Galerkin method. In all cases, the harmonic balance method is formulated analytically for each problem.

As it was said in conclusions to chapter 1, fundamentals of contact analysis should be followed by consideration of fracture mechanics elements. It will allow investigation of functional dependences between crack parameters and amplitude of force response that can be used for crack presence/development analysis.

2.2 Fatigue and endurance calculation of structure elements

It is known that blade failures in aircraft gas-turbine engines have a severe impact on the engine operability and, consequently, on aircraft airworthiness. Blade failures can be caused by different mechanisms under engine operating conditions. In general, blade failures can be grouped into two categories: fatigue, including both high [40] and low cycle fatigue [81] and creep rupture [110].

In the maintenance experience numerous cases of the structural elements and assemblies faults due to fatigue of material are known. Such faults are caused by the alternating or repeated loadings. For fatigue caused failures the considerably smaller maximum load is required than at failure due to static loading. In operation many gas-turbine engine details and components are subjected to the alternating loads action. And though their low nominal values, they can lead to fatigue fracture. Almost always it is possible to observe the fatigue failures and it is very the failures due to static loadings. Different theories of fatigue failures were developed to the present time [25].

The fatigue failure peculiarity is strains absence in the fracture zone. Similar appearances are observed even in such materials as the soft steels, which have high-plasticity at the static failure.

It is dangerous attribute of fatigue failure because there are any indications of the possible fractures. Originating fatigue indications usually are very difficult for detection, while they will not reach the macroscopic size. Further they develop very quickly and in short period the full failure occurs. Thus, timely detection of fatigue cracks becomes very challenging problem. Most often the fatigue cracks originate in the deformation zones or in the zones of surfaces defects.

Such defects and also infinitesimal change of structure working section do not affect on static strength because plastic deformations reduce the stress concentration influence. At the same time at fatigue failure the plastic deformations, as a rule, are insignificant. Owing to what, stress decrease in the concentration zone does not occur and stress concentration assessment becomes very important.

As it is known, the static failure is generally determined by probability of major loading origination in flight, for example, from air gust, when acting on aircraft loading exceeds limit of the static structural strength. Thus, possibility of static failure is, in essence, the problem of probability of major loading occurrence.

The fatigue failure, at the given assumptions, is caused by application of certain number of loading cycles or accomplishing of certain number of flights on certain distance.

The main distinction between fatigue and static loadings consists in the following:

- Fatigue strength main factor at the given loadings distribution, even taking into account data variability, is the number of loading variations or expected service life; for the static strength it is operating loading;
- Character of probabilistic approach to fatigue loading considerably differs from character of probabilistic approach to static loading. For particular operation conditions the probability to meet single major loading does not depend on time. It can happen at the beginning and at the end of operation life. The probability of fatigue failure varies while in service, considerably increasing to the end of the service life. Thus, designers and scientists assume that the assigned resource and probability level should be such that the frequency of fracture recurrence has a small enough value. Such probability value is 10^{-9}, as it is accepted by leading aviation corporations.

2.2.1 Alternating loads

All gas-turbine engine blades undergo cyclic loading resulting in structural deterioration, which can lead to failure. It is highly required to understand the importance of the probable damage at any particular time to monitor the health of the blade [56, 72]. Failure at variable loads has local character and it does not affect all entire material.

An experience shows that gradually developing cracks originate only at alternating stresses. In most cases the consideration is limited only by alternation of stress in time (Fig. 2.8):

$$\sigma = \sigma_c + \sigma_a \sin(\omega t + \varphi), \tag{2.66}$$

where σ is the alternating stress, σ_c is the mean stress, σ_a is the stress amplitude, ω is circular frequency, φ is the initial phase, t - time.

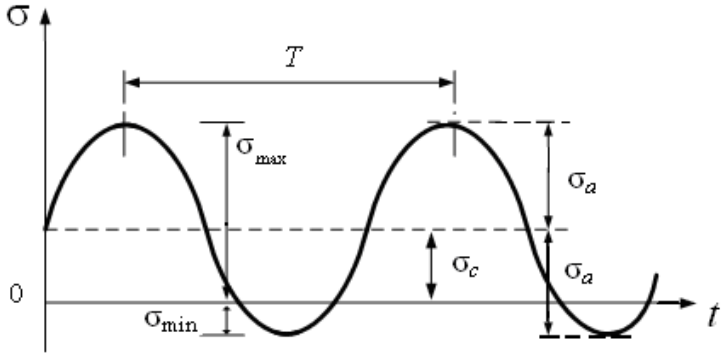

Fig. 2.8. Cycle of alternating stresses

Value

$$T = \frac{2\pi}{\omega} \tag{2.67}$$

is termed as period. Stress change during the period is termed as stress cycle.

The greatest stress of cycle is marked out as σ_{max} (or τ_{max}), and the minimum – σ_{min} (or τ_{min}).

Mean stress σ_c (or τ_c):

$$\sigma_c = \frac{\sigma_{max} + \sigma_{min}}{2}. \tag{2.68}$$

Amplitude of cycle:

$$\sigma_a = \sigma_{max} - \sigma_c = \sigma_c - \sigma_{max} = \frac{\sigma_{max} - \sigma_{min}}{2}. \tag{2.69}$$

It is obvious, that

$$\sigma_{max} = \sigma_c + \sigma_a ;\ \sigma_{min} = \sigma_c - \sigma_a . \tag{2.70}$$

Value $r = \frac{\sigma_{min}}{\sigma_{max}}$ is termed as cycle ratio.

In some cases it is more convenient to use concept of the cycle performance:

$$k_c = \frac{\sigma_a}{\sigma_c}. \tag{2.71}$$

Stress cycles, for which the cycle ratio (or performance) values are equal termed as the similar. If r = - 1 (k_c=∞) the cycle is called symmetrical (Fig. 2.9); if $r \neq$-1 ($k_c \neq \infty$) the cycle is unsymmetrical (Fig. 2.10).

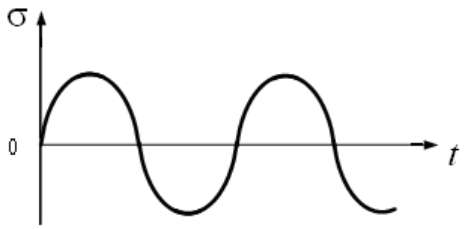

Fig. 2.9 Symmetrical loading cycle

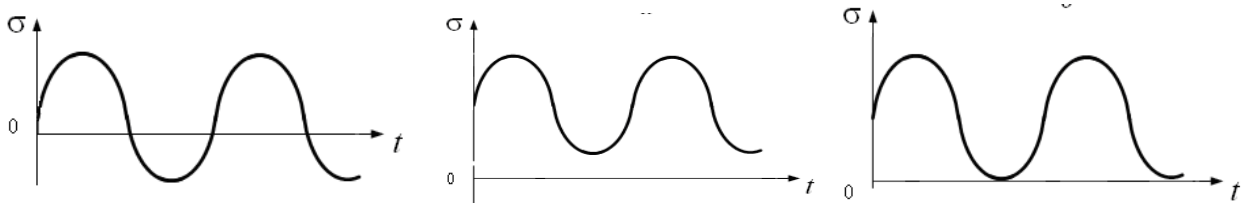

Fig. 2.10. Asymmetrical loading cycles

Unsymmetrical cycle can be of alternating or of constant sign. Special case of constant sign cycle is the pulsing cycle, at which $\sigma_{max} = 0$ or $\sigma_{min} = 0$.

Values σ_{max}, σ_{min}, σ_a, σ_c and r (k_c) are parameters of alternating stresses cycle. Each cycle is completely determined by any two of its parameters.

2.2.2 Fatigue curve and limit stresses diagram

Ability of the material to perceive the long-term action of the alternating stresses is known as endurance. Special endurance tests (on fatigue) are performed to obtain material mechanical characteristics required for strength calculations at alternating stresses.

Endurance (fatigue) curves matching to adopted value of the mean stress σ_c are obtained on the basis of experimental results.

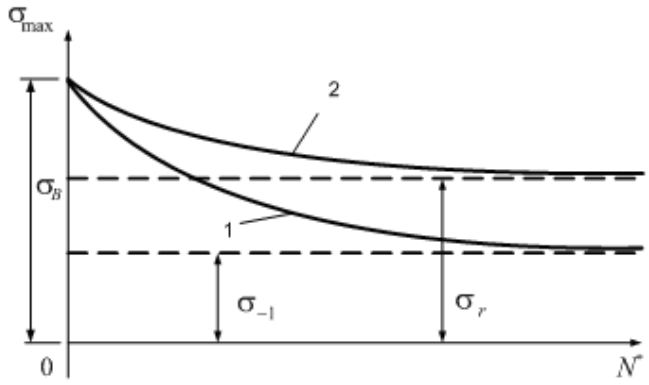

Fig. 2.11. Fatigue curve

On Fig. 2.11 the fatigue curves for steel at $\sigma_c = 0$ (curve 1 – symmetrical cycle) and $\sigma_c = A$ (curve 2) are presented.

Fatigue curve displays that with σ_{max} decrease the number of cycles, at which the material fracture appears, increases. Each fatigue curve has horizontal asymptote. Stress σ_{max} equal to asymptote ordinate is termed fatigue limit (or fatigue value). The fatigue limit is marked out as σ_r, and at symmetrical cycle it is marked out as σ_{-1} ($r = -1$).

During material tests on fatigue the number of cycles is limited to N_b, which is known as the base number of cycles. For steel – $N_b = 10^7$.

Practically, the greatest value of the maximum stress σ_{max}, at which the material withstands the base number of cycles (at the given r value) without failure, is accepted as the fatigue limit.

Fatigue curve for non-ferrous metals and alloys do not have horizontal asymptote. Therefore, the concept of fatigue limit for these materials is conventional. Basically, this limit is determined at very big number of base cycles (to $N_b = 10^8$).

Influence of the cycle type on the strength of material at alternating stresses can be described by limit stresses diagram (Fig. 2.12). Each fatigue curve (Fig. 2.11) allows one point calculation of the limit stresses diagram. The abscissa of this point is equal to the value of mean stress σ_c, matching to the given fatigue curve. The ordinate of this point is equal to limit cycle amplitude σ_a, i.e. such cycle, at which σ_{max} is equal to the fatigue limit σ_r.

It is required a significant number of experiments to build-up the limit stresses diagram. Often the true limit stresses diagram is substituted by schematised, which uses one (σ_{-1}) or two (σ_{-1} and σ_0) parameters determined experimentally.

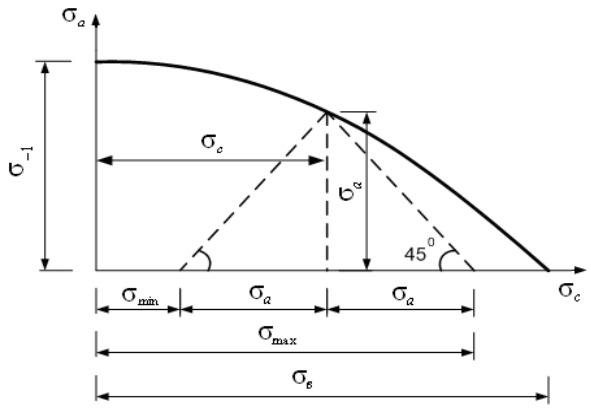

Fig. 2.12. True limit stresses diagram

Let's observe the schematised limit stresses diagram (Fig. 2.13) offered by Serensen and Kinasoshvili [70]. This diagram can be built, if fatigue limits are determined experimentally at symmetrical (σ_{-1}) and pulsing (σ_0) cycles. We note point *A* matching to the limiting symmetrical cycle. Point *E* corresponds to the limiting pulsing cycle and it has abscissa and ordinate equal to $\frac{\sigma_0}{2}$. In this case:

$$\sigma_a = \sigma_c = \frac{1}{2\sigma_{\max}}. \tag{2.72}$$

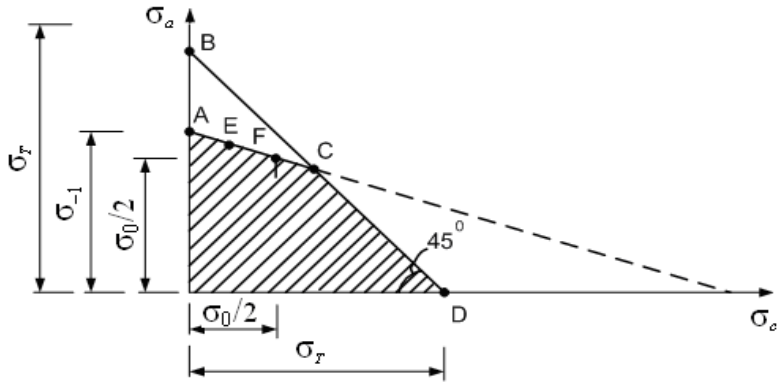

Fig. 2.13. Schematised limit stresses diagram

At the limiting pulsing cycle $\sigma_{max} = \sigma_0$. Let's draw the line *AE* up to the interception in the point *C* with the line of yield strengths *BD*. The area of safety operation (at which there are no fatigue failure and plastic deformations) is cross-hatched.

The equation of direct line *AC* looks like:

$$\sigma_a = \sigma_{-1} - \psi_\sigma \sigma_c, \tag{2.73}$$

where

$$\psi_\sigma = \frac{2\sigma_{-1}}{\sigma_0} - 1. \tag{2.74}$$

By formula (2.73) it is possible to determine amplitude of the limiting unsymmetrical cycle. Further:

$$\sigma_{\max} = \sigma_c + \sigma_a = \sigma_{-1} + (1 - \psi_\sigma)\sigma_c . \tag{2.75}$$

Since for the limit cycle $\sigma_{max} = \sigma_r$, it can be obtained obtain:

$$\sigma_r = \sigma_{-1} + (1 - \psi_\sigma)\sigma_c . \tag{2.76}$$

By the formula (2.76) it is possible to determine the fatigue limit of the standard specimens at unsymmetrical cycle.

2.2.3 Distribution curve of cyclical durability

The curve of cyclical durability characterises dependence of the cyclical durability on the fracture probability. It is built using the results of fatigue tests at constant values of amplitude and mean stress of the cycle. As example, in Fig. 2.14 the distribution curves of cyclical durability are presented for different values of σ_{max}.

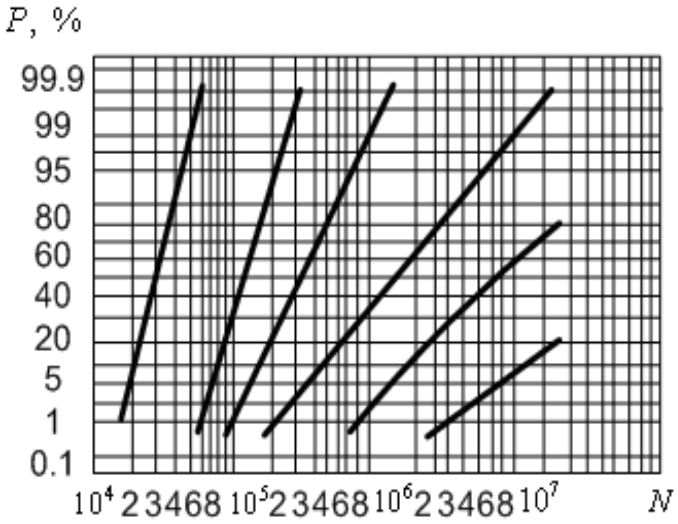

Fig. 2.14. Curves of cyclical durability distribution for different σ_{max}

Having curves of cyclical durability distribution, it is possible to build curves of the equal probability of fatigue failure, which are the base for practical calculations on fatigue.

The curve of equal probability of fatigue failure is the graph characterising relation between the maximum stress or cycle stress amplitude and durability, which corresponds to the given probability of the fatigue failure. Curves of equal probability of fatigue failure can be built using the curves of cyclical durability distribution (Fig. 2.14) at various probability values. At the same time, parameters σ_{max} and N are fixed (Fig. 2.15).

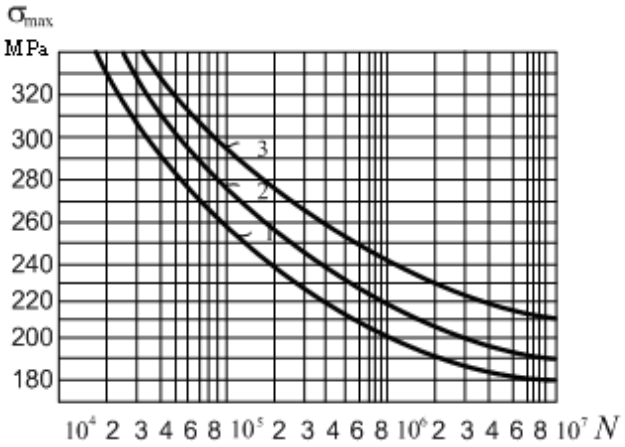

Fig. 2.15. Curves of equal probability of fatigue failure

It is known that "reliability" R is determined as value, which is equal to unity minus probability of fracture P, i.e.:

$$R = 1 - P. \tag{2.77}$$

It means, for example, that curve of 1 % of probability of fatigue failure (Fig. 2.15, curve 1) can be called as the curve of reliability of 99 % (R = 0.99). Curves of equal probability of fatigue failure are used, in particular, for durability estimation of the structures subjected to the cyclical loadings.

2.2.4 Damage accumulation. Durability estimation

More often in practice, stress cycle amplitude does not remain constant and it varies under some law forming so-called loading spectrum. Therefore, it is impossible to use the fatigue curve at calculations directly, since they are under construction at the fixed stress cycle amplitude σ_a.

Effect of cyclical stresses leads to accumulation of the fatigue damages. When accumulated damage attains some critical value the fatigue failure occurs. To the present time some hypotheses of damage accumulation are offered. We will consider the hypothesis of Palmgren-Miner or rule of the linear damage summation.

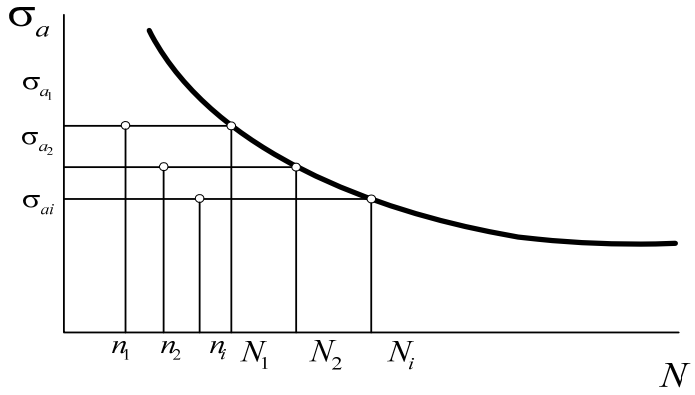

Fig. 2.16. Fatigue curve for durability estimation

At loading with constant stress amplitude σ_{a1} the fracture will happen in N_1 cycles. As a result of the same stress σ_{a1} during n_1 cycles ($n_1 < N_1$), there will be the fault characterised by number D_1, which is termed damage. The hypothesis of the linear damage summation supposes that damage at any fixed value σ_{a1} is ratio of n_1 to N_1, i.e.:

$$D_1 = \frac{n_1}{N_1}. \tag{2.78}$$

Fracture will happen, when:

$$D_1 + D_2 + \ldots + D_m \geq 1, \tag{2.79}$$

where m – number of various loading levels.

Thus, the rule of linear damage summation can be written as:

$$\sum_{i=1}^{m}\left(\frac{n_i}{N_i}\right) \geq 1. \tag{2.80}$$

According to this rule, the fatigue failure will happen, if the requirement (2.80) is satisfied. Owing to the simplicity, the rule (2.80) has found wide application in the practice. However, it has number of deficiencies, main of them that the loading sequence effect is not considered.

Experimentally it has been established, that process of damage accumulation can be dissected into phase of crack origination and phase of its development up to definitive fracture. Considering this condition, Manson applied the rule of linear damage summation to each of these phases separately and he offered the bilinear rule of damage summation.

The fatigue crack originates at:

$$\sum_{i=1}^{m}\left(\frac{n_i}{N_i^1}\right) = 1.$$

Consequently, the fracture owing to the crack presence happens at:

$$\sum_{j=1}^{q}\left(\frac{n_j}{N_{pj}}\right) = 1. \tag{2.82}$$

Here N^1 is the number of cycles before crack origination; N_p is the number of performed cycles during crack development. Values N^1 and N_p are determined by following relations:

$$\left.\begin{aligned} N^1 &= N_f - 14N_f^{0,6} \\ N_p &= 14N_f^{0,6} \end{aligned}\right\} \quad \textbf{a}t \;\; N_f > 730 \text{ cycles}, \tag{2.83}$$

$$\left.\begin{aligned} N^1 &= 0 \\ N_p &= N_f \end{aligned}\right\} \quad \textbf{a}t \;\; N_f > 730 \text{ cycles},$$

where N_f is the full number of cycles before fracture.

Thus, before crack origination it is necessary to use the formula (2.81) and then to estimate fracture possibility by expression (2.82).

2.3 Structure crack resistance calculation

For maximal usage of strength properties of a structure it is necessary to be able to determine such a state of the structure, which could extend the period of up to crack development and resistance. The main parameter used in such calculations is the stress intensity coefficient allowing elaboration of different failures criteria.

2.3.1 Stress intensity coefficient

Let's observe an infinite elastic body subjected to the plane problem of elasticity theory. In the body a small narrow interior crack of length $2a$ (Fig. 2.17) is present. Let the crack to propagate under the pressure $p(x)$, which varies along the crack sides. Axis x is the symmetry axis. Therefore, the problem is reduced to displacements and stresses determination in the elastic half-plane $y \geq 0$. Boundary conditions in this case look like:

$$\begin{aligned} &\tau_{xy} \quad -\infty < x < \infty, \\ &\sigma_y = -p(x), \qquad |x| \leq a; \\ &y = 0, \qquad |x| \geq a. \end{aligned} \tag{2.84}$$

where σ_y are normal and τ_{xy} tangential stresses, y is the displacement along y axis.

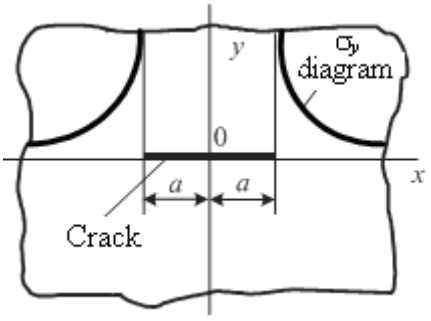

Fig. 2.17. Crack in elastic body

It is considered the case when pressure distribution is applied to the crack sides, i.e. $p(x) = p$ = const at $|x| < a$. Solving the boundary value problem (2.84), which is the plane problem of elasticity theory, we discover:

$$\sigma_y(x,0) = p\left[\frac{|x|}{\left(x^2 - a^2\right)^{1/2}} - 1\right] \text{ at } |x| > a. \tag{2.85}$$

The stress σ_y diagram obtained by formula (2.85) is displayed in Fig. 2.17. Stress σ_y is going to infinity near the crack tip, i.e. has singularity in the tip. For character determination of the normal stress near the crack tip it is necessary to find asymptotic representation for σ_y at $x \to +0$. Letting in the formula (2.85) x to $a + 0$ and rejecting fixed item, it will give:

$$\sigma_y(x,0) \approx \frac{pa^{1/2}}{2^{1/2}(x-a)^{1/2}}, \qquad x \to a+0. \tag{2.86}$$

If to introduce:

$$K_1 = p(\pi a)^{1/2}, \tag{2.87}$$

Expression (2.86) becomes:

$$\sigma_y(x,0) = \frac{K_1}{(2\pi)^{1/2}(x-a)^{1/2}}, \qquad x \to a+0. \tag{2.88}$$

Value K_1 is termed the stress intensity coefficient of normal separation. The formula (2.87) determines the stress intensity coefficient for plate with individual crack when uniform pressure p is applied to crack or when the plate is subjected to the uniform extension normal to the crack line. In this case the stress intensity coefficient depends on pressure and crack size. It is possible to display that (2.88) is also valid when the crack is in elastic finite body and pressure p is not constant. However, in these cases expression for K_1 will differ from (2.87). For finite body the stress intensity coefficient also depends on the body size.

The concept of stress intensity coefficient is appeared rather useful in the linear fracture mechanics.

The stress intensity coefficient can be calculated by known stresses or displacements. From expression (2.88) it is derived:

$$K_1 = \lim_{x \to a+0} \left[(2\pi)^{1/2} (x-a)^{1/2} \sigma_e(x,0) \right]. \tag{2.89}$$

Expression (2.89) allows calculation of the stress intensity coefficient of normal separation by known stress. Value K_1 can be also calculated by known displacements:

$$K_1 = \frac{(2\pi)^{1/2}\,\mu}{1+\chi} \lim_{x \to a-0} \left[\frac{v(x,+0) - v(x,-0)}{(a-x)^{1/2}} \right], \tag{2.90}$$

$$K_1 = -\frac{2\mu}{1+\chi} \lim_{x \to a-0} \left\{ (2\pi)^{1/2} (a-x)^{1/2} \frac{\partial}{\partial x} \left[v(x,+0) - v(x,-0) \right] \right\}, \tag{2.91}$$

where $\chi = 3 - 4\nu$ – for plane deformation and $\chi = (3 - \nu)/(1 + \nu)$ – in the case of generalised plane stress problem.

There are similar formulas for stress intensity coefficients definition of transversal shear K_2 and longitudinal shear K_3.

Stress intensity coefficient plays the main role in the fracture mechanics. Essential part of problems solutions within the limits of the linear fracture mechanics consists in determination of the stress intensity coefficient dependence on crack length for a given structure. Different analytical, numerical and experimental methods are applied to calculate the stress intensity coefficient. During analytical and numerical methods application it is necessary to obtain the solution of corresponding boundary values problem.

For simplification of the problem linked with definition of the stress intensity coefficient it is possible to use principle of Bueckner [13]. The principle consists in substituting of more complex problem with loading applied in arbitrary points by the simplified problem when the loading is applied to crack sides (Fig. 2.18).

Let the right-angled plate with crack to be extended by forces P applied in points A_1 and A_2 (Fig. 2.18). It is required to determine the stress intensity coefficient. Firstly, we consider the same plate, but without crack. Stress σ_y distribution in the crack section (in this case at $y = 0$, $|x| < a$) is determined theoretically or experimentally (Fig. 2.18). Then the stress σ_y distribution is applied to the crack sides and the stress intensity coefficient is calculated. It will be of the same value as for initial problem.

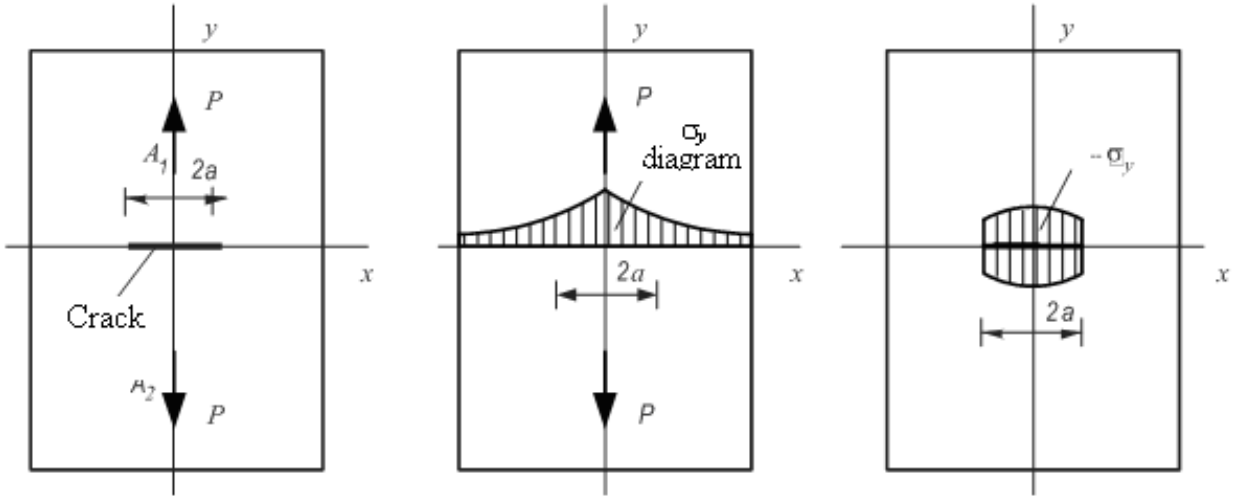

(a) (b) (c)

Fig. 2.18. Idea of Bueckner's method: (a) initial plate with crack, (b) same plate without crack and σ_y diagram, (c) calculated plate with crack and σ_y diagram

Reference data on stress intensity factors are found in the works [10, 79, 93]. Also the work [78] is devoted to the questions of their determination.

Let’s consider the stress intensity factors determination for the most often encountered cases.

1. Uniform tension of the plate with single crack.The load is applied normally to the crack location (Fig. 2.19a). In this case [44, 71]:

$$K_1 = \sigma(\pi a)^{1/2}. \tag{2.92}$$

2. Plate with central traversal crack at axial extension (Fig. 2.19b). In this case [44, 71, 96]:

$$K_1 = \sigma(\pi a)^{1/2} F_1(\alpha), \alpha = 2a/W. \tag{2.93}$$

Approximate solution:

$$F_1(\alpha) = \left(\sec\frac{\alpha\pi}{2}\right)^{1/2}, \tag{2.95}$$

More exact solution:

$$F_1(\alpha) = \left(1 - 0{,}025\alpha^2 + 0{,}06\alpha^4\right)\left(\sec\frac{\alpha\pi}{2}\right)^{1/2}. \tag{2.96}$$

3. Plate with eccentrically located traversal crack at extension (Fig. 2.19c). In this case [71]:

$$K_{1A} = \sigma(\pi a)^{1/2}\ F_{1A}(\alpha,\beta); \alpha = 2a/(W-2e); \beta = 2e/W. \tag{2.98}$$

$$F_{1A}(\alpha,\beta) = \left(\sec\frac{\pi\alpha}{2}\frac{\sin 2\alpha\beta}{2\alpha\beta}\right)^{1/2}.$$

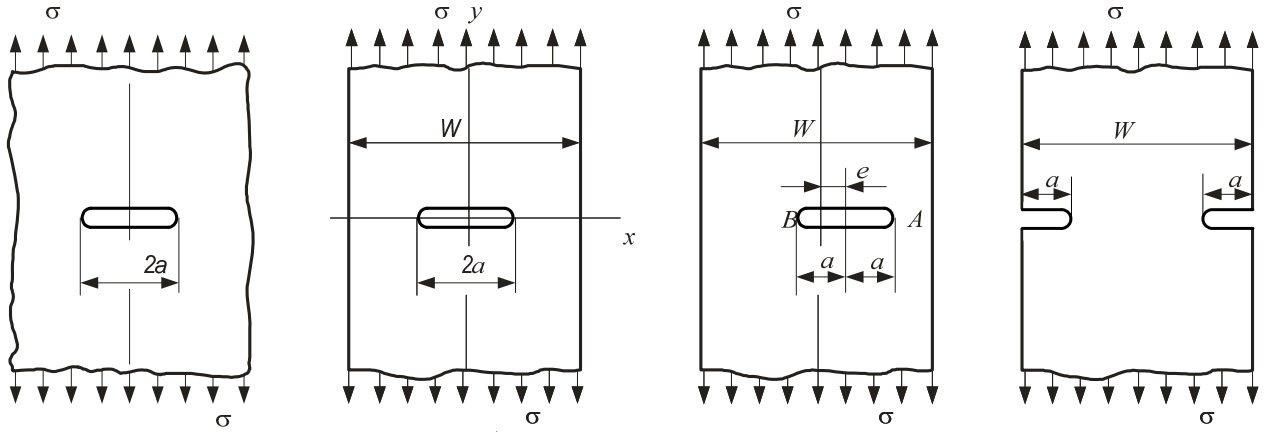

(a) (b) (c) (d)

Fig. 2.19. Crack location cases: (a) plane with crack, (b) plate with central crack, (c) plate with eccentrically shifted crack, (d) plate with edge cracks

4. Plate with two symmetrical edge cracks at axial extension (Fig. 2.19d). In this case [10–11, 71, 86]:

$$K_{1A} = \sigma(\pi a)^{1/2}\ F_{1A}(\alpha); \alpha = 2a/W; \tag{2.99}$$

$$F_1(\alpha) = \left(1 + 0{,}122\cos^2\frac{\pi\alpha}{2}\right)\left(\frac{2}{\pi\alpha}\operatorname{tg}\frac{\pi\alpha}{2}\right)^{1/2}.$$

The greatest practical interest is represented by the elements with determined dimensions at least in one direction. To gain the exact solution for elements with cracks it is necessary to use

complex mathematical methods. However, in variety of cases, it is enough to gain approximate solution. One of such approaches is the modified method of sections [93].

The main idea of the modified method of sections consists in the use of solution of problem, which is close to the considered.

Let's consider the plate with central traversal crack at axial extension (Fig. 2.19b). As the close problem the analogous problem of the elastic plate is taken (Fig. 2.19a). For the elastic plate subjected to the uniform stress applied to the crack side:

$$\sigma_y(x,0) = \sigma\left[\frac{|x|}{\left(x^2-a^2\right)^{1/2}}-1\right], \qquad |x| > a. \tag{2.100}$$

Using Bueckner's principle to transfer to the scheme of loading displayed in Fig. 2.19a, we will gain:

$$\sigma_y(x,0) = \frac{\sigma|x|}{\left(x^2-a^2\right)^{1/2}}, \qquad |x| > a. \tag{2.101}$$

Substituting this expression in (2.88):

$$K_1^0 = \sigma(\pi a)^{1/2}.$$

Taking into account the ratio (2.88) the expression (2.101) becomes:

$$\sigma_y(x,0) = \frac{K_1^0|x|}{(\pi a)^{1/2}\left(x^2-a^2\right)^{1/2}}, \qquad |x| > a. \tag{2.102}$$

It corresponds to the elastic plate with crack (Fig. 2.19a). In order to transfer to problem about elastic plate (Fig. 2.19b), we suppose for the plate:

$$\sigma_y(x,0) = \frac{K_1|x|}{(\pi a)^{1/2}\left(x^2-a^2\right)^{1/2}}, \qquad |x| > a. \tag{2.103}$$

where K_1 is the stress intensity coefficient for the plate with crack (Fig. 2.19b).

Value K_1 can be calculated using equilibrium condition. Let's throw out lower symmetric part of the plate from Fig. 2.19b. Equilibrium state of the upper part is shown in Fig. 2.20.

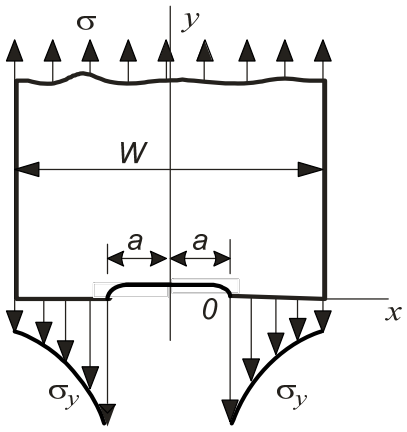

Fig. 2.20. Upper part of the plate with crack

The equilibrium equation $\sum Y = 0$ becomes:

$$\sigma W / 2 - \int_a^{W/2} \sigma_y(x,0)dx = 0. \tag{2.104}$$

Substituting here expression (2.102), we will have:

$$\sigma W / 2 = \frac{K_1}{(\pi\alpha)^{1/2}} \int_a^{W/2} \frac{xdx}{\left(x^2 - \alpha^2\right)^{1/2}}. \tag{2.105}$$

Computing integral, we obtain:

$$K_1 = \sigma(\pi a)^{1/2} F_1(\alpha); \alpha = 2a/W;$$

$$F_1 = \left(1 - \alpha^2\right)^{-1/2}. \tag{2.106}$$

On Fig. 2.21 the dependence of correction factor F_1 on parameter α is displayed; curve 1 – practically exact solution by (2.96) and curve 2 – solution by (2.106).

As it seen from Fig. 2.20, the method of sections leads to satisfactory results.

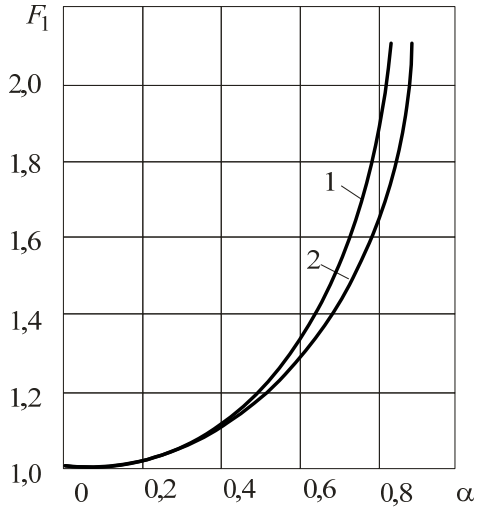

Fig. 2.21. Correction function F_1: curve 1 – the exact solution, curve 2 – approximate solution

2.3.2 Force criterion of cracked structures strength

In 1920 Griffiths using the energy approach gained the fracture condition of the infinite plate (Fig. 2.19) with slotted crack of length l:

$$\sigma_\kappa = \left(\frac{4\gamma E}{\pi l}\right)^{1/2}, \tag{2.107}$$

where E is the modulus of elasticity; γ is the material surface energy; σ_k is the critical stress corresponding to unstable crack origination. The requirement (2.107) determines catastrophic crack distribution and it is valid for brittle materials or ceramics.

By this approach the crack will not propagate with increase of the stress until it will not attain some value σ_k, which is critical for the given crack. As soon as it will be attained, there will be unstable, spontaneous propagation of the crack.

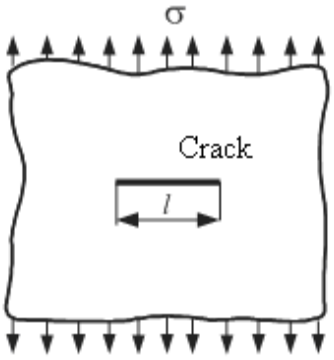

Fig. 2.22. Infinite plate with crack

Theory of Griffiths did not allow consideration of some prominent aspects of the fracture process. Therefore, Orovan and Irwin [10, 43, 79] revealed that "brittle" fracture of the high-strength materials is accompanied by essential plastic deformations in the lamina near the crack surface. Such fracture has been termed pseudo-brittle. They proposed the concept of pseudo-brittle fracture. Its main idea consists in considering of the energy required for plastic deformation.

For the problem simplification the case of normal separation will be considered. The stress state at the front of crack for elastic body is completely determined by the stress intensity coefficient K_1. Therefore, its value underlies force criterion of the linear fracture mechanics. The first criterion of such type was offered by Irwin for pseudo-brittle fracture.

Criterion of Irwin is formulated as follows: crack begins to propagate in the elastic body when value of the stress intensity coefficient attains some critical value for the given material.

Value $K_{1,}$ at which the crack will propagate in the unstable way, is the constant of material termed as fracture toughness or critical stress intensity coefficient. The critical stress intensity coefficient is designated as K_{1C} in the case of static load application in the conditions of plane deformation. In the case of generalised plane stress state it is designated as K_C.

Thus, requirement of the cracked body fracture looks like:

$$K_1 = K_{1C} \text{ or } K_1 = K_C. \tag{2.108}$$

Hence, the crack will not grow if $K_1 < K_{1C}$ or $K_1 < K_C$.

The coefficient K_1 depends on loading, crack size and cracked structure geometry. It is determined, as a rule, theoretically using methods of the elasticity theory. K_{1C} and K_C values are determined experimentally and they are the material constants. Values of K_{1C} and K_C depend on temperature and strain velocity and K_C also depends on plate width. Therefore, it is necessary to consider the problem of these values definition.

Measured values of K_C essentially differ with thickness of samples and this difference is related with fracture character determined by the fracture surface. For example, the fracture surface of the flat sample with crack consists of two parts. Edges of such sample contain sharp parts, whereas the middle part is destroyed in brittle way by flat surface, which is perpendicular to the axis of load application (Fig. 2.23a). With increase of plate thickness t the share of brittle failure increases and value of parameter K_C (Fig. 2.23 b) decreases.

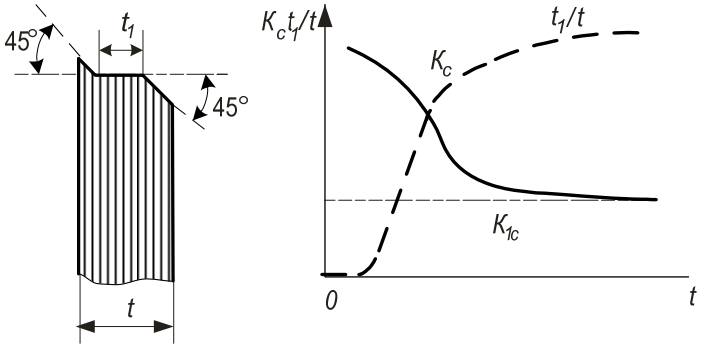

Fig. 2.23. Fracture of plate sample with crack

With the increase of the plate thickness the material state becomes more and more closer to the straight type of fracture surface and K_C value reaches its minimum value of K_{1C} (Fig. 2.23). If the plate with crack has fracture near the crack in the form of shear the requirement of the plane stress state is remained valid. It corresponds to $r_y/t \geq 1$. This requirement is characterised by distribution of plastic zone through the sample thickness, fracture plane presence with angle of 45^0 to direction of loadings and absence of the brittle fracture elements. The highest strength of material is thus reached.

The requirement of plane deformation looks like $r_y/t \leq 1/5\pi$. Usually it exists for the samples of large sections. For such samples completely brittle fracture without shear is known.

K_C value can be used for strength estimation of elements only when samples from examined material have thickness equal to the thickness of investigated structures.

K_C and K_{1C} values characterise ability of the material to resist to the crack propagation and at the same time they are included in the fracture condition. This condition establishes the value of stress intensity coefficient, at which uncontrollable crack growth appears.

2.3.3 Critical stress and critical length of crack. Safety factor

Methods of fracture mechanics allow determination of critical crack length at which its inconsistent growth begins. It is possible to calculate critical stress for element with crack of the given length as stress, at which the immediate fracture will happen. Safety factor of the element is determined as ratio of critical stress (in the presence of crack of the given length) to acting loading.

Let's observe plate of the finite width (Fig. 2.19b). For it (2.93):

$$K_1 = \sigma(\pi a)^{1/2} F_1(\alpha), \alpha = 2a/W .$$

At the moment of inconsistent crack growth beginning from requirement (2.108) we have $K_1 = K_{1C}$ or $K_1 = K_C$.

Hence, during this moment:

$$K_{1C} = \sigma_k (\pi a)^{1/2} F_1(\alpha,). \tag{2.109}$$

From here we obtain:

$$\sigma_k = \frac{K_{1C}}{(\pi a)^{1/2} F_1(\alpha)}. \tag{2.110}$$

By formula (2.110) it is possible to calculate critical stress σ_k for plate with crack of the given length at plane deformation.

Analogously, at the generalised plane stress state:

$$\sigma_k = \frac{K_C}{(\pi a)^{1/2} F_1(\alpha)}. \tag{2.111}$$

The stresses at the crack tip exceed yield strength of material before the critical state owing to formation of plastic zone, in which material hardening is observed (Fig. 2.24). This zone presence leads to the errors of calculations. Plastic zone influence in some cases can be neglected, if some correction is applied. Additionally, the plastic zone influence can be neglected, if its dimensions are essentially small in comparison with length of crack and material thickness.

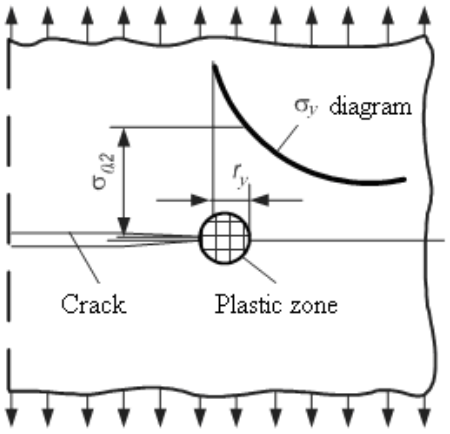

Fig. 2.24. Plastic zone at crack tip

The plastic zone size at the crack tip can be determined assuming $\sigma_y = \sigma_{0,2}$ and $(x - a) = r$. It will result in expression:

$$r_y = \frac{1}{2\pi}\left(\frac{K_1}{\sigma_{0,2}}\right)^2. \tag{2.112}$$

At the moment of fracture $K_1 = K_C$ and the limiting size of plastic zone will be equal to:

$$r_y^* = \frac{1}{2\pi}\left(\frac{K_C}{\sigma_{0,2}}\right)^2. \qquad (2.113)$$

Here $\sigma_{0,2}$ is the conventional yield strength of material.

By formula (2.113) it is possible to determine the limiting size of plastic zone in the case of generalised plane stress state. For the plane deformation case the limiting size of plastic zone:

$$r_{1y}^* = \frac{1}{6\pi}\left(\frac{K_{1C}}{\sigma_{0,2}}\right)^2. \qquad (2.114)$$

In order to take into account the plastic zone influence in the linear fracture mechanics Irwin proposed to consider that crack tip located on the distance r_y from the boundary line of actual material division.

In the case of generalised plane stress state the correction on plastic zone size should be considered. Taking into account this correction formula (2.111) becomes:

$$\sigma_k = \frac{K_C}{\pi^{1/2}\left(a + r_y^*\right)^{1/2} F_1\left(\alpha^*\right)},\ \alpha^* = 2\left(a + r_y^*\right)/W. \qquad (2.115)$$

By this formula the critical stresses σ_k is calculated at different values of a. Using these data, dependence of σ_k on α can be built.

Let's consider the problem on structure safety factor definition. The actual safety factor n_c of the cracked structure is equal to the ratio of critical stress σ_k (in the presence of crack of the given size) to acting loading, i.e.:

$$n_c = \frac{\sigma_k}{\sigma}. \qquad (2.116)$$

It is possible to plot the dependence of safety factor on crack size (Fig. 2.25) at the set loading σ. It follows from this plot that safety factor decreases with increase of crack size.

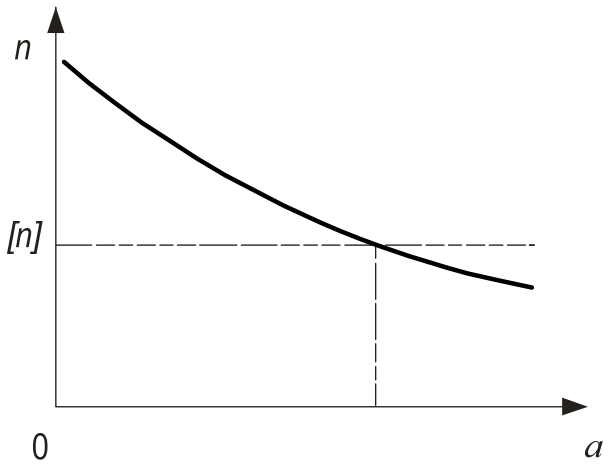

Fig. 2.25. Safety factor n plot

From strength requirement the following condition should be executed:

$$n_c \geq [n_c], \tag{2.117}$$

where $[n_c]$ is the required safety factor.

2.3.4 Example of residual strength calculation of the cracked structure

Initial data for calculation: stress intensity coefficient – K_C = 84.4 MPa·m$^{1/2}$, conventional yield stress – $\sigma_{0,2}$ = 400 MPa, loading – σ=140 MPa, element width – $2W$ = 0.20 m, height – $2h$ = 0.40 m, thickness – t = 0.002 m, eccentricity e=0.02 m. Schemes of the cracked plates are shown in Fig. 2.19. The dimensions of specimen are of arbitrary values and they are not related with real structures. They were chosen for the purpose of presentation of the algorithm of residual strength and, consequently, residual durability calculation.

For plate with central crack the relation between the stress intensity coefficient of normal separation K_1 and the set loading intensity σ is expressed by (2.93):

$$K_1 = F_1(\alpha)\sigma\sqrt{\pi a}\ ,\ \alpha = \frac{a}{W}$$

where a initial length of crack; F_1 (α) is the function, which depends on structure and crack geometry.

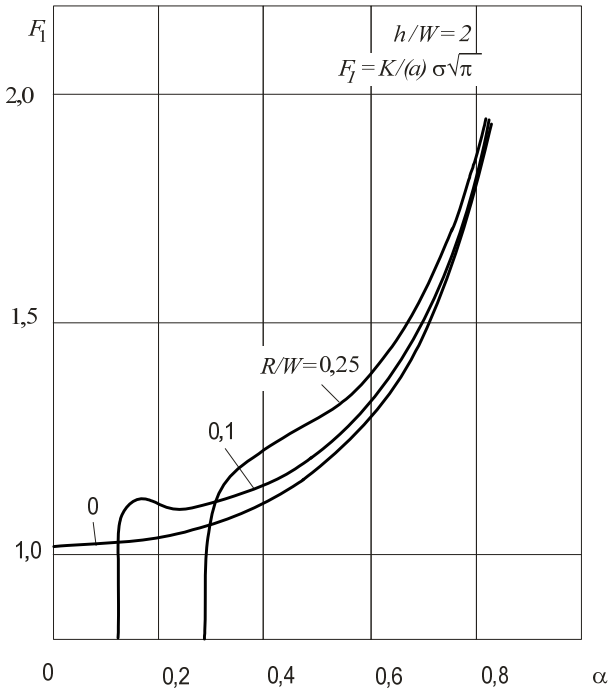

Fig. 2.26. Relation of function F_1 (α) from α

By presented above data, graphical dependence of K_1 on crack length a is constructed (Fig. 2.27).

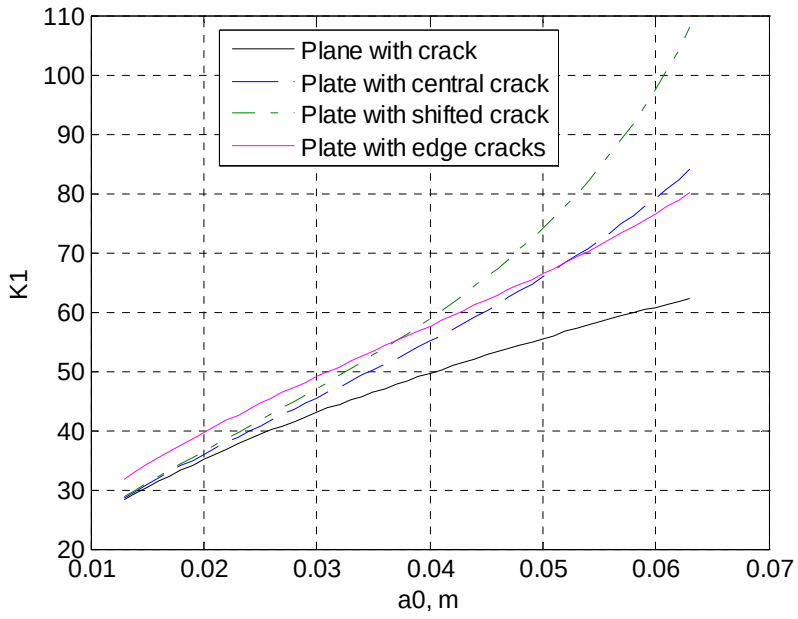

Fig. 2.27. Dependence of stress intensity coefficient K_1 (MPa·m$^{1/2}$) on crack length a

For the analysis of stress state in the neighbourhood of crack tip is performed by formulas for stress σ_x, σ_y, σ_{xy} calculation. In this case the stress concentration is caused by small radius of crack tip rounding.

In the case of normal separation at the plane stress state:

$$\sigma_x = \frac{K_1}{(2\pi r)^{1/2}} \cdot \cos\frac{\theta}{2}\left(1 - \sin\frac{\theta}{2} \cdot \sin\frac{3\theta}{2}\right) + \ldots;$$

$$\sigma_y = \frac{K_1}{(2\pi r)^{1/2}} \cdot \cos\frac{\theta}{2}\left(1 + \sin\frac{\theta}{2} \cdot \sin\frac{3\theta}{2}\right) + \ldots; \qquad (2.118)$$

$$\tau_{xy} = \frac{K_1}{(2\pi r)^{1/2}} \cdot \cos\frac{\theta}{2} \cdot \sin\frac{\theta}{2} \cdot \cos\frac{3\theta}{2} + \ldots \quad .$$

Using formulas (2.118) and plasticity of Mises, the plastic zone size near the crack tip will be:

$$r_y = \frac{K_1^2}{2\pi\sigma_{0,2}^2} \cdot \cos^2\frac{\theta}{2}\left(1 + 3\sin\frac{\theta}{2}\right). \qquad (2.119)$$

At the moment of fracture $K_1 = K_C$. Then the boundary size of plastic zone at $\theta = 0$ can be determined by formula:

$$r_y^* = \frac{K_C^2}{2\pi\sigma_{0,2}^2}. \qquad (2.120)$$

In this case at $K_C = 84.4$ MPa·m$^{1/2}$:

$$r_y^* = \frac{84{,}4^2}{2 \cdot \pi \cdot 400^2} = 7{,}086 \cdot 10^{-3}\,\text{m} \ . \qquad (2.121)$$

For the given plate $\frac{r_y^*}{t} = \frac{7{,}086}{2{,}0} = 3{,}543 > 1$ that satisfies the condition of plane stress state ($\frac{r_y^*}{t} \geq 1$).

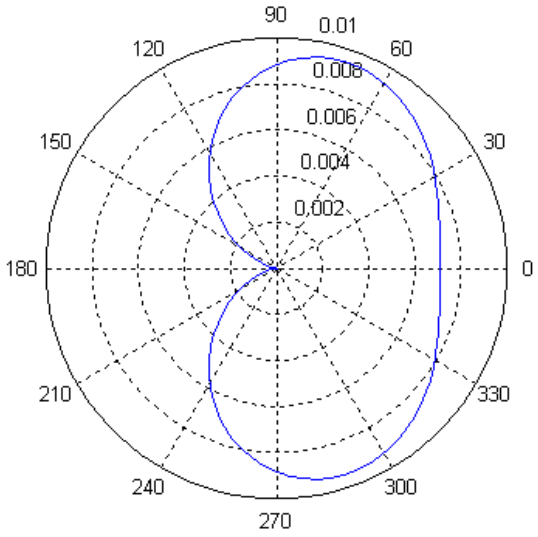

Fig. 2.28. Plastic zone representation for the case of the plate with central crack

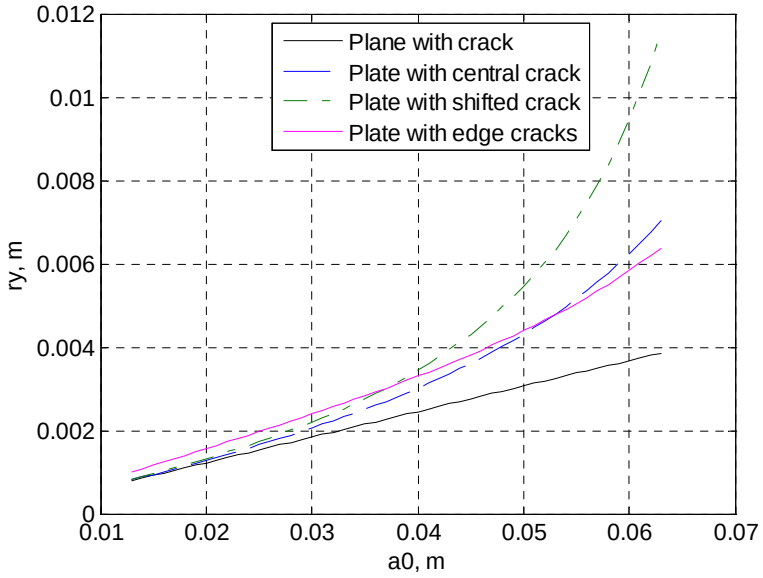

Fig. 2.29. Plastic zone size dependence on crack length

So, in this case we have the fracture in the form of shear. As a result, the plastic zone develops through all thickness and there is no brittle fracture. The highest strength of material is thus attained.

Critical stress is determined with plastic zone taking into account σ_k^* and without it – σ_k. From Irwin criterion the criterion of crack propagation at normal separation looks like $K_1 = K_C$. So, at the moment of the inconsistent crack growth beginning:

$$K_C = F_1(\alpha)\sigma_k\sqrt{\pi a}$$

Then, the critical stress without plastic zone can be determined by formula (2.111):

$$\sigma_k = \frac{K_C}{\sqrt{\pi a}F_1(\alpha)}.$$

The critical stress taking into account plastic zone is determined by (2.115):

$$\sigma_k^* = \frac{K_C}{\sqrt{\pi(a+r_y^*)}F_1(\alpha^*)},\ \alpha^* = \frac{a+r_y^*}{W}.$$

By results of calculations it is possible to say that crack will not propagate, if Irwin criterion is satisfied:

$$K_1 < K_C.$$

In this case Irwin criterion is executed, if crack length will not exceed its critical length of a_k = 0.062 m (plane with central crack). Accordingly, at the static loading application the crack will not increase.

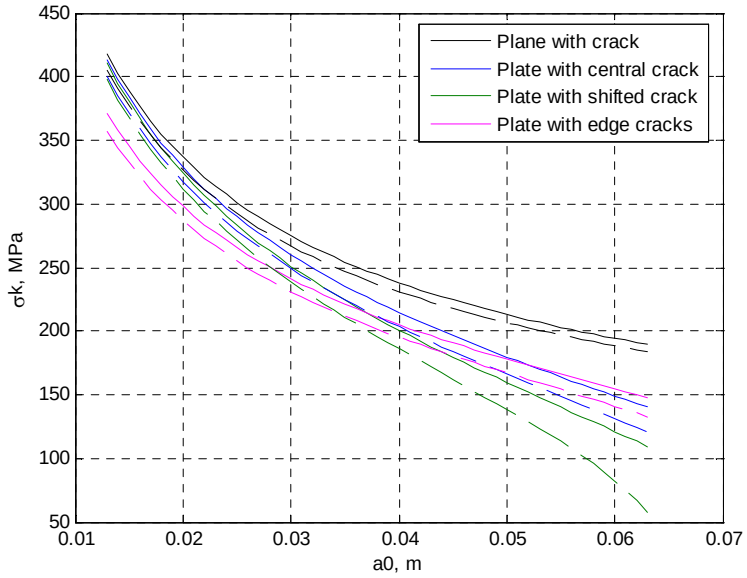

Fig. 2.30. Dependence of critical stress σ_k on crack length a: continuous line – without plastic zone near crack tip, hatched line – taking into account plastic zone

The safety factor n_c in the case of a=0.04 m and σ_k = 211.529 MPa – $n_c = \frac{211{,}529}{140} = 1{,}51 \geq [n_c] = 1.5$

Admissible value of critical stress will be $[\sigma_k]=[n_c]\cdot\sigma$. In this case, $[\sigma_k]=1.5\cdot 140=210\text{MPa}$. Then, according to Fig. 2.30, it is possible to make conclusion that in the observed cracked plate the length of crack a_i should not be more than admissible value $[a]=0.04045\text{m}$ at $[\sigma_k]=210\text{MPa}$.

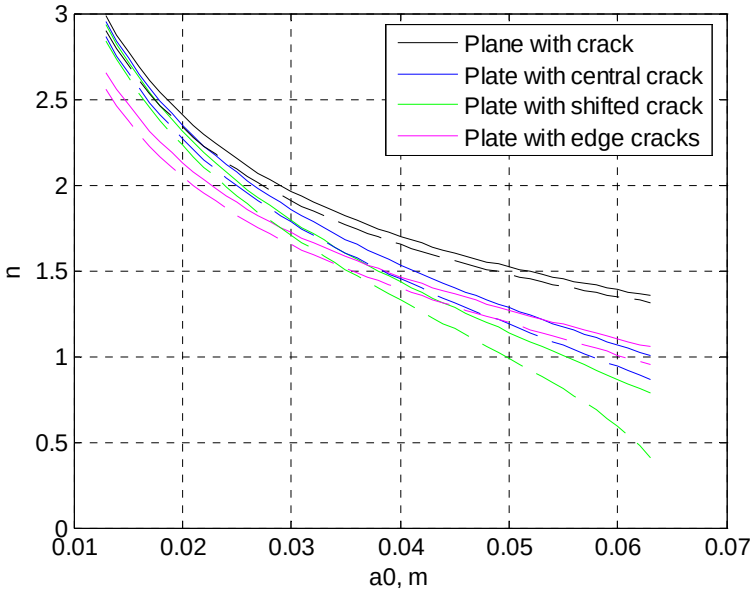

Fig. 2.31. Dependence of safety factor n_c on crack length a: continuous line – without plastic zone near crack tip, hatched line – taking into account plastic zone near crack tip

2.4 Residual durability of structure with crack

It was said before that stress originating in machine components while in service in most cases varies in time. If level of alternating stress exceeds certain limit, the process of gradual damage accumulation begins. It will lead to crack initiation, propagation and definitive fracture of the structure.

Some researchers on the basis of various physical representations obtained dependences of the crack growth rate on number of applied loading cycles and crack length. Deficiency of these relations is that they well present only some certain sites of fatigue crack growth curves and do not describe their common character. With development of fracture mechanics it became possible to observe process of fatigue cracks growth from common positions. It has been established that crack growth rate is the function of stress intensity coefficient K.

Some relations linking among themselves crack growth rate v_c and stress intensity coefficient were offered. The most known are:

Paris' equation [80]:

$$v_c = C_1(\Delta K)^n \qquad (2.\ 122)$$

Erdogan's equation [80]:

$$v_c = C_2 K_{\max}^{m} (\Delta K)^n = C_2 K_{\max}^{m+N} (1-r)^n \qquad (2.\ 123)$$

Forman's equation [27]:

$$v_c = \frac{C_3 (\Delta K)^n}{(1-r)K_C - \Delta K}, \qquad (2.\ 124)$$

where $K = K_1$; $\Delta K = K_{\max} - K_{\min}$; $K_{\max}$ and $K_{\min}$ are stress intensity factors consequently at the maximum and minimum cycle loading, r is the cycle asymmetry factor; C_1, C_2, C_3, m, n are empirical constants.

Fatigue crack at cyclical loading will continue propagating up to the moment when it will reach its critical size. After it fast propagation will take place up to the failure. Usually, time of fatigue crack propagation takes main time part of the structural element operation time.

2.4.1 Diagram of material cyclical crack resistance

Generally, the experimental data about fatigue development in materials are presented in the form of diagram of material fatigue failure, also known as diagram of material cyclical crack resistance. This diagram relates crack growth rate v_c with stress intensity coefficient in cycle ΔK, or its maximum value $K_{\max}$. At the alternating loading cycle the fracture diagram is built using $K_{\max}$.

The diagram is built in logarithmic co-ordinates (Fig. 2.32) and consists of two curvilinear parts (1) low crack growth rate ($v_c > 10^{-6}$ m/cycle) and (3) high $v_c > 10^{-6}$ ($v_c > 10^{-6}$ m/cycle) crack growth rate and the middle site (2) approximated by straight line.

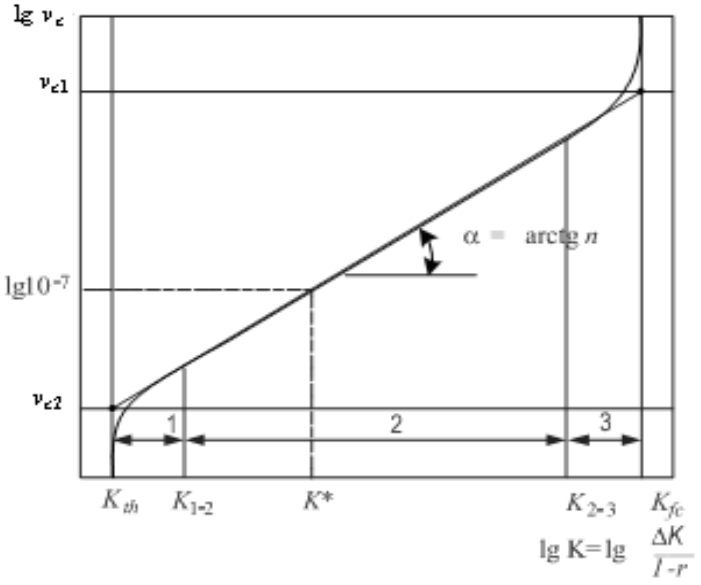

Fig. 2.32. Diagram of fatigue failure

Since the cycle asymmetry coefficient r remains constant during experiments, diagrams of fatigue failure are equivalent and they differ only by scale on abscissa axis.

The diagram of fatigue failure gives the fullest information about material resistance to crack development at cyclical loading. It establishes following basic performances of material fatigue crack resistance:

- threshold of stress intensity coefficient K_{th} is the maximum value of the greatest stress intensity coefficient of cycle, at which the crack does not propagate during the given number of cycles;
- critical stress intensity coefficient (cyclical fracture toughness) K_{fC} is the maximum cycle stress intensity coefficient, at which sample fails;

Approximated middle site of the diagram of fatigue failure can be represented by expression:

$$v = 10^{-7}(K_{\max}/K^*)^n, \tag{2.125}$$

where K^* and n are relation parameters.

Additional performances of the material crack resistance at cyclical loading are values of the maximum stress intensity coefficient of the cycle. They define the beginning ($K_{1\text{-}2}$) and the end ($K_{2\text{-}3}$) of the middle site of the diagram of fatigue failure.

Selection of parameters n and K^* is due to the fact that with their help (independently on K_{th} and K_{fC} values) it is possible to present middle site of the diagram of fatigue failure. This site is the most important from the application point of view and, generally, researches confine themselves to its definition.

Use of equations (2.122–2.124) for the diagram of fatigue failure is less convenient because coefficients C_1, C_2, C_3 are not independent values and, consequently, they can not be accepted as material properties. In expression (2.125) parameters n and K^* are parameters of material cyclical crack resistance. Parameter K^* has accurate physical sense of the greatest stress intensity coefficient of cycle at crack growth rate of 10^{-7} m/cycle. Velocity $v^* = 10^{-7}$ m/cycle is always within middle site of majority of known diagrams of fatigue failure.

For the analytical presentation of fatigue failure diagram in the full range of $K_{\max}$ change ($K_{th} < K_{\max} < K_{fC}$) it is possible to use the equation:

$$v_c = v_{c0}\left(\frac{K_{\max} - K^*_{th}}{K^*_{fC} - K_{\max}}\right)^q . \tag{2.126}$$

If values K_{th} and K_{fC} are known, it is accepted that $K^*_{th} = K_{th}$ и $K^*_{fC} = K_{fC}$. Otherwise values K^*_{th} K^*_{fC} are also determined together with constant values v_{c0} and q.

On the basis of fatigue failure diagram the performances of materials cyclical crack resistance are established. Using these parameters the materials selection and estimation of

operation conditions are performed. With fatigue failure diagram it is possible to determine durability of element with crack, i.e. number of cycles before fracture.

2.4.2 Definition of residual durability of structure with crack

Usually, during fatigue calculations the stage of fatigue crack growth is considered, whereas the stage of fatigue crack origination is not taken into account. It is supposed, hence, that initial cracks are already present in the structure or they appear at early operation stage.

Thus, the primal problem consists in describing fatigue crack growth kinetics and expected service life estimation.

Expression (2.126) is used for structure durability calculation. Considering that $v_c = da/dN$, it is represented as:

$$\frac{da}{dN} = 10^{-7}\left(K_{\max} / K^*\right)^n . \tag{2.127}$$

where N is the number of loading cycles and a is the crack length (semi-length) .

Equation (2.127) is the differential equation of crack propagation. It links among themselves crack length a and number of cycles N. Equation (2.127) should be rewritten in order to be integrated:

$$dN = 10^7\left(\frac{K^*}{K_{\max}}\right)^n da . \tag{2.128}$$

Integrating this equation, we will gain:

$$N_K - N_0 = 10^7 \int_{a_0}^{a_K}\left(\frac{K^*}{K_{\max}}\right)^n da . \tag{2.129}$$

where a_0 is the initial crack length corresponding to the number of cycles N_0; a_k is the critical crack length corresponding to the number of cycles at the moment of fracture N_k.

Then, it is necessary to specify cracked structure geometry. For example, we take plate with central crack at axial extension (Fig. 2.19a). In this case:

$$K_1 = \sigma(\pi a)^{1/2} F_1(\alpha),\ \alpha = 2a/W,$$

where function $F_1(\alpha)$ is given by ratio (2.96).

In the case of alternating stresses:

$$K_{1\max} = K_{\max} = \sigma_{\max}(\pi a)^{1/2} F_1(\alpha). \tag{2.130}$$

Substituting (2.130) in (2.129) and transferring to integration variable α we will obtain:

$$N_K - N_0 = 10^7\left(\frac{K^*}{K_{\max}}\right)^n \frac{1}{\pi^{n/2}}\left(\frac{W}{2}\right)^{\frac{n}{2}-1} \int_{\alpha_0}^{\alpha_K} \frac{dx}{\alpha^{n/2} F_1^n(\alpha)}, \tag{2.131}$$

where $\alpha_0 = 2a_0 / W$ and $\alpha_K = 2a_K / W$.

The difference ($N_K - N_0$) represents the residual durability of the structure with crack.

The integral in expression (2.131) can be computed in the closed form. Therefore, for its calculation it is necessary to apply one of quadrature formulas (for example, Simpson formula).

Usually the main part of durability (service life) is within the period of crack growth initial stage. In the process of crack propagation its growth rate increases and only small part of service life falls on high growth rate stage.

2.4.3 Example of cracked structure residual durability calculation

Calculation of the number of cycles before fracture (residual durability) and the analysis of cracked structure state at different initial crack lengths are performed (Fig. 2.29) Unsymmetrical cycle of loading is accepted to be applied to the structure.

Initial data for calculation: stress intensity coefficient – K_C = 84.4 MPa·m$^{1/2}$, conventional yield strength – $\sigma_{0,2}$ = 400 MPa, maximum stress intensity coefficient of cycle – K^*=92.3 MPa· m$^{1/2}$, parameter – n=4, cycle asymmetry coefficient – r = 0.33, maximum loading – σ_{max} =140 MPa; width – $2W$ = 0.2 m, height – $2h$ = 0.4 m, thickness – t = 0.002 m. Schemes of the cracked plates cases are shown in Fig. 2.19.

Crack growth rate is computed as:

$$v_c = \frac{\Delta a}{\Delta N} = 10^{-7}\left(\frac{K_{\max}}{K^*}\right)^n, \tag{2.132}$$

where Δa is the crack length increment, ΔN is loading cycles increment, $K_{\max} = \dfrac{\Delta K}{1-r}$ is the stress intensity coefficient of the cycle, which has maximum algebraic value at maximum loading, K_{min} is the stress intensity coefficient of cycle, which has minimum algebraic value at minimum loading, $\Delta K = K_{\max} - K_{min}$ is the stress intensity coefficient span.

Formula (2.132) can be presented as:

$$v_c = 10^{-7}\left[\frac{\Delta K}{(1-r)K^*}\right]^n. \tag{2.133}$$

From problem statement:

$$\sigma_{\min} = r\sigma_{\max} = 0{,}33\sigma_{\max},$$

Then, the stress range of the cycle is calculated:

$$\Delta\sigma = \sigma_{\max} - \sigma_{min} = (1 - r)\,\sigma_{\max}.$$

Substituting expression (2.130) to (2.133), we will gain the differential equation of crack propagation rate:

$$v_c = \frac{da}{dN} = 10^{-7}\left[\frac{\Delta\sigma\sqrt{\pi a}F_1(\alpha)}{(1-r)K^*}\right]^n \tag{2.134}$$

or

$$dN = 10^{-7}\left[\frac{K*}{\sigma_{\max}\sqrt{\pi}}\right]^n \frac{da}{\left(\sqrt{a}F_1(\alpha)\right)^n}. \qquad (2.135)$$

Integrating (2.135) and considering initial conditions, it is possible to obtain the number of cycles before fracture (residual durability of cracked structure):

$$\int_{N_0}^{N_K} dN = 10^{-7}\left[\frac{K*}{\sigma_{\max}\sqrt{\pi}}\right]^n \int_{a_0}^{a_K} \frac{da}{\left(a^{n/2}F_1^n(\alpha)\right)}. \qquad (2.136)$$

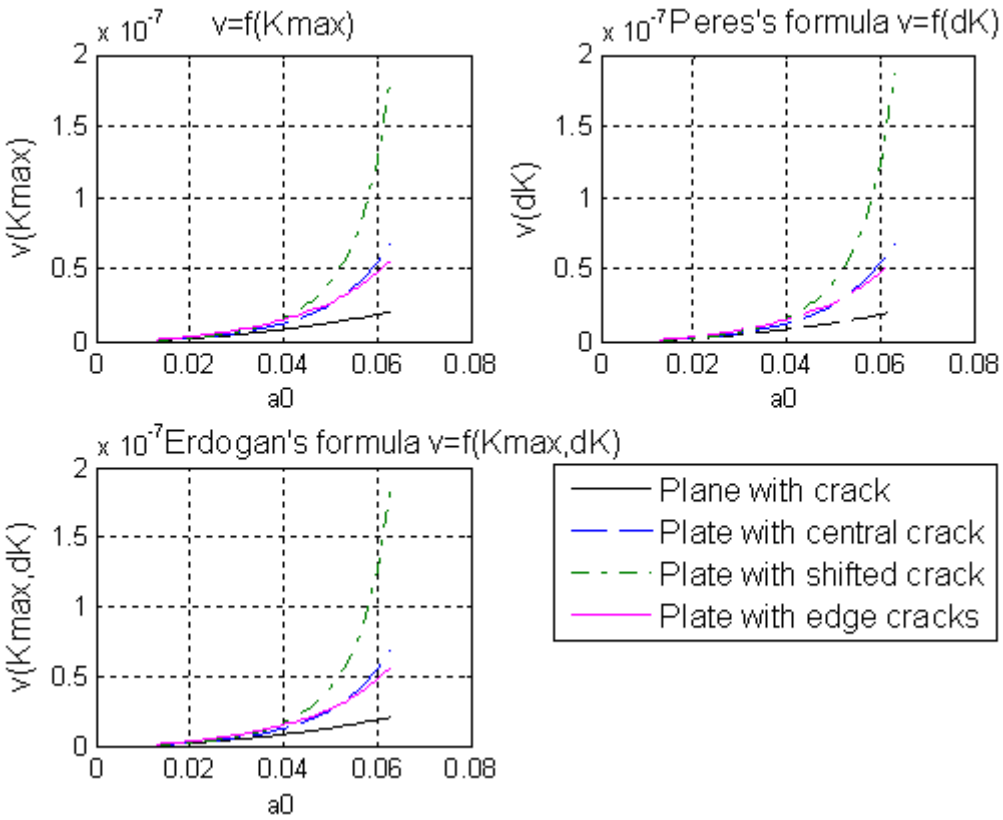

Fig. 2.33. Dependence of crack growth rate on initial crack length

Accepting $\alpha = \frac{a}{W}$, the integral (2.136) turns to:

$$N_K - N_0 = 10^{-7}\left[\frac{K*}{\sigma_{\max}\sqrt{\pi}}\right]^n \left(\frac{1}{W}\right)^{n/2-1\alpha} \int_{a_0}^{a_K} \frac{da}{\left(a^{n/2}F_1^n(\alpha)\right)}. \qquad (2.137)$$

Critical crack length a_k is determined from the fracture criterion of Irwin, when $K_1 = K_C$ (Fig. 2.28) or $\sigma_k = \sigma_{\max}$ (Fig. 2.29). In this case $K_1 = K_C = 84.4$ MPa, $\sigma_k = \sigma_{\max} = 140$ MPa.

Using Simpson's formula, the integral from (2.137) is computed.

The label is inducted:

$$f(\alpha) = \frac{1}{a^{n/2}F_1^n(\alpha)}.$$

Then:

$$\int_{a_0}^{a_K}\frac{da}{\left(a^{n/2}F_1^n(\alpha)\right)}=\int_{\alpha_0}^{\alpha_K}f(\alpha)d\alpha=\frac{\alpha_K-\alpha_0}{3m}[f(\alpha_0)+f(\alpha_b)+ \\ +2\{f(\alpha_2)+f(\alpha_4)+f(\alpha_6)\}+4\{f(\alpha_1)+f(\alpha_3)+f(\alpha_5)+f(\alpha_7)\}], \tag{2.138}$$

where m is the number of points, in which values of sub-integral function are known.

After integral calculation, expression (2.137) is used to calculate the number of cycles before fracture:

$$N_b-N_0=10^{-7}\left[\frac{K*}{\sigma_{\max}\sqrt{\pi}}\right]^n\left(\frac{1}{W}\right)^{n/2-1\alpha}\int_{a_0}^{a_K}\frac{da}{\left(a^{n/2}F_1^n(\alpha)\right)}= \\ =10^7\left[\frac{92{,}3}{140\sqrt{\pi}}\right]^4\left(\frac{1}{0{,}10}\right)\cdot 4{,}22=0{,}81\cdot 10^7.$$

Analysis of the cracked structure state subjected to asymmetric loading cycle is performed varying crack initial length. In this case, changing initial crack length from minimum to admissible value (a=0.04 m), it is possible to gain functional dependence of residual durability (number of cycles before fracture) on initial crack length $\Delta N = f(a_0)$. Obtained data are illustrated in Fig. 2.34.

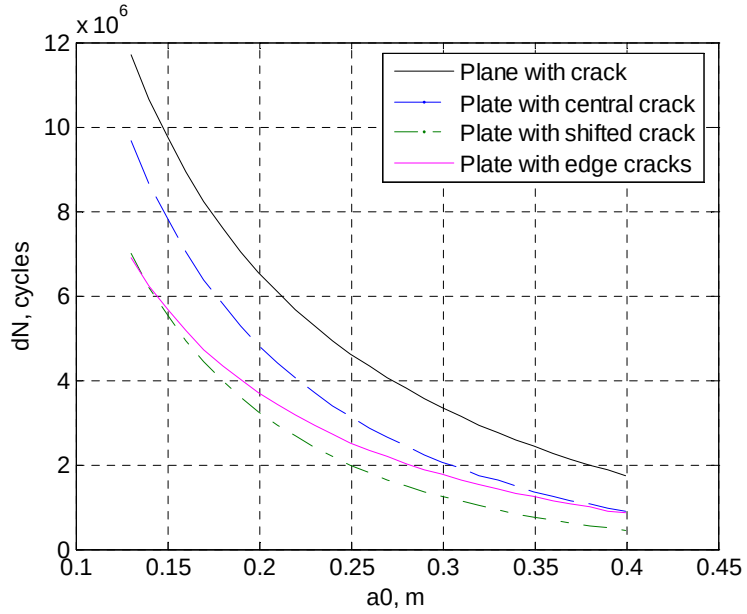

Fig. 2.34. Dependence of remained cycles number on initial crack length

Conclusions

The chapter was devoted to consideration of the contact analysis elements, because namely such approach will be used for creation of the cracked blade model in the following chapter. Main attention was paid to the frictionless case of contact interaction as only normal contact without sliding will be considered at crack breathing process simulation.

Reviewed aspects of fracture mechanics and cracked structure durability under alternating loading help to establish the main idea of the study – try to predict residual service life of cracked blade, which has been detected by measures of engine health monitoring. Shown results of the simple examples are close by their nature to the more complex ones, which will be interrogated in the following chapters.

Conjunction of the fracture mechanics elements with further presented cracked blade model will be presented in chapter 3. It will be used to estimate dependence of durability parameters of considered cracked blade model (stress intensity coefficient and number of remained cycles) on crack length. Also it will be used for proper selection of crack parameters (crack length and location) for cracked blade modelling. Having justified chosen crack parameters, simulation of cracked blade identification would be performed. Its goal is to show ability of cracked blade identification with residual durability allowing safety operation of gas-turbine engine or its well-timed maintenance.

Chapter 3

Non-linear analysis of the cracked structures in dynamics

Generally the non-linear dynamic systems are not easy to analyse because there are not any common problem-solving approaches among variety of different methods. The non-linear problems posed by a crack presence are not an exception.

For numerical calculations of the non-linear forces occurring in the crack contact zone some methods applicable for a non-linear system can be used. Most of the methods allow calculation of the non-linear forces only in a time domain and they are not applicable for a frequency domain.

This chapter describes a possible solution to a non-linear problem of the cracked blade behaviour in the frequency domain. It can be considered as the easiest and most efficient approach to obtain a periodic solution to the problem. The approach is based on application of the harmonic balance method. An assessment of the approach will be done by its comparison with a solution obtained by the direct time integration.

Usually, a cracked blade presentation consists in simulation of the crack presence supposing the crack to be always open. In this case, crack influence on forced response is simulated by stiffness reduction when solving the eigenvalues problem. Most researchers use always-open crack models in their studies and claim that the change in natural frequencies might be a parameter of crack detection. However, the assumption that the crack is always open subject to a vibration is not realistic as compressive loads may close the crack.

The crack models can be divided into two categories:

- open crack models - linear statement;
- breathing crack models - non-linear statement [18, 54, 57].

The main results obtained through simulations or experimental studies showed that the observed decrease of natural frequencies is not sufficient for a description with the open crack model. Thus, the real resonance changes may be calculated by making use of the non-linear formulation of the cracked blade behaviour. In numerical presentation its solution is

supposed to be between the linear cracked blade model solution and the one for the uncracked blade.

Two approaches of the non-linear formulation of crack presence can be used:

– introduction of periodically varying stiffness [18, 49]

– contact simulation between crack sides at time of crack closing [50, 54].

In most cases analytical solutions for the non-linear dynamic systems are practically impossible to obtain. As a result researchers and engineers turn to numerical techniques. At the first stage the systems are discretized as a set of non-linear ordinary differential equations and then direct time integration techniques are applied. However, the process is too time-consuming to obtain steady-state response under periodic load. For that reason more efficient techniques are to be found to reduce the computational costs. One of such techniques is harmonic balance (HB) method. A reduction procedure should also be applied to the system under consideration. It is of critical importance especially for the non-linear solution because of the blade geometry requiring fine meshing. It will lead to the model with a big number of degrees of freedom (DOFs). And in the case of HB method application number of DOFs is multiplied on $(2K+1)$, where K is the number of retained harmonics.

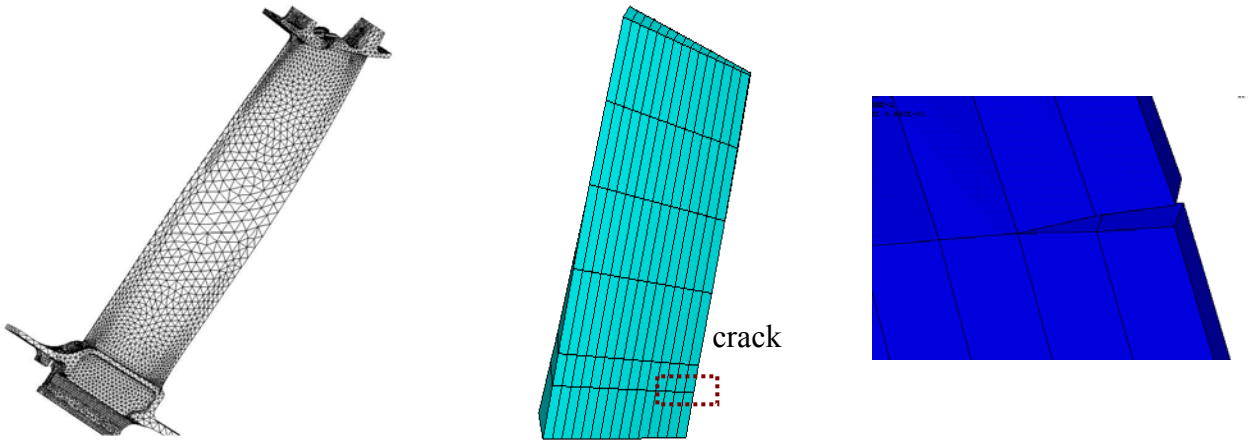

(a) (b) (c)

Fig. 3.1. Blade finite element model: (a) realistic model, (b) simplified cracked blade model, (c) crack location zone (zoom)

3.1 A solution to a non-linear dynamic problem

Any non-linear system in its simplified description can be presented by an expression subjected to optimization procedure:

$$F(U) = 0\,, \tag{3.1}$$

where F is the non-linear function of U. Common methods for the equation (3.1) solution are presented in Annex 1.

In our case the equation of motion is obtained taking into account presence of the non-linear member:

$$\mathbf{M}\ddot{\mathbf{u}} + \mathrm{C}_{\xi}\dot{\mathbf{u}} + \mathrm{K}\mathbf{u} + \mathbf{F}_{nl}(t,u,\dot{u}) = \mathbf{F}_{ext}(t), \tag{3.2}$$

where **M** is the mass matrix, **K** is the stiffness matrix, C_{ξ} is the damping matrix, **u** is the displacements' vector, $\mathbf{F}_{nl}$ is the non-linear force vector, $\mathbf{F}_{ext}$ is the external excitation time-varying periodic force vector.

Two approaches are commonly used for a solution to the problem: the direct time integration of equation (3.2) or application of the frequency domain methods. Selection of an approach depends on the forced response, which can be periodic, quasi-periodic or chaotic one. The direct time integration can be used as to the last two types of response. In this case the solution is preferably sought for with a frequency domain method or shooting method in the time domain.

3.1.1 Time domain methods for a solution to the non-linear problem

Time integration approaches are used to work directly with differential equations, namely with differential equations of the second order describing system movement. The most frequently used are methods of Newmark, Runge-Kutta, Euler, Adams-Moulton-Bashforth, Milne-Simpson,. The main advantage of the time integration approach is that for its application only few hypotheses about system behaviour are used.

Generally, the time-integration is performed following two principal schemes: explicit and implicit. In case of the implicit methods, the solution in the time point k+1 is performed when equation of system motion is considered at time t_{k+1}, whereas in that of the explicit methods it is in the state of the time t_k. Due to this fact, computational expenses under implicit formulation are higher because of the necessity to solve non-linear equation at each time step. The explicit formulation unlike avoids this, though requires a small time step to maintain the solution stable. The implicit schemes are usually used for structural inertial problems for which the response is dominated by small number of modes. The explicit solution methods are applied for solving problems of wave propagation (dynamic problems) with high frequency contributions.

Additionally, each schema can be classified in accordance with the number of steps, which must be performed to describe system state at the time t_k. A solution method can be a single-step or multi-step one.

In order to solve dynamic problems, equation of motion of the system (3.2) can be presented in a form of the system of ordinary differential equations of the first order. This doubles the number of equations:

$$\begin{bmatrix}\dot{\mathbf{u}}\\ \ddot{\mathbf{u}}\end{bmatrix}=\begin{pmatrix}\mathbf{0} & \mathbf{I}\\ -\mathbf{M}^{-1}\mathbf{K} & -\mathbf{M}^{-1}\mathbf{C}_{\zeta}\end{pmatrix}\begin{bmatrix}\mathbf{u}\\ \dot{\mathbf{u}}\end{bmatrix}+\begin{pmatrix}\mathbf{0}\\ -\mathbf{M}^{-1}\left(-\mathbf{F}_{nl}+\mathbf{F}_{ext}\right)\end{pmatrix}. \tag{3.3}$$

Equation (3.3) should be verified for consecutive time points from the interval $[t_k, t_{k+1}]$. It means that the incremental time integration schemes of different formulation and accuracy order are to be applied.

Consider various time integration schemes. General integration scheme for all methods can be presented in view of the recurrent expression [73]:

$$\begin{bmatrix}\mathbf{u}_k\\ \dot{\mathbf{u}}_k\end{bmatrix}=\sum_{j=1}^{q}\alpha_j\begin{bmatrix}\mathbf{u}_{k-j}\\ \dot{\mathbf{u}}_{k-j}\end{bmatrix}+(t_k-t_{k-1})\sum_{j=0}^{q}\beta_j\begin{bmatrix}\dot{\mathbf{u}}_{k-j}\\ \ddot{\mathbf{u}}_{k-j}\end{bmatrix}, \tag{3.4}$$
$$k=1,2,...;q\le k$$

The parameters α_j and β_j (j = 1,…,q) are specific constants of a particular method used for the problem solution. Number q allows performing classification of methods by the step number (one step or multi-step) and scheme type (explicit or implicit). If q = 1, it means that the number of previous time steps is equal to one and the method is classified as the one step method. If the integration scheme uses more than one successive system state (q>1), it is classified as a multi-step method. The **method of Adams** is most commonly used one. A useful feature of the multi-step methods is a prospect to determine a local error of truncation and include a correcting term, which increases accuracy on each step. Besides, a step length increase is also possible to find out without reduction of the solution accuracy. The solution requires application of the **prediction-correction methods**, among which **Adams-Bashforth-Maulton method** and that of **Milne-Simpson** are the most recognized ones.

Both one-step and multi-step methods can either be explicit or implicit. If parameter β_0 is not equal to zero, the vector of system state $\mathbf{u}_k$ at time t_k depends on its own derivative at the same time and this makes the integration algorithm to be implicit. In the opposite case ($\beta_0 = 0$) $\mathbf{u}_k$ can be evaluated on base of the previous system of states and therefore the time integration algorithm can be considered to be explicit.

Some other time integration techniques must be reviewed in brief. There are a set of methods based on extrapolation approach and decomposition in Taylor's series. The method of **Taylor's series** is used supposing displacements, velocities and accelerations in equation (3.3) to be known at the time moment t_k and they have to be determined at the moment t_{k+1}= t_k+h:

$$\begin{cases}\mathbf{u}_{k+1}=\mathbf{u}_k+h\dot{\mathbf{u}}_k+\int_{t_k}^{t_{k+1}}\ddot{\mathbf{u}}(t)dt\\ \dot{\mathbf{u}}_{k+1}=\dot{\mathbf{u}}_k+\int_{t_k}^{t_{k+1}}(t_{k+1}-t)\ddot{\mathbf{u}}(t)dt\end{cases}. \tag{3.5}$$

The integrals in equation (3.5) can be calculated using numerical integration by quadratures representing $\ddot{\mathbf{u}}(t)$ at time interval $[t_k, t_{k+1}]$:

$$\begin{cases} \mathbf{u}_{k+1} = \mathbf{u}_k + h\dot{\mathbf{u}}_k + \dfrac{h^2}{2}((1-\beta)\ddot{\mathbf{u}}_k + \beta\ddot{\mathbf{u}}_{k+1}) \\ \dot{\mathbf{u}}_{k+1} = \dot{\mathbf{u}}_k + h((1-\alpha)\ddot{\mathbf{u}}_k + \beta\ddot{\mathbf{u}}_{k+1}) \end{cases}, \tag{3.6}$$

where coefficients α and β corresponds to a particular quadrature type. If $\alpha = \beta = 1/2$, it means that constant acceleration scheme of numerical integration was used at the interval $[t_k, t_{k+1}]$. In the case of linear acceleration scheme $\alpha = ½$, and $\beta = 1/3$.

Runge-Kutta methods, for example, are derived from Taylor's series method of same *n*-th order. The derivatives of higher orders have not to be computed analytically that is the main deficiency of the method of Taylor's series. Runge-Kutta methods are advantageous in attaining the highest accuracy at minimum time, but they do not always provide solution convergence for strictly non-linear problems.

Periodic solution by time integration

Time integration methods are also appropriate for problem solution under domination of the periodical response. The solution period $[0, T]$ is divided into *M* sub-intervals $[t_k, t_{k+1}]$ (k=1,…,M). The main task is to find out value $\mathbf{u}_k$, which is approximate to $\mathbf{u}_k(t_k)$. For **method of finite differences (central)** the time derivatives are supposed to be replaced with the following expressions:

$$\begin{cases} \dot{\mathbf{u}}_k = \dfrac{1}{2\Delta t}(\mathbf{u}_{k+1} - \mathbf{u}_{k-1}) \\ \ddot{\mathbf{u}}_k = \dfrac{1}{\Delta t^2}(\mathbf{u}_{k+1} - 2\mathbf{u}_k + \mathbf{u}_{k-1}) \end{cases}, \tag{3.7}$$

where Δt is the time sub-interval of constant length.

Insertion of equation (3.5) into equation (3.2) yields the non-linear algebraic system:

$$\mathbf{H(U)} = \mathbf{AU} + \mathbf{b(U)} = 0, \tag{3.8}$$

which should be solved as $\mathbf{U} = [\mathbf{u}_0 ... \mathbf{u}_i ... \mathbf{u}_{M-1}]$. Matrix **A** has block-diagonal structure and vector **b** takes into account the non-linear member. Their equivalents in the frequency domain will be presented at the discussion of the harmonic balance method.

Shooting method is an appropriate scheme to look for a periodic solution to the non-linear problem. The method is used in mathematics for solving problems of boundary values. In the field of vibration mechanics the method was firstly applied to Duffing oscillator [77]. With this method the initialization is searched for inside of the solution period and then followed by the time

integration over the period that results in a stationary response. Thus, a periodic solution, which is unknown a priori, can be obtained.

Normally, we perform integration of equation of motion over the interval $[t_0, t_0 + T]$ with the set of initial conditions $\mathbf{y}(0) = \mathbf{y}_0, \dot{\mathbf{y}}(0) = \dot{\mathbf{y}}_0$. It is being continued up to the moment till periodic solution is obtained. The operation under shooting method is restarted every time with new initial conditions. As a result, shooting method is an iterative like procedure, which contains time integration over the period at each stage. Equation (3.6) is rewritten for shooting method as:

$$\begin{cases} \dot{\mathbf{y}}(t) = \mathbf{A}\mathbf{y}(t) + \mathbf{b}(t, \mathbf{y}) \\ \mathbf{y}(t_0) = \mathbf{y}_0 \end{cases}. \tag{3.9}$$

If the solution to (3.9) noted as $\mathbf{y}(t, t_0, \mathbf{y}_0)$ is periodic, then $\mathbf{y}(t_0 + T, t_0, \mathbf{y}_0) = \mathbf{y}_0$. In order to adjust initial conditions, zeros of the next function should be found:

$$\mathbf{H}(\mathbf{y}_0) = \mathbf{y}(t_0 + T, t_0, \mathbf{y}_0) - \mathbf{y}_0 = 0. \tag{3.10}$$

3.1.2 Frequency domain methods for a solution to the non-linear problem

For all linear systems subjected to mono-harmonic excitation their responses will also be mono-harmonic. This consideration is derived from the theory of linear differential equations. But it cannot be directly applied to the non-linear system case. It is only possible to suppose that non-linear system response is periodic.

Sometimes it happens that non-linear response is only quasi-periodic or even chaotic. But in majority of cases the periodic solution is obtained. So, the periodic solution to the non-linear system can be decomposed into Fourier series. The main idea of the frequency domain methods consists in this decomposition.

Let's suppose that a solution has period *T* of response and it is stable. The solution can be decomposed into the infinite base of trigonometric functions. Numerically, it is not reasonable to process the infinite sum and the hypothesis is suggested that the solution can be approximated by truncated Fourier series. To continue with the approximation we will deal with one constant term and *K* first members:

$$u^{exact}(t) \approx u^{appr}(t) = a_0 + \sum_{k=1}^{K} a_k \cos k\omega t + \sum_{k=1}^{K} b_k \sin k\omega t, \tag{3.11}$$

where $\omega = 2\pi / T$ is the excitation frequency. Making use of the expression (3.11), the solution is approximated in vector space of the finite dimension created by the base of trigonometric functions.

The validity of the presented approximation directly depends on order of the truncated series: as more terms in series will be retained, thus much of $u^{appr}(t)$ will be closer to $u^{exact}(t)$.

However, to provide this approximation, the base of trigonometric functions must be taken in full. It means that all terms of the series are to be taken into account. In some cases, it is possible that certain coefficients a_k or b_k can be almost zero or their effect will be negligible with regard to other coefficients. Thus, harmonics referred to these coefficients can be omitted. Unfortunately, there are no criteria that allow judging, which of the harmonics should be retained.

With the approximated solution (3.11) inserted into the differential equation of system motion we will obtain:

$$R_e(t,\mathbf{U}) = \mathbf{M}\ddot{\mathbf{u}}^{appr}(t) + \mathrm{C}_\xi \dot{\mathbf{u}}^{appr}(t) + \mathrm{K}\mathbf{u}^{appr}(t) + \mathbf{F}_{nl}(u^{appr}, \dot{u}^{appr}, t) - \mathbf{F}(t) \qquad (3.12)$$

$$\mathbf{U} = \begin{bmatrix} a_0 & a_1 & b_1 & \dots & a_K & b_K \end{bmatrix}^T.$$

The non-zero residual term $R(t,\mathbf{U})$ is the error of truncation procedure, which measures the error of exact solution $u^{exact}(t)$ approximated by $u^{appr}(t)$.

Formulation of harmonic balance method

There are several ways to implement harmonic balance (HB) method and three approaches are particularly attractive: the classical harmonic balance method, the high-dimensional harmonic balance method, and the incremental harmonic balance method. HB method yields rather accurate results but it is difficult for implementation as to the high-dimensional systems or systems with a complex or non-smooth non-linearity. On the other hand, high-dimensional HB method [64] is easily applicable for high-dimensional systems regardless of the non-linear complexity. But it may produce spurious solutions in addition to the physically meaningful solutions. Besides, the incremental HB method is capable of dealing with strongly non-linear systems of any desired accuracy [19]. The classic formulation of HB method will be applied as to the problem under consideration.

In non-linear case the equation of system motion is expressed by:

$$\mathbf{M}\ddot{\mathbf{u}} + \mathrm{C}_\xi \dot{\mathbf{u}} + \mathrm{K}\mathbf{u} + \mathbf{F}_{nl}(u_{nl}, t) = \mathbf{F}_{ext}(t), \qquad (3.13)$$

where non-liner forces are shown to be dependent only on non-linear degrees of freedom in the time domain.

The damping matrix was calculated on the base of the structural damping ratio ξ from the next relation:

$$\mathbf{C}_\xi = \xi\mathbf{K}. \qquad (3.14)$$

Then we are searching for the $u(t)$ in the form of the truncated trigonometric series of $k = 1, \dots, K$ harmonics:

$$u(t) = a_0 + \sum_{k=1}^{K} a_k \cos k\omega t + \sum_{k=1}^{K} b_k \sin k\omega t. \qquad (3.15)$$

The *j*-th non-linear degree of freedom could be expressed in the same way as (3.16):

$$u_{nl}^{j} = a_{nl0} + \sum_{k=1}^{K} a_{nlk} \cos k\omega t + \sum_{k=1}^{K} b_{nlk} \sin k\omega t. \tag{3.16}$$

If to put equations (3.15) and (3.16) into (3.13), it will be changed to:

$$\mathbf{A}\tilde{\mathbf{u}} + \mathbf{b}(\tilde{\mathbf{u}}) = \tilde{\mathbf{F}}, \tag{3.17}$$

where **A** is diagonally symmetric in the block matrix:

$$\mathbf{A} = \begin{bmatrix} \mathbf{L}_0 & 0 & \dots & 0 \\ 0 & \mathbf{L}_1 & \dots & 0 \\ \dots & \dots & \dots & \dots \\ 0 & 0 & \dots & \mathbf{L}_N \end{bmatrix}_{N_{dof}(2k+1)\times N_{dof}(2k+1)} \tag{3.18}$$

$$\mathbf{L}_0 = \mathbf{K}; \mathbf{L}_k = \begin{bmatrix} \mathbf{K} - (k\omega)^2 \mathbf{M} & k\omega \mathbf{C}_\xi \\ -k\omega \mathbf{C}_\xi & \mathbf{K} - (k\omega)^2 \mathbf{M} \end{bmatrix}.$$

(b) non-linear member:

$$\mathbf{b}(\tilde{\mathbf{u}}) = \begin{bmatrix} \frac{1}{T_s}\int_0^{T_s} F_{nl}\,dt \\ \left\{ \begin{array}{l} \frac{2}{T_s}\int_0^{T_s} F_{nl} \cos(k\omega t)\,dt \\ \frac{2}{T_s}\int_0^{T_s} F_{nl} \sin(k\omega t)\,dt \end{array} \right\} \\ \dots \end{bmatrix}_{N_{dof}(2k+1)\times 1}, \tag{3.19}$$

where $T_s = 2\pi/\omega$ is an excitation period.

$\tilde{\mathbf{F}}$ is an external excitation force member:

$$\tilde{\mathbf{F}} = \begin{bmatrix} \frac{1}{T_s}\int_0^{T_s} F\,dt \\ \left\{ \begin{array}{l} \frac{2}{T_s}\int_0^{T_s} F \cos(k\omega t)\,dt \\ \frac{2}{T_s}\int_0^{T_s} F \sin(k\omega t)\,dt \end{array} \right\} \\ \dots \end{bmatrix}_{N_{dof}(2k+1)\times 1}, \tag{3.20}$$

$\tilde{\mathbf{u}}$ is the vector of Fourier series coefficients:

$$\tilde{\mathbf{u}} = \begin{bmatrix} a_0 & a_1 & b_1 & \dots & a_K & b_K \end{bmatrix}^T. \tag{3.21}$$

Any conventional numerical integration techniques could be applied for integral calculation in (3.20) and (3.21). The trapezoidal method will be used in our case. The procedure of Newton-Raphson will be applied to solve the non-linear equation (3.18).

3.1.3 Methods for reduced order modelling

When doing an analysis of vibration performances of a structure with essentially high-required accuracy, we encounter the problem of the enormous number of DOFs to take part in the solution. For example, the three-dimensional model of the blade can have up to 60000 DOFs, which creates computational problems due to costs of the calculation time and memory shortage. Therefore, we have to reduce a system size by implementing one of the existent techniques of reduced order modelling based on system sub-structuring. The main advantages of the approach are the following: partition of the analyzed object on some independent sub-structures, modification of a sub-structure without influence on the remainder, working with one sub-structure in the case of a number of identical sub-structures (e.g. cyclic symmetry). Some well-known procedures of system reduction by sub-structuring are: fixed interface sub-structuring method of Craig-Bampton and free interface sub-structuring method of Mac Neal, reduction by substitution.

Fixed interface method

This method is well known from the work of Craig and Bampton [20]. It is well adapted and suitable for its use in the bladed disk structures [9, 88]. Implementation of the method involves defining two types of DOFs in the structure subjected to reduction: DOFs of interface with subscript *m* and internal DOFs of the structure with subscript *s*.

In this case the equation of system motion (without damping) can be expressed in the following way:

$$\begin{bmatrix} \mathbf{M}_{\mathrm{mm}} & \mathbf{M}_{\mathrm{ms}} \\ \mathbf{M}_{\mathrm{sm}} & \mathbf{M}_{\mathrm{ss}} \end{bmatrix} \begin{bmatrix} \ddot{\mathbf{u}}_{\mathrm{m}} \\ \ddot{\mathbf{u}}_{\mathrm{s}} \end{bmatrix} + \begin{bmatrix} \mathbf{K}_{\mathrm{mm}} & \mathbf{K}_{\mathrm{ms}} \\ \mathbf{K}_{\mathrm{sm}} & \mathbf{K}_{\mathrm{ss}} \end{bmatrix} \begin{bmatrix} \mathbf{u}_{\mathrm{m}} \\ \mathbf{u}_{\mathrm{s}} \end{bmatrix} = \begin{bmatrix} \mathbf{F}_{\mathrm{m}} \\ \mathbf{F}_{s} \end{bmatrix} \tag{3.22}$$

Let's approximate the movement of a sub-structure by Rayleigh-Ritz method on the base of eigenmodes with fixed interface $\mathbf{\Phi}$ (eigenvectors obtained with interface nodes fixed) and static modes $\mathbf{G}$ (they are defined as the static deformation of the structure with unit displacements applied to interface DOFs):

$$\begin{gathered} \mathbf{U} = \mathbf{G}\mathbf{u}_m + \mathbf{\Phi}\mathbf{Q} = \begin{bmatrix} \mathbf{G} & \mathbf{\Phi} \end{bmatrix} \begin{bmatrix} \mathbf{u}_m \\ \mathbf{q} \end{bmatrix}, \\ \mathbf{Q} = \begin{bmatrix} \mathbf{u}_m \\ \mathbf{q} \end{bmatrix} \end{gathered} \tag{3.23}$$

The normal modes of fixed interface could be obtained for condition $\mathbf{u}_m = 0$:

$\mathbf{M}_{ss}\ddot{\mathbf{u}}_s + \mathbf{K}_{ss}\mathbf{u}_s = 0$

For the static modes of connection the equilibrium condition will be used:

$$\begin{bmatrix} \mathbf{K}_{\mathrm{mm}} & \mathbf{K}_{\mathrm{ms}} \\ \mathbf{K}_{\mathrm{sm}} & \mathbf{K}_{\mathrm{ss}} \end{bmatrix} \begin{bmatrix} \mathbf{u}_{\mathrm{m}} \\ \mathbf{u}_{\mathrm{s}} \end{bmatrix} = \begin{bmatrix} \mathbf{F}_{\mathrm{m}} \\ \mathbf{0} \end{bmatrix} \tag{3.24}$$

From this we will obtain:

$$\mathbf{u}_s = -\mathbf{K}_{ss}^{-1}\mathbf{K}_{sm}\mathbf{u}_{\mathrm{m}} \tag{3.25}$$

The equilibrium state can be also presented using the interface DOFs:

$$\mathbf{U} = \begin{bmatrix} \mathbf{I} \\ \mathbf{K}_{ss}^{-1}\mathbf{K}_{sm} \end{bmatrix} \mathbf{u}_m \tag{3.26}$$

Then equation (3.23) can be written as:

$$\mathbf{U} = \begin{bmatrix} \mathbf{I} & \mathbf{0} \\ \mathbf{K}_{ss}^{-1}\mathbf{K}_{sm} & \mathbf{\Phi} \end{bmatrix} \mathbf{Q} \tag{3.27}$$

The system transformation matrix is formed on the base of redundant static constraint modes and fixed-interface normal modes

$$\mathbf{T} = \begin{bmatrix} \mathbf{I} & \mathbf{0} \\ \mathbf{G}_{sm}\mathbf{\Phi}_{ss} \end{bmatrix}, \tag{3.28}$$

where $\mathbf{G}_{sm} = -\mathbf{K}_{ss}^{-1}\mathbf{K}_{sm}$ are the redundant static constraint modes and $\mathbf{\Phi}_{ss}$ are the fixed-interface normal modes.

Using the transformation matrix from equation (3.28), it is possible to define system's matrices (mass and stiffness) on the new base. For this purpose the formulations of the kinetic energy and energy of deformation are used:

$$E_c = \frac{1}{2}\dot{\mathbf{U}}^T\mathbf{M}\dot{\mathbf{U}} = \frac{1}{2}\dot{\mathbf{Q}}^T\mathbf{M}_{red}\dot{\mathbf{Q}}; \tag{3.29}$$

$$E_d = \frac{1}{2}\mathbf{U}^T\mathbf{K}\mathbf{U} = \frac{1}{2}\mathbf{Q}^T\mathbf{K}_{red}\mathbf{Q}, \tag{3.30}$$

where $\mathbf{M}_{red}$, $\mathbf{K}_{red}$ – reduced mass and stiffness matrices, which can be obtained by formulas:

$$\mathbf{M}_{red} = \mathbf{T}^T \begin{bmatrix} \mathbf{M}_{\mathrm{mm}} & \mathbf{M}_{\mathrm{ms}} \\ M_{\mathrm{sm}} & \mathbf{M}_{\mathrm{ss}} \end{bmatrix} \mathbf{T} \tag{3.31}$$

$$\mathbf{K}_{red} = \mathbf{T}^T \begin{bmatrix} \mathbf{K}_{\mathrm{mm}} & \mathbf{K}_{\mathrm{ms}} \\ \mathbf{K}_{\mathrm{sm}} & \mathbf{K}_{\mathrm{ss}} \end{bmatrix} \mathbf{T} \tag{3.32}$$

Free interface method

Another approach to system reduction is known as the method of Mac Neal or free interface method [68]. A movement of each sub-structure is characterized taking its eigenmodes with free interface $\mathbf{\Phi}$ and approximated by Rayleigh-Ritz method:

$$\mathbf{U} = \mathbf{\Phi q}, \tag{3.33}$$

where $\mathbf{\Phi}$ is the matrix containing the base of truncated eigenmodes with free interface for each sub-structure.

The truncation could cause some unacceptable errors in dynamic properties of the structure. So, it was proposed to take into account static effect of the higher order truncated modes by introducing a correction for residual flexibility. The flexibility matrix of *N*-th order system is expressed by equation:

$$\mathbf{G} = \sum_{k=1}^{N} \frac{\mathbf{\Phi}_k \mathbf{\Phi}_k^T}{\omega_k^2 - \omega^2}. \tag{3.34}$$

This matrix is obtained from particular solution of the system motion equation, and then the forced response can be written in the form:

$$\mathbf{U}_0 = \mathbf{\Phi q}_0 + \mathbf{GF}, \tag{3.35}$$

where $\mathbf{\Phi q}_0$ is the solution of the homogenous equation, $\mathbf{GF}$ is the particular solution.

In general, equation (3.36) is very important numerically. Using Rayleigh-Ritz approximation (3.34) and decomposing the exact solution in two parts (one depends on *m* forms of the interface and other is the function of the higher order forms) we obtain:

$$\mathbf{U}_0 = \mathbf{U}_1 + \mathbf{U}_2, \tag{3.36}$$

where $\mathbf{U}_1 = \mathbf{\Phi}_1 \mathbf{q}_1 + \mathbf{G}_1 \mathbf{F}$ directly corresponds to approximation (3.33) and $\mathbf{U}_2 = \mathbf{\Phi}_2 \mathbf{q}_2 + \mathbf{G}_2 \mathbf{F}$ is the difference between exact and approximated solutions.

With the first-order approximation of the flexibility matrix (3.34), the matrix of static flexibility is obtained:

$$\mathbf{G}_0 = \sum_{k=1}^{N} \frac{\mathbf{\Phi}_k \mathbf{\Phi}_k^T}{\omega_k^2}. \tag{3.37}$$

In reality equation (3.37) is not applicable because it requires calculation of all modes of a structure. Therefore, some approaches are used for flexibility matrix calculation.

For the term $\mathbf{U}_2$ it is residual flexibility, obtained from the difference between static flexibility and the sum of the flexibilities of the retained modes:

$$\mathbf{G}_{res} = \mathbf{G}_0 - \sum_{k=1}^{m} \frac{\mathbf{\Phi}_k \mathbf{\Phi}_k^T}{\omega_k^2} \tag{3.38}$$

Consequently, main relation for each sub-structure will be noted as:

$$\mathbf{U} = \mathbf{\Phi q} + \mathbf{G}_{res}\mathbf{F}, \tag{3.39}$$

where $\mathbf{\Phi q}$ is the approximated solution of the forced response on the base of retained modes, $\mathbf{G}_{red}\mathbf{F}$ is the correction term.

Two coupling relations at the interface are applied to assemble the structure:

- displacements compatibility
- forces equilibrium.

Modal substitution approach

The technique is appropriate for systems that have the principal element to which additional elements (called *branches*) can be attached [6]. The main point of the method consists in defining movement of the principal sub-structure on the base of its natural modes with free interface. Same improvements can be achieved using loaded interface. It means that mass and stiffness matrices of the secondary sub-structure interface are added to the mass and stiffness matrices of the principal sub-structure interface correspondently.

It should be noted that principal sub-structure analysis is not longer independent of the branches. Its equation of motion depends on stiffness and mass matrices of the secondary sub-structures reduced at the interface. In order to overcome it, the reference sub-structure is often used for principal sub-structure calculation. Then, to take into account the differences between branches, the perturbation technique is used. Reduction of the secondary sub-structures is in most cases performed by fixed-interface method using natural modes at fixed interface and static modes of junction.

3.2 Cracked blade dynamic model

Let the cracked blade non-linear dynamic behaviour be described by the equation:

$$\mathbf{M}\ddot{\mathbf{u}} + \mathrm{C}_{\xi}\dot{\mathbf{u}} + \mathrm{K}\mathbf{u} + \mathbf{F}_{nl}(u_{nl}) = \mathbf{F}_{ext}(t). \tag{3.40}$$

where $\mathbf{M}$, $\mathbf{C}_{\xi}$, and $\mathbf{K}$ are the symmetric mass, damping, and stiffness matrices of the blade model, $\mathbf{F}_{ext}$ is the amplitudes' vector of external excitation forces, $\mathbf{F}_{nl}$ is the non-linear forces vector, which depends on non-linear DOFs u_{nl}.

In the linear case we assume that $\mathbf{F}_{nl}(u_{nl}) = 0$ and crack is always open. The system response is steady-state and it has the form $\mathbf{U}(t) = \mathbf{u}e^{i\omega t}$ that yields to the set of algebraic equations

$$\mathbf{Hu} = \mathbf{F}, \tag{3.41}$$

where $\mathbf{H} = \mathbf{K} - \omega^2\mathbf{M} + i\omega\mathbf{C}_\xi$ is the impedance matrix at the excitation frequency ω.

Application of external excitation forces is shown in Fig. 3.2. Forces are applied in the points of the blade tip: on the leading and trailing edges.

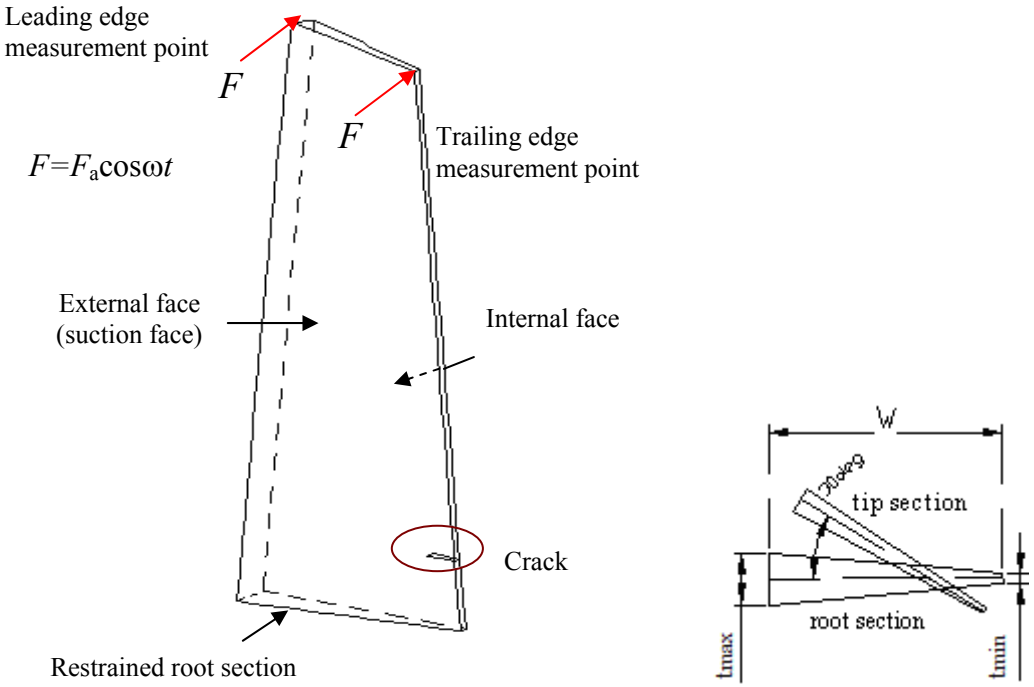

Fig. 3.2. Cracked blade model subjected to forced response analysis

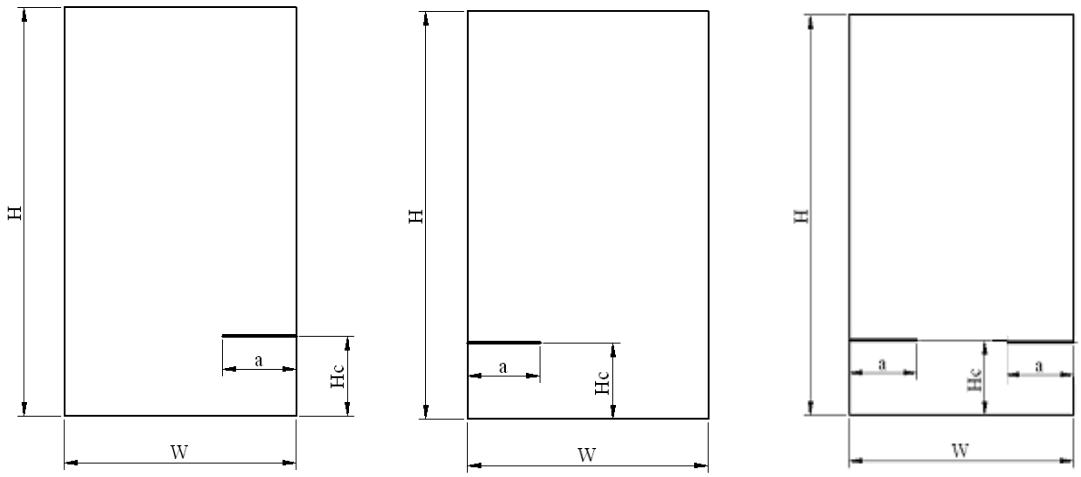

(a) (b) (c)

Fig. 3.3. Crack location variants:

(a) crack on trailing edge, (b) crack on leading edge, (c) symmetric cracks

Blade model geometrical dimensions: the height is H = 0.08m, the maximum width is W = 0.03m, the crack location height is Hc = 0.10m, the maximum and minimum blade thicknesses are t_{max} = 0.006 m and t_{min} = 0.003 m, excitation force amplitude F_a=0.3N. Cross-section area of the blade profile is changed depending on equation (1.1) in dependence on blade height. Material

properties of the blade model: Young's modulus – $2 \cdot 10^{11}$ Pa, Poisson's ratio – 0.3, material density – $7.8 \cdot 10^{3}$ kg/m^3.

The finite elements model of the cracked blade (Fig. 3.1b) was created in ANSYS environment with following meshing parameters: number of elements divisions along blade height – 5, number of elements divisions along blade width – 15, number of elements divisions along blade thickness – 1. Meshing of the crack zone supposes one element per 1mm of crack length.

Eigenproblem solution to the cracked blade in linear formulation is presented in Table 3.1. Two main hypotheses are accepted: the crack is initially open (with gap) and gyroscopic effect is not considered during solution. From its results we can easily see a decrease of eigenfrequencies caused by a crack presence.

Table 3.1

Change of the cracked blade eigenfrequencies due to crack presence

Crack location **Hc**, mm	Crack size **a**, mm	Deviation from uncracked blade model, %							
		Crack on trailing edge				Crack on leading edge			
		1st mode	2nd mode	3rd mode	4th mode	1st mode	2nd mode	3rd mode	4th mode
10	2	0.0035	0.0203	0.0297	0.3186	0.3664	0.2729	0.1949	0.8465
	4	0.0247	0.1503	0.1781	2.1491	2.3357	1.7400	1.1844	5.1722

In non-linear case the blade resonance frequency can be obtained only from frequency response analysis requiring problem non-linear formulation. The non-linear member $\mathbf{F}_{nl}(u_{nl})$ in equation (3.40) is the force of contact interaction between the crack sides, with u_{nl} representing a displacement between them. These displacements are selected as non-linear one at the non-linear problem solution by harmonic balance method.

The motivation to use HB method for our problem solution comes from inside crack contact process caused by crack breathing. It induces non-linear behaviour of the cracked blade subjected to periodic external excitation. The response of the system is supposed to be periodic. Earlier a simple mathematical model to simulate such a non-linearity had been created [54]. In such a way it was possible to prove correctness of the method formulation by comparing its results with direct integration of equation (3.43). Now this approach can be projected on more complex cracked blade model.

3.2.1 Reduction of the cracked blade model

Fig. 3.4 shows sub-structures of the cracked blade model. The crack location forms an interface between two sub-structures. The lower sub-structure is restrained at the root section. In our

case we do not have a classical sub-structuring because upper and low sub-structures share some DOFs of the interface uncracked partition. To continue with the model size reduction, the fixed interface method was implemented.

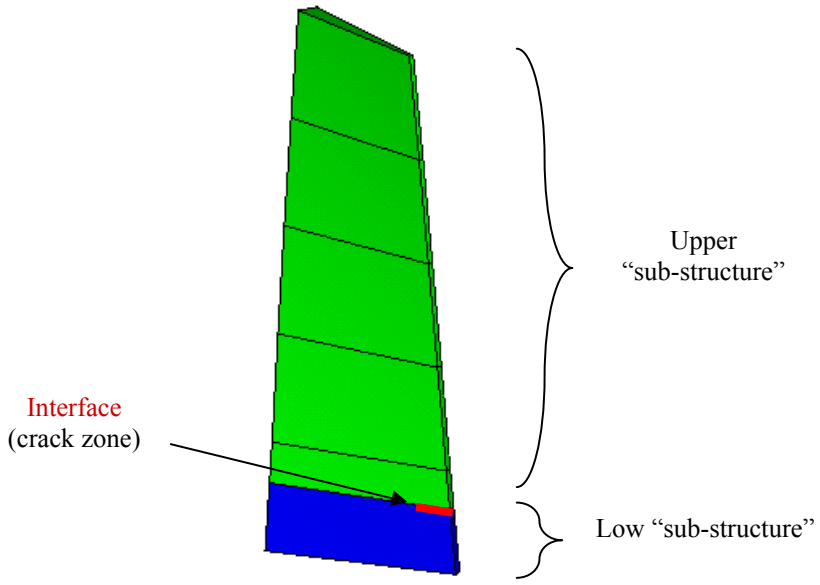

Fig. 3.4. Cracked blade model sub-structuring

In order to facilitate calculation, the relative displacements were introduced for each contact pair. The contact pair is defined by two nodes subscribed as the reference node and observed node. Thus, the relative displacement can be described as (Fig. 3.5):

$$u^{j}{}_{rel} = u^{j}{}_{obs} - u^{j}{}_{ref}, \tag{3.42}$$

where the subscripts *ref* and *obs* refer to the reference and the observed nodes respectively, j - index of j-th contact pair.

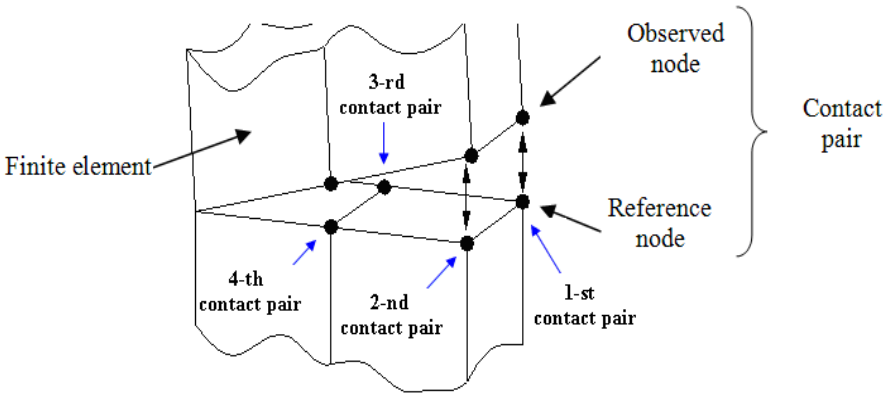

Fig. 3.5. Relative displacements between contact nodes

In the case of cracked blade we do not have a classical sub-structuring because some DOFs remain shared between the upper and lower sub-structures. The fixed interface modes are presented by the modes of the blade uncracked state. The static modes are the modes of the crack opening, as unit displacemets are applied to the crack relative DOFs.

The initial full model consisted of 588 DOFs (a=4 mm) and it was reduced to the model of 23 DOFs (12 DOFs describing relative displacements of four contact pairs, 6 DOFs in two points of external loading application and 5 additional modes). Reduction of uncracked blade model was performed using reduced cracked blade model by deleting from its mass and stiffness matrices elements, which correspond to relative DOFs. Results of the reduction procedure application to the cracked blade model are shown in Tables 3.2–3.3.

Cracked blade model eigenfrequencies (in Hz)

Table 3.2

Mode number	Crack on trailing edge					
	a=2 mm		a=4 mm		uncracked blade	
	Full model	Reduced model	Full model	Reduced model	Full model	Reduced model
1	566.9	566,9	566.8	566.8	566.9	566,9
2	2455.7	2461.1	2452.4	2457.9	2456.2	2461.6
3	3029.5	3031.8	3024.8	3027.3	3030.4	3032.7
4	4433.1	4536.3	4354.8	4453	4446.7	4550.8
5	7053.2	7110.5	7030.4	7084.9	7058.5	7116.5
6	8135.5	8252.9	8135	8252.4	8135.6	8253.1
7	13272	14373	13220	14332	13285	14383
8	15032	17799	15025	17794	15034	17800
9	15950	29950	15925	29582	15957	30006
10	17232	37587	17178	37181	17241	37638

Cracked blade model eigenfrequencies (in Hz)

Table 3.3

Mode number	Crack on leading edge					
	a=2 mm		a=4 mm		uncracked blade	
	Full model	Reduced model	Full model	Reduced model	Full model	Reduced model
1	564.85	564.9	553.9	554	566.9	566.9
2	2449.5	2454.9	2413.9	2419.5	2456.2	2461.6
3	3024.6	3026.8	2995.1	2997.2	3030.4	3032.7
4	4411.2	4512.6	4237.9	4327	4446.7	4550.8
5	7054.5	7112.5	7033.7	7091.6	7058.5	7116.5
6	8125	8241.4	8070.9	8181.5	8135.6	8253.1
7	13269	14366	13191	14282	13285	14383
8	15030	17800	15011	17799	15034	17800
9	15954	29833	15935	28602	15957	30006
10	17225	37389	17086	36082	17241	37638

To continue with the subsequent dynamic analysis, all vertical DOFs of all contact pairs were accepted as the non-linear DOFs. It halves the number of non-linear DOFs and adequately

reduces the calculation time cost for the non-linear problem solution. It is also much easier to control displacements between nodes in contact with the use of relative displacements. The relative contact displacements simplify the non-linear force formulation for application of the harmonic balance method.

3.2.2 Application of the penalty method for non-linear force representation

Representation of the non-linear force is one of the most important tasks in any non-linear solution procedure or in the harmonic balance method. In our case, we have some non-linear contact force, the Lagrange multipliers or penalty methods could be used [57]. The easiest way is to use the penalty method to approximate this force by the following expression:

$$F_{nl} = k_{nl} \cdot \left(\frac{u_{nl} + |u_{nl}|}{2} \right), \tag{3.43}$$

where k_{nl} is the penalty stiffness coefficient, u_{nl} is the non-linear DOF. A penalty stiffness value should be chosen to provide minimum penetration in the contact zone.

It should be mentioned that a drawback of such a non-linear force approximation appears when it crosses the zero. So then u_{nl}=0, $\partial F_{nl} / \partial u_{nl}$ is discontinuous. It results in calculation of the Jacobian will be theoretically unattainable. In order to avoid this problem, the smoothing function should be applied. The work [19] showed how the tangent function was used for smoothing. We applied it with some modification and obtained the following expression:

$$F_{nl} = \frac{1}{\pi} k_{nl} (\arctan(s u_{nl}) - \frac{\pi}{2}) u_{nl}, \tag{3.44}$$

where s is the coefficient, the sufficiently high level of which is required to accurately represent force-displacement relationship smoothing (Fig. 3.6) .

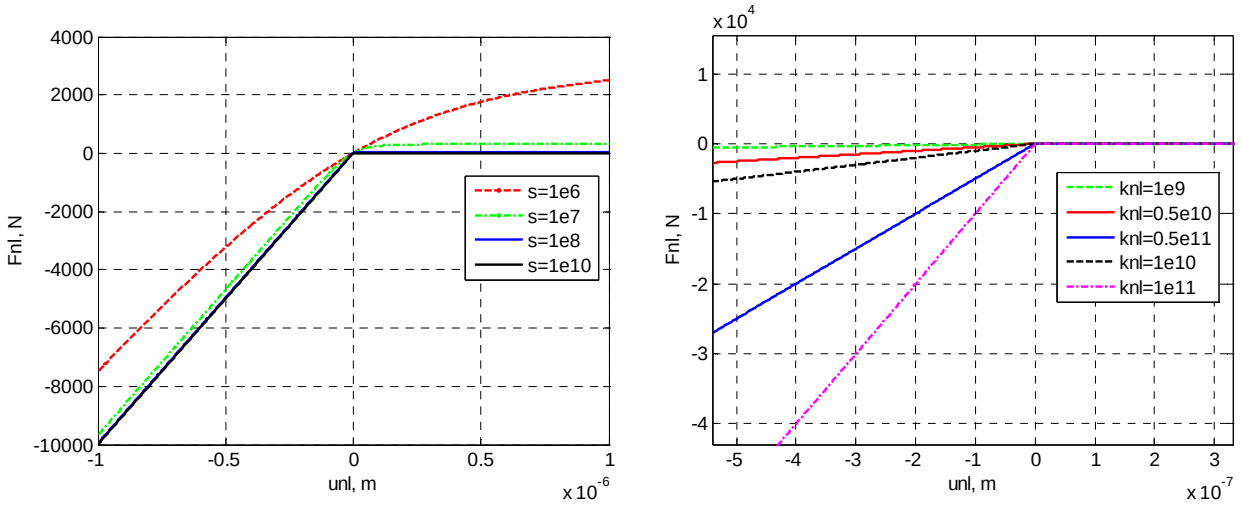

(a) (b)

Fig. 3.6. Non-linear force smoothing representation: (a) at different values of s coefficient and fixed k_{nl} =10^{10}N/m, (b) at different values of penalty stiffness k_{nl} and fixed s=10^{10}

3.2.3 Non-linear solution for the problem

A non-linear solution requires taking into account the system non-linearity, in our case it is a non-linear contact force between two nodes (3.44). The governing equation $\mathbf{A}\tilde{\mathbf{u}} + \mathbf{b}(\tilde{\mathbf{u}}) = \tilde{\mathbf{F}}$ of HB method represents by itself the system of non-linear equations. Newton-Raphson procedure of non-linear equations system solution can be applied after some transformations:

$$\begin{gathered} \tilde{\mathbf{u}}_{n+1} = \tilde{\mathbf{u}}_n + \Delta\tilde{\mathbf{u}}_n \\ \mathbf{A}(\tilde{\mathbf{u}}_n + \Delta\tilde{\mathbf{u}}_n) + \mathbf{b}(\tilde{\mathbf{u}}_n + \Delta\tilde{\mathbf{u}}_n) = \tilde{\mathbf{F}} \\ \mathbf{A}\tilde{\mathbf{u}}_n + \mathbf{A}\Delta\tilde{\mathbf{u}} + \mathbf{b}(\tilde{\mathbf{u}}_n) + J\mathbf{b}(\tilde{\mathbf{u}}_n)\cdot\Delta\tilde{\mathbf{u}} - \tilde{\mathbf{F}} = 0; \end{gathered} \tag{3.45}$$

where n is the iteration number.

Expression (3.45) represents the local linear transformation of (3.18) and $J\mathrm{b}(\tilde{\mathrm{u}}_n)$ is the Jacobian of the non-linear member:

$$J\mathbf{b}(\tilde{\mathbf{u}}) = \begin{bmatrix} \frac{1}{T_s}\int_0^{T_s}\frac{\partial F_{nl}}{\partial u}[\mathbf{I}_{N_{dof}}, \mathbf{I}_{N_{dof}}\cos(k\omega t), \mathbf{I}_{N_{dof}}\sin(k\omega t),...]dt \\ \left\{\begin{matrix} \frac{2}{T_s}\int_0^{T_s}\frac{\partial F_{nl}}{\partial u}[\mathbf{I}_{N_{dof}}, \mathbf{I}_{N_{dof}}\cos(k\omega t), \mathbf{I}_{N_{dof}}\sin(k\omega t),...]\cos(k\omega t)dt \\ \frac{2}{T_s}\int_0^{T_s}\frac{\partial F_{nl}}{\partial u}[\mathbf{I}_{N_{dof}}, \mathbf{I}_{N_{dof}}\cos(k\omega t), \mathbf{I}_{N_{dof}}\sin(k\omega t),...]\sin(k\omega t)dt \end{matrix}\right\} \\ ... \end{bmatrix}_{N_{dof}(2k+1)\times N_{dof}(2k+1)}, \tag{3.46}$$

where $\mathrm{I}_{N_{DOF}}$ is the unity matrix of dimension $N_{DOF}\times N_{DOF}$., N_{DOF} is the number of the system degrees of freedom.

The solution vector update is calculated from the expression:

$$\Delta\tilde{\mathbf{u}}_n = \mathbf{J}^{-1}\cdot\mathbf{R}_n, \tag{3.47}$$

where,

$$\begin{gathered} \mathbf{J} = \mathbf{A} + J\mathbf{b}(\tilde{\mathbf{u}}_n) \\ \mathbf{R}_n = \mathbf{A}\tilde{\mathbf{u}}_n + \mathbf{b}(\tilde{\mathbf{u}}_n) - \tilde{\mathbf{F}}. \end{gathered} \tag{3.48}$$

The non-linear solution in the time domain is reconstructed by the inverse Fourier transformation and shown for relative vertical displacement between two coinciding contact nodes: the “crack point” and the “tip point”, i.e., a horizontal displacement of excitation force application node (leading edge measurement point). Amplitude of response presented in all following graphs corresponds to the maximum amplitude in measurement point. Crack location variants are schematically shown in Fig. 3.3, supposing it to be either on the leading or trailing edges or on both edges (symmetric cracks).

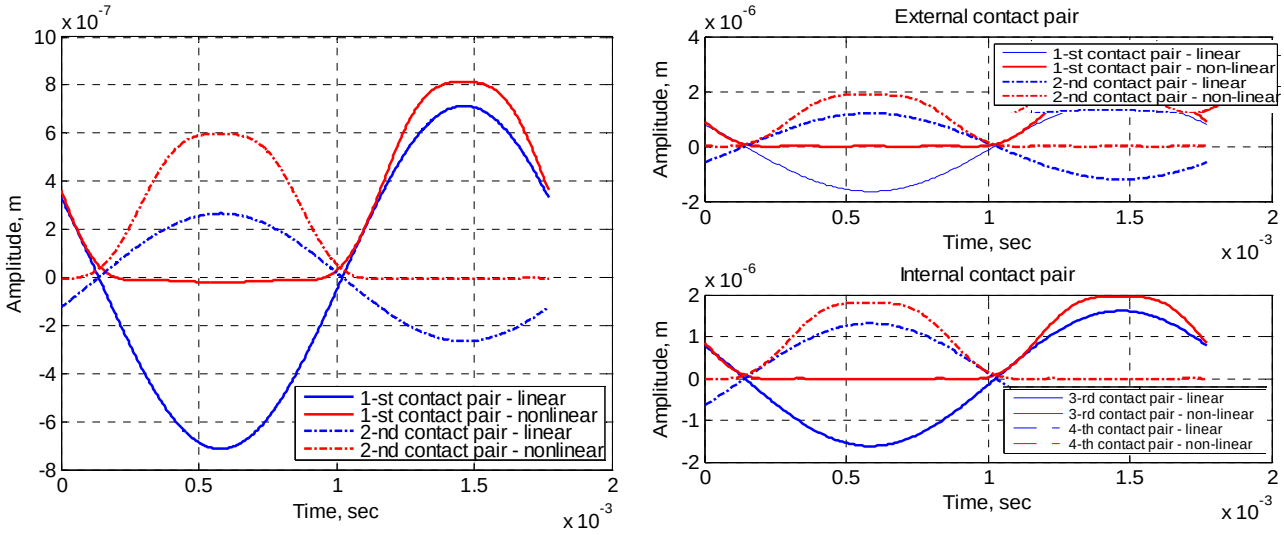

(a) (b)

Fig. 3.7. System response in the time domain in "crack point" (*trailing edge crack*, ω = 3550 rad/sec): (a) *a*=2 mm, (b) *a*=4 mm

From the results of the cracked blade model non-linear solution we can observe the effect of the contact force presence (Fig. 3.7). The set value of penalty stiffness is enough to avoid penetration and non-linear force approximation (3.47) and allows precisely simulate system non-linear behavior. Five harmonics were retained in this case at excitation frequency 3500 rad/sec., which is close to the resonance frequency of the first flexural mode of the cracked blade model.

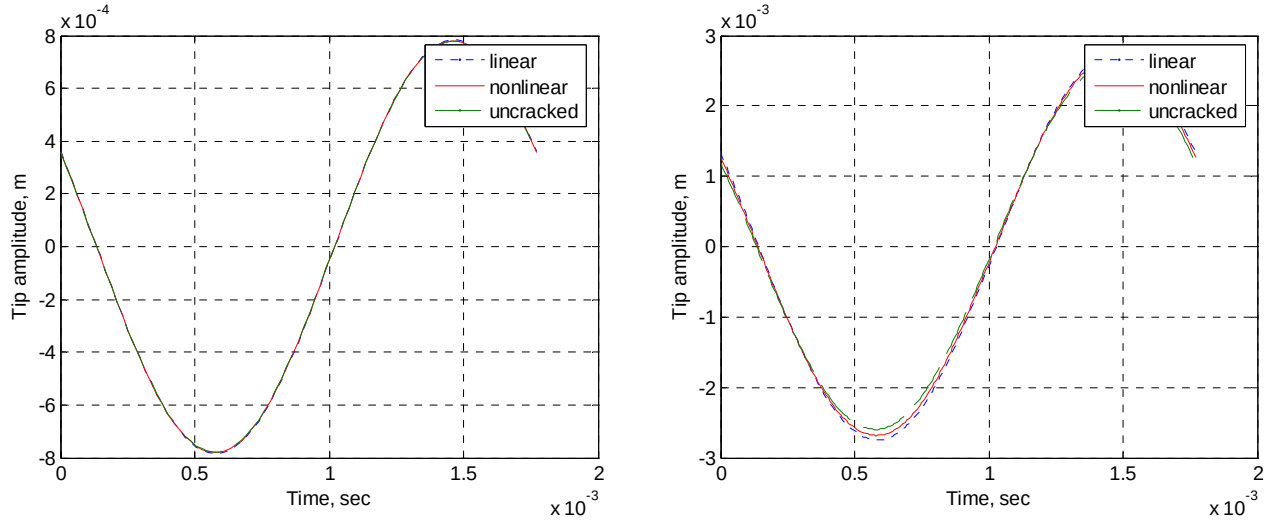

(a) (b)

Fig. 3.8. System response in the time domain in "tip point" (*trailing edge crack*, ω = 3550 rad/sec): (a) *a*=2 mm, (b) *a*=4 mm

From the results of the solution to the cracked blade model in the time domain with introduced crack of length = 2 mm on the trailing edge, it is seen that the influence of the crack presence on blade tip response is almost invisible (Fig. 3.8a). Even in linear case, the results of modal analysis show the minimum shift in the first eigenmode frequency for such a crack option (Table 3.1.) For the case, in which the crack has a length of 4 mm, we have a visually detectable

difference between both linear and non-linear solutions (Figs. 3.7b, 3.8b) because of the higher level of stiffness

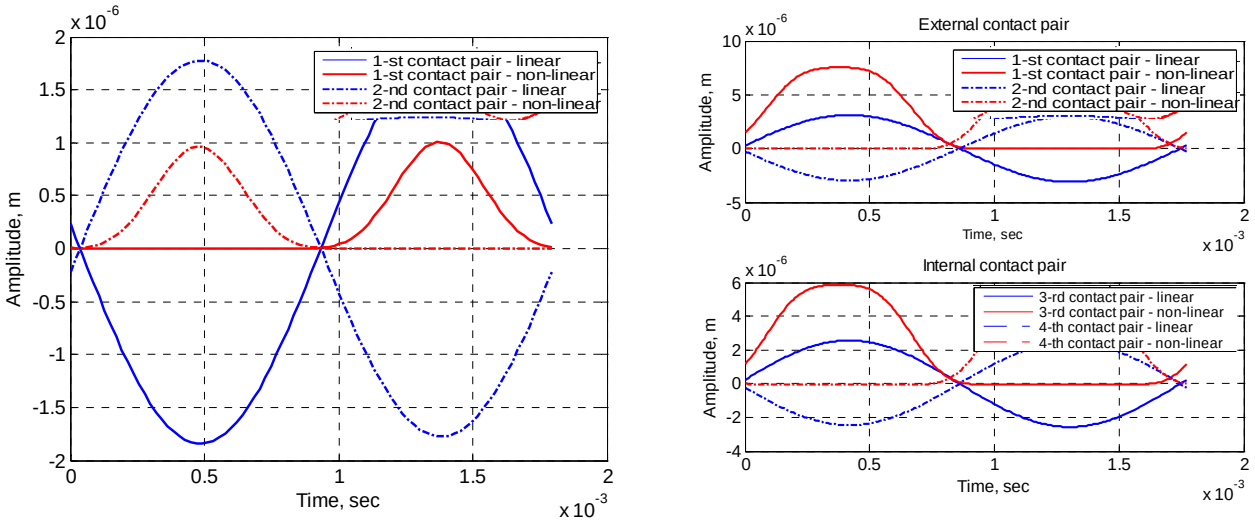

(a) (b)

Fig. 3.9. System response in the time domain in "crack point" (*leading edge crack*, ω = 3550 rad/sec): (a) *a*=2 mm, (b) *a*=4 mm

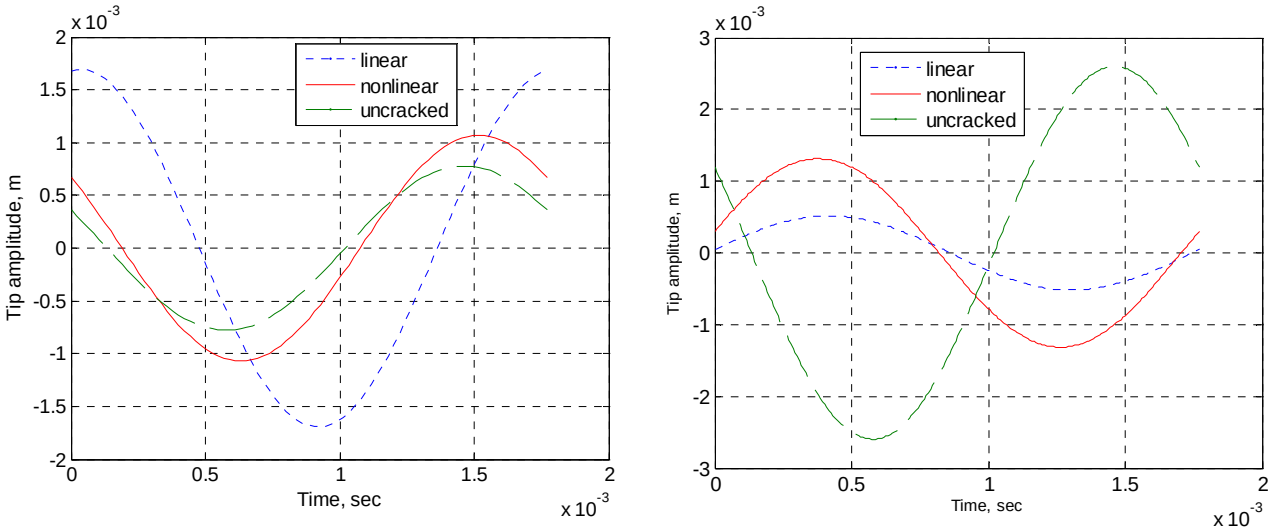

(a) (b)

Fig. 3.10. System response in the time domain in "tip point" (*leading edge crack*, ω = 3550 rad/sec): (a) *a*=2 mm, (b) *a*=4 mm

In the case of the response in the time domain of the cracked blade with crack = 4 mm, it is evident that influence of the crack is much stronger (Figs. 3.9b, 3.10b). The observation is also valid for the case of crack location on the trailing edge. The number of contact pairs through the crack thickness is two (external and internal, Fig. 3.5). This allows more accurate description of the displacements between the crack sides in dynamics.

A simulation of the cracked blade response with two symmetrically located cracks was performed as well. Schematically cracks locations are shown in Fig. 3.3c. In our case we used 2 and 4 mm cracks for simulations of the cracked blade dynamic behaviour (Figs. 3.11–3.13).

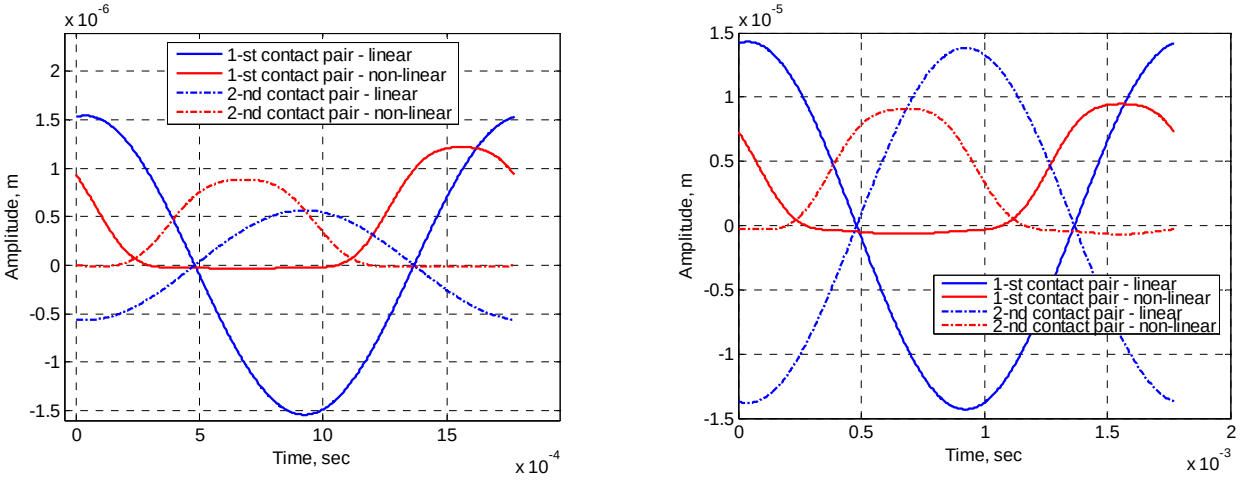

(a) (b)

Fig. 3.11. System response with symmetric cracks in the time domain in "crack point" (a = 2 mm, ω = 3550 rad/sec): (a) crack located on trailing edge, (b) crack located on leading edge

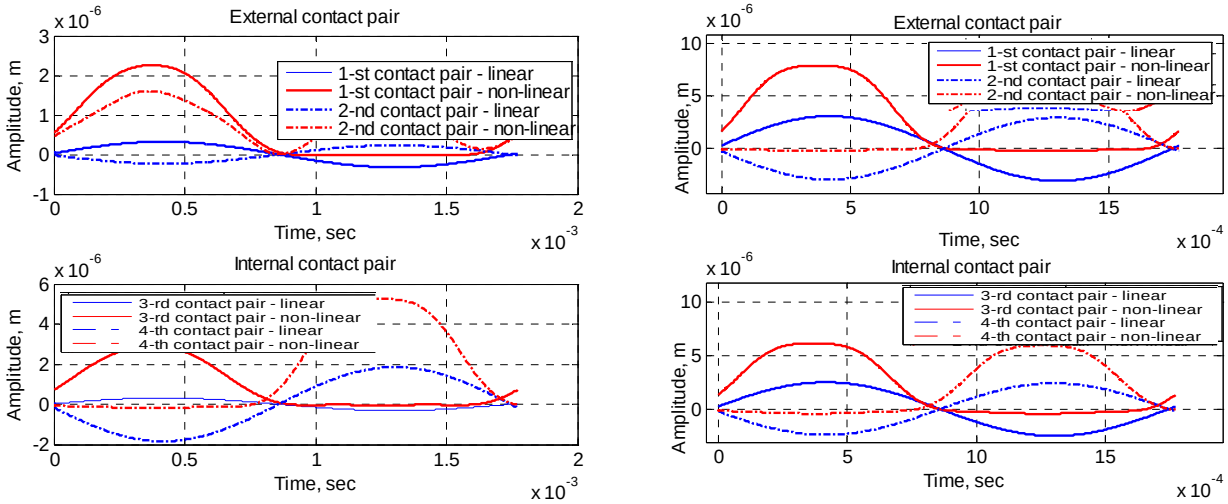

(a) (b)

Fig. 3.12. System response with symmetric cracks in the time domain in "crack point" (a = 4 mm, ω = 3550 rad/sec): (a) crack located on trailing edge, (b) crack located on leading edge

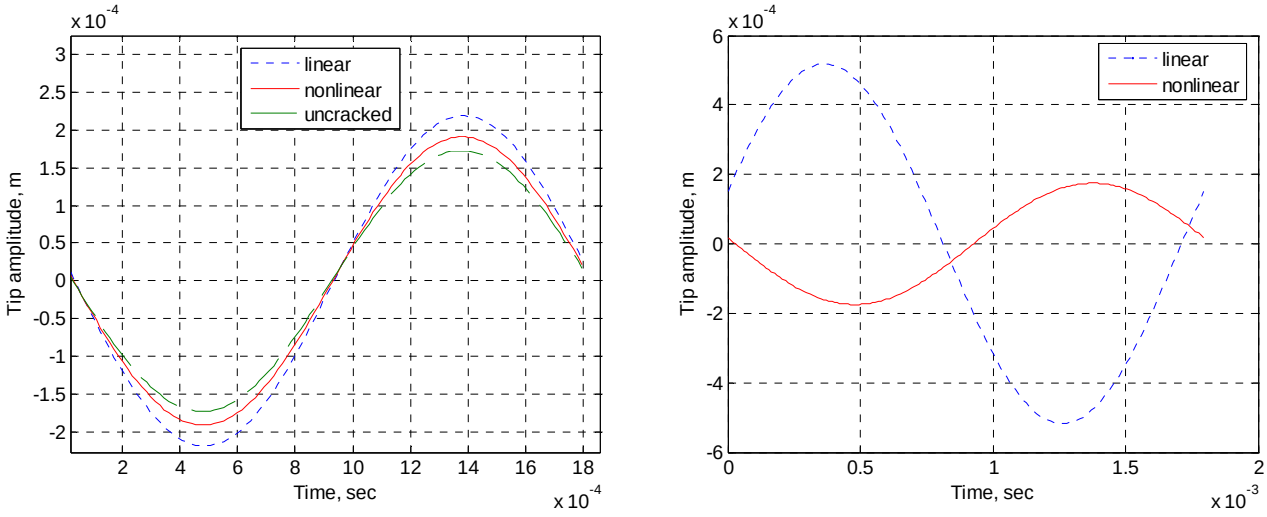

(a) (b)

Fig. 3.13. System response with symmetric cracks in the time domain in "tip point" (ω = 3550 rad/sec): (a) a = 2 mm, (b) a = 4 mm

Reviewing the results of the response of the cracked blade with symmetric cracks, we can see that it is mostly influenced by the leading edge crack partition, and even the crack with the length = 2 mm becomes detectable.

It is also necessary to emphasize that considerable difference between the non-linear and linear solutions does not always reflect the real difference in amplitudes. It results from resonance shift because the excitation frequency is not far from the first eigenmode frequency of the linear or non-linear models. The contraposition in the time-history of relative DOFs for two blade faces is caused by an excited natural mode. In our case, the forces applied at two tip points (the leading and trailing edge force points, Fig. 3.2) excite the first flexural mode of the blade model. Frequency points are located in the range of this mode and it results in such difference.

3.2.4 Validation of the harmonic balance method results through direct time integration

Validation of the results obtained by the harmonic balance method was carried out through their comparison them with outcomes of direct integration of the system motion equation. A procedure of finding a solution for the high-dimensional structures is time consuming and therefore a two-dimensional model was chosen for numerical tests.

In our case the cracked structure is simulated by the flat 0.1*0.1 m plate restrained at its bottom line (Fig. 3.14a). The presence of a crack in the structure was simulated by introducing an additional node that created a contact pair. The external load was applied to the top right corner of the plate as the point force with amplitude of 100 N and excitation frequency of 2100 rad/sec. The frequency is close to the first eigenfrequency of the cracked plate model (2300 rad/sec).

Firstly, the cracked blade forced response simulations supposing contact interaction between the sides of the crack were fulfilled by the finite element method. Interaction of the cracked interface was simulated by a node-to-node contact element with the use of the penalty method. The normal penalty level was assumed to be 10^{11} N/m. The results of the contact simulation are presented for small time interval that results in an unsteady response (Fig. 3.14b.)

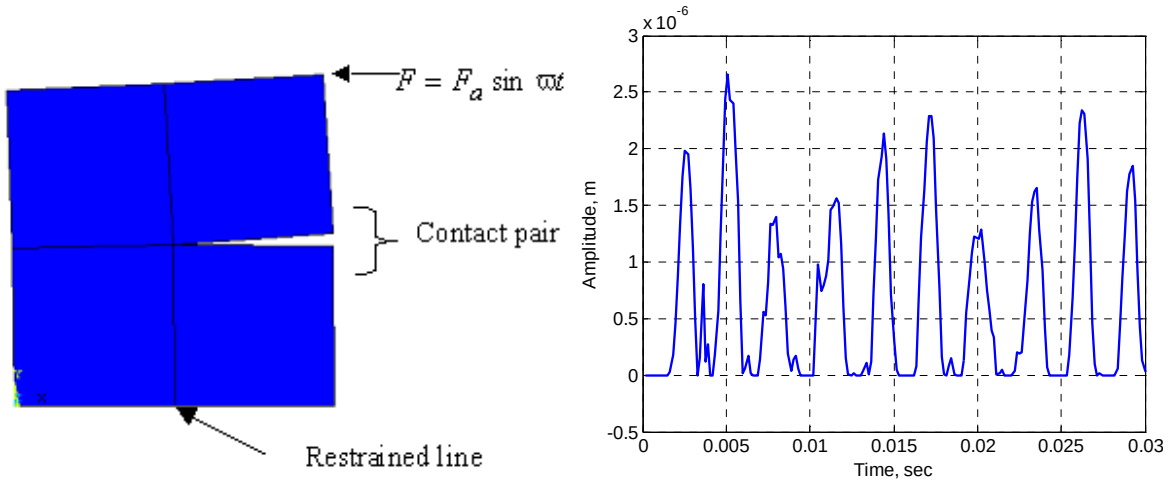

(a) (b)

Fig.3.14: (a) Simplified two-dimensional model of the cracked structure, (b) Time-history of the relative vertical displacement between crack tips in ANSYS

The solution to the same model was calculated in the work [57] by the direct time integration approach. It dealt with full and two reduced systems, obtained by the fixed and free interface methods of system sub-structuring. For contact simulation the Lagrange multipliers method and the penalty method were applied. The present work uses the Lagrange multipliers method for comparison with HB method.

An integration time interval should be sufficiently large to allow obtaining of a steady-state solution by direct time integration of the system motion equation. The time step should be small enough to provide an accurate solution.

Fig. 3.15 shows solutions for the system motion equation obtained by using both the harmonic balance and the direct time integration approach. The solutions prove that the harmonic balance method is more effective in terms of computation time because it is sufficient to have the time interval equal to the excitation period.

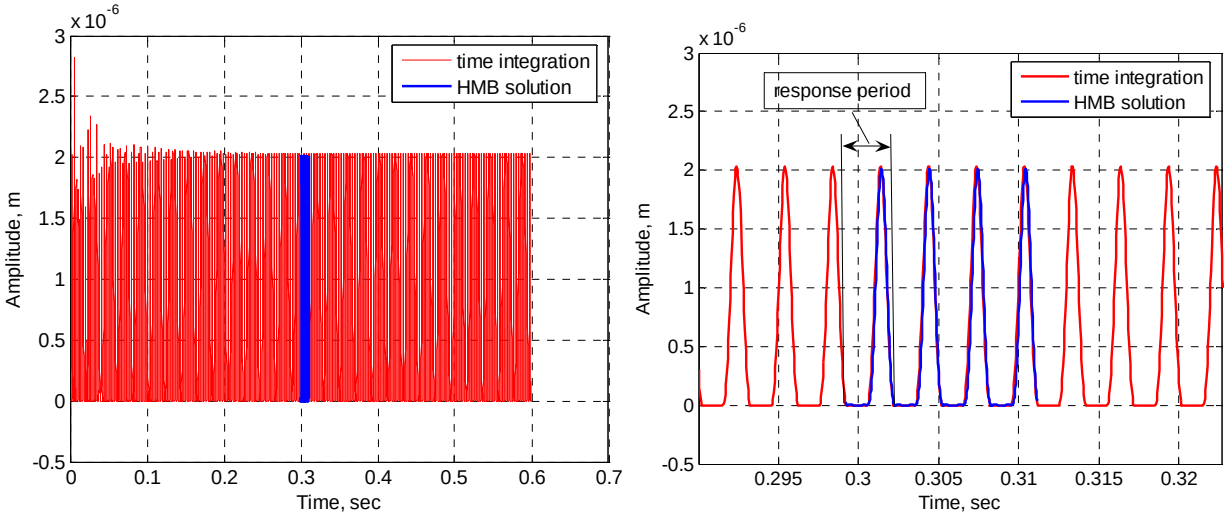

(a)

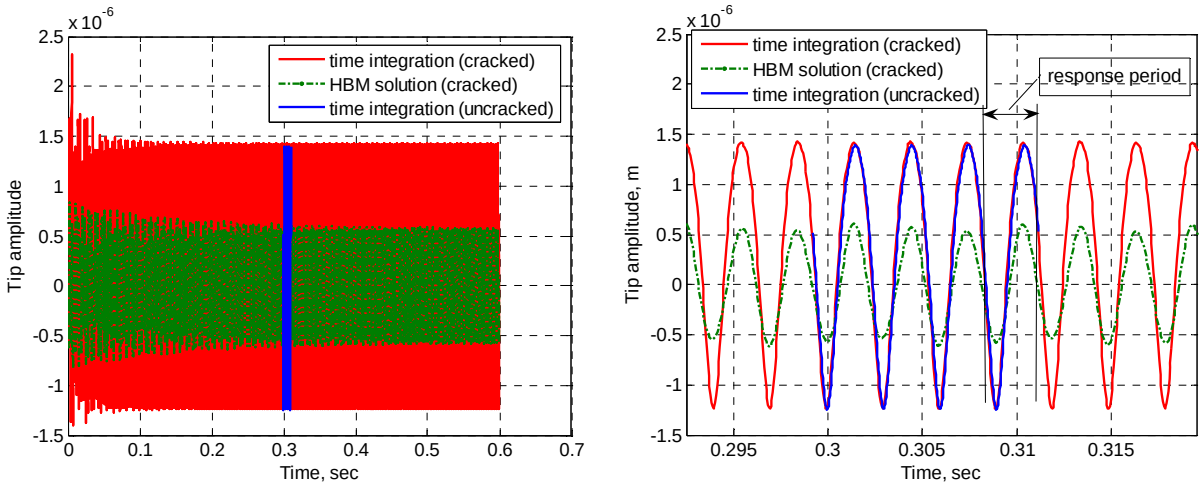

(b)

Fig. 3.15. Non-linear solution by HB method and direct integration approach:
(a) in the “crack point”, (b) in the “tip point”

3.2.5 Frequency response of the non-linear cracked blade model

Construction of the frequency response of the cracked blade model is performed for the same cases as it was presented in the time domain. Measurements of maximum response amplitude are performed in the points of external forces application. Comparison of the frequency response was made among the linear cracked, non-linear cracked and linear uncracked blade models. The frequency range covers the first three eigenmodes: first and second flexural modes and first torsion mode. As we did not know exactly the eigenfrequencies of the cracked blade model because of the crack-induced non-linearity, a frequency discretisation was done around eigenmode frequencies of the linear cracked model. As a result of this, the resonances peaks of the non-linear model sometimes appear to be not smooth and with amplitude a bit lower than it should be. Maximum amplitudes of the blade tip horizontal displacements are shown for graphical representation.

The preceding subchapter dealt with the system solution at a particular excitation frequency, with the non-linear procedure having been initialized by the solution to the linear system. Such an approach is appropriate to a frequency range distant from the resonance, where the difference between linear and non-linear solutions is barely visible. However, the initialization in resonance area can lead to a longer convergence process or even to the solution divergence. To overcome this problem, the non-linear solution obtained at the preceding frequency point was used as the initialization for a particular frequency point. One more tool to deal with the solution nom-convergence is a frequency continuation approach, when the next frequency point is searched by a prediction on the base of polynomial approximation [36].

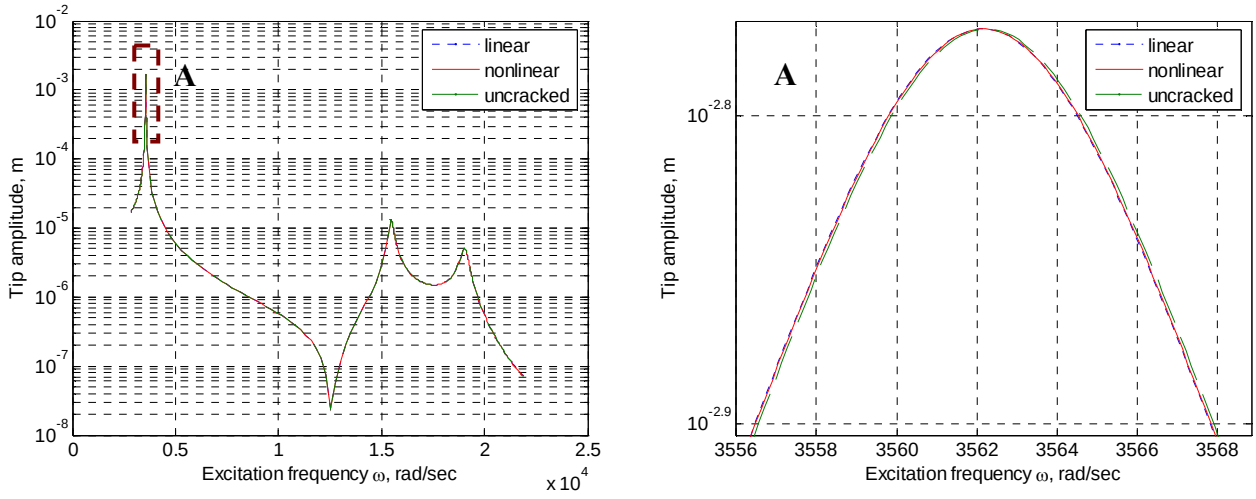

(a)

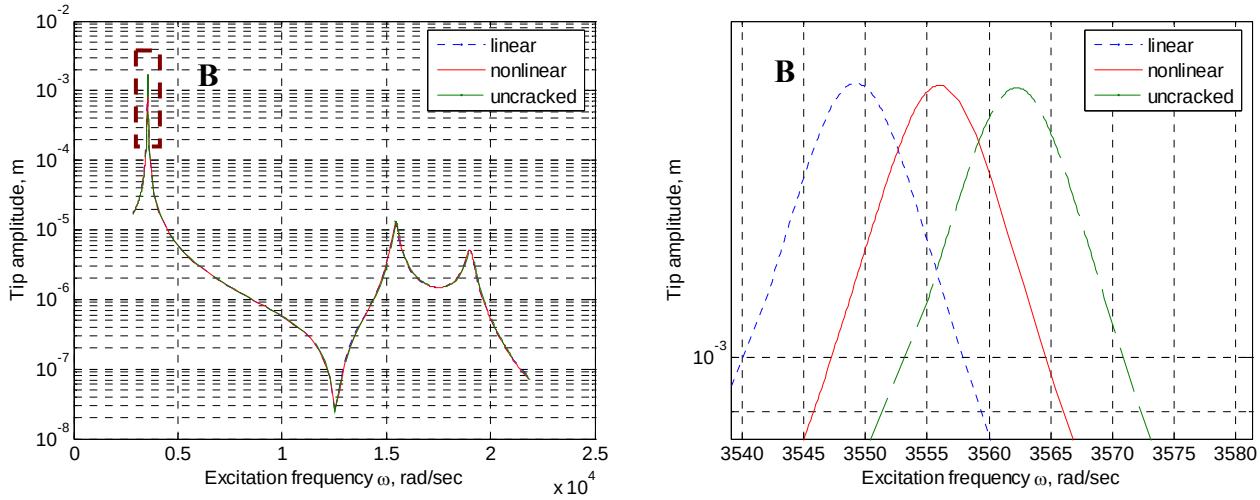

(b)

Fig. 3.16. Cracked blade frequency response (a = 2 mm):

(a) trailing edge crack, (b) leading edge crack

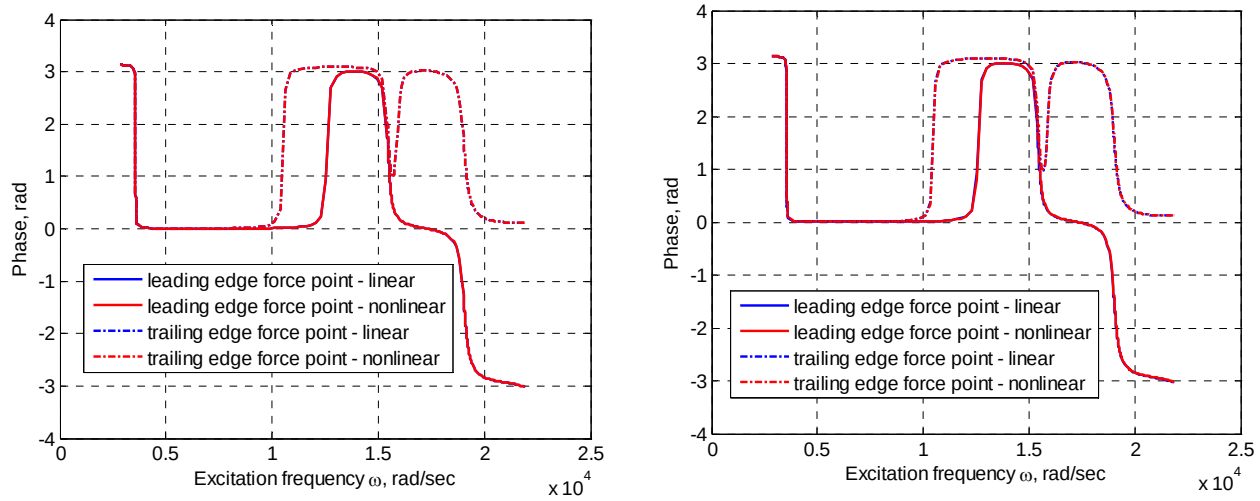

a b

Fig. 3.17. Cracked blade response phase change (a = 2 mm):

(a) trailing edge crack, (b) leading edge crack

In a way similar to solution for the problem in time domain, the procedure starts with examination of the smallest crack of the length=2mm. The frequency response of the cracked blade with such crack size can have a visible effect of crack presence only in the leading edge crack case. When the crack is located on trailing edge its effect becomes more or less observable only for higher order eigenmodes (Fig. 3.16a.) The crack of this size can be considered to be the minimum crack size, when it is impossible to identify a crack presence in the blade.

On the next step, the case of the 4–mm crack is simulated (Fig. 3.18.) The phase change at force application points is shown (Fig. 3.19).

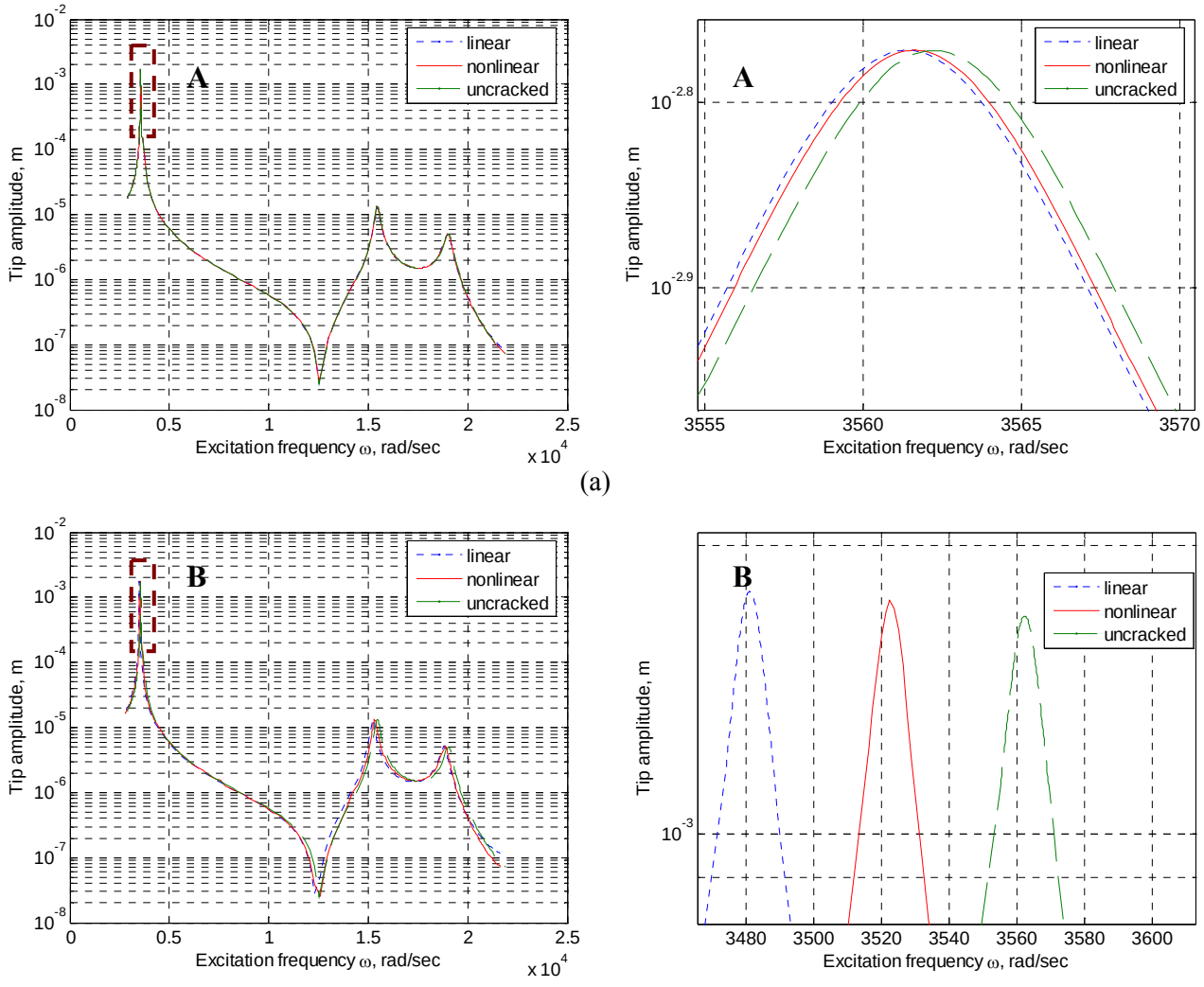

(a)

(b)

Fig. 3.18. Cracked blade frequency response (a = 4 mm):

(a) trailing edge crack, (b) leading edge crack

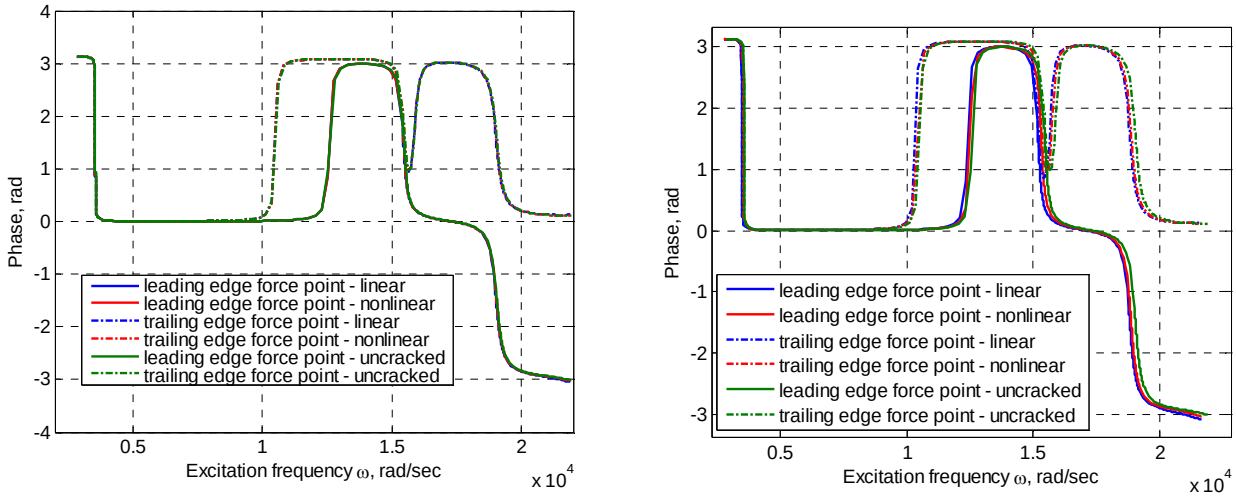

Fig. 3.19. Cracked blade response phase change (a = 4 mm):
(a) trailing edge crack, (b) leading edge crack

In the case of the 4–mm crack the crack effect is evident at all resonance points for both leading and trailing edge crack locations (Fig. 3.18.) The blade tip amplitude of the cracked blade shows sufficiently high difference relatively to the uncracked blade even in the case of the trailing edge crack. The crack presence detectability grows due to shift of the resonance peaks in case of the crack location on the leading edge (Fig. 3.18b.) This crack size will be used in the following studies in combination with the tip-timing method simulation as the most representative one. It will be also used at development of the bladed disk model with the cracked blade.

A sufficient difference between solutions for the cracked and uncracked blade models (Fig. 3.19.) can be observed from alterations of the cracked blade response phase. It is only fixed for the 4–mm cracks, while the difference is almost unobservable for smaller crack sizes.

In addition to crack locations on the trailing or leading edges, a case of symmetric cracks is shown in Figs. 3.22–3.23. Fig. 3.3c shows a schematic arrangement of the cracks.

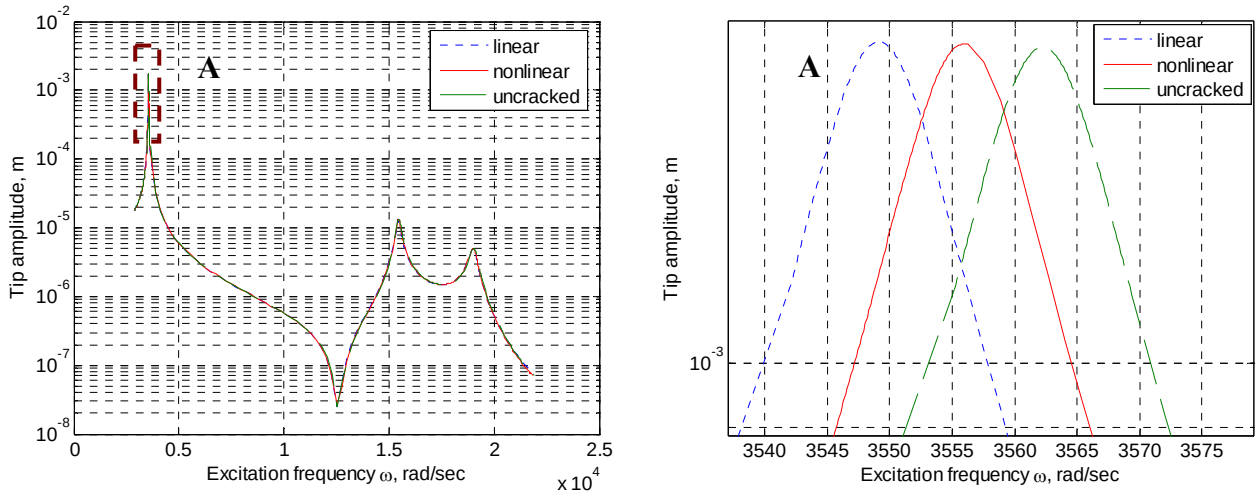

Fig. 3.20. Cracked blade frequency response (symmetric crack, a = 2 mm)

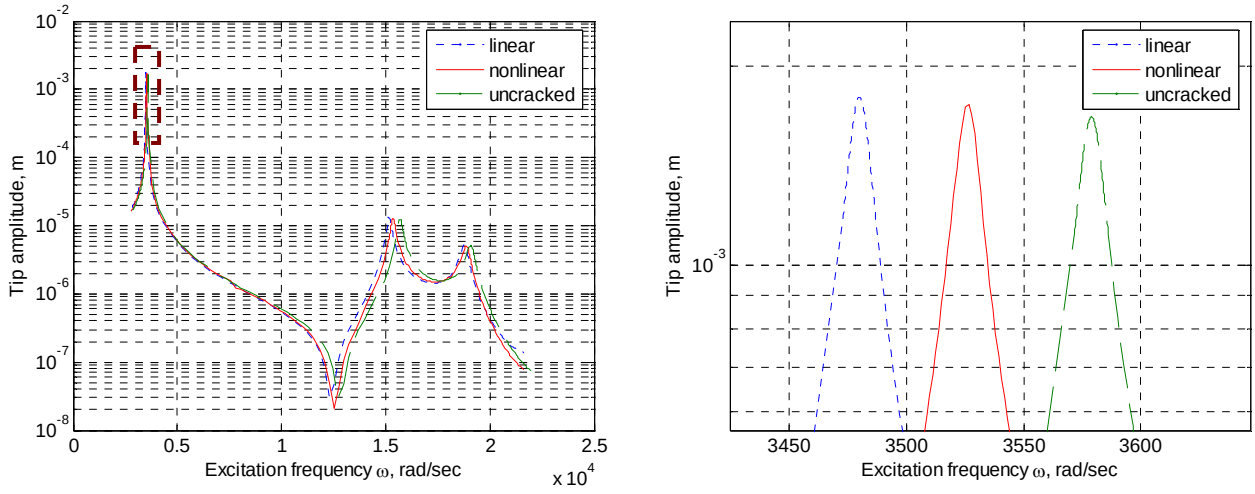

Fig. 3.21. Cracked blade frequency response (symmetric crack, a = 4 mm)

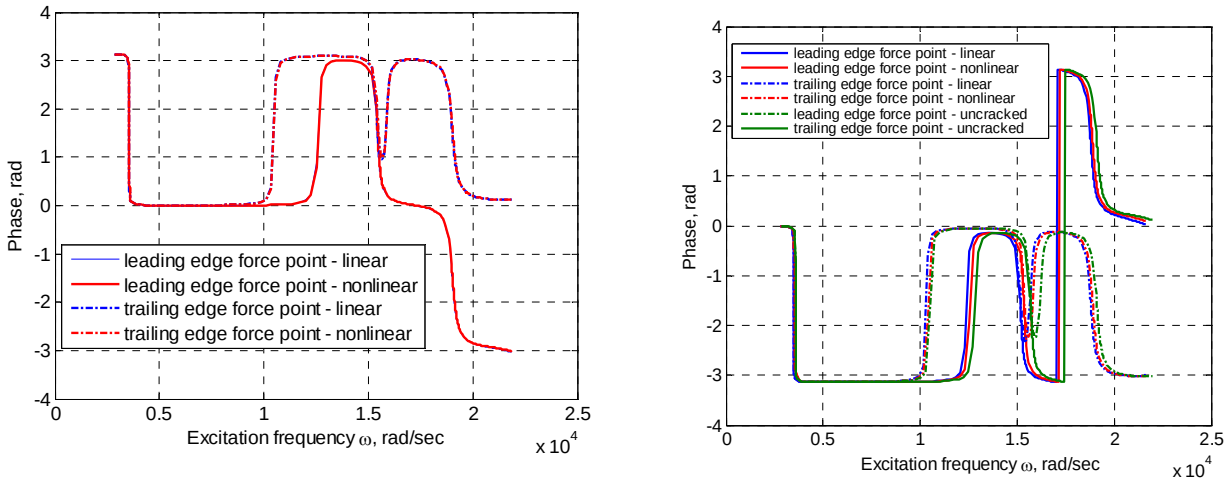

(a) (b)

Fig. 3.22. Cracked blade response phase change (symmetric crack): (a) a = 2 mm, (b) a = 4 mm

From simulation of the cracked blade frequency response, supposing presence of two symmetrically located cracks, a conclusion can be drawn that the case under consideration is the most severe one for the structure. Even presence of 2–mm cracks becomes evident. The response of the system to such cracks is mostly evoked by the cracks located on the leading edge.

All above simulated cases show that response of the non-linear cracked blade model has an intermediate position between responses of the linear cracked and uncracked blade models. During crack closure the added energy dissipation is expected that results in lower magnitude of cracked blade at its non-linear formulation. The crack detectability will apparently be affected further when a crack blade is considered within frameworks of the bladed disk model.

3.2.6 Centrifugal forces effect on cracked blade non-linearity

The above-considered simulation assumed a cracked blade to be the fixed one. It portrays laboratory conditions of the clamped and excited blade. Effect of the gyroscopic **N** and centrifugal **P** matrices can be neglected (1.16).

Estimation of an effect of centrifugal forces is quite a challenging task in an attempt to expose precisely all physical phenomena associated with the bladed disk dynamics and to improve the non-linear cracked blade model used in forced response predictions [33]. The centrifugal forces reveal themselves in the analysis of the cracked blade by affecting the vibration response of the non-linear cracked blade model. A few numerical examples are used to prove the theoretical assumption and a successful application of the suggested model lends some validity to the approach.

Effect of the centrifugal forces will be studied in the following way. The centrifugal forces act radially outward and develop a gap between the crack sides. The gap can be assumed to be a crack initial opening during its breathing process. The initial value of the gap depends on:

- crack length
- crack location (either on the trailing or leading edge)
- amplitude of an external loading
- rotor frequency.

The estimation procedure takes the finite element model of the cracked blade used in the previous simulation. Fig. 3.23 presents results of the crack initial opening simulation for different rotor frequencies. The solution is shown for all contact pairs assuming presence of the 4–mm crack either on the trailing or leading edges.

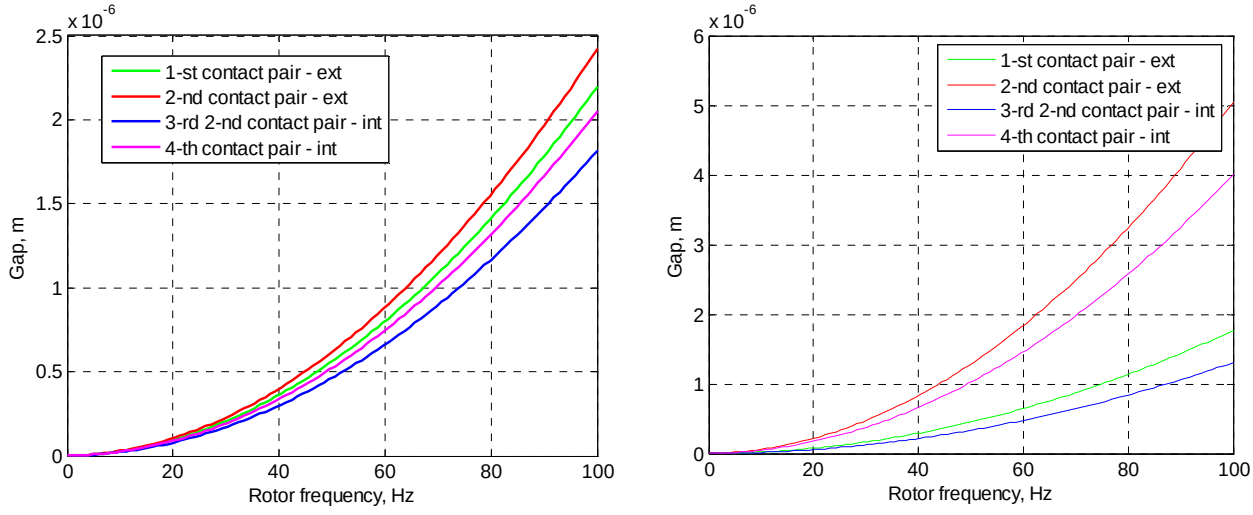

(a) (b)

Fig. 3.23. Initial crack opening due to effect of centrifugal forces:

(a) trailing edge crack, (b) leading edge crack

Table 3.4

Crack initial opening at different rotor frequency, m

Contact pair	Trailing edge crack					Leading edge crack				
	Rotor frequency, Hz									
	10	20	30	50	70	10	20	30	50	70
1-st	$2.6\cdot10^{-8}$	$9.5\cdot10^{-8}$	$2.1\cdot10^{-7}$	$5.6\cdot10^{-7}$	$1.1\cdot10^{-6}$	$2.1\cdot10^{-8}$	$7.7\cdot10^{-8}$	$1.7\cdot10^{-7}$	$4.5\cdot10^{-7}$	$8.7\cdot10^{-7}$
2-nd	$2.9\cdot10^{-8}$	$1.0\cdot10^{-7}$	$2.3\cdot10^{-7}$	$6.2\cdot10^{-7}$	$1.2\cdot10^{-6}$	$5.9\cdot10^{-8}$	$2.2\cdot10^{-7}$	$4.8\cdot10^{-7}$	$1.3\cdot10^{-6}$	$2.5\cdot10^{-6}$
3-rd	$2.2\cdot10^{-8}$	$7.9\cdot10^{-8}$	$1.7\cdot10^{-7}$	$4.6\cdot10^{-7}$	$9.0\cdot10^{-7}$	$1.6\cdot10^{-8}$	$5.6\cdot10^{-8}$	$1.2\cdot10^{-7}$	$3.3\cdot10^{-7}$	$6.5\cdot10^{-7}$
4-th	$2.4\cdot10^{-8}$	$8.9\cdot10^{-8}$	$1.9\cdot10^{-7}$	$5.2\cdot10^{-7}$	$1.0\cdot10^{-6}$	$4.8\cdot10^{-8}$	$1.7\cdot10^{-7}$	$3.8\cdot10^{-7}$	$1.0\cdot10^{-6}$	$2.0\cdot10^{-6}$

The data from Fig. 3.23 and Table 3.4 will be used to calculate a forced response of the cracked blades by means of the harmonic balance method. Initial gap values are substituted in the equation of contact force approximation (3.47). Simulation of the cracked blade response in a time domain will be presented at different gap values with fixed excitation frequency. In this case engine order of excitation will be changed in order to provide constant excitation frequency. By this approach it will be possible to vary gap value and, at the same time, rotor frequency Ω. Excitation frequency of 3500 rad/sec was maintained constant for all simulation cases.

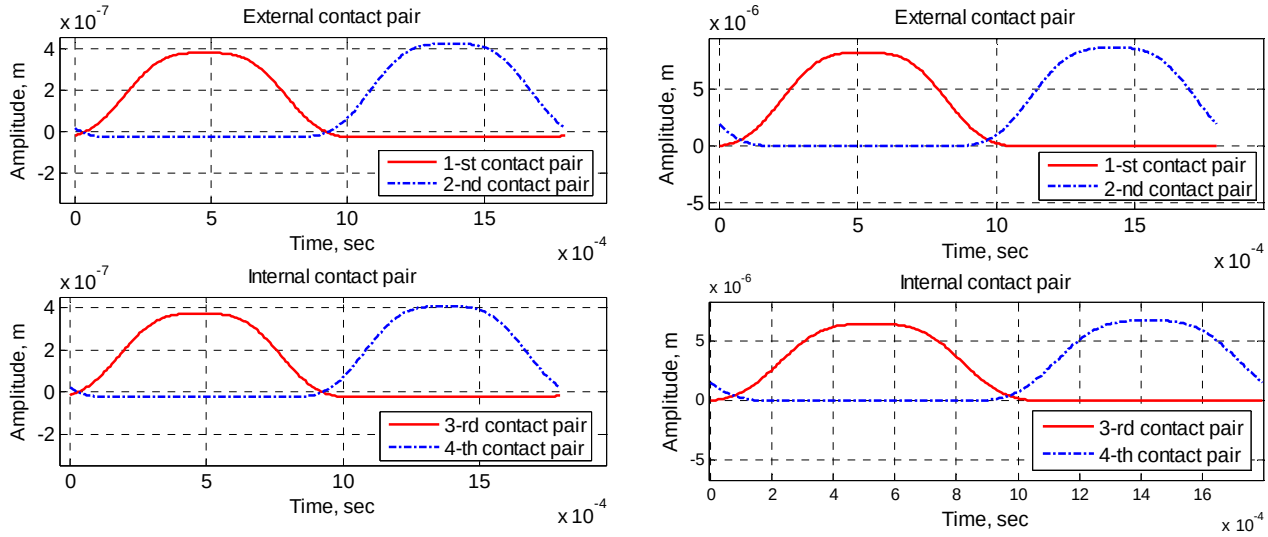

(a) (b)

Fig. 3.24. Non-linear solution by HB method at initial crack opening (Ω=10 Hz):

(a) trailing edge crack, (b) leading edge crack

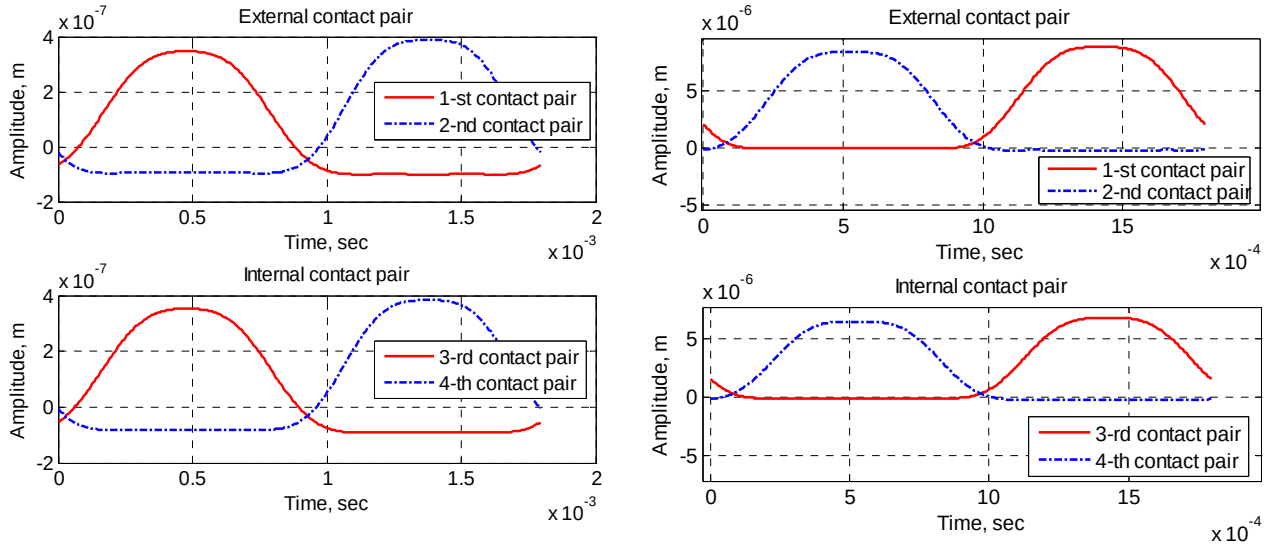

(a) (b)

Fig. 3.25. Non-linear solution by HB method at initial crack opening (Ω=20 Hz):

(a) trailing edge crack, (b) leading edge crack

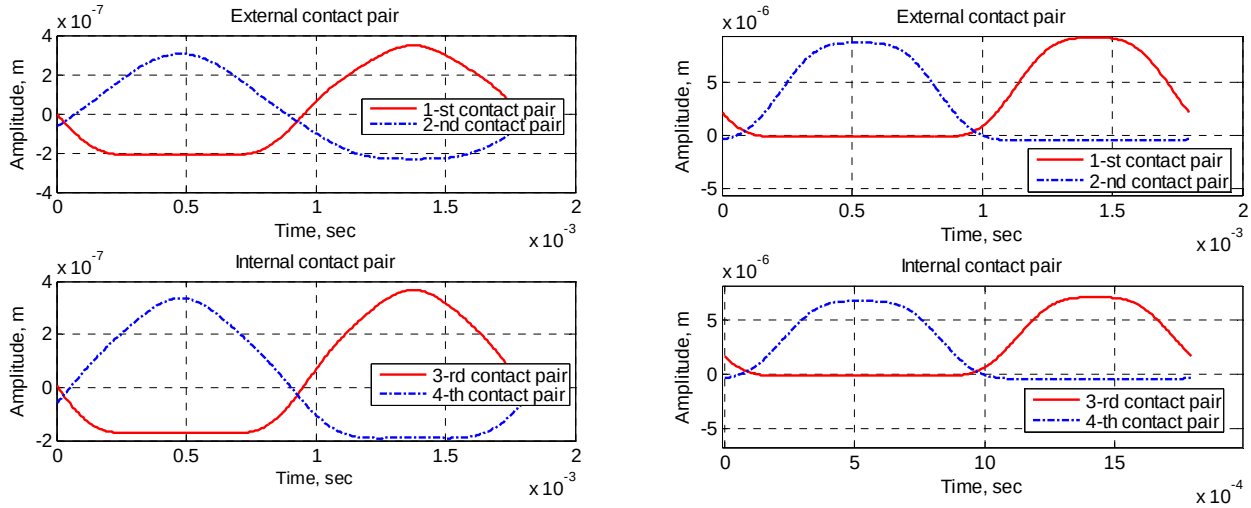

(a) (b)

Fig. 3.26. Non-linear solution by HB method at initial crack opening (Ω=30 Hz):

(a) trailing edge crack, (b) leading edge crack

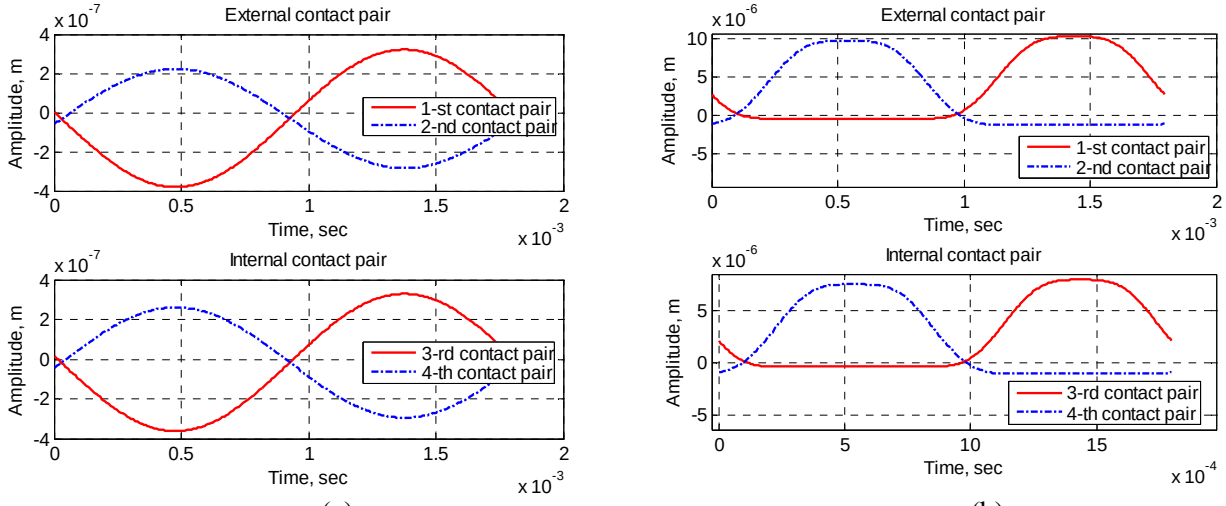

(a) (b)

Fig. 3.27. Non-linear solution by HB method at initial crack opening (Ω=50 Hz):

(a) trailing edge crack, (b) leading edge crack

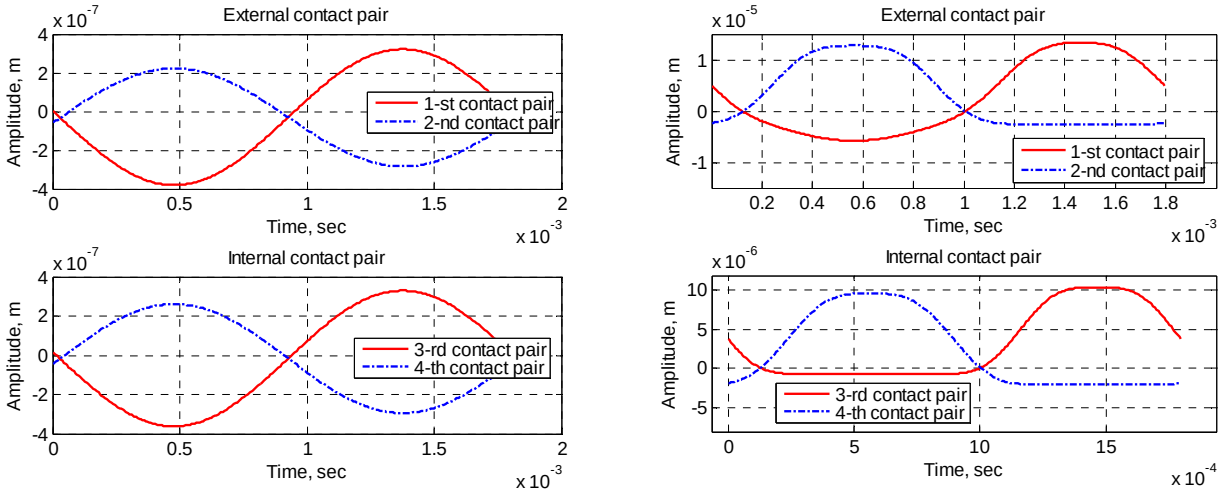

(a) (b)

Fig. 3.28. Non-linear solution by HB method at initial crack opening (Ω=60 Hz):
(a) trailing edge crack, (b) leading edge crack

Main conclusion, which may be drawn upon analyzing the outcomes presented in Figs. 3.24–3.28, is that taking into account an effect of the centrifugal forces leads to useless non-linear formulation of the cracked blade dynamic behaviour. Such a phenomenon is observed with an increase of rotor frequency. It becomes evident earlier for the trailing edge crack due to its smaller opening in comparison with the initial crack one. Still, the crack induced non-linearity should be taken into account at all presented rotor frequencies for the crack on the leading edge.

The simulation performed above is very important from the point of view of the computation time cost as it allows using the cracked blade linear model in some range of the rotor frequency change.

3.2.7 Fracture mechanics elements application to cracked blade model

The present subchapter is provided to show applicability of considered in subchapters 2.3–2.4 formulations to cracked blade model. Regarding to the main task of the study, it is required to estimate, at least approximately, influence of the considered crack cases on blade durability. It will allow understanding how far we are from the possible damage of the blade during engine operation. Additionally, such estimation can be integrated as a module to the overall engine health monitoring system based on tip-timing measurements.

Equations (2.92)–(2.99) were elaborated for some simplified cases of cracked structures. Stress intensity factor derived from them is the main parameter used for calculation of residual durability of cracked structure (2.127). In the case of considered 3d model of cracked blade, these equations are not applicable due to complexity of blade geometry.

To overcome the problem of stress intensity coefficient determination, it was proposed to use simplified brick-type finite elements model of the blade (Fig. 3.29). It does not have twisting

and it is of constant thickness along the height. The model has overall dimensions, which are the same with used through the chapter. The cracked blade scheme corresponds to the scheme shown in Fig. 3.3b (crack on leading edge). The crack length is set to vary between 0.001 m and 0.005 m.

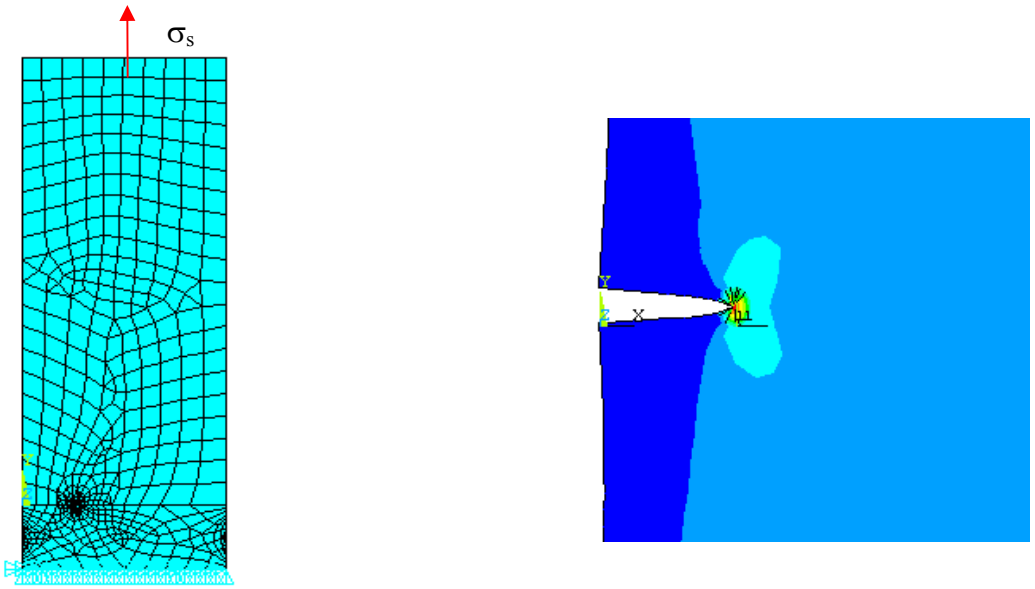

a b

Fig. 3.29. Brick-type cracked blade model subjected to durability analysis:
(a) finite elements model, (b) stress deformed state around crack tip

Using finite elements model from Fig. 3.29a, it is possible to approximately calculate stress intensity coefficient at the crack tip using finite elements software. The main loading is imposed by centrifugal forces leading to crack opening (Fig. 3.29b). In this case, first crack mode will be dominant. Varying crack length, stress intensity coefficient dependence on crack length can be constructed (Fig. 3.30a). Number of remained cycles to structure failure was calculated by equation (2.127). Initial data for cyclic loading correspond to those from subchapter 2.4.3.

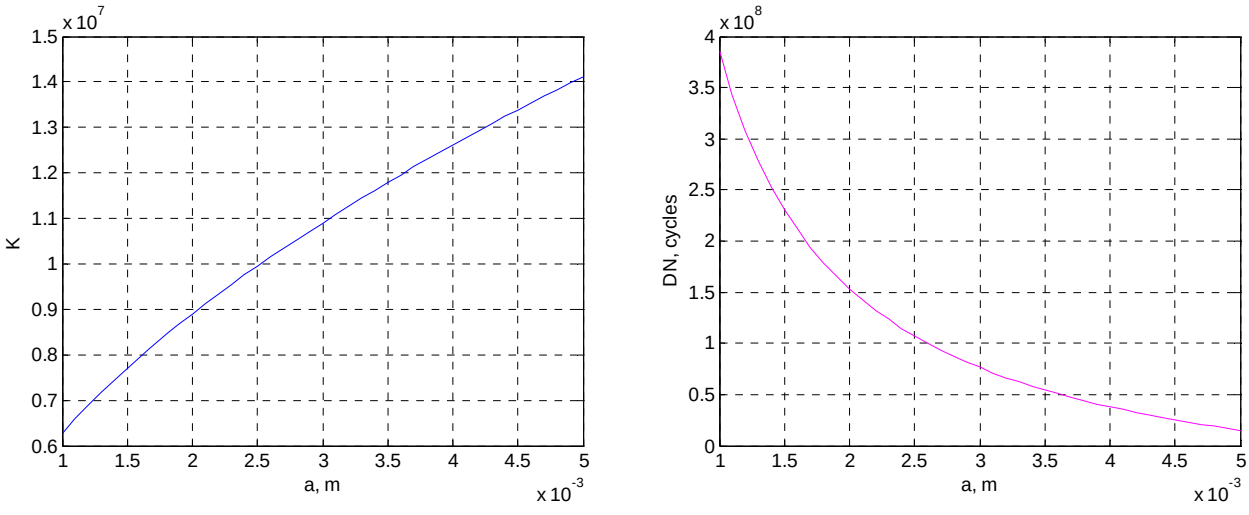

a b

Fig. 3.30. Cracked blade durability parameters dependence on initial crack length:
(a) stress intensity coefficient K (Pa·m$^{1/2}$), (b) remained cycles number dN

From the results of approximated calculation of residual durability (Fig. 3.30b), we can make conclusion that studied cracked blade with crack lengths of 2 or 4 mm is within the frameworks of safety operation. Number of remained cycles is of order of 10^7 cycles that corresponds to number of base cycles used for calculation of fatigue limit of materials (10^7 cycles – for steel and 10^8 cycles – for alloys and non-ferrous materials). Moreover, it is evident that crack growth rate will be much less then of order of 10^{-7}m/cycle that is average order of fatigue crack growth rate.

It should be noted that such kind of simulation should be accomplished for realistic model. Since realistic loading data (engine operation mode, external conditions) and material properties will definitely change results and, very likely, in direction of decrease of residual durability.

As far as crack parameters used in preceding simulations provide cracked structure safety operation, they can be retained for following development of bladed disk model containing cracked blade. After that, analysis of cracked blade detectability by tip-timing method will be performed using the bladed disk model. Preliminarily, it is possible to say that successful detection of cracked blade with considered crack parameters makes possible normal engine monitoring in operation and its well-timed maintenance planning.

3.3 Dynamic model of bladed disk with a cracked blade

The bladed disk dynamic problems in themselves are cases for application of the cyclic analysis technique because of their behaviour symmetry in the circumferential direction. The presence of mistuning, alias spread of structural properties from one blade to other, or in cyclic representation among the sectors, disrupts the symmetry. And even in this case, there is an opportunity [9] to continue with cyclic analysis of the mistuned bladed disks. The present study is not limited with just a mistuning caused by manufacturing inequalities. The crack presence in the blade induces its non-linear behaviour that makes impossible to use the cyclic analysis and requires a full-assembled disk model to simulate the crack effect on the disk forced response.

In order to create a full bladed disk model containing one or several cracked blades, the finite element model of the disk sector with a cracked blade was initially developed in ANSYS (Fig. 3.32a). Then its structural matrices were transferred to MATLAB to continue sequential assembling process. The disk with 31 blades is used for the simulation (Fig. 3.32b). It has the same material properties of the blades and disk: Young's modulus – $2 \cdot 10^{11}$ Pa, Poisson's ratio – 0.3 and material density – $7.8 \cdot 10^3$ kg/m^3. Geometrical data of the model: disk radius – 0.3 m, crack length – 0.004 m or 0.002 m located on leading edge. Excitation force has amplitude of 0.3N.

For a simple illustration of the assembling, let a circular symmetric structure to contain 4 identical sectors. The displacement vector of the *j*-th sector can be partitioned in detail as:

$$\mathbf{u}_j = \left[u_{\text{int}\,L,j}, u_j, u_{\text{int}\,R,j}\right]^T, \tag{3.49}$$

where, $u_{\text{int}\,L,j}$, $u_{\text{int}\,R,j}$ are the left and right interfaces of DOFs partitions; u_j is the interior DOFs partition. The interior DOFs partition consists of physical displacements when assembling is performed using the full model of the disk sector. They can also be presented by physical displacements of master DOFs and contain a certain number of retained modes, if assembling is accomplished using the reduced model of the disk sector.

After assembling the displacement vector of the bladed disk model will be:

$$\mathbf{u} = \left[u_{\text{int}\,L,1+\text{int}\,R,4}, u_1, u_{\text{int}\,R,1+\text{int}\,L,2}, u_2, u_{\text{int}\,R,2+\text{int}\,L,3}, u_3 u_{\text{int}\,R,3+\text{int}\,L,4}, u_4\right]^T. \tag{3.50}$$

It is necessary to use the transformation matrix for calculation of mass **M** and stiffness **K** matrices of the assembled bladed disk model. This matrix can be obtained from a comparison of the two disk models: the fully assembled and partially opened one, which does not have a connection between the first and last (4-th) sectors. The displacement vector of the partially opened model and its relationship to the fully assembled model are:

$$\mathbf{u}^* = \left[u_{\text{int}\,L,1}, u_1, u_{\text{int}\,R,1+\text{int}\,L,2}, u_2, u_{\text{int}\,R,2+\text{int}\,L,3}, u_3 u_{\text{int}\,R,3+\text{int}\,L,4}, u_4, u_{\text{int}\,R,4}\right]^T$$

$$\mathbf{u}^* = \mathbf{B}\mathbf{u} \tag{3.51}$$

where, **(B)** is the transformation matrix.

The transformation matrix can be expressed as:

$$\mathbf{B} = \begin{bmatrix} & \mathbf{I}_{\text{full}} & \\ \mathbf{I}_{\text{int}} & 0 & 0 \end{bmatrix}, \tag{3.52}$$

where, $\mathbf{I}_{\text{full}}$ is the unity matrix with dimensions corresponding to the fully assembled disk model; $\mathbf{I}_{\text{int}}$ is the unity matrix with dimensions corresponding to the number of interface DOFs.

Assembling of the structural matrices will consists in summing the DOFs partitions of corresponding interfaces of each sector. In this way, mass **M** and stiffness **K** of the fully assembled bladed disk model are obtained. Then with the expression of system kinetic energy $E_c = \frac{1}{2}\ddot{\mathbf{u}}^T\mathbf{M}\ddot{\mathbf{u}}$, the expression allowing calculation of the structural matrices with the use of the transformation matrix **B** can be written as:

$$\mathbf{M} = \mathbf{B}^T\mathbf{M}^*\mathbf{B}, \mathbf{K} = \mathbf{B}^T\mathbf{K}^*\mathbf{B}. \tag{3.53}$$

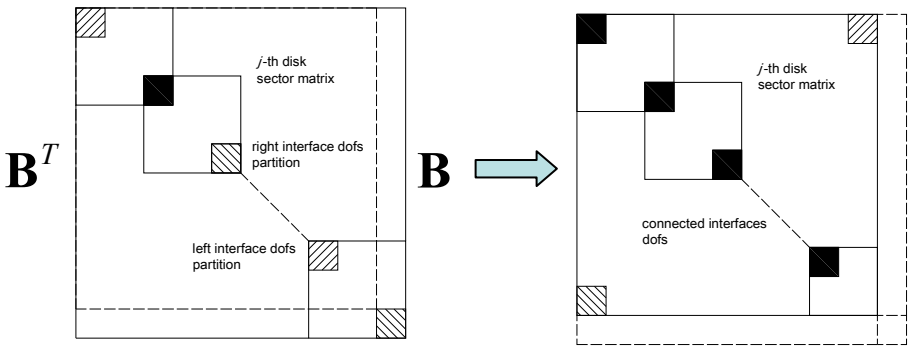

Fig. 3.31. Bladed disk assembling

The expressions (3.53) are applied to obtain the bladed disk model for its deployment through all succeeding analyses. Earlier it was already elucidated that the sector with a cracked blade was taken as the initial one. In order to obtain the disk model with one or some cracked blades it is enough to merge DOFs in the cracked areas of the blades accepted as uncracked. This procedure is simplified with the use of the relative DOFs between crack sides (Fig. 3.5). They present by themselves displacements between nodes, which comes into contact at the crack breathing. By this approach, elements corresponding to the relative DOFs are deleted from structural matrices of the bladed disk model to pass to the uncracked state.

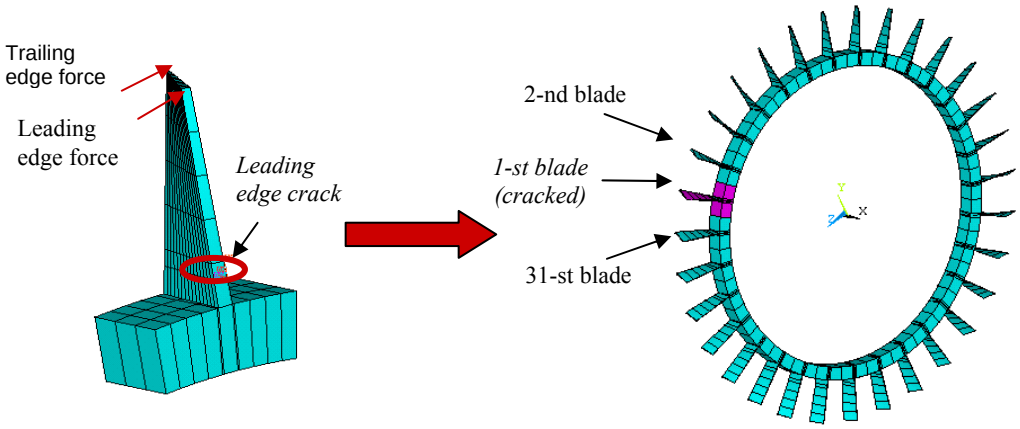

(a) (b)

Fig. 3.32. Bladed disk finite-elements model:

(a) sector with cracked blade, (b) assembled disk with applied external forces

It should be noted that main source of excitation for the bladed disk in our case is the preceding stator vane. Number of stator blades is always different from the number of rotor (disk) blades that result in excitation forces phase lag for each blade individually.

3.3.1 Reduction of the bladed disk model

In the case of the disk model with a cracked blade, the sub-structuring approach can be explained on the individual cracked blade. The crack location forms an interface between two blade parts (Fig. 3.4) It should be noted that in this case there is no classical sub-structuring because these parts are not fully independent. Some DOFs remain shared between upper and lower blade sub-structures (subchapter 3.2.1).

In the case of the bladed disk model it is possible to apply two approaches to the system reduction using sub-structuring:

- The reduction on the base of the fully assembled system. Here the low sub-structure is represented by a cracked blade partition under the crack interface and the bladed disk (Fig. 3.33a). The upper sub-structure is the cracked blade partition over the interface.
- The reduction on the base of the disk sector (with a cracked blade, Fig. 3.33b). In this case the cracked blade sector is reduced and then assembling of the whole system is performed. This approach is more preferable when the initial disk sector has an essentially big number of DOFs and the assembling process is very expensive in time. To continue with the model analysis the second stage of reduction is required in order to obtain the system size, which will be comparable with the previous approach.

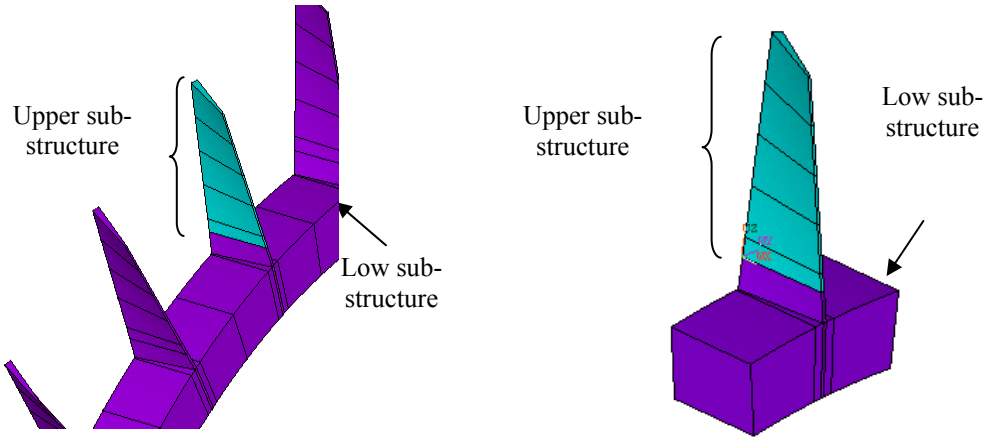

Fig. 3.33. Bladed disk model sub-structuring:
(a) on the base of the full assembled system, (b) on the base of the disk sector

Having established two ways of reduction for the bladed disk model, the fixed interface method may be applied. A relative displacement between contact pairs was accepted as the interface or master DOFs. Additionally, a certain number of modes were retained that describe behaviour of the uncracked bladed disk. DOFs of nodes of external forces application were added to this set as well. The initial full model of the assembled bladed disk contained 28284 DOFs. It was reduced to

the model with 136 master DOFs. The eigenvalues problem was solved by varying the number of the additionally retained modes (Fig. 3.34)

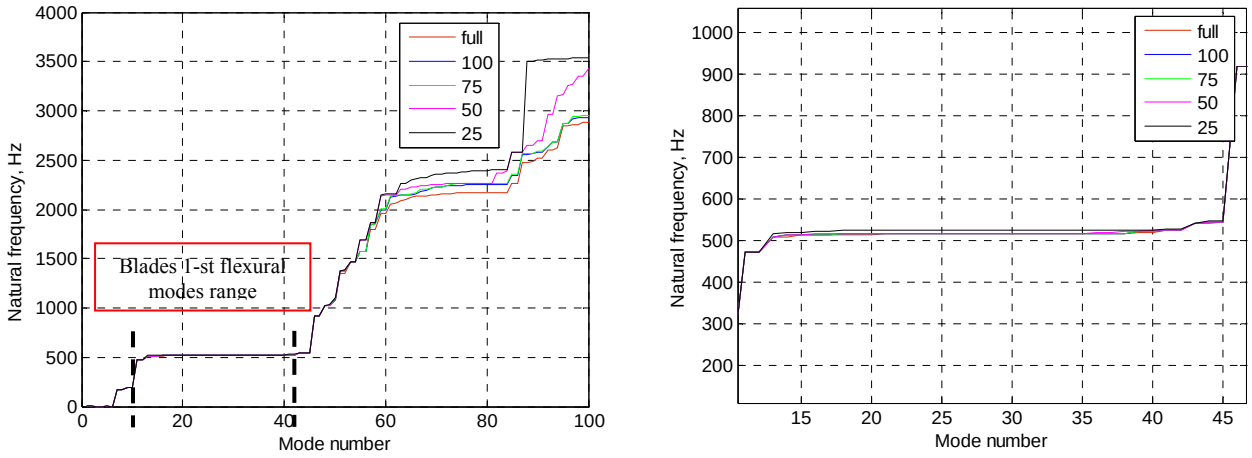

Fig. 3.34. Eigenfrequencies distribution at different number of retained modes

Fig. 3.34 shows that it is sufficient to retain 50 additional modes to attain proper approximation of the dynamic behaviour of the full model within the range of the first blade flexural mode. This range was selected because of a greater effect of the crack presence and sufficiently high resonance amplitudes. It will be shown that these stipulations are quite adequate for simulation under application of blade tip-timing method. Ultimately, the system size after reduction is 186 DOFs. The eigenfrequencies of both full and reduced bladed disk model is presented in Table 3.5.

Comparison of the full and reduced system frequency responses is performed supposing the linear cracked blade behaviour and 4–mm leading edge crack (Fig. 3.35). Application of the external excitation forces is shown in Fig. 3.32b. The system frequency response is calculated within the range that also covers the first flexural modes of blades.

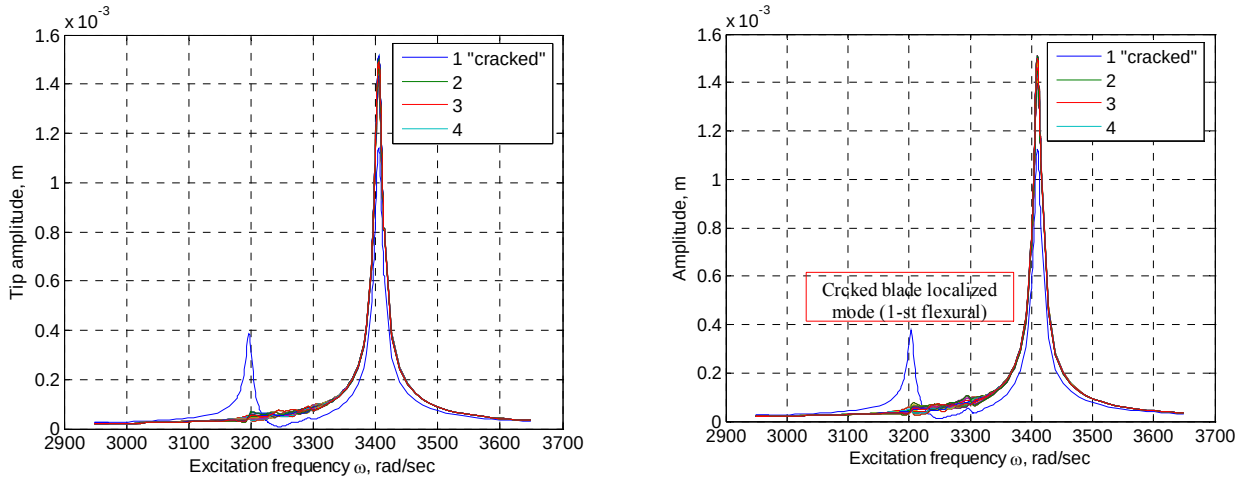

(a) (b)

Fig. 3.35. Full (a) and reduced (b) bladed disk models frequency responses

Bladed disk model eigenfrequencies (in Hz)

Table 3.5

Mode number	Full model	Reduced model	Uncracked model	Mode (dominated nature)
5	472.44	472.81	472.89	disk
6	472.78	472.88	472.89	disk
7	508.77	509.91	514.31	blade
8	509.42	514.31	514.31	blade
9	513.88	514.62	516.3	blade
10	514.11	516.3	516.3	blade
11	514.89	516.34	516.43	blade
12	515.07	516.43	516.43	blade
13	515.4	516.47	516.56	blade
14	515.49	516.56	516.56	blade
15	515.74	516.6	516.67	blade
16	515.94	516.67	516.67	blade
17	515.99	516.7	516.74	blade
18	516.06	516.74	516.74	blade
19	516.1	516.77	516.8	blade
20	516.16	516.8	516.8	blade
21	516.24	516.82	516.84	blade
22	516.26	516.84	516.84	blade
23	516.29	516.85	516.86	blade
24	516.32	516.86	516.86	blade
25	516.36	516.87	516.87	blade
26	516.38	517.03	517.06	blade
27	516.39	517.06	517.06	blade
28	516.4	517.69	517.78	blade
29	516.41	517.78	517.78	blade
30	516.42	519.25	519.43	blade
31	517.12	519.43	519.43	blade
32	517.15	521.27	521.43	blade
33	520.89	521.43	521.43	blade
34	520.96	525.15	525.56	blade
35	524.51	525.56	525.56	blade
36	524.86	525.87	526.02	blade
37	541.77	542.7	542.92	blade
38	542.83	543.49	543.55	disk
39	543.34	543.55	543.55	disk

Under absence of the phase lag of excitation forces (all forces applied to blades have the same phase) two response peaks of the system are observed: a principal peak of all blades and an additional peak, which corresponds to frequency localization of the cracked blade.

The localization phenomenon is very important diagnostic sign, which will give us the most information about crack presence in the blade. Simulations for cases of the cracked blade localization will be treated in combination with mistuning and excitation forces phase lag in subchapter in 3.3.4.

Also it should be noted the good agreement of results of bladed disk and uncoupled cantilevered blade. For example, frequency response of the first mode of the cracked blade (Fig. 3.18b, first bending mode) can represent qualitatively forced response of the bladed disk for the same crack case (leading edge crack of 4 mm) and such particular dynamic behaviour (blade-dominated first bending mode).

3.3.2 Choosing the number of retained harmonics for the bladed disk model

The outcomes of application of HB method to the non-linear model of uncoupled cracked blade make evident that the number of retained harmonics directly affects the computational time cost. The dependence will be more sizeable in case of the bladed disk model.

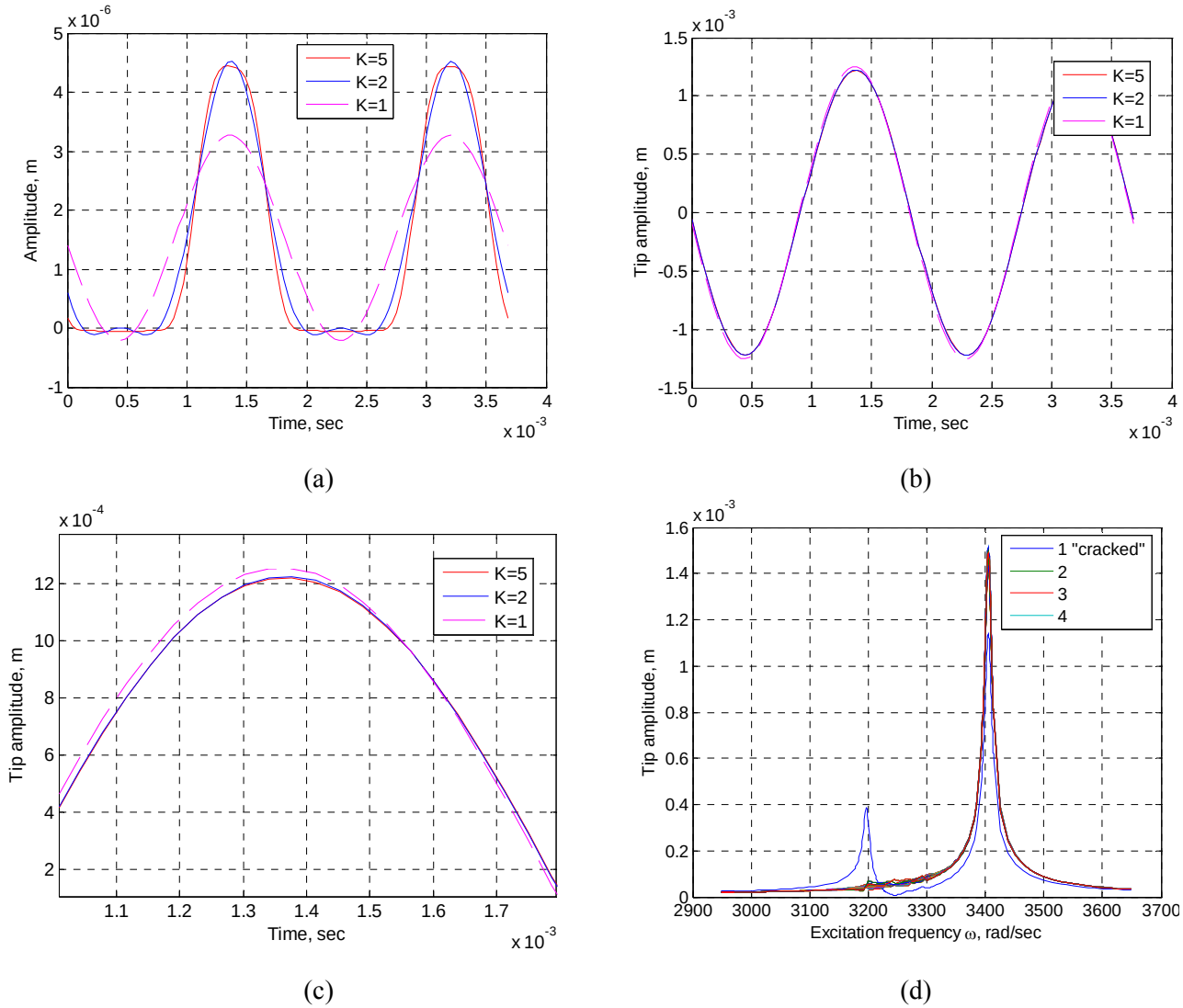

Fig. 3.36. Non-linear solution by HB method for different harmonics numbers: (a) “crack point”, (b) “tip point”, (c) “tip point” (zoom), (d) frequency response at “tip point”

Fig 3.34 shows the simulations made for different numbers of retained harmonics (3.15–3.16.) The non-linear model with two harmonics will be used for all subsequent simulations as it quite exactly describes the system non-linear behaviour. The system response at the blade tip is

observed to remain practically sinusoidal and this will be used for a simpler formulation of the tip-timing method governing equation.

3.3.3 Effect of the phase lag of excitation forces on the bladed disk forced response

A phase lag between the forces applied to different blades must be taken into account on constructing a vector for the external excitation forces of the bladed disk model because of a difference between numbers of blades of the rotor wheel and preceding stator vane. An engine order excitation is assumed, which is harmonic in time and differs only in phase from blade to blade. The excitation force on j-th blade can be expressed as:

$$\mathbf{F}_j = \mathbf{F}_{aj} e^{i\psi} e^{i\omega t},\ \psi = 2\pi \frac{n_s}{n_r}(j-1), \tag{3.54}$$

where $\mathbf{F}_{aj}$, is the excitation force amplitudes vector of j-th blade; ψ is the phase; ω is the excitation frequency; n_s is the number of stator blades; n_r is the number of rotor blades.

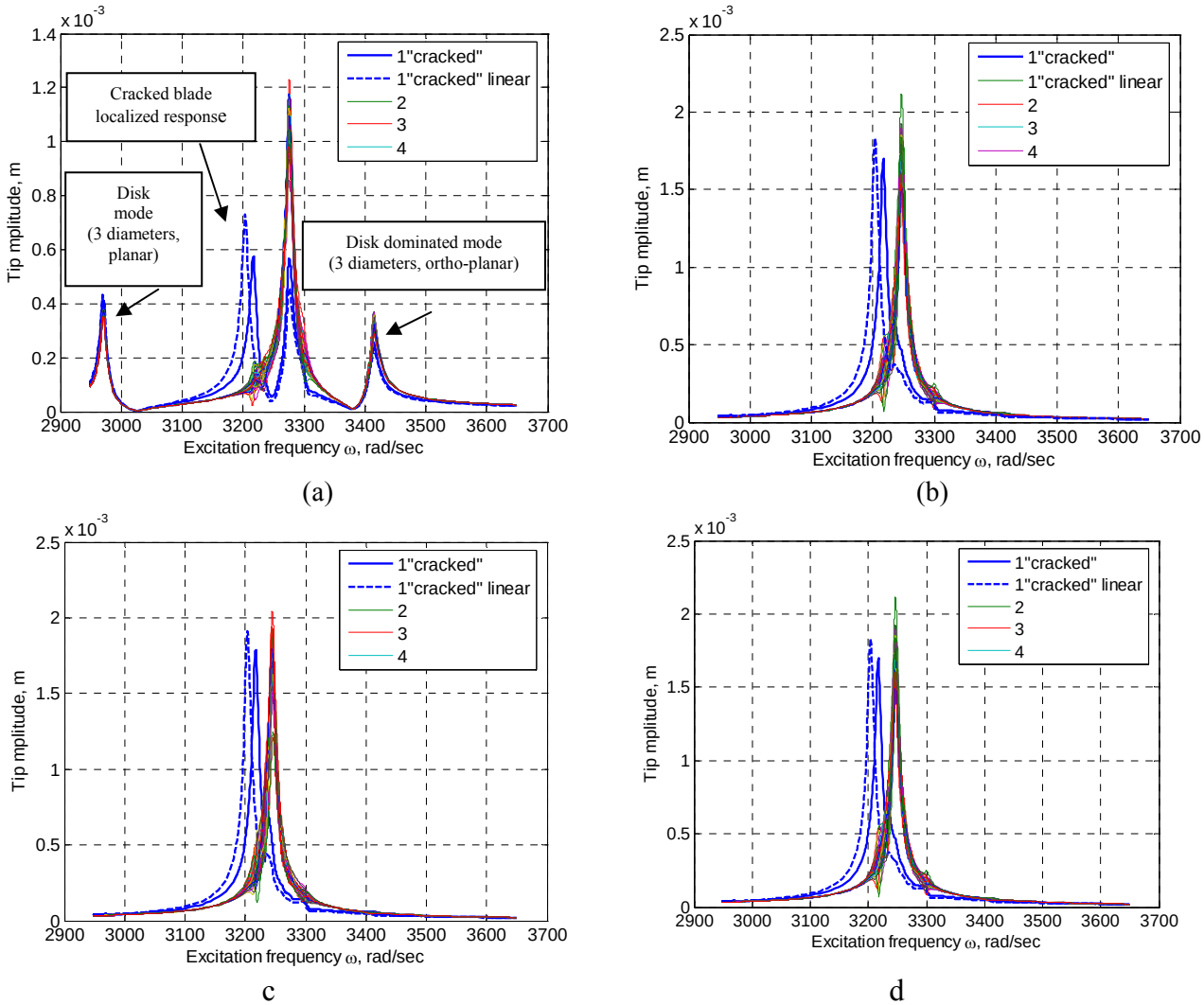

Fig. 3.37. Effect of the phase lag of excitation forces: (a) n_s=28, (b) n_s=25, (c) n_s=23, (d) n_s=20

The simulations of the bladed disk frequency response are shown by varying number of stator blades (Fig. 3.37). The bladed disk response with a cracked blade subjected to linear formulation is shown on all graphs as the reference one (dashed line).

The results (Fig. 3.37) provide evidence that maximum of the cracked blade response increases with arising difference between numbers of the stator and rotor blades. It becomes comparable with the maximum of principal response of all blades. It is caused by an increase of the number of excited diameters (1.31) that results in decrease of coupling between neighboring blades. Consequently, it results in a more independent behaviour of the localized cracked blade.

Furthermore, it should be explained the appearance of two additional resonances in the case of 28 stator blades (Fig. 3.37a). They are disk-dominated modes of three nodal diameters, which are excited by the rules of zig-zag diagram [17, 104].

3.3.4 Mistuning effect on the bladed disk forced response

The reasoning discussed as to simulation of the mistuned bladed disk vibration is aimed at perfection of the suggested non-linear bladed disk model.

Having discussed effect of the phase lag of the excitation force, the next must be examined a mistuning effect on the bladed disk forced response. A possibility to localize the cracked blade forced response will be simulated at a certain level of mistuning. Absence of the cracked blade frequency localization will be studied as well. In this case, it seems to be that only a difference between amplitudes can be used for identification of the crack presence. The procedure seems to be hardly possible even at a low mistuning level.

Many writers admit that prediction of the mistuning effect on the bladed disk response is a challenging problem [9, 62, 69, 82, 87]. There are two main things that arise the difficulties:

- a random nature of the blade-to-blade structural properties variation, and
- the fact that mistuning corresponds to fluctuations in the system properties, i.e., stiffness, mass and damping.

The mistuning presence in the bladed disk can be represented by a mistuning of the blade stiffness. As far as the range of the blade the first flexural mode is considered in the analysis, the mistuning can be simulated by perturbation of the individual blade partition of the bladed disk stiffness matrix:

$$\mathbf{K}_{bmj} = (1 + m_j)\mathbf{K}_{bj}, \tag{3.55}$$

where, m_j is the mistuning coefficient relatively to the first blade and it is randomly generated by normal low with mean $\mu = 0$ and standard deviation σ.

With the fundamental mistuning model obtained, a major concern is an ability to detect a cracked blade on the base of the mistuned bladed disk forced response. It can be easily achieved, if we have an event of the cracked blade frequency localization. As it was shown, the cracked blade frequency localization resulted in appearance of the additional resonance peak caused by the crack presence (Fig. 3.38). At the linear formulation the crack presence can be equated to the blade mistuning. Therefore, a frequency localization of the uncracked blades can be obtained at a certain mistuning level. This may also arise some problems for detection of the cracked blade.

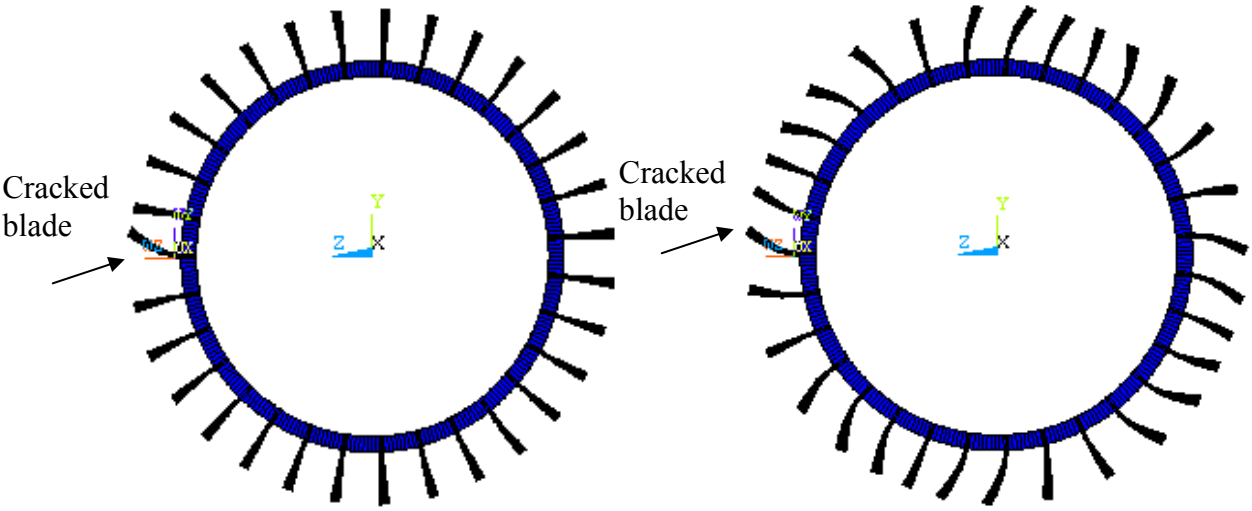

(a) (b)

Fig. 3.38. A bladed disk natural mode: (a) a case of cracked blade frequency localization, (b) a case of absence of the cracked blade frequency localization

The maximum forced vibration response of a blade of a mistuned structure is often larger than that of a perfectly tuned structure. Mechanical energy of this blade is different from that of other blades, which is identified as the vibration localization of the mistuned structure. The phenomenon of the vibration localization is expected to occur in any nearly periodic structure for which perfect periodicity is disrupted by small irregularities (mistuning). In the case of localization, the energy is simply absorbed in particular area within the structure. Localization occurs because the waves propagating away from the energy source are rejected by a boundary between slightly different subsystems constituting a nearly periodic structure. The resulting energy accumulation may locally cause much higher amplitudes than it can be predicted if perfect periodicity has been supposed. This possibly can have disastrous effects, for example in turbomachinery [76].

Simulations of the bladed disk frequency response are performed at different mistuning levels and excitation forces phase lag (Figs. 3.39–3.40). The mistuning levels used in the simulations: 1% and 2% that corresponds to $\sigma = 0.01$ and $\sigma = 0.02$.

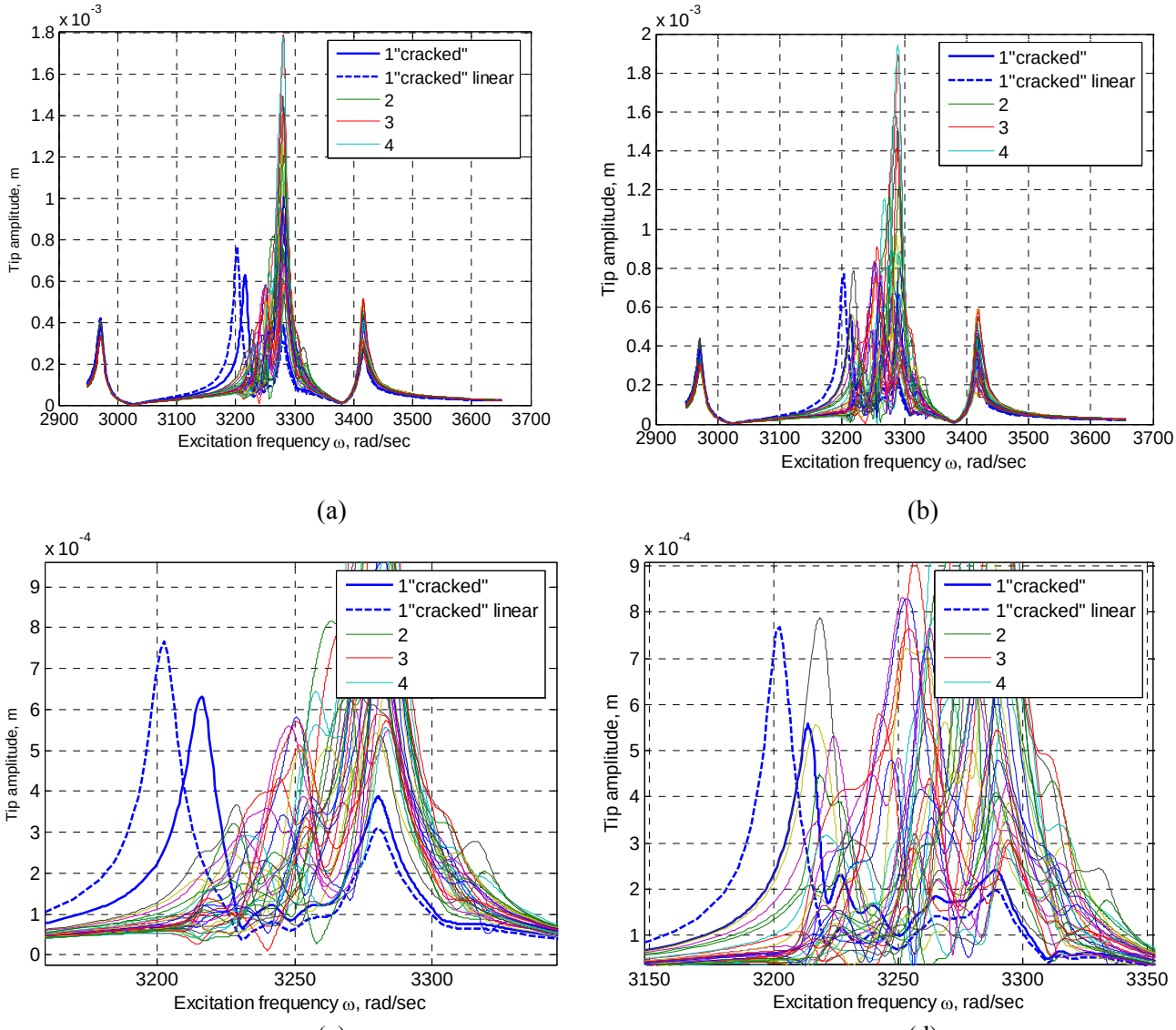

Fig. 3.39. Effect of mistuning on the bladed disk forced response (n_s=28):

(a) σ = 0.01, (b) σ = 0.02, (c) σ = 0.01 (zoom), (d) σ = 0.02 (zoom)

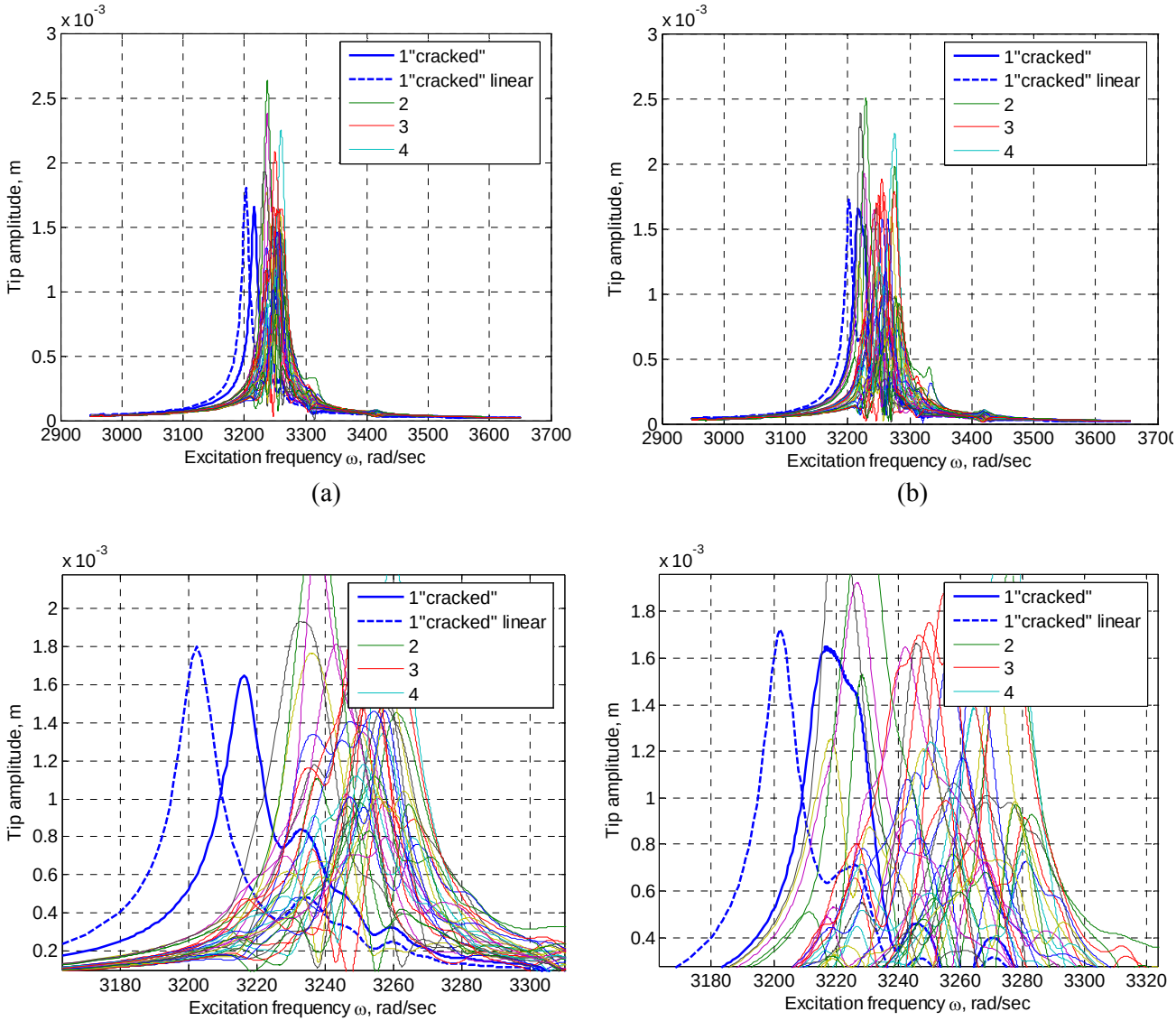

Fig. 3.40. Effect of mistuning on the bladed disk forced response (n_s=23):

(a) σ = 0.01, (b) σ = 0.02, (c) σ = 0.01 (zoom), (d) σ = 0.02 (zoom)

The results of simulations of different mistuning levels (Figs. 3.39–3.40) prove evidence to what has already been stated: if the cracked blade non-linear behaviour is taken into account, it arises difficulties in identification of a cracked blade. Sometimes it becomes impossible to distinguish cracked blade vibration localization. The linear formulation of the crack presence in the blade allows cracked blade identification even at the mistuning of 2%, while the non-linear formulation makes this process unachievable at this mistuning level.

With the cracked blade localization achieved some questions still remain. Will the mistuning level be more critical for cracked blade detection under absence of the localization phenomenon? Will it be necessary to simulate the crack behaviour by non-linear approach? The problem is as it was before, in spite of the fact that the crack length decreased to the length of 2 mm.

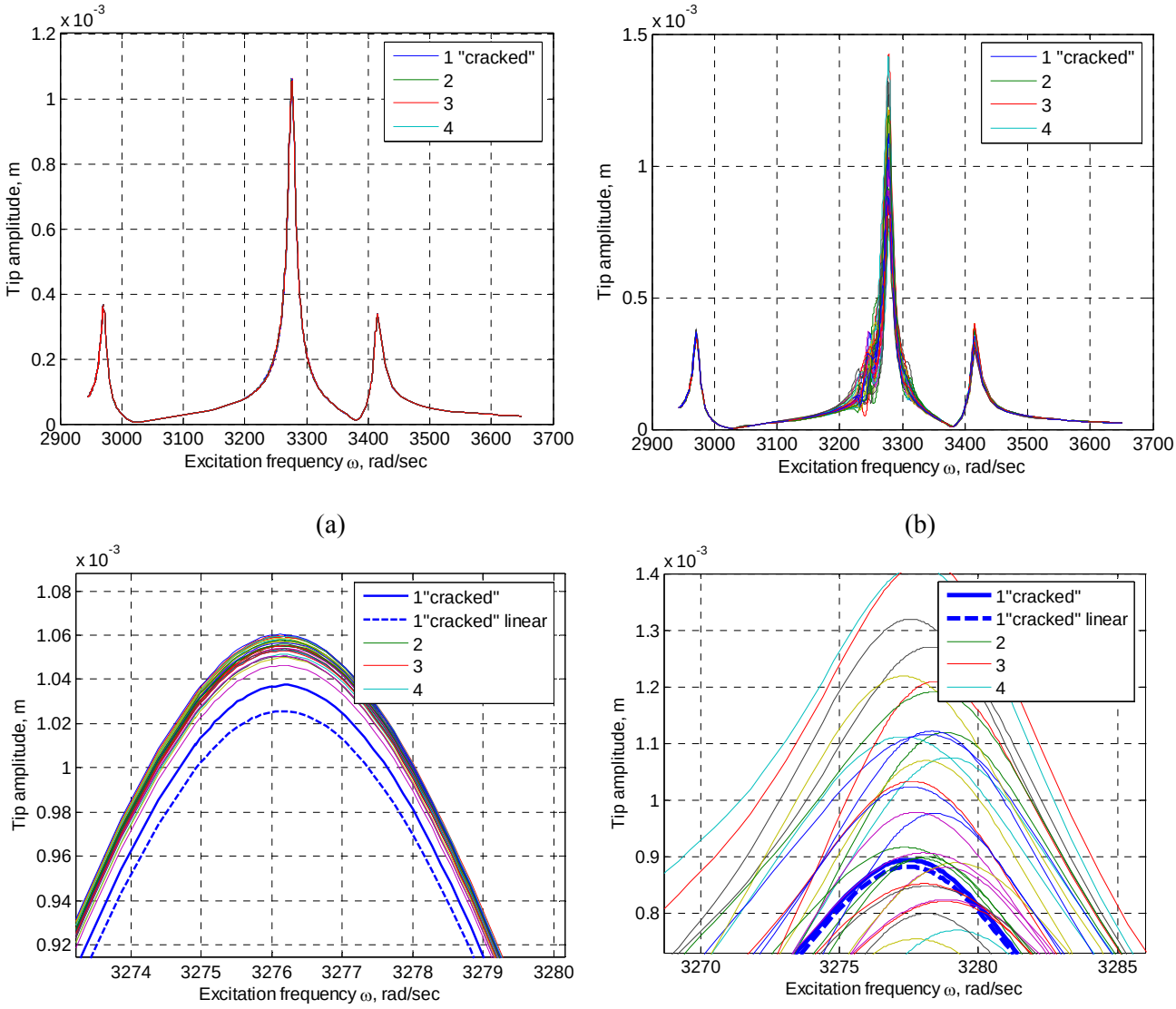

Fig. 3.41. Effect of mistuning on the bladed disk forced response (n_s=28):

(a) no mistuning, (b) σ = 0.005, (c) no mistuning (zoom), (d) σ = 0.005 (zoom)

A conclusion can be drawn that under absence of frequency response localization even a relatively small level of the mistuning makes impossible to separate the cracked blade response from those of the rest of blades (Fig. 3.41). Moreover, no resonance shift is observed by comparing results of the linear and non-linear model solutions. Only a small difference in amplitude levels is seen between both model solutions under absence of mistuning. These observations allow the following use of the linear formulation of the crack presence in the blade under absence of localization of the cracked blade vibration.

3.3.5 Prediction of mistuned bladed disk frequency response

For this purpose zig-zag diagram presented in the subchapter 1.1.3 can be used. recently it has been considered in conjunction with cyclic symmetry analysis. Since presence of the cracked blade disrupts cyclic symmetry, equation (1.31) is not longer valid. However, it can be expected the dominance of the number of excited nodal diameters even in such case. To confirm it the time history of bladed disk forced response should be shown graphically at the resonance frequency of all-blades principal response (Figs. 3.42–3.47). These figures present bladed disk forced response in time domain in the view of 3D surface, where diagonal lines correspond to disk nodal diameters.

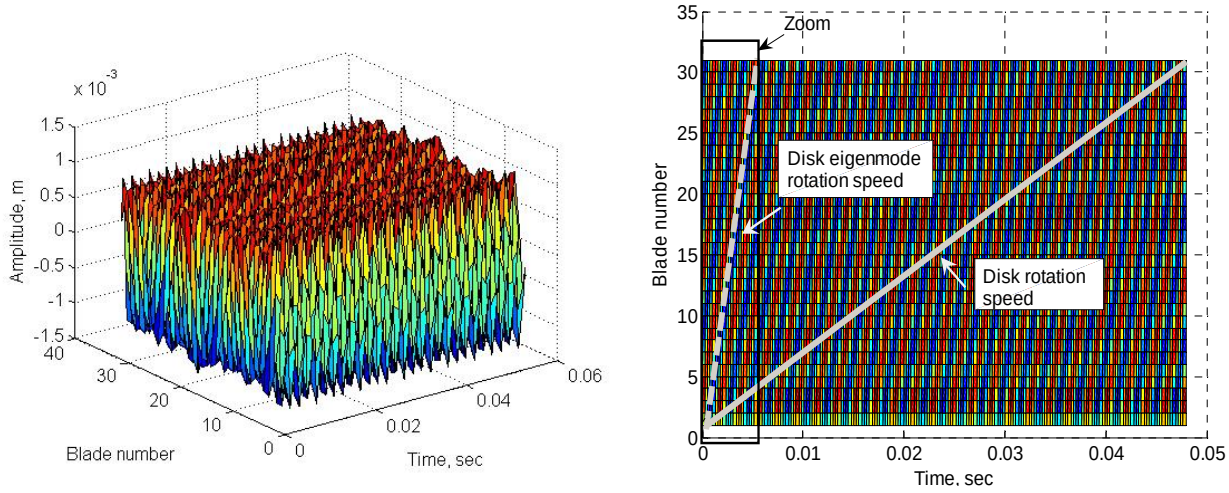

Fig. 3.42. Time-history of bladed disk forced response (n_s=28, no mistuning): (a) full 3D view, (b) view in 2D

Time period of simulation of the bladed disk forced response is calculated using disk rotation speed corresponding to particular resonance frequency:

$$T = \frac{2\pi}{\Omega} = \frac{2\pi}{(\omega_{res} / n_s)} , \tag{3.56}$$

where ω_{res} is the resonance frequency.

At the absence of mistuning (Fig. 3.42) the strict dominance of the number of excited diameters at the resonance frequency is seen. From this plot, three nodal lines corresponding to three excited nodal diameters are distinguished. Such kind of plot can be more readable, if in all following figures zooms of small time intervals will be shown. These time intervals match the time period of eigenmode rotation. The time period (3.56) depends on disk rotation speed, which is much less then speed of disk eigenmode rotation.

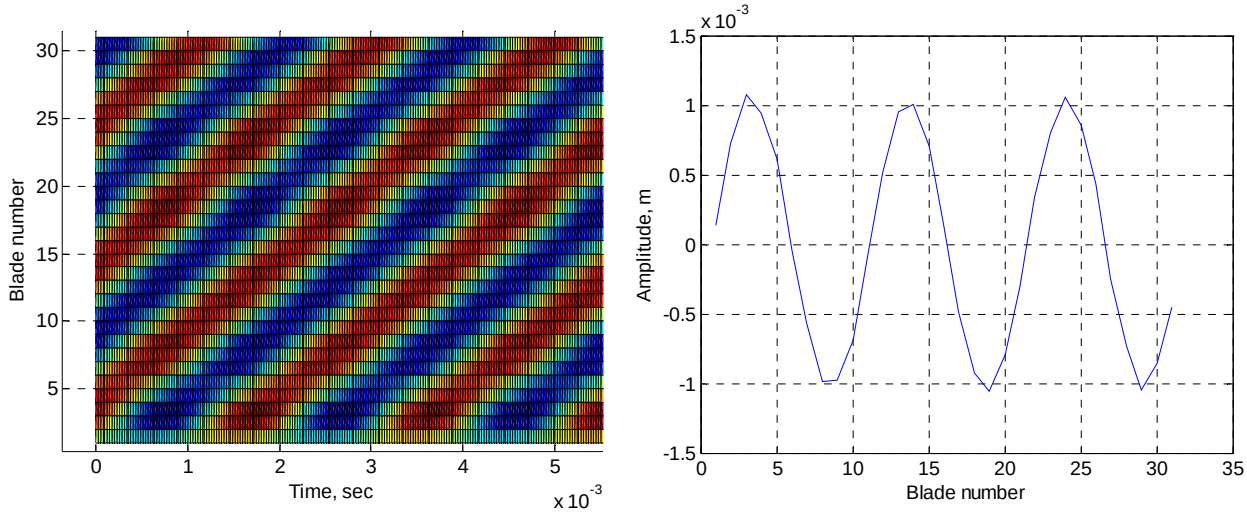

(a) (b)

Fig. 3.43. Time-history of bladed disk forced response (n_s=28, no mistuning):
(a) through the time period, (b) at time t=0

In Fig. 3.43a three nodal lines corresponding to the mode with three excited diameters are present. They have same direction of rotation as disk rotation speed. Same results showing dominance of the number of excited diameters are derived from Fig. 3.43b at time t=0.

Figs. 3.44–3.45 are devoted to the same simulation approach as Figs. 3.42–3.43, but with presence of mistuning. Two levels of mistuning are accepted as in previous section: σ=0.01 and σ=0.02. The increase of mistuning level leads to appearance of horizontal lines corresponding to localized behaviour of mostly mistuned blades. Such blades will represent by themselves the interfaces between blade sectors, where accorded behaviour of blades with known diameters number should be preserved.

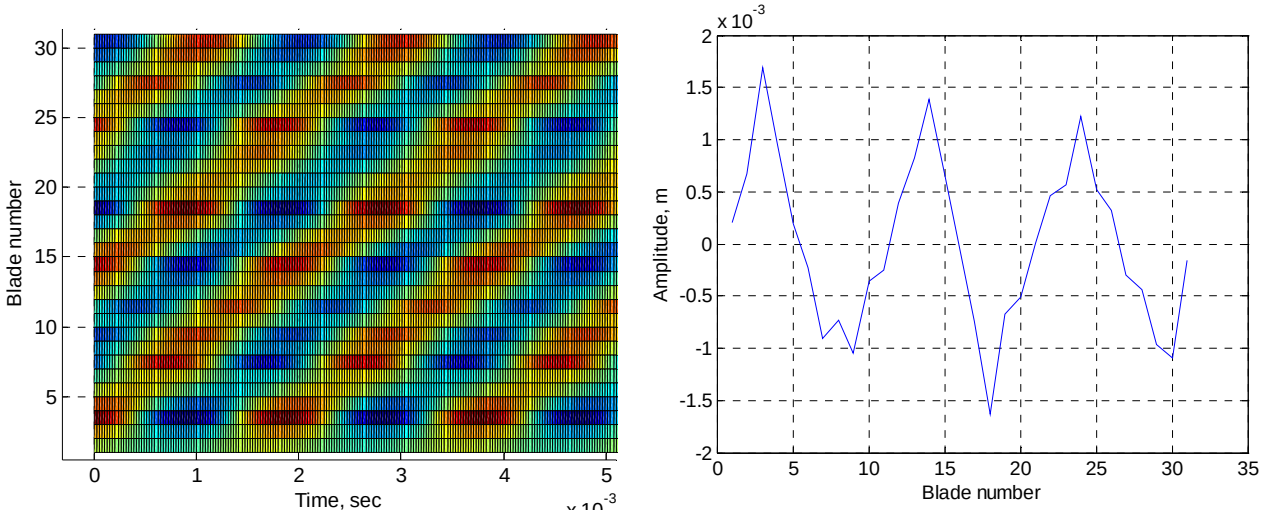

(a) (b)

Fig. 3.44. Time-history of bladed disk forced response (n_s=28, σ=0.01):
(a) through the time period, (b) at time t=0

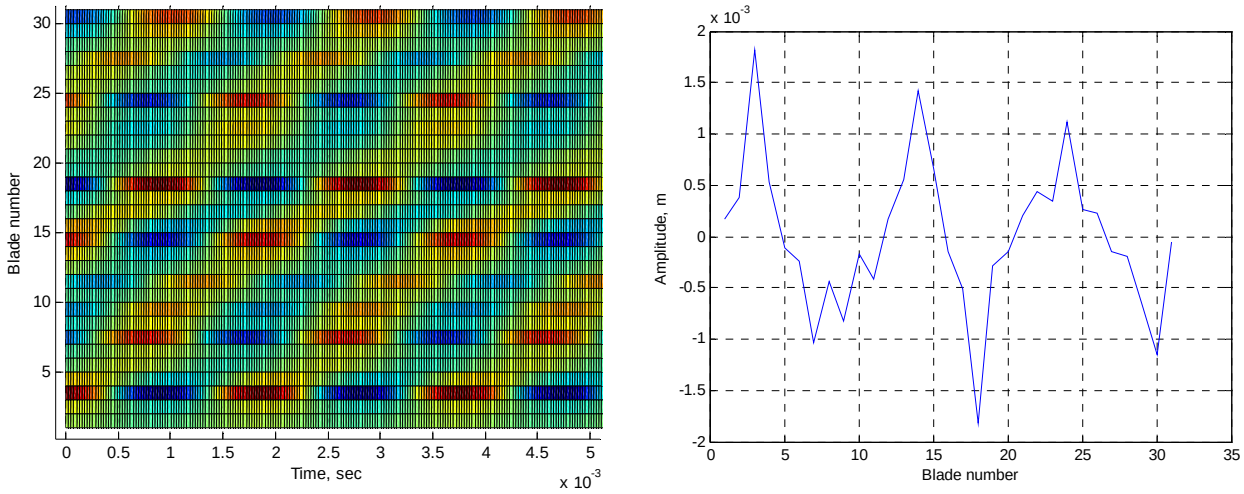

(a) (b)

Fig. 3.45. Time-history of bladed disk forced response (n_s=28, σ=0.02):
(a) through the time period, (b) at time t=0

Figs. 3.44–3.45 show that mistuning leads to difficulties of identification of number of excited diameters. Increase of mistuning level will make vanish eigenmode rotation.

It can be supposed that effect of mistuning would be more representative in the case when number of stator blades is bigger then number of rotor blades (Figs. 3.46-3.47). To consider such situation, 34 blades of stator vane and 31 rotor blades were chosen as initial data. Equation (1.31) will also give the mode with three excited diameters.

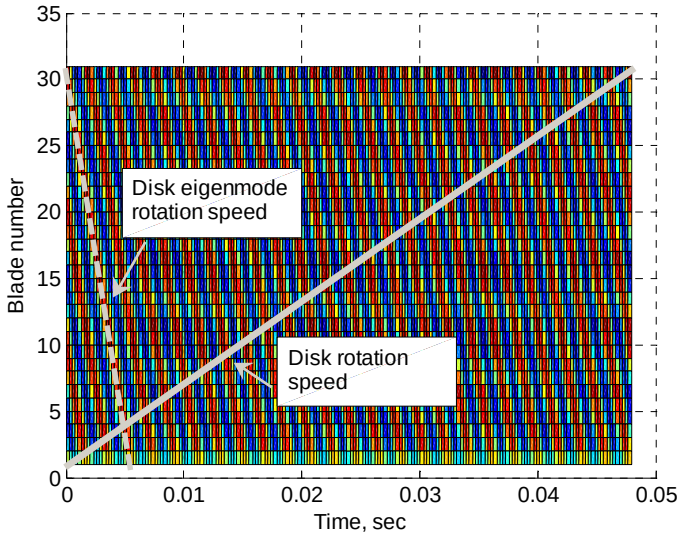

Fig. 3.46. Time-history of bladed disk forced response (n_s=34, no mistuning)

Same ratio between disk eigenmode rotation speed and speed of bladed disk rotation is observed from Fig. 3.46. Excited eigenmode has opposite direction of rotation. This can be explained by the fact that excitation forces vector (3.54) change its rotation direction when numbers of stator blades exceeds number of rotor blades.

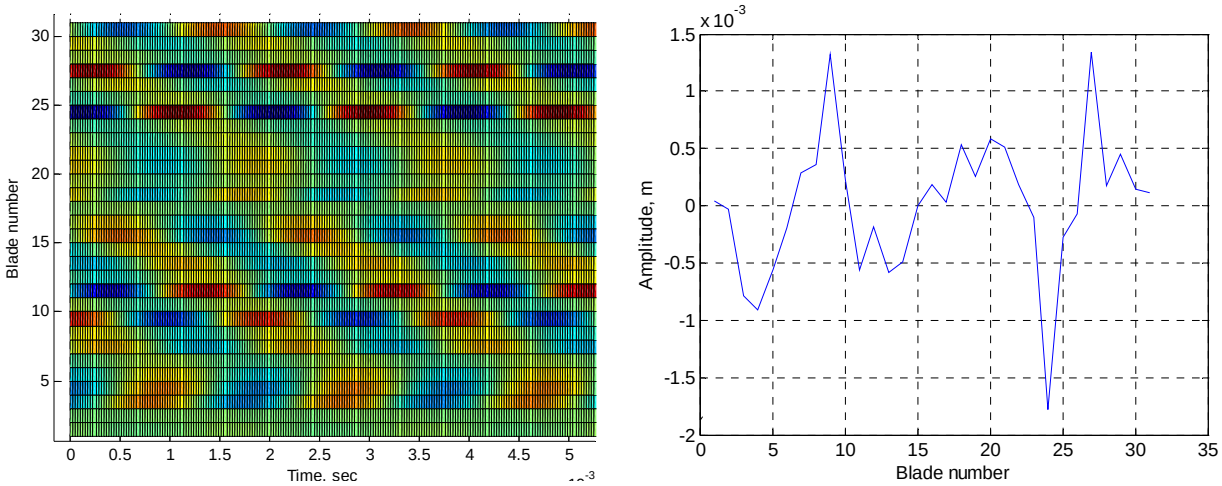

(a) (b)

Fig. 3.47. Time-history of bladed disk forced response (*EO*=34, σ=0.02):
(a) through the time period, (b) at time *t*=0

Results from Fig. 3.47 show that effect of mistuning makes almost invisible the presence of nodal lines. This fact can be explained by higher frequency of excitation that results in higher sensibility of the structure to mistuning presence.

Conclusions

Development of the cracked blade non-linear model and its application to the bladed disk dynamic model were discussed.

The cracked blade non-linear dynamic model was created with the use of the harmonic balance method in combination with contact approach of the crack breathing process simulation. This model allows simulation of the cracked blade behaviour at any loading amplitude and excitation frequency. We can more or less accurately observe the crack influence on the blade model dynamic behaviour. It is possible to derive some very important factors from the developed model, which can be used for detection of a crack presence:

- eigenmode frequency reduction
- increase of the blade tip amplitude

All these factors are very important and can be accepted as diagnostic signals and used for simulation by means of the tip-timing method. An effect of the centrifugal forces was also simulated. The crack initial opening was found to lead to the crack non-linear representation, which is useless at some rotation frequencies.

Also it was shown that crack induced non-linearity influence is:

- easily detectable in the zone of crack and;
- almost unobservable at the blade tip, where forced response remains to be fundamental.

The influences of the phase lag of the combined excitation forces and bladed disk structural mistuning were studied within the framework of the bladed disk dynamic model. A certain level of mistuning was found to be critical for the cracked blade detection. The cracked blade non-linear behaviour taken into account decreases opportunity for detection of a cracked blade. It is caused by a shift of the cracked blade resonance peak closer to the resonance of the uncracked state. Furthermore, presence of mistuning was found to make almost invisible a cracked blade presence under absence of its frequency localization. In this case the linear model can be used for simulation of a crack presence.

The bladed disk forced response prediction using zig-zag diagram was performed. Its results highlight the diagram applicability for structures with disrupted symmetry and moderately low level of mistuning.

Chapter 4

Tip-timing method application for cracked blade detection

It is well known that the common failure mode for aircraft gas-turbine engines is the high-cycle fatigue of the turbine and compressor blades. It is caused by dynamic loading resulting in resonance blade vibration within operating range of rotor frequency. Majority of engine shut-downs are caused by blade failures due to resonance vibration or flutter.

Therefore, it is very urgent for aviation engine health monitoring to have reliable information about blade vibration state. This information can be acquired through the measurement of blade dynamic performances. The conventional practice of the vibration measurement consists in utilization of strain gauges mounted on the blade surface [31, 60]. The testing signal is received using a wireless telemeter system [89]. By this approach the responses of the selected blades can be captured continuously. However, such system requires a costly installation and must withstand the centrifugal forces and high temperatures. It provides only few data points simultaneously. Also for working wheel vibration measurements the holographic interferometry can be used. The measurements are based on the feature that light reflected by rotating structure leads to wave length alternation.

Nowadays, researches in the field of possibility to use non-invasive methods have gained wide spread. Some of them are based on measurement of blade tip deflections using blade tip arriving time when blade tip passes the probe(s). These probes are stationary installed on engine casing. Such technique is known as blade tip-timing method (BTTM) [5, 22, 107, 111]. Without vibration blade tip arriving time depends on rotor rotation speed only. But, if blade vibrates, it will also depend on vibration amplitude. Tip-timing method can be used to create an on-line system of blade dynamic performances definition. This system should be able to solve the following tasks:

- initial data measurement (time of the blade tip passing through the probe) using single probe or multi- probes measurements;

- calculation of characteristic parameters (vibration amplitude, blade tip deflection) on the base of the measured data;
- processing of characteristic parameters in order to describe a chosen blade dynamic behaviour.

In tip-timing analysis we should assemble the nature of blade responses into two groups: synchronous and asynchronous vibrations [22].

Asynchronous vibrations mainly occur because of aerodynamic instabilities. Thereby, both the e frequency and the phase of response can be arbitrary. Flutter instabilities, rotating stall or acoustic resonance also lead to such type of vibration. In this case, the main goal of the tip-timing measurements is to determine blade tip amplitude and resonance frequency. Probes are repartitioned regularly ensuring regularity of signal sampling.

Synchronous (or integral order) vibrations are excited by multiples of the rotor rotation speed. They are mainly caused by mechanical (number of obstacles before working wheel) and aerodynamic (irregular pressure distribution in air flow) effects. At given speed, the phase of the response remains fixed relatively to a stationary probe. The case of synchronous vibrations will be considered through this chapter.

It is essential to pay attention to the hardware of blade tip-timing system where the main place is taken by probes. They are subjected to some requirements: operational temperatures range, high definition accuracy, possibility to avoid engine casing preparation, withstandability to different contaminations, etc. At the present time, the following probe types are used: eddy-current probes, capacitance probes and optical probes. Short analysis of the probes performances is presented in Table 4.1

Table 4.1

Sensor type	Advantage/disadvantage
Eddy current [26-27]	**Advantage:** Simple structure, light weight, durable, unaffected by gas stream properties (contamination, water vapour, moisture etc.) **Disadvantage:** Measuring signals depend on material properties of the blade
Capacitive [88, 110]	**Advantage:** Simple structure **Disadvantage:** Durability and changing dielectric properties of the gas stream can cause problems, needs high voltage power supply
Optical [95, 109]	**Advantage:** High precision, direct measurement of the position **Disadvantage:** Cooling requirements and associated added weight; installation complexity and susceptibility to optical contamination

It should be mentioned the problem, which appears during tip-timing measurements. It is known as under-sampling of the measured data. It comes from the fact that frequency of sampling is always less then frequency of the first natural mode of the blade. The problem can be avoided by applying an interpolation procedure of the under-sampled signals [92] for proper reconstitution of the blade vibration signal.

4.1 Blade amplitude reconstruction from multi-probe measurements data

Blade tip-timing method can be used for both single blade and for multi-blades measurements. Firstly, the approaches for one blade measurement simulation were developed [107].

Let's consider Fig. 4.1b. There is the blade rotating at speed Ω and shown for two positions in time. It is further assumed that the origin is chosen such that the blade is at angular position ε at time $t = 0$. Time required for the blade without vibration to pass through the probe in k rotations is equated:

$$t_{uv} = \frac{\varepsilon + \phi}{\Omega} + \frac{2\pi k}{\Omega}, \tag{4.1}$$

where Ω is the frequency of rotor rotation.

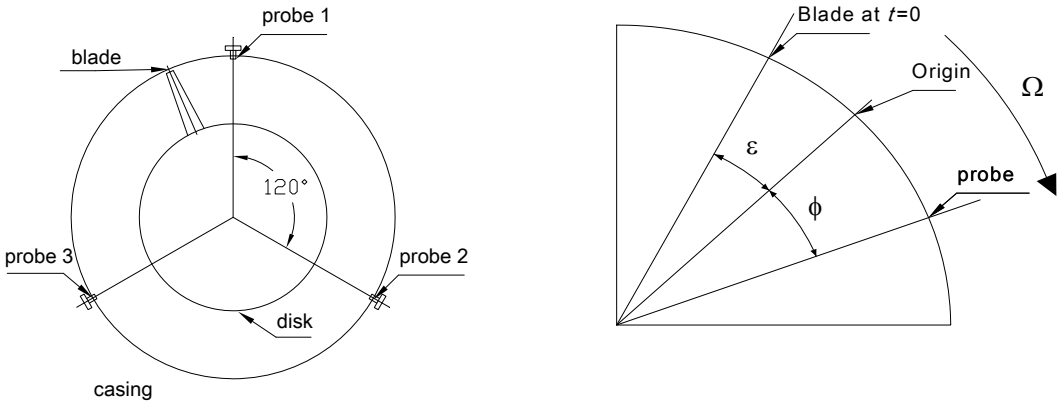

(a) (b)

Fig. 4.1. Blade tip-timing method presentation:

(a) blade behaviour as the subject to BTTM procedure, (b) blade positioning

It will be accepted during consequent simulations that "Origin" coincides with angular position of the first probe.

The blade response is assumed to be synchronous and of *EO*-th engine order. Forced excitation for the blade at the arbitrary angular position could be expressed as follows:

$$F = F_a \sin(\omega t + EO\varepsilon) \tag{4.2}$$

To measure the blade synchronous resonance vibration it is enough to have one probe installed in the circumferential location ϕ. Assuming that the blade response amplitude-phase relationship can be approximated to that of a single degree of freedom system, its tip displacement on *k*-th rotation can be expressed as:

$$x(t_k) = A(\omega)\sin(\omega t_k + EO\varepsilon + \psi(\omega)) \tag{4.3}$$

where $A(\omega)$ and $\psi(\omega)$ are the amplitude and phase of the complex frequency response, *EO* is the engine order, $\omega = EO\Omega$ is the excitation frequency.

During rotation the blade passes the following angular distances:

- to probe – $c = \varepsilon + \phi + 2\pi k$;
- due to rotation – $d_r = \Omega t$;
- due to vibration – $d_v = \left[\frac{A(\omega)\sin(\omega t + EO\varepsilon + \psi(\omega))}{R}\right]$.

Accepting $c = d_r + d_v$, the governing equation of blade tip-timing method will be derived to calculate actual arriving time [38]:

$$\Omega t_k - (2\pi k + \varepsilon + \phi) + \left[\frac{A(\omega)\sin(\omega t_k + EO\varepsilon + \psi(\omega))}{R}\right] = 0\,. \tag{4.4}$$

Equation (4.4) is solved by a method of non-linear equation solution (Newton's method) in order to obtain arriving time of each blade tip at each probe.

Let's consider a rotor with *N* blades and *n* installed probes. The location of probe is referenced by angular position ϕ on the engine casing. Angular position of the first probe is set to 0º. From this reference the angular positions of the remained probes are calculated.

Rotor speed is assumed constant in each measurement point. But in reality such supposition is not longer valid. Rotor speed changes during one rotation resulting in a change of excitation frequency. In the case of high rate of rotor acceleration, the error in amplitude calculation will not be negligible. It means that a blade will pass through the probes at different frequencies of excitation. It can be avoided by decreasing rotor acceleration or approximation of the rotor acceleration curve by step-function. I.e., during each measurement the rotor speed should be maintained constant, especially in the resonance area. Such conditions can be performed during engine maintenance procedures aimed on determination of bladed disk vibration performances and possible damages detection.

In our case, the origin coincides with first probe and all measurements are performed supposing the fact that first impulse belongs to the first blade. It results in the offset angle ε to be calculated as:

$$\varepsilon_i = \frac{2\pi}{N}(j-1), \tag{4.5}$$

where *j*=1…*N*.

The linear distance passed by the tip of *j*-th blade without vibration is equal to $R\Omega t^{i}_{k,p}$, which is measured for *p*-th probe at *k*-th rotation of the working wheel. Without vibration this distance will be constant. But, if the blade is subjected to vibration, it will be possible to capture the arriving time difference and to reconstruct blade tip amplitude. The numerical expression of blade response captured by *p*-th probe using arriving time data can be written in the following manner:

$$a^{j}_{k,p} = R\Omega\Delta t^{j}_{k,p},\ j = 1...N,\ p = 1...n \tag{4.6}$$

where $\Delta t^{j}_{k,p} = (t^{j}_{k,v} - t^{j}_{k,uv})_{p}$ is arriving time difference between vibrating blade and blade without vibration, which is synchronized to the impulse of the first blade without vibration captured at the origin.

Derivation of formula (4.6) can be illustrated using Fig. 4.2. There are curve of time-history of a blade tip and tracking lines of three probes presented. Since probes are fixed and we are in rotating reference frame, probes tracking line will have direction, which is opposite to the rotor rotation.

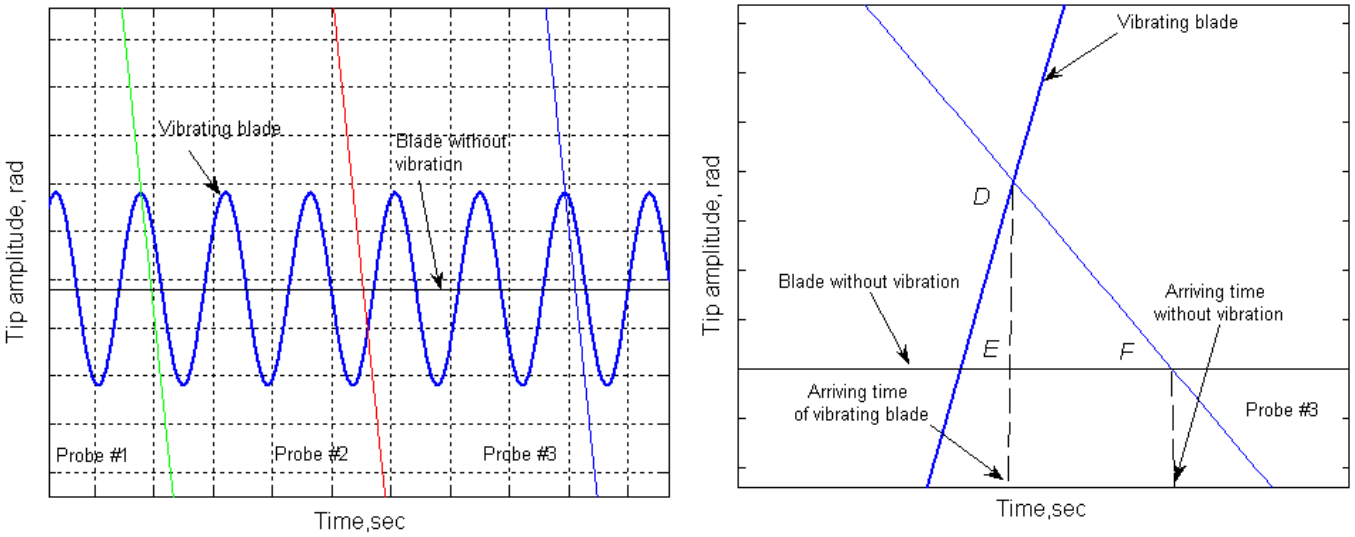

(a) (b)

Fig. 4.2. Tip-timing measurements presentation:

(a) amplitude of blade tip measurement by three probes, (b) zoom around first probe measurement

Amplitude of blade tip vibration is presented in Fig. 4.2 by section *DE*. Section *EF* is arriving time difference $\Delta t^{i}_{k,p}$ measured by a probe. From this geometrical presentation, we can easily obtain presented above equation (4.6).

Also it is necessary to accentuate that in the case of synchronous vibrations the reconstruction of the blade tip amplitude depends on engine order and number of probes used in simulation [111]. For example, using three probes, all speed synchronous vibrations can be measured, except for the engine orders 3, 6, 9 etc. These will remain invisible, since in these cases, the blades pass all probes in the same state of vibration (Fig. 4.3). When five probes are used, the engine orders 5, 10, 15, etc are omitted.

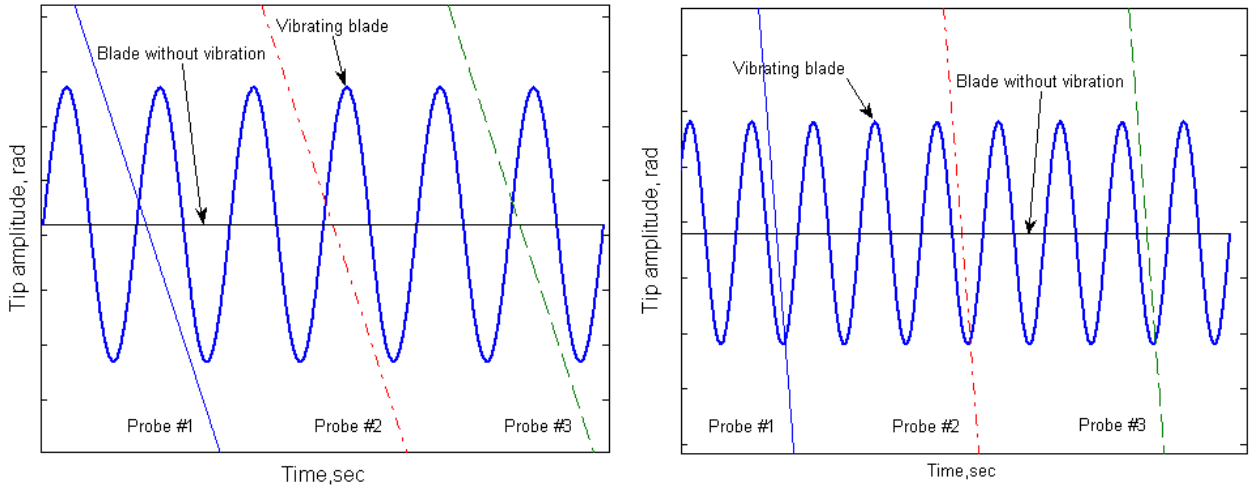

(a) (b)

Fig. 4.3. Disability of uniformly spaced probes to capture amplitude of blade tip at *EO*, which is multiple of probes number: (a) *EO*=6, (b) *EO*=9

Using expression (4.6), it is possible to calculate maximum tip amplitude of each blade [53, 55]. As it was mentioned previously, during each rotation we have *n* data points of blade tip response (*n* - number of probes). It was supposed that tip response is sinusoidal and it can be represented in the point *D* (Fig. 4.2) as:

$$a_p^j = A_k^j \sin(\omega_k t_{k,v} + \psi_k),\ j = 1...N,\ p = 1...n \tag{4.7}$$

where A_k^j is maximum amplitude of *j*-th blade tip in *k*-th measurement point and ψ_k is the phase.

In the case of three probes, equation (4.7) leads to the system of three equations with two unknowns A and ψ, which corresponds to blade tip amplitude and phase. For a blade at particular frequency (measurement point) the system to solve will be:

$$\begin{cases} A\sin(\omega t_{1v} + \psi) = R\Omega(t_{1v} - t_{1uv}) \\ A\sin(\omega t_{2v} + \psi) = R\Omega(t_{2v} - t_{2uv}) \\ A\sin(\omega t_{3v} + \psi) = R\Omega(t_{3v} - t_{3uv}) \end{cases} \tag{4.8}$$

System (4.8) can be rewritten in the following way in order to apply a solution method of system of linear equations:

$$\begin{cases} b\cos(\omega t_{1v}) + c\sin(\omega t_{1v}) = R\Omega(t_{1v} - t_{1uv}) \\ b\cos(\omega t_{2v}) + c\sin(\omega t_{2v}) = R\Omega(t_{2v} - t_{2uv}) \\ b\cos(\omega t_{3v}) + c\sin(\omega t_{3v}) = R\Omega(t_{3v} - t_{3uv}) \end{cases} \tag{4.9}$$

$$A = \sqrt{b^2 + c^2},\ \psi = \arctan(c/b)$$

Structurally process of the blade tip amplitude reconstruction consists of:

- blade tip arriving time generation with and without vibration using equation (4.4);
- synchronizing of arriving time to the arriving time of first blade without vibration captured by first probe;

– calculation of blade tip amplitude captured by a probe using formula (4.6);
– reconstruction of the maximum blade tip amplitude using system of equations (4.9).

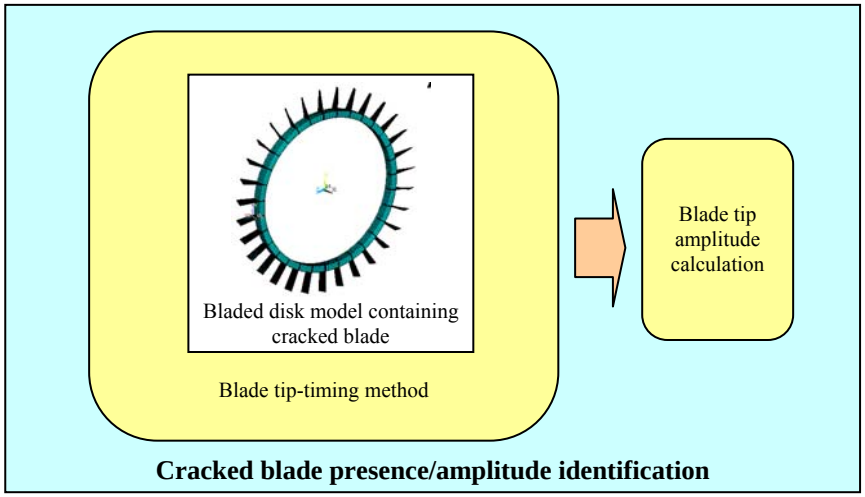

Fig. 4.4. Simulation of blade tip-timing procedure

During the simulation process it is possible to make k measurements of each blade vibration state, which is equal to the rotor rotations number accomplished in the time of rotor acceleration:

$$k = \Omega_1 Tr + \left(\frac{\Omega_2 - \Omega_1}{Tr}\right)\frac{Tr^2}{2} = \Omega_1 Tr + (\Omega_2 - \Omega_1)\frac{Tr}{2}, \quad (4.10)$$

where Ω_2, Ω_1 are the rotor rotation frequencies at the end and beginning of the rotor acceleration time, Tr is the rotor acceleration time. Rotation speed is supposed to be changed linearly during rotor acceleration.

4.2 Blade tip-timing method application to the bladed disk model

Simulations of the tip-timing method applications will be performed using the same crack locations cases as it was considered in the chapter 3 (Fig. 3.3). Each crack location case corresponds to the bladed disk model containing one cracked blade and subjected to the loading mode shown in Fig. 3.32.

On Fig. 4.5 the general structure of research is presented. At the absence of experimental validation only simulation of the process of the cracked blade identification was performed. The dynamic model of the bladed disk was developed in the previous chapter with theoretical background presented in chapters 1 and 2. The last stage consists in application of the tip-timing method, which will be considered in this chapter.

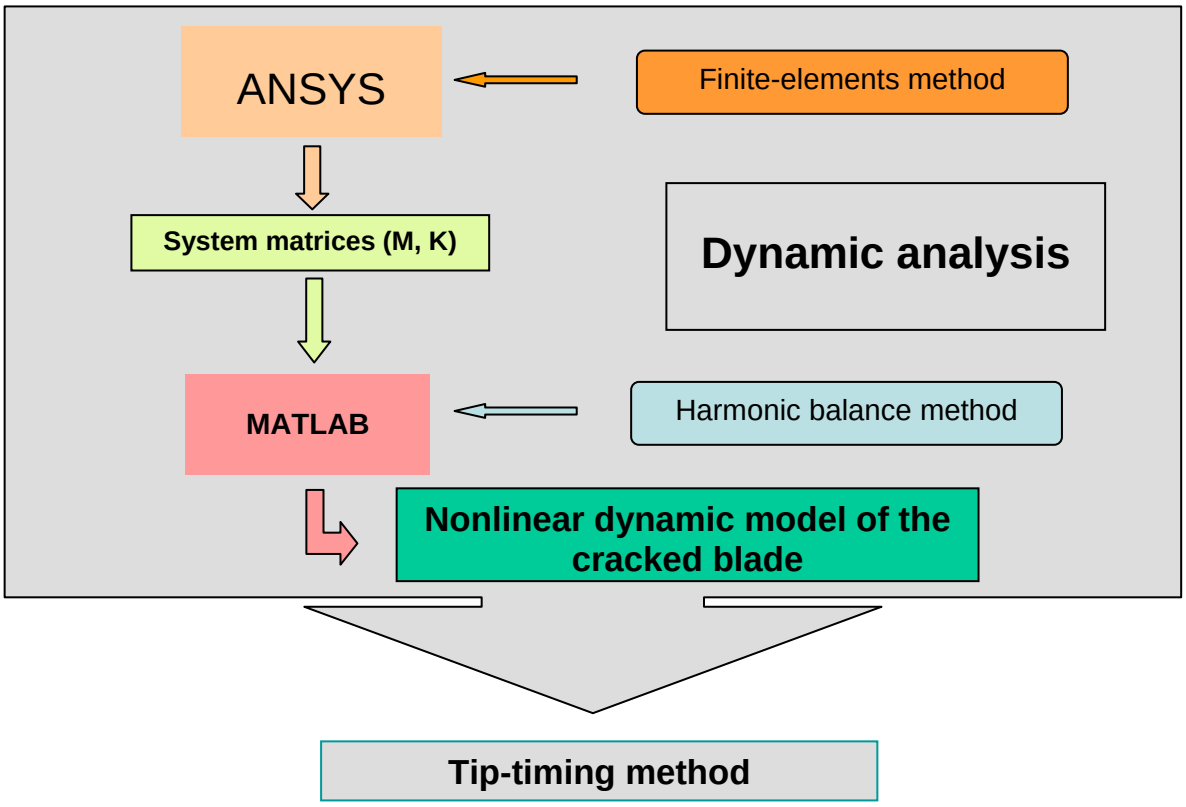

Fig. 4.5. The research structural scheme

4.2.1 Simulation of tip-timing measurements

The initial data for blade tip-timing method simulation are:

- engine acceleration time – Tr=2 sec.;
- rotor frequency range – Ω=20…25 Hz;
- engine order of excitation – EO=23;
- excitation force amplitude – F_a=0.3N;
- rotor radius – R=0.38 m.;
- number of measurements – k=21;
- number of probes – n=3.

For each simulation case the comparison of the frequency response obtained using arriving time data and harmonic balance method will be performed. All-blades response in particular measurement point (excitation frequency) will be presented in order to test the ability to distinguish cracked blade. It will show us the possibility to identify cracked blade by tip amplitude difference not only near the resonance peak. An attention should be paid to the engine acceleration time, which is urgent to

properly follow frequency response curve of the investigated object. Some numerical tests were performed to confirm correctness of the chosen value of rotor acceleration time.

Measurement points of blade tip-timing method simulation

Table 4.2

Measurement number	Rotor frequency Ω, Hz	Excitation frequency ω, rad/sec
1	20.0	2889
2*	20.2	2924
3	20.5	2961
4	20.8	2998
5	21.0	3033
6	21.2	3069
7*	21.5	3105
8	21.8	3142
9*	22.0	3178
10	22.3	3214
11*	22.5	3250
12	22.8	3287
13*	22.0	3322
14	23.2	3358
15	23.5	3394
16*	23.8	3430
17	24.0	3467
18	24.3	3503
19	24.5	3539
20	24.8	3575
21	25.0	3611

*) measurement points used for graphical presentation

For presentation on graphs the measurement points 2, 7, 9, 11, 13, 16 were chosen to describe the bladed disk frequency response: next to cracked blade localized response, all-blades principal response and at the frequencies distant from the resonance peaks (Table 4.2). By formula (4.9) the maximum number of measurements k will be equal to 45.

It should be noted that all following simulation presented in this subchapter are performed having supposed mistuning absence and the linear formulation of cracked blade behaviour. The linear formulation was used due to necessity of only blade tip-timing method simulation in the subchapter. In the next sections, where mistuning influence on cracked blade detectability will be examined, the non-linear model formulation will be applied for simulations performing.

Each plot representing blade tip amplitudes in particular measurement (excitation frequency) point contains three curves: “cracked by FRF” – bladed disk response calculated by frequency response function (linear formulation of the crack presence), “cracked by TTM data” – bladed disk response calculated using blade tip arriving time data and “uncracked by FRF” – bladed disk response without any cracked blade calculated by frequency response function. The bladed disk model used in this subchapter is supposed to have no mistuning (except cracked blade presence, which in linear case can be considered as mistuned one).

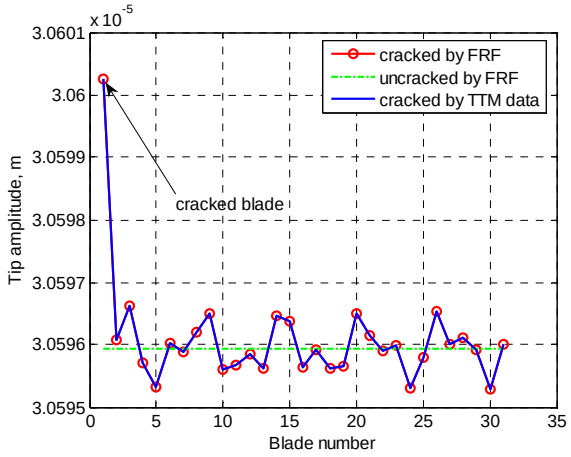

a: *point* #2 (ω=2924 rad/sec)

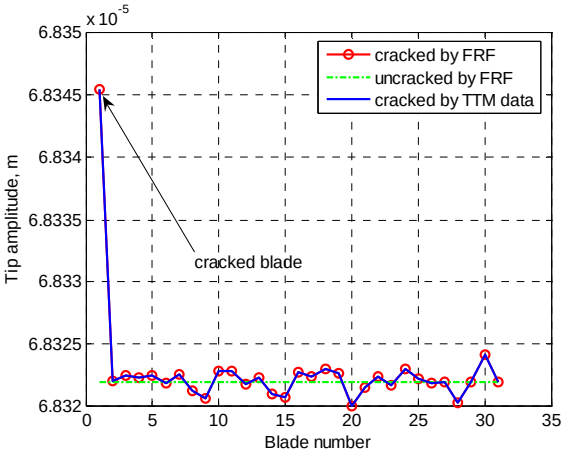

b: *point* #7 (ω=3105 rad/sec)

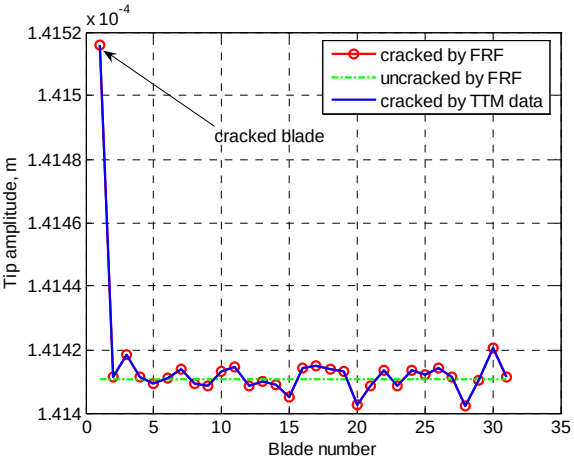

c: *point* #9 (ω=3178 rad/sec)

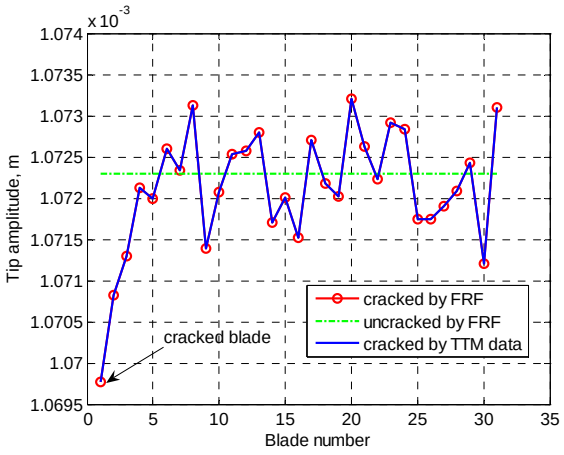

d: *point* #11 (ω=3250 rad/sec)

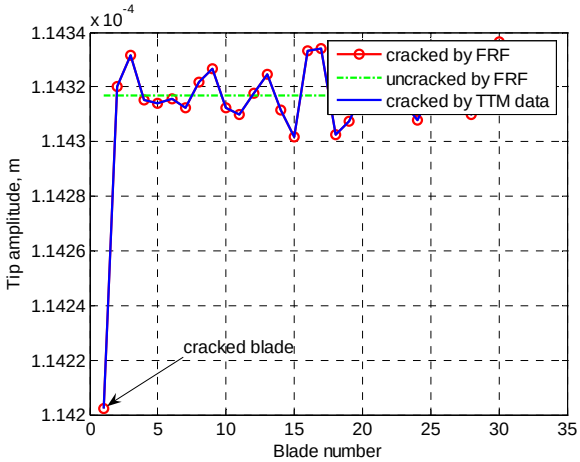

e: *point* #13 (ω=3332 rad/sec)

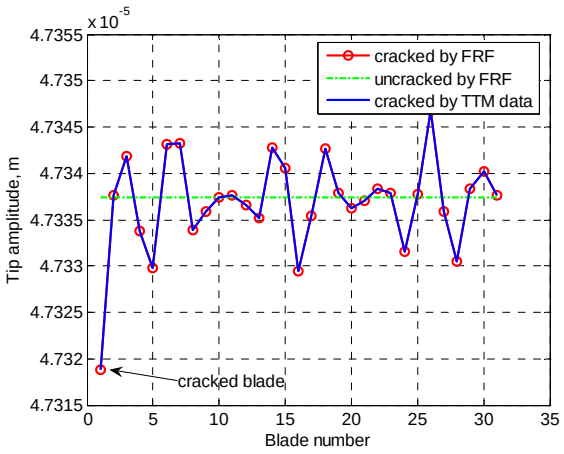

f: *point* #16 (ω=3430 rad/sec)

Fig. 4.6. All-blades response in the measurement point: trailing edge crack, *a*=2 mm.

Results of blade tip-timing method simulation show possibility to distinguish the blade with crack of 2 mm length and located on the trailing edge (Fig. 4.6). The cracked blade is easily detected in each measurement point. It should be noted that the model does not contain mistuning and this fact is favourable for cracked blade identification.

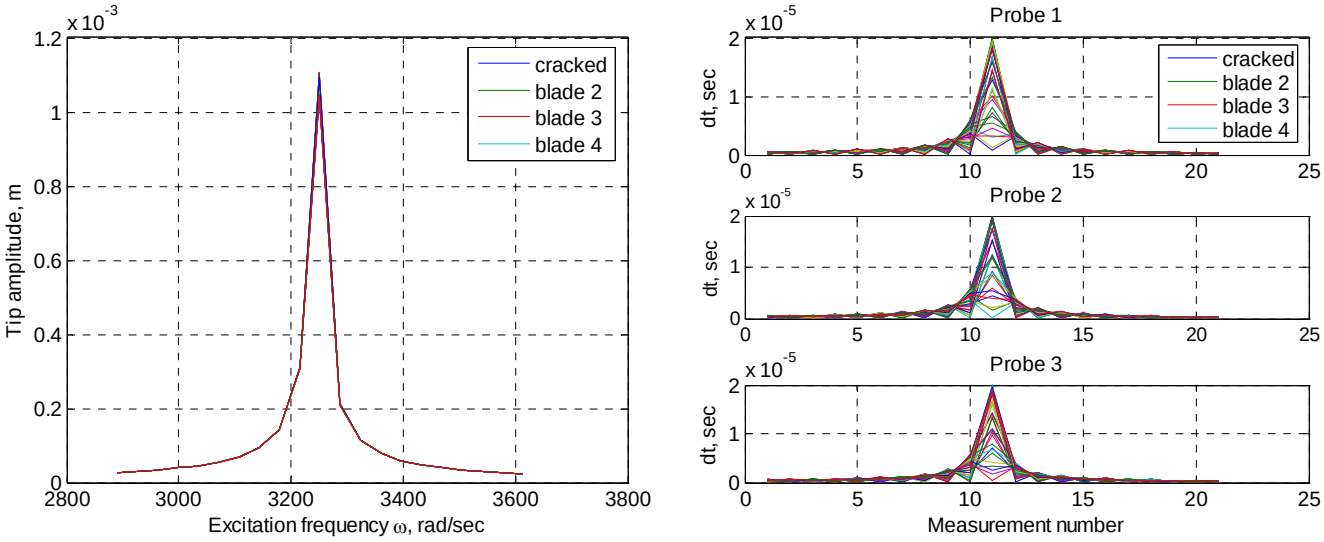

(a) (b)

Fig. 4.7. Trailing edge crack (a=2 mm.): (a) frequency response of all-blades by tip-timing method data, (b) arriving time differences of all-blades captured by probes

Frequency response of the bladed disk (Fig. 4.7a) does not have cracked blade frequency localization. In this case bladed disk frequency response can be used only for estimation of blade amplitudes levels and resonance frequencies calculation. Cracked blade can be separated from it, if sufficiently big number of measurements was performed during rotor acceleration. On Fig. 4.7b differences between arriving time of vibrating blade and blade without vibration are presented, which are used for calculation of blade tips amplitudes by expression (4.6). Their functional dependence on excitation frequency (rotor frequency) has the same form as the bladed disk frequency response. Consequently, it can be directly used for resonance frequencies determination.

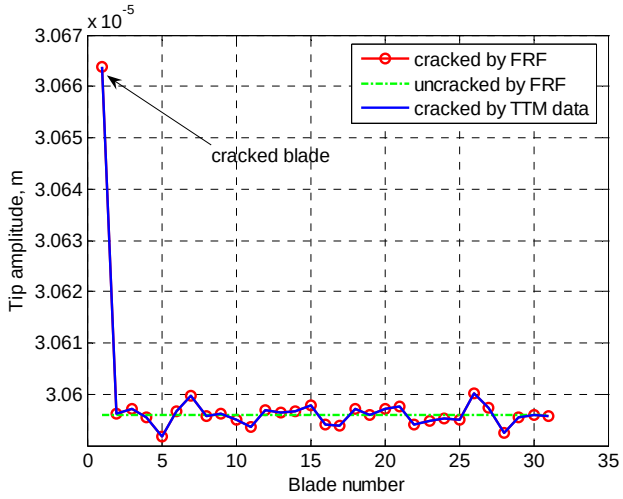

a: *point* #2 (ω=2924 rad/sec)

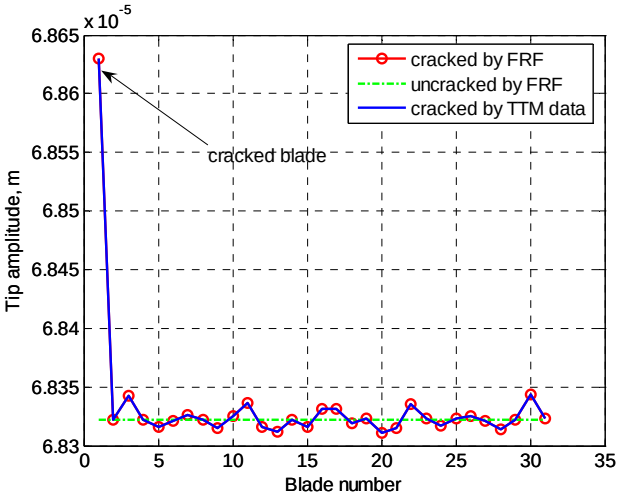

b: *point* #7 (ω=3105 rad/sec)

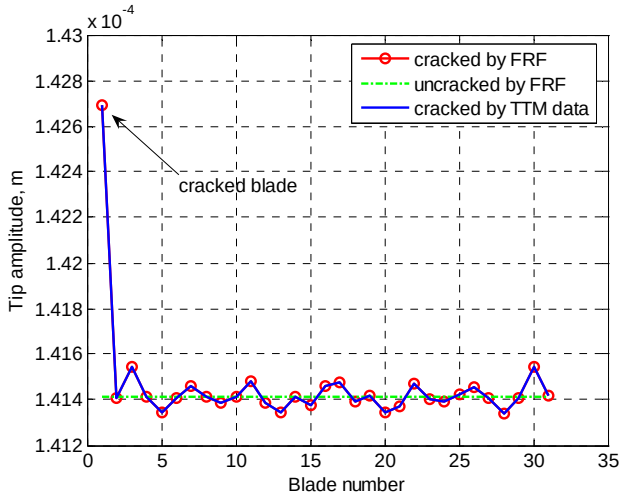

c: *point* #9 (ω=3178 rad/sec)

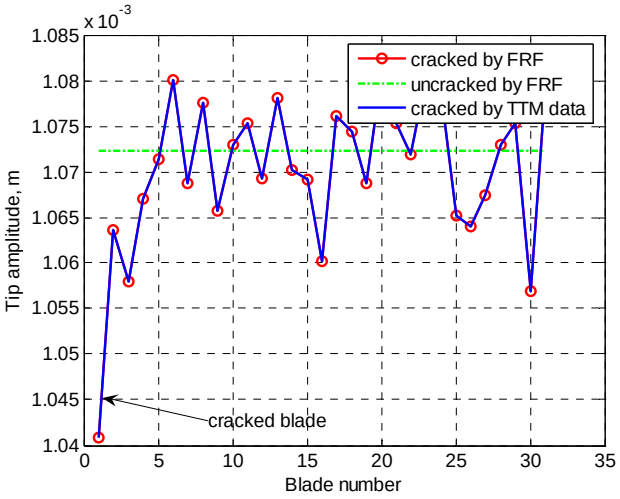

d: *point* #11 (ω=3250 rad/sec)

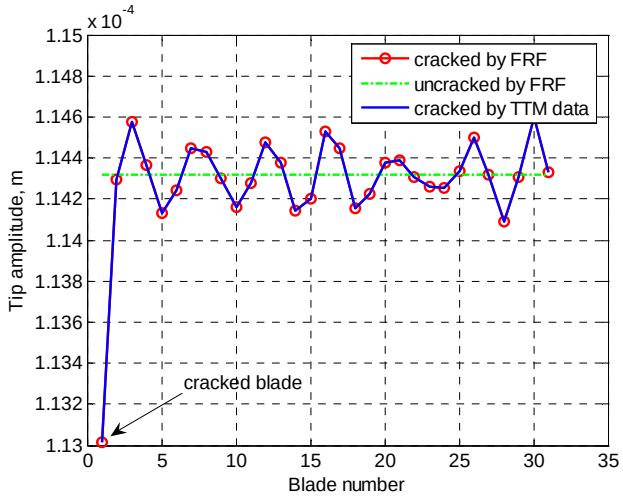

e: *point* #13 (ω=3332 rad/sec)

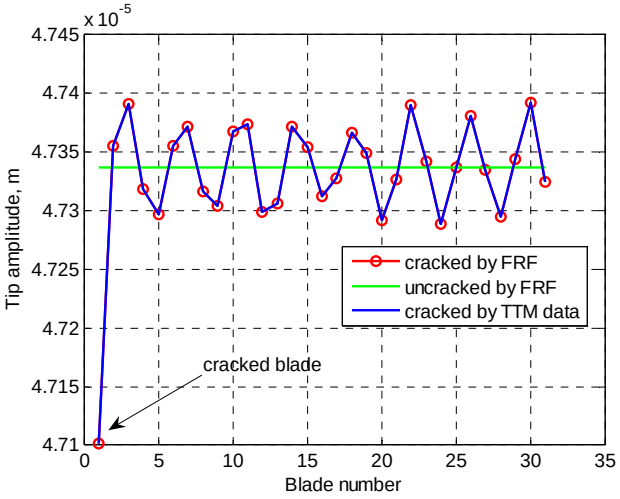

f: *point* #16 (ω=3430 rad/sec)

Fig. 4.8. All-blades response in the measurement point: trailing edge crack, *a*=4 mm.

Tip-timing method simulation results of trailing edge crack option with increased to 4 mm. crack length (Fig. 4.8) allow cracked blade identification using all-blades response at particular frequency. It is possible in all presented measurement points. At the same time, there are some difficulties of cracked blade identification in the point #11 (Fig. 4.8 d), which is located close to the all-blades principal resonance. It is caused by effect of excitation forces phase lag, when different blades resonate at different frequencies, which are very close to each other. This also leads to impossibility to distinguish cracked blade by the resonance frequency shift at the absence of cracked blade frequency localization. Additionally, the shortage of measurement points plays his role in reduction of cracked blade identification possibilities.

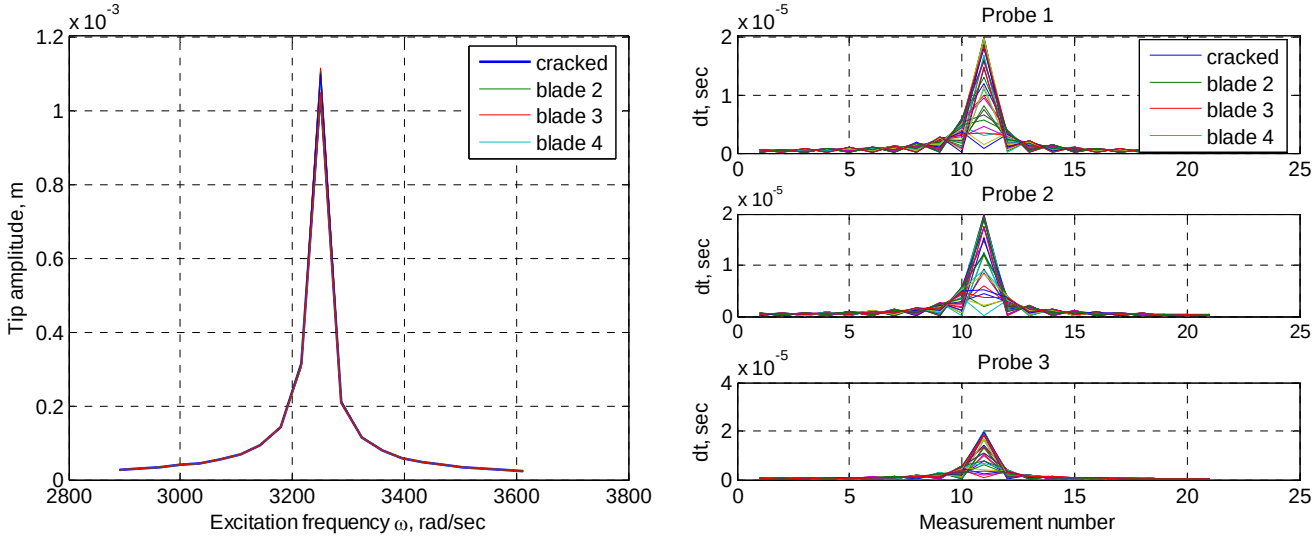

(a) (b)

Fig. 4.9. Trailing edge crack (a=4 mm.): (a) frequency response of all-blades by tip-timing method data, (b) arriving time differences of all-blades captured by probes

Frequency response of the bladed disk (Fig. 4.9a) also does not provide information required for cracked blade presence identification in the disk. It can be used for calculation of blade tip amplitudes and resonance frequencies determination. Resonance frequencies can be determined, as well, by differences of arriving time measured for each probe (Fig. 4.9b).

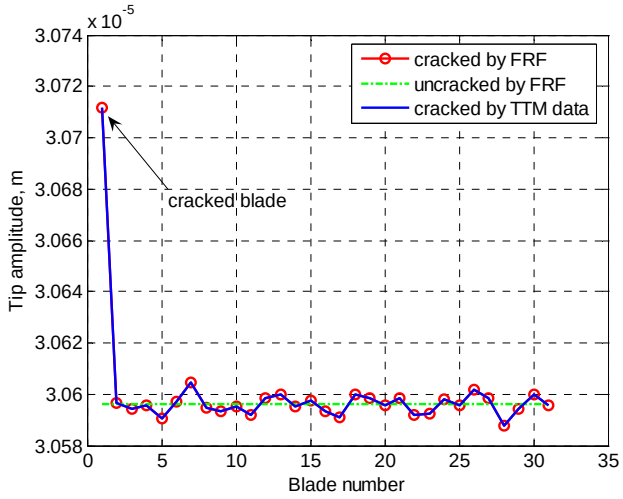

a: *point* #2 (ω=2924 rad/sec)

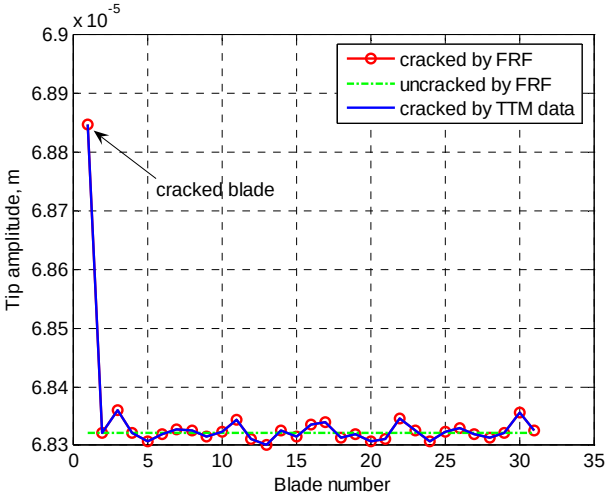

b: *point* #7 (ω=3105 rad/sec)

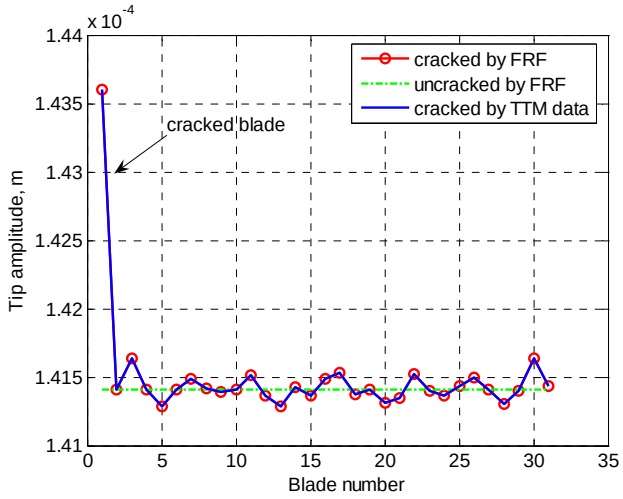

c: *point* #9 (ω=3178 rad/sec)

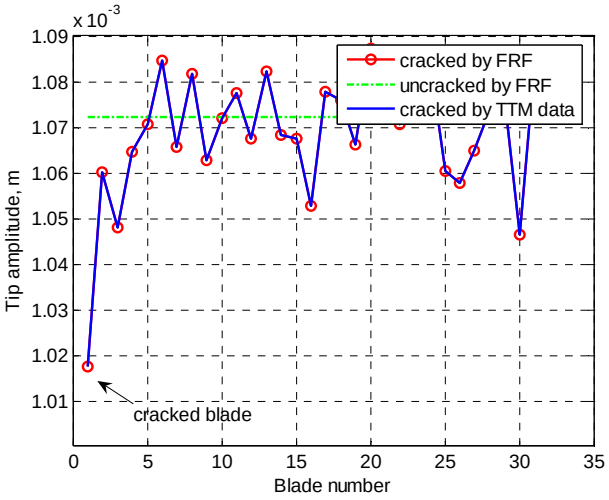

d: *point* #11 (ω=3250 rad/sec)

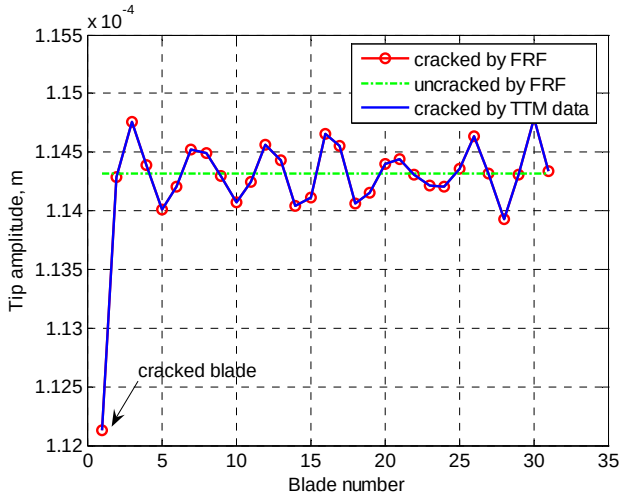

e: *point* #13 (ω=3332 rad/sec)

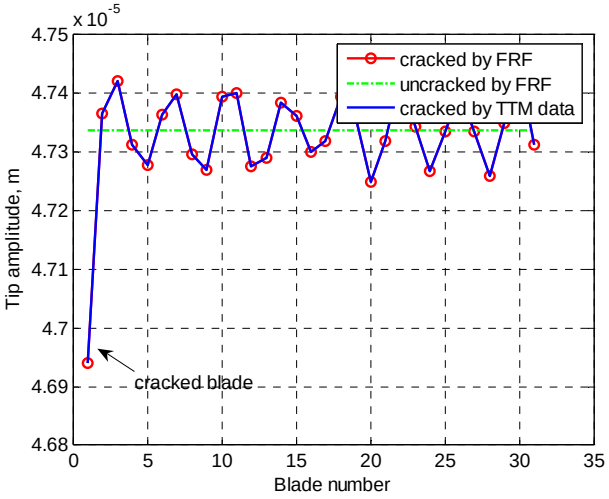

f: *point* #16 (ω=3430 rad/sec)

Fig. 4.10. All-blades response in the measurement point: leading edge crack, *a*=2 mm.

Crack located on the leading edge can give much more information for the cracked blade identification. Response of the blade tip becomes more distinguishable. It was well illustrated during the simulations of uncoupled cracked blade dynamic behaviour (Figs. 3.8, 3.10). Blade tip-timing method results at different measurement points (Fig. 4.10) are very similar to the 4 mm. trailing edge crack location option. Cracked blade identification is possible in all measurement (excitation frequency) points without any difficulties.

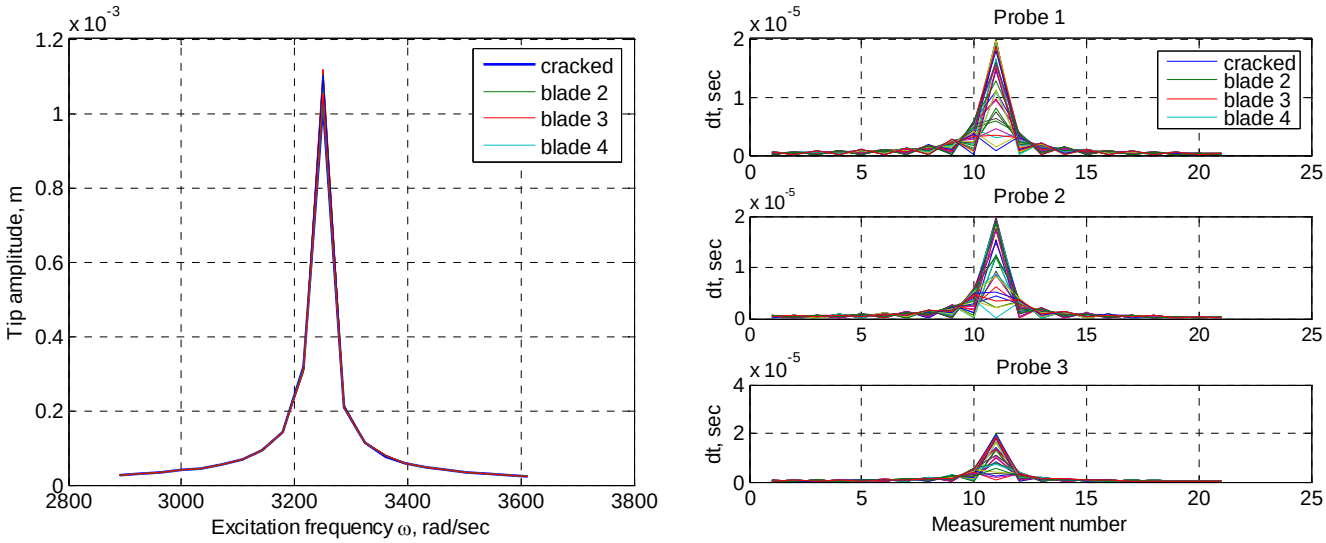

(a) (b)

Fig. 4.11 Leading edge crack (a=2 mm.): (a) frequency response of all-blades by tip-timing method data, (b) arriving time differences of all-blades captured by probes

Frequency response of the bladed disk in the case of leading edge crack is very interesting and informational. At certain crack length it is possible to reach cracked blade frequency localization occurrence. But in the case of 2 mm. crack length (Fig. 4.11a) this phenomenon is not reached. Anyway crack identification from the frequency response is achievable when sufficiently big number of measurements is performed. In this case it is possible to smoothly trace the frequency response curves of all blades.

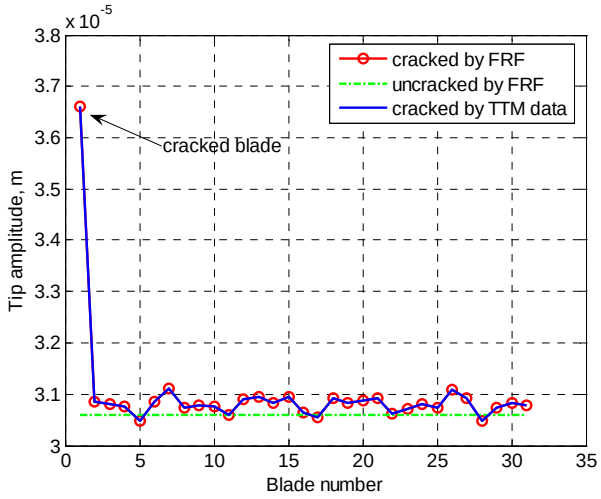

a: *point* #2 (ω=2924 rad/sec)

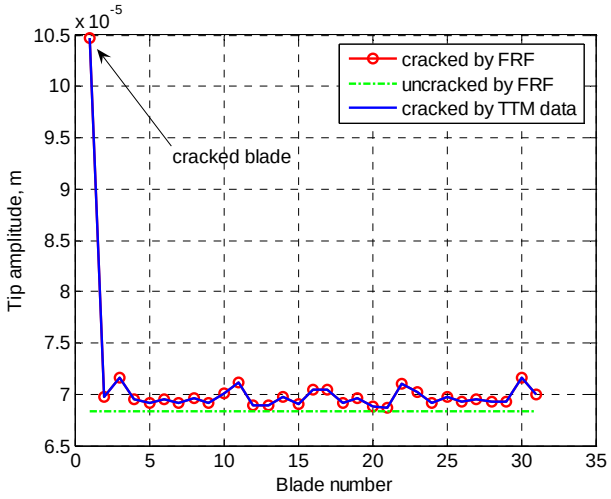

b: *point* #7 (ω=3105 rad/sec)

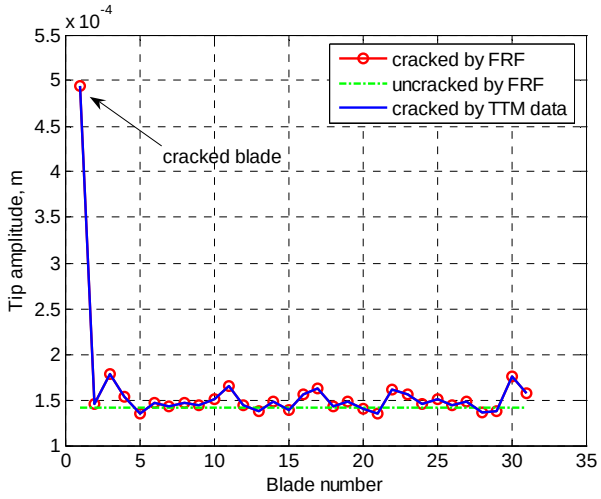

c: *point* #9 (ω=3178 rad/sec)

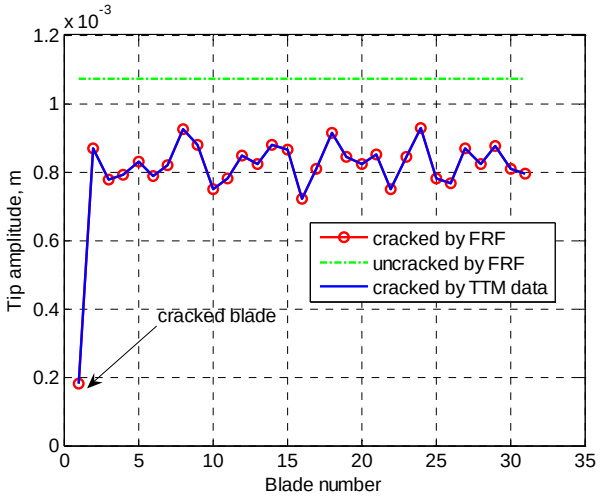

d: *point* #11 (ω=3250 rad/sec)

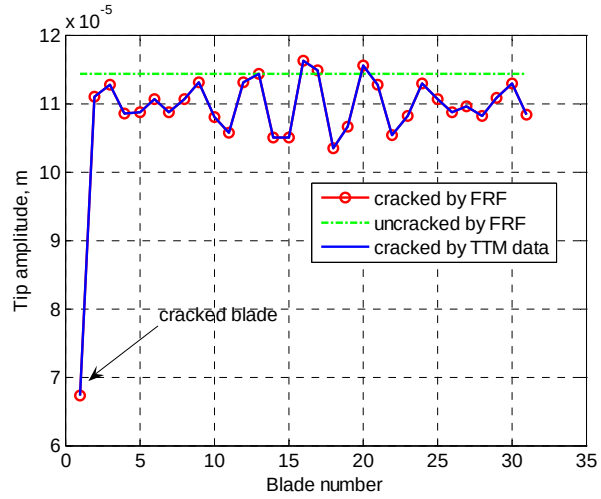

e: *point* #13 (ω=3332 rad/sec)

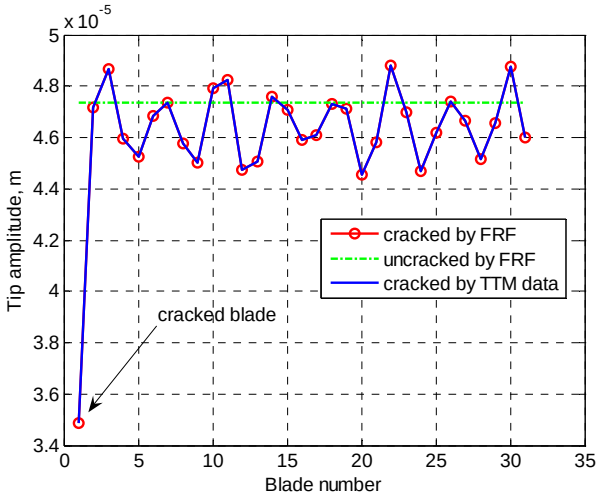

f: *point* #16 (ω=3430 rad/sec)

Fig. 4.12. All-blades response in the measurement point: leading edge crack, *a*=4 mm.

Leading edge crack of 4 mm. length, as it is known from dynamic analysis of the bladed disk model (subchapter 3.3, Fig. 3.35), produces cracked blade frequency localization. Owning to the bigger crack size and its effect on the blade stiffness we have higher tip amplitude of the cracked blade in comparison with previous simulations. In this case crack identification is possible in all presented measurement points without any difficulties (Fig. 4.12).

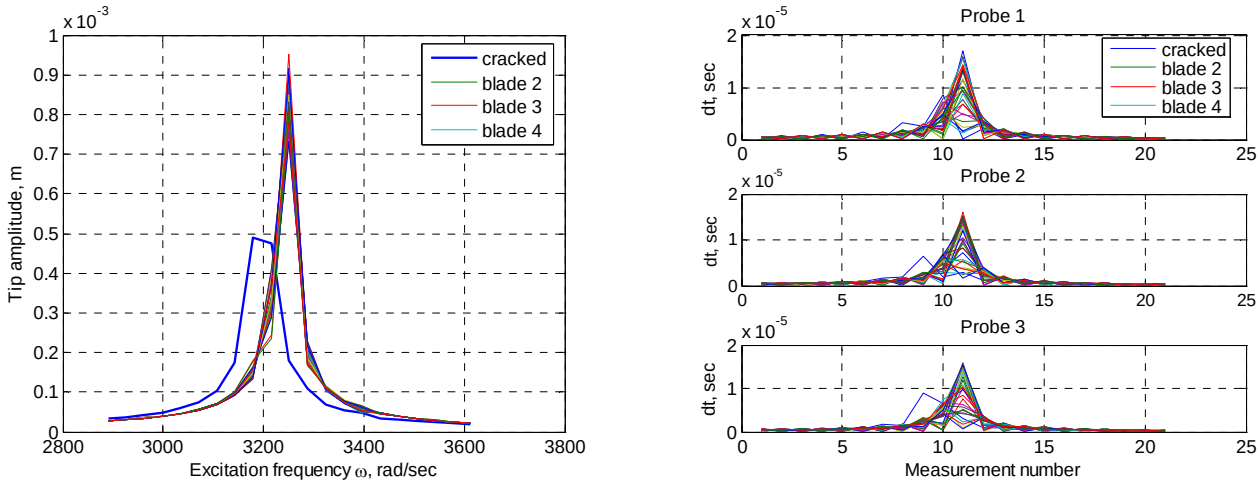

(a) (b)

Fig. 4.13. Leading edge crack (a=4 mm.): (a) frequency response of all-blades by tip-timing method data, (b) arriving time differences of all-blades captured by probes

Cracked blade frequency localization seen from the bladed disk frequency response (Fig. 4.13a) can be directly used as the diagnostic sign of the cracked blade presence in the disk. The same results of the cracked blade localization we can derive from Fig. 4.13b, where time differences captured by the probes are shown. Here achieving of the localization phenomenon is very important event in the view of mistuning presence in the real disk assemblies. Without mistuning presence cracked blade identification can be performed in all considered cases. Whereas, mistuning allows separating cracked blade response only in the case of cracked blade frequency localization.

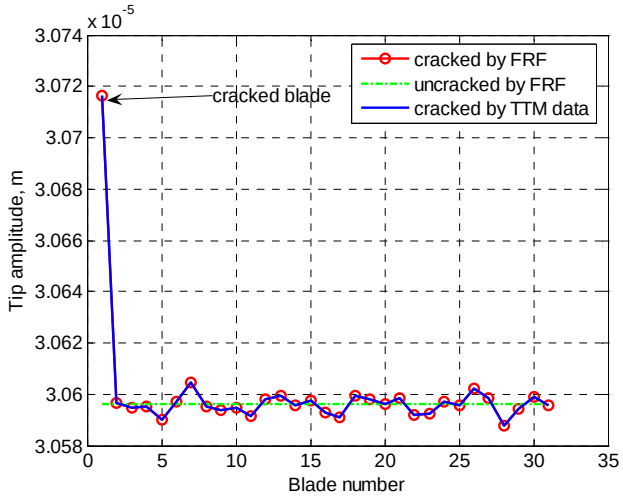

a: *point* #2 (ω=2924 rad/sec)

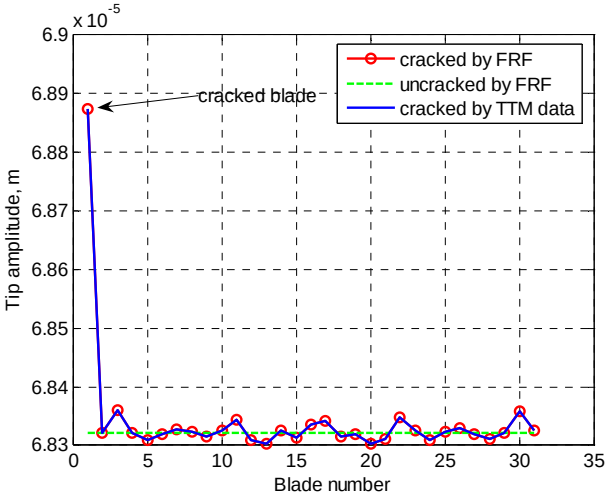

b: *point* #7 (ω=3105 rad/sec)

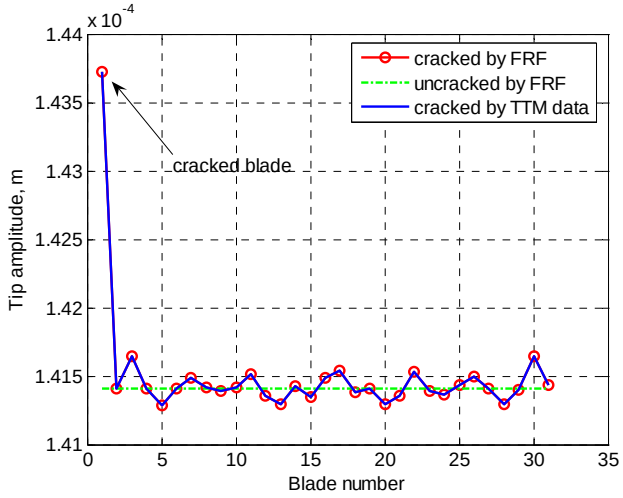

c: *point* #9 (ω=3178 rad/sec)

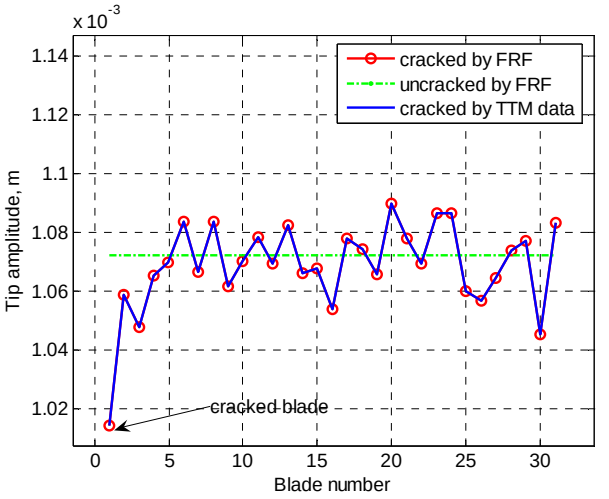

d: *point* #11 (ω=3250 rad/sec)

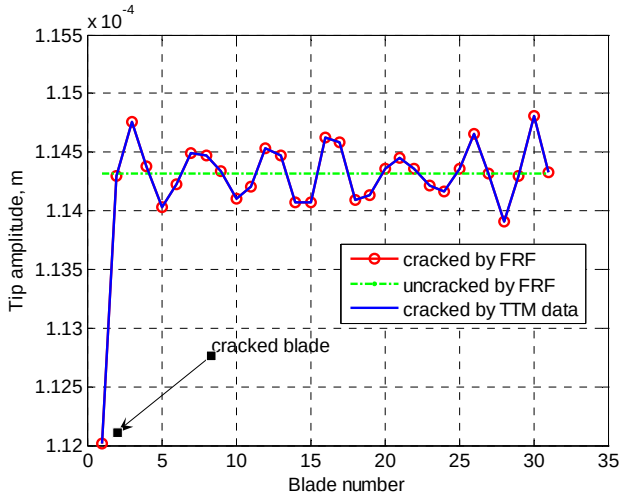

e: *point* #13 (ω=3332 rad/sec)

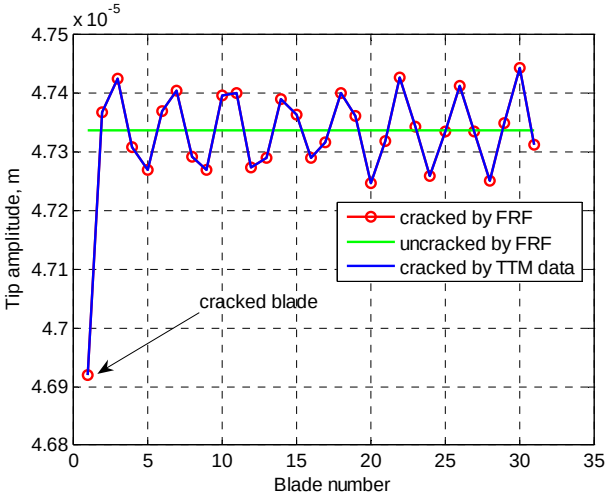

f: *point* #16 (ω=3430 rad/sec)

Fig. 4.14. All-blades response in the measurement point: symmetric cracks, *a*=2 mm.

Presence of the second symmetrically located crack of the same size essentially facilitates cracked blade identification. It is mostly owing to the influence of the leading edge crack partition. In the case of 2 mm. symmetrically located cracks we do not have occurrence of cracked blade frequency localization. At the same time the presentation of blade tip amplitudes in particular measurement point (Fig. 4.14) provides the possibility to identify cracked blade presence by its increased tip amplitude response.

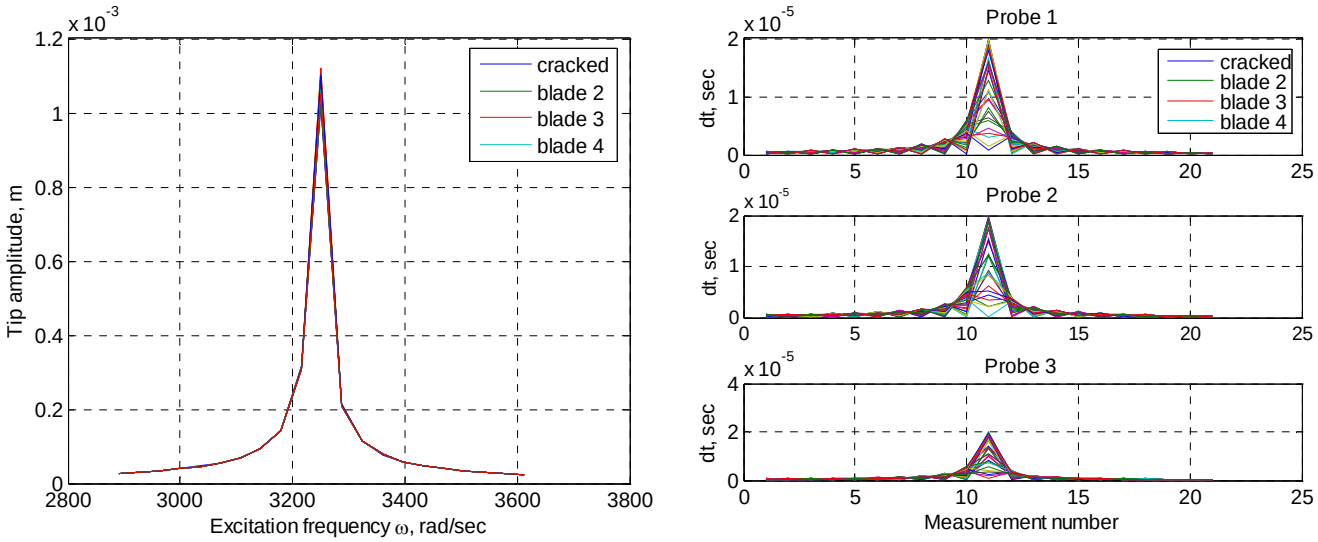

(a) (b)

Fig. 4.15. Frequency response function (symmetric cracks, *a*=2 mm.): (a) frequency response of all-blades by tip-timing method data, (b) arriving time differences of all-blades captured by probes

Both frequency response of the bladed disk (Fig. 4.15a) and arriving time differences (Fig. 4.15b) can be also used for cracked blade identification only at sufficiently big number of measurement points that allows distinguishing of the differences between resonance frequencies. It is also observed that tip amplitude of the cracked blade differs from the rest of blades at the resonance frequency.

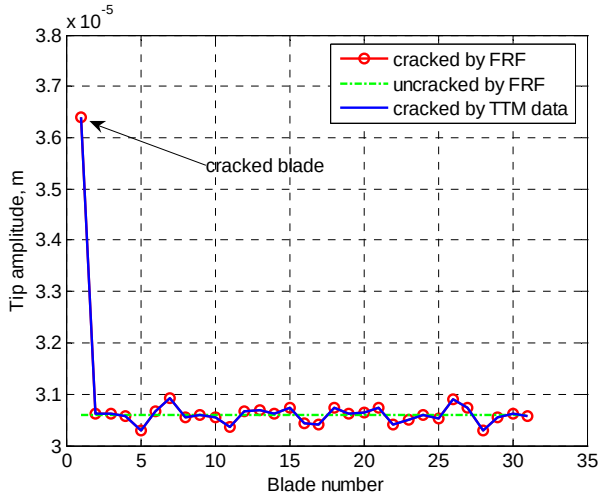

a: *point* #2 (ω=2924 rad/sec)

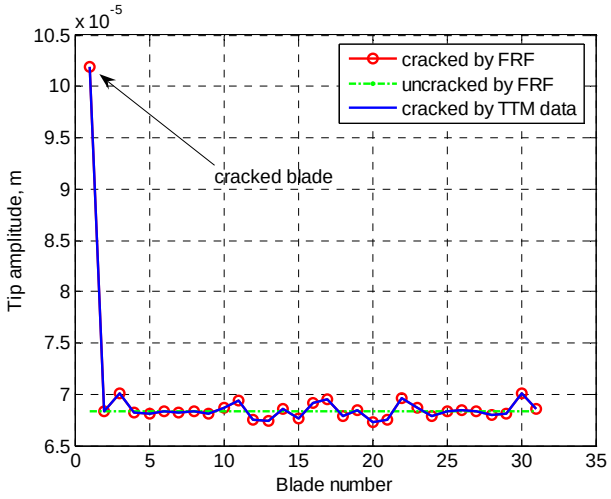

b: *point* #7 (ω=3105 rad/sec)

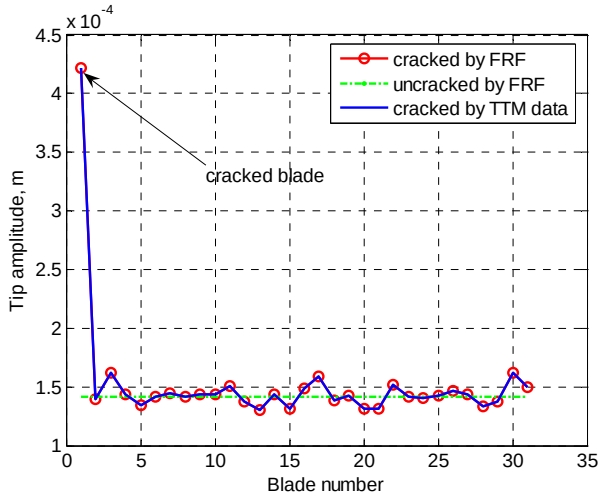

c: *point* #9 (ω=3178 rad/sec)

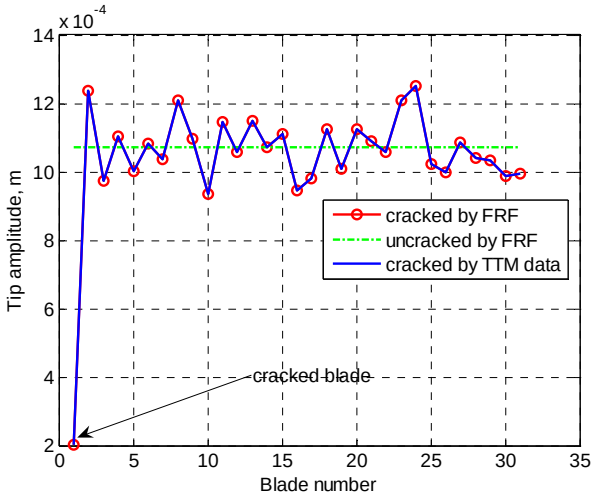

d: *point* #11 (ω=3250 rad/sec)

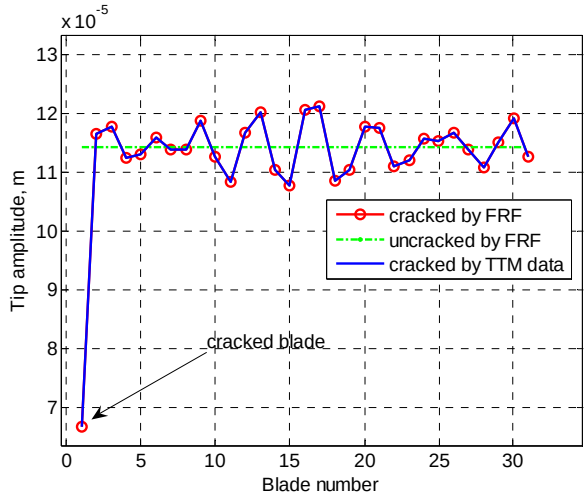

e: *point* #13 (ω=3332 rad/sec)

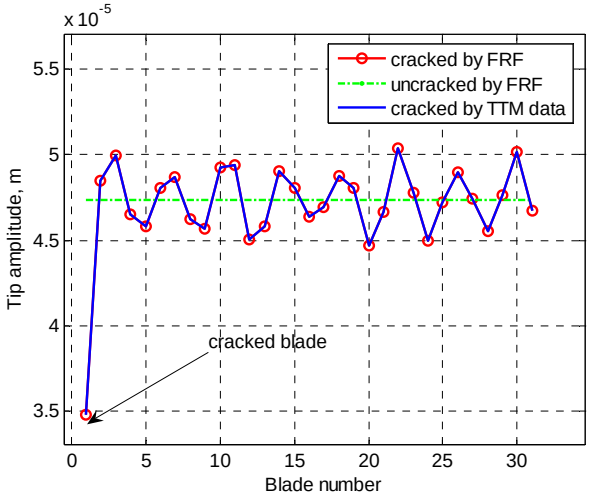

f: *point* #16 (ω=3430 rad/sec)

Fig. 4.16. All-blades response in the measurement point: symmetric cracks, *a*=4 mm.

Results of tip-timing method application in the case of 4 mm. symmetric cracks permit to distinguish cracked blade tip amplitude response among the rest of the blades in all presented measurement (frequency) points (Fig. 4.16).

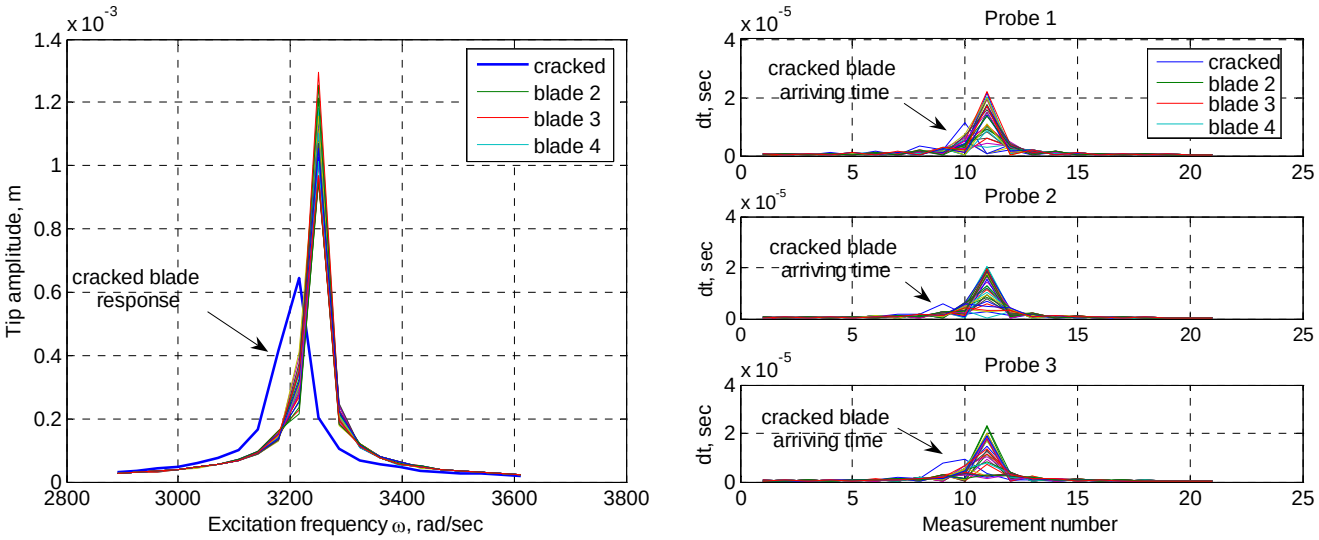

(a) (b)

Fig. 4.17. Frequency response function (symmetric cracks, *a*=4 mm.): (a) frequency response of all-blades by tip-timing method data, (b) arriving time differences of all-blades captured by probes

Frequency response of the cracked blade (Fig. 4.17a) is clearly distinguished among the all-blades frequency responses of the bladed disk model. It is due to cracked blade frequency localization and blade tip amplitudes difference.

General conclusion about results of blade tip-timing method simulation can be formulated in the following way. Looking on its results with different crack location options we can continue with said in chapter 3. Only cracked blade frequency localization can provide in almost all cases cracked blade detection. Frequency response of the bladed disk obtained on the base of the time data has not precise view due to shortage of measurement points. But it can be easily used for resonance frequencies calculation.

We can divide all our simulation cases on 2 main categories:

- with cracked blade frequency localization;
- without cracked blade frequency localization
  - crack size allows cracked blade response identification;
  - numerical errors makes cracked blade identification unattainable due to low blade tip amplitude in measurement points distant from the resonance peak.

Cracked blade identification for the second category seems to be impossible at further introduction of mistuning.

4.2.2 Comparison of frequency response reconstructed by tip-timing method data with harmonic balance method results

In order to validate measured data obtained from blade tip-timing method simulation the harmonic balance method results are used. For comparison process only cracked blade frequency response of the bladed disk model is taken.

Initial data for tip-timing method are the same as in previous subchapter with only one difference: simulations are accomplished for different numbers of measurement points k = 21 and k=45 (maximum possible number at the set rotor frequency range and rotor acceleration time). On each graph three curves are presented: "FRF by HBM" corresponds to cracked blade frequency response calculated by harmonic balance method, "FRF by TTM (k=21)" and "FRF by TTM (k=45)" show results of cracked blade frequency response calculated by arriving time data at different k numbers. Graphical comparison is presented for the frequency range covering all-blades principal response.

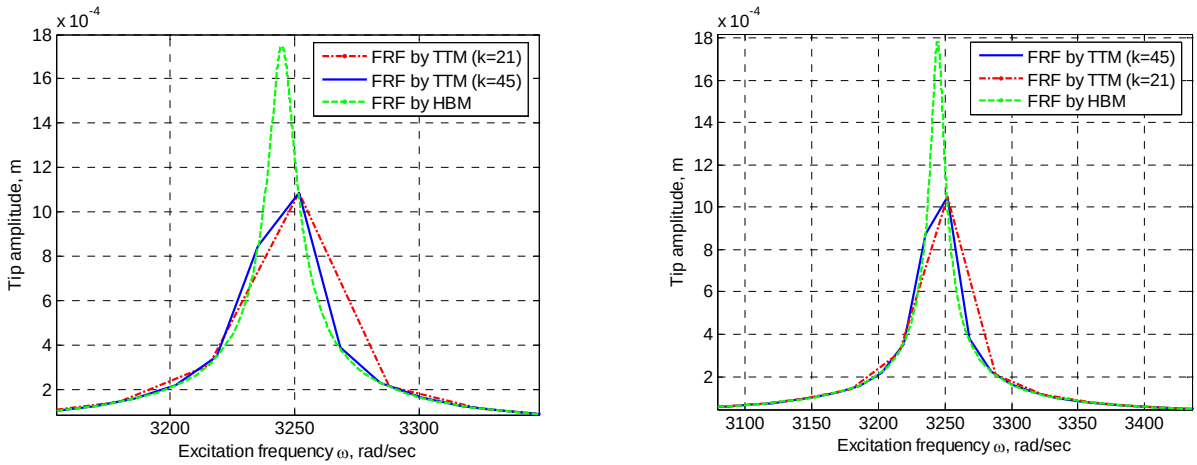

Fig. 4.18. Cracked blade frequency response (trailing edge crack): (a) a=2 mm, (b) a=4 mm

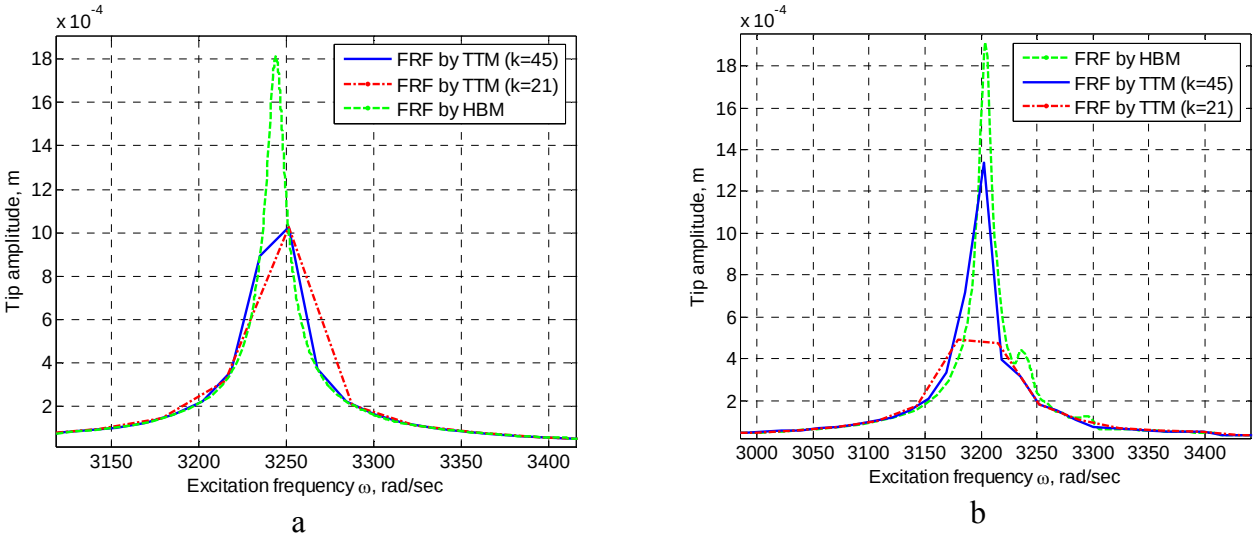

Fig. 4.19. Cracked blade frequency response (leading edge crack): (a) a=2 mm, (b) a=4 mm

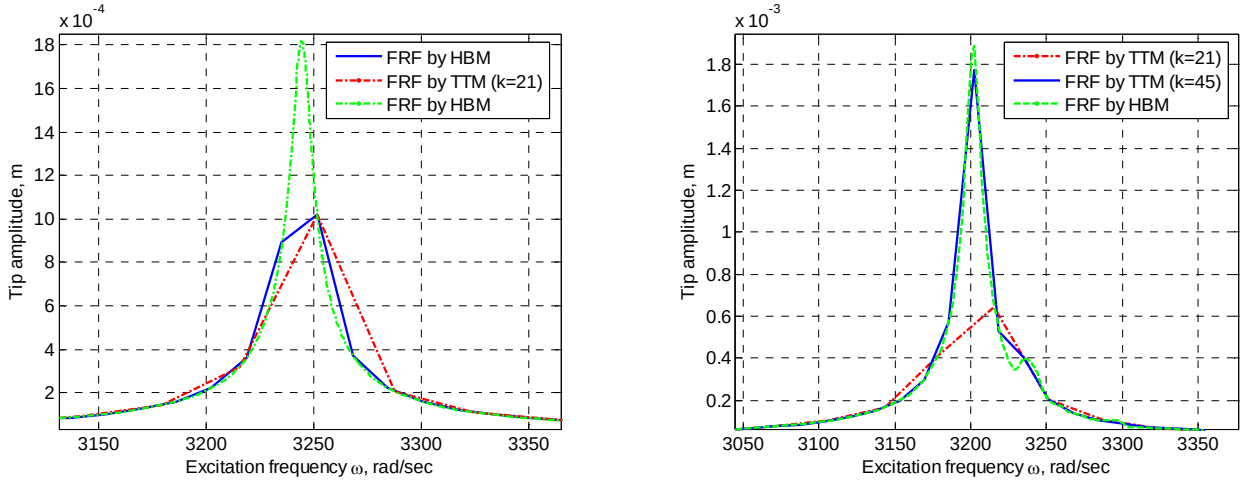

a b

Fig. 4.20. Cracked blade frequency response (symmetric cracks): (a) a=2 mm, (b) a=4 mm

From the comparison of cracked blade frequency response obtained by tip-timing measurements and harmonic balance method (Figs. 4.18–4.20) we can conclude following: both methods give almost same results near the resonance peak and they are sufficiently different at the resonance frequency. The last one is caused by shortage of points of tip-timing method measurements. Their maximum number is limited by rotations number accomplished by the engine rotor. Besides it should be noted the possibility to determine accurately enough the resonance frequency by blade tip-timing method.

Anyway, such comparison shows validity of blade tip-timing method simulation and proposed approach of blade tip amplitude response reconstruction on the base of arriving time data.

4.3 Tip-timing measurements simulation at different mistuning levels

4.3.1 Presence of cracked blade frequency localization

For blade tip-timing method simulation in the case of mistuning application following initial data were chosen: engine order – EO=28, rotor frequency range – Ω=16…20 Hz, rotor acceleration time – Tr=5 sec., rotor radius – R=0.38 m., number of probes – n=3. The bladed disk model contains cracked blade with 4 mm. leading edge crack. Engine order 28 was chosen for the reason to compare bladed disk frequency response obtained during non-linear analysis and presented in Fig. 3.39. The mistuning levels used for analysis are 0.5% (σ=0.005), 1% (σ=0.01) and 2% (σ=0.02). In this case blade tip-timing method simulation is performed using non-linear formulation of the cracked blade behaviour within the frameworks of the bladed disk dynamic model. Non-linear formulation was used because of two factors affecting the crack identification: presence of mistuning and shift of the non-linear cracked blade response close to the uncracked one. Both of these factors can lead to impossibility

to separate cracked blade response. As we know, during tip-timing measurements we are limited by maximum number of measurements, which also can reduce the quality of reconstructed bladed disk frequency response.

Maximum number of measurements by equation (4.9) at the set rotation frequency and engine acceleration time will be 90. To each measurement point an excitation frequency value corresponds. It was mentioned during the bladed disk model elaboration that cracked blade was supposed to be the first. Consequently, first blade is designated as cracked on all plots.

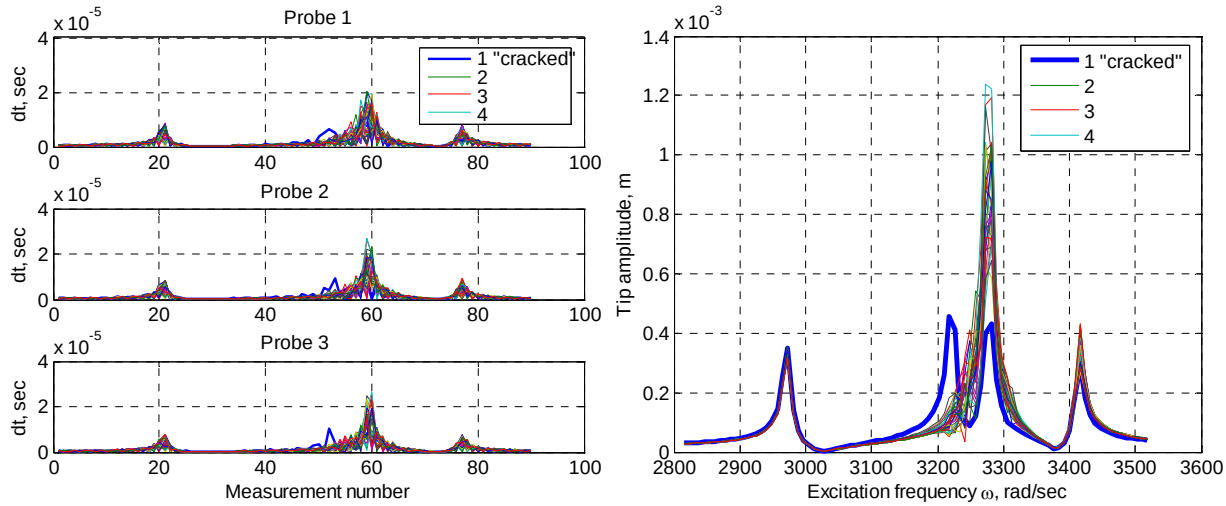

(a) (b)

Fig. 4.21. Blade tip timing method application results (0.5% of mistuning):

(a) arriving time differences “seen” on the probes, (b) bladed disk frequency response by TTM data

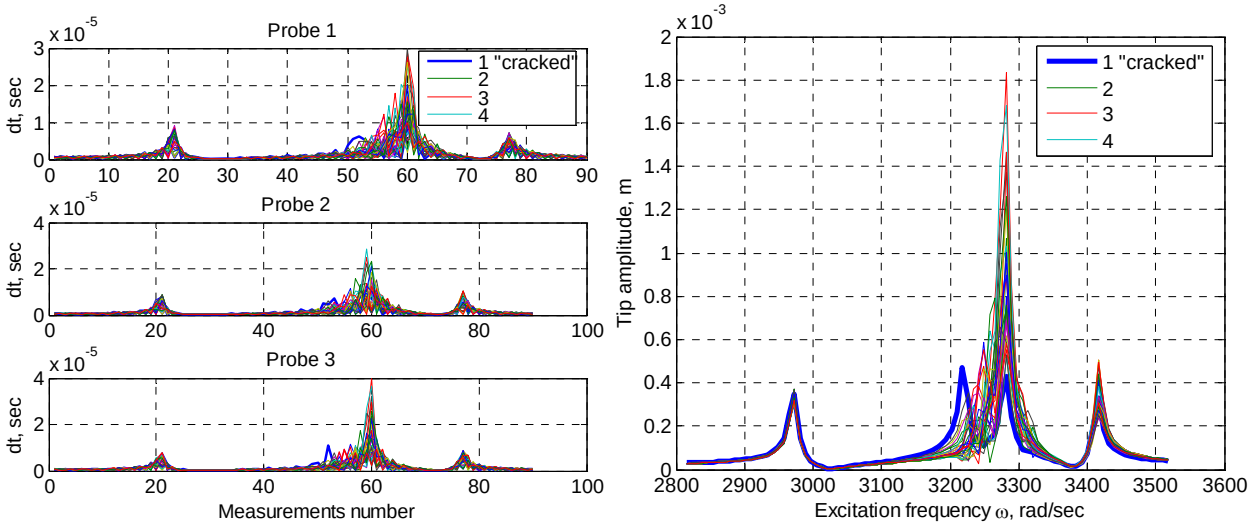

(a) (b)

Fig. 4.22. Blade tip timing method application results (1% of mistuning):

(a) arriving time differences “seen” on the probes, (b) bladed disk frequency response by TTM data

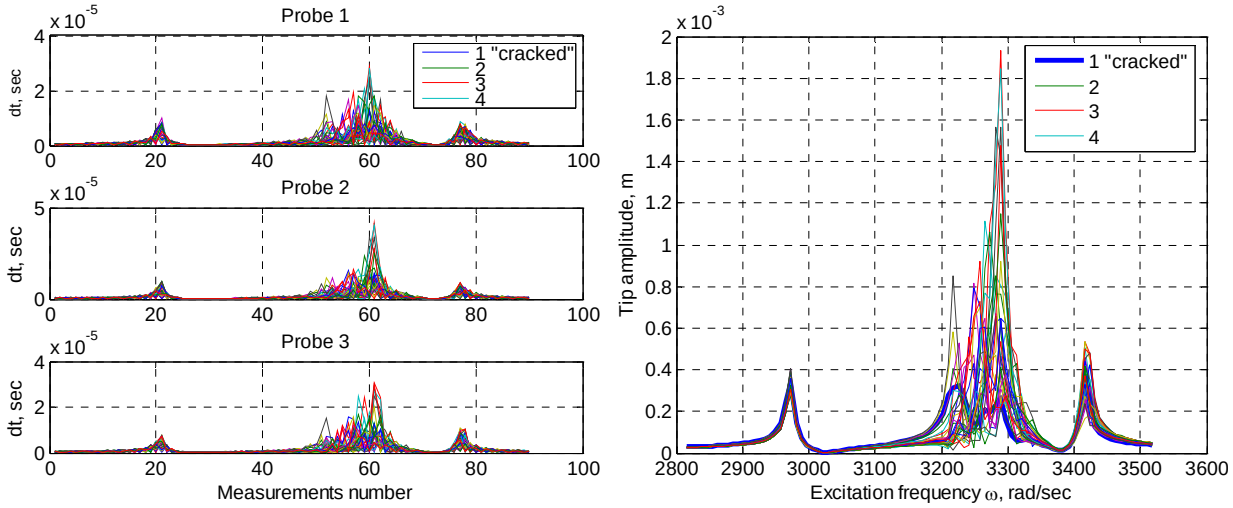

(a) (b)

Fig. 4.23. Blade tip timing method application results (2% of mistuning):

(a) arriving time differences "seen" on the probes, (b) bladed disk frequency response by TTM data

Simulation of bladed disk forced response measurement with 0.5% of mistuning (Fig. 4.21) is the reference to the case of bladed disk frequency response without cracked blade frequency localization. Mistuned bladed disk measurements at absence of the localization will be discussed in the next subchapter.

In Figs. 4.21–4.23 the results of tip-timing measurements at different levels of mistuning are presented. They show blade tip-timing method applicability to the blade tip amplitude measurements and construction of the bladed disk frequency response. The results confirm stated in the subchapter 3.3.4 that mistuning level of 2% makes unachievable the task of cracked blade identification, whereas it is possible at the mistuning level of 1% (Fig. 3.39a). We observe again the deterioration of cracked blade detectability applying the non-linear formulation of cracked blade behaviour. It was shown earlier that at its linear formulation we are still able to distinguish cracked blade response at 2% of mistuning, but the non-linear formulation makes this process unfeasible (Fig. 3.39b).

Blade tip-timing method simulation allows comparison of maximum amplitude responses of all blades in each measurement point (Figs. 4.24–4.25). For such purposes, four measurement points were chosen: before cracked blade localized response (Fig. 4.24a, point #30), around cracked blade localized response (Fig. 4.24b, point #52), around all-blades principal response (Fig. 4.24c, point #59), after all-blades principal response (Fig. 4.24d, point #82). Each measurement point is described by three curves showing blade tip amplitude responses calculated by harmonic balance method ("by HB method"), using tip-timing method data with non-linear ("by TTM data (non-linear case)") and linear formulation of cracked blade behaviour ("by TTM data (linear case)").

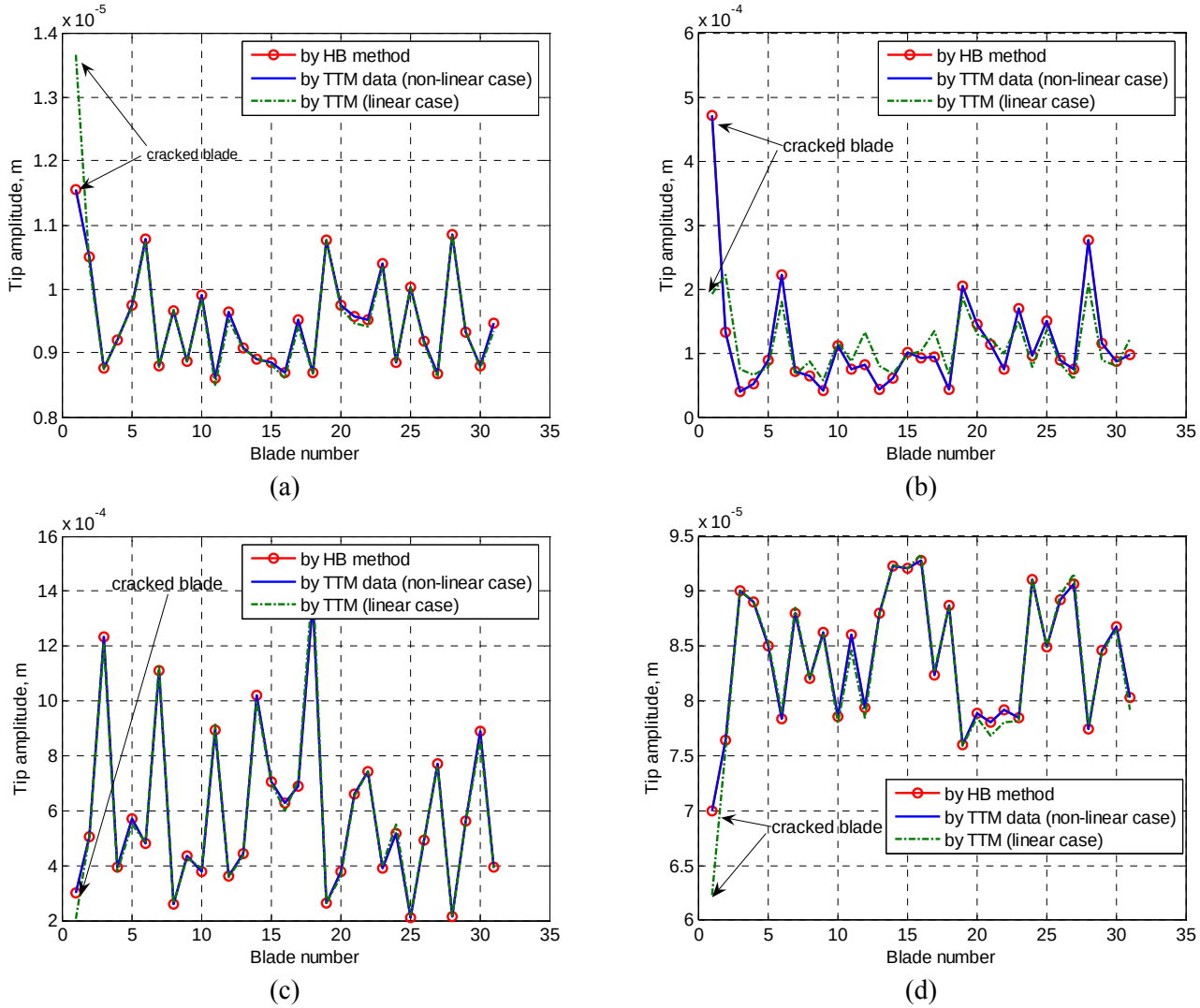

Fig. 4.24. All-blades response in the measurement point (1% of mistuning):

(a) ω=3044.2 rad/sec, (b) ω=3218.1 rad/sec, (c) ω=3273.5 rad/sec, (d) ω=3455.3 rad/sec

Analyzing results of mistuned bladed disk response in each measurement point, we can see again the decrease of the cracked blade detectability at the mistuning presence. In the case of the mistuning level of 1% (Fig. 4.24) it is still remained possible to separate the amplitude of cracked blade tip in almost all measurement point except #59 (Fig. 4.24c). This point is located close to the all-blades resonance peak, which is the most mistuned.

We can see from more detailed look on all-blades amplitudes distribution that cracked blade amplitude response is the highest before the all-blades principal response. Around it the cracked blade is almost impossible to be detected. While after it the blades respond in more structured manner and we are able again to separate cracked blade, because its response is the lowest.

The comparison of measurement results with the non-linear and linear formulations of the crack shows that linear formulation simplifies cracked blade identification in all measurement points. It is not possible only in the point #52 (Fig. 4.24b), which lies close to the resonance frequency of cracked blade in non-linear formulation.

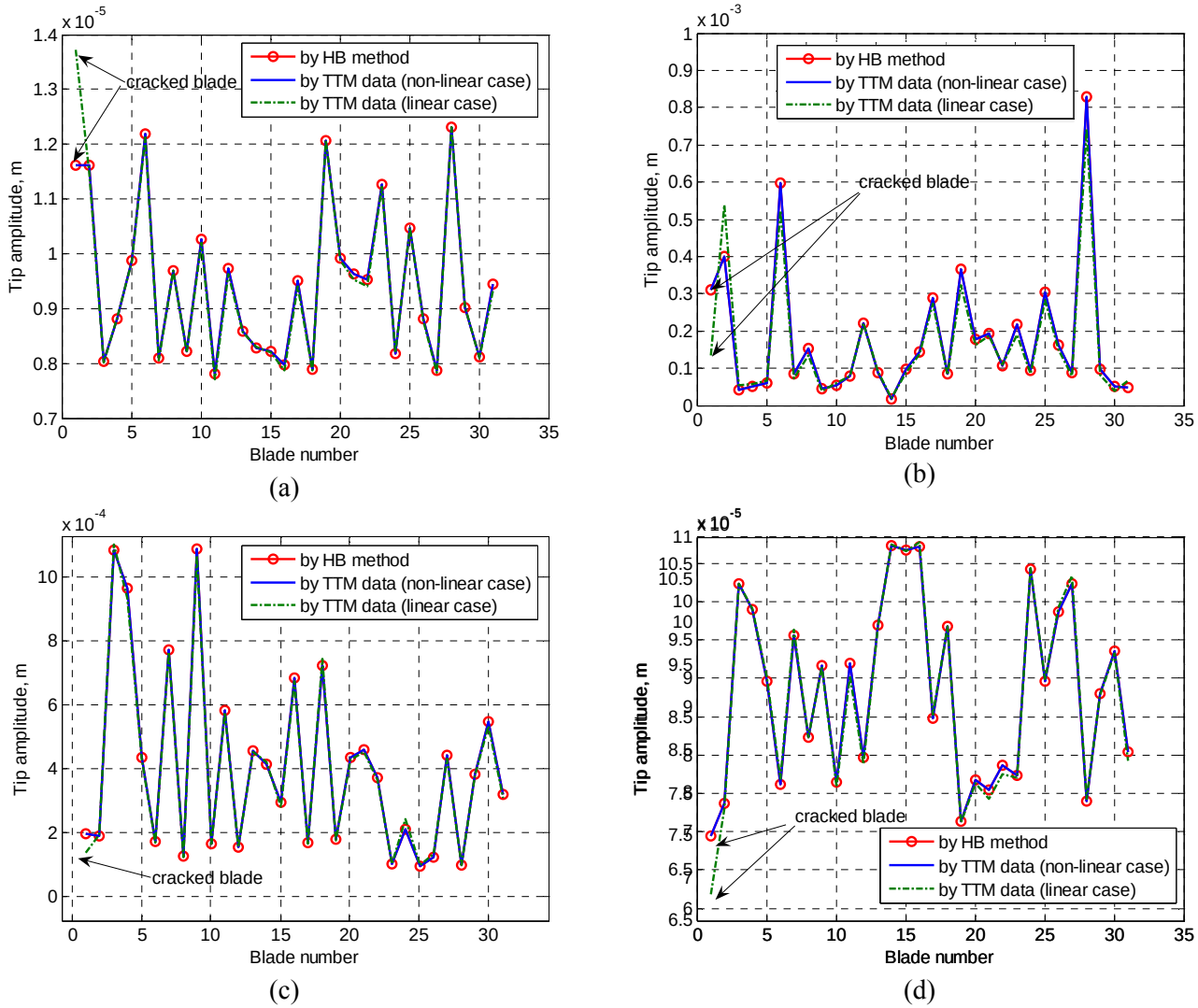

Fig. 4.25. All-blades response in the measurement point (2% of mistuning):

(a) ω=3044.2 rad/sec, (b) ω=3218.1 rad/sec, (c) ω=3273.5 rad/sec, (d) ω=3455.3 rad/sec

If to increase the mistuning level up to 2% (Fig. 4.25) even the results in the measurement point do not permit the separation of cracked blade tip amplitude. The random nature of mistuning leads to reduction of certain blades stiffness up to values, which are comparable with crack induced stiffness reduction. Also it is confirmed the stated in the subchapter 3.3.4. Linear formulation allows cracked blade identification at the higher mistuning level then it can be performed, if non-linear cracked blade model is used.

Generally speaking, study of the mistuning influence on the cracked blade detectability is very demanding problem. In most cases it leads to total inability of cracked blade identification, even if its frequency localization was reached.

4.3.2 Absence of cracked blade frequency localization

The bladed disk model containing leading edge crack of 2 mm. length was used to simulate blade tip-timing measurements of the model, which does not produce the cracked blade frequency localization. Initial data of blade tip-timing method are the same as for the previous simulations. Earlier it was supposed that even very small mistuning level can lead to the impossibility of cracked blade identification. Here two cases will be presented: blade tip amplitude measurements of the model without mistuning (Fig. 4.26) and tip-timing measurements of the bladed disk frequency response with presence of mistuning level 0.5% (Fig. 4.27).

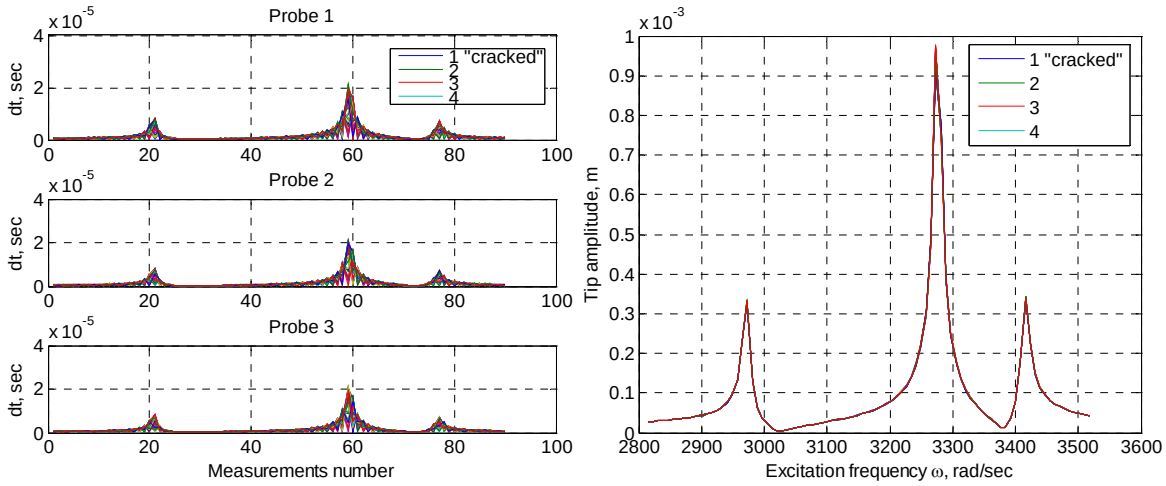

(a) (b)

Fig. 4.26. Blade tip timing method application results (no mistuning):

(a) arriving time differences “seen” on the probes, (b) bladed disk frequency response by TTM data

Model of the bladed disk without mistuning presence, which does not produce frequency localization, has been studied earlier during description of blade tip-timing method simulation. It is shown only for comparison with the same, but mistuned model.

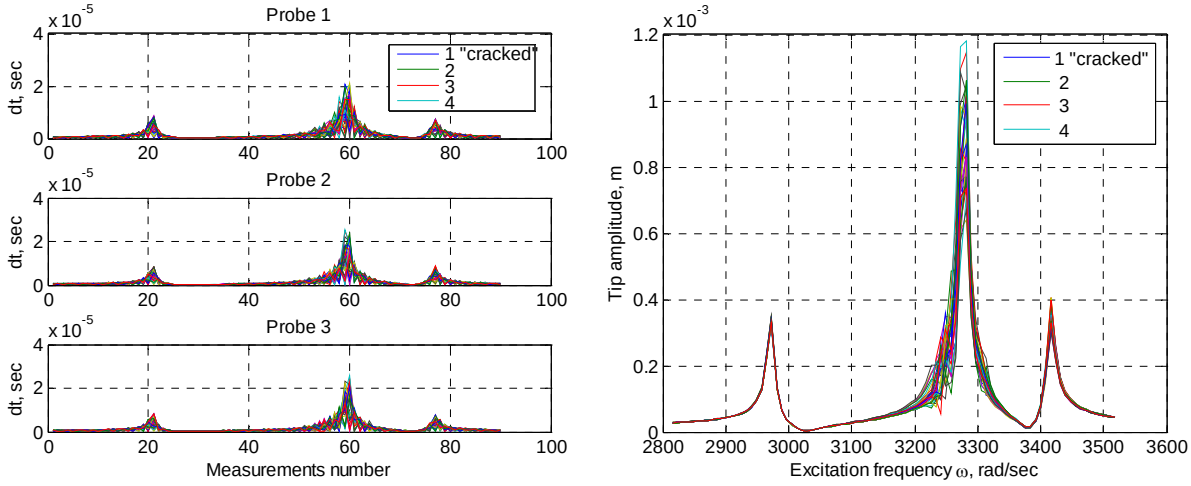

(a) (b)

Fig. 4.27. Blade tip timing method application results (0.5% of mistuning):

(a) arriving time differences “seen” on the probes, (b) bladed disk frequency response by TTM data

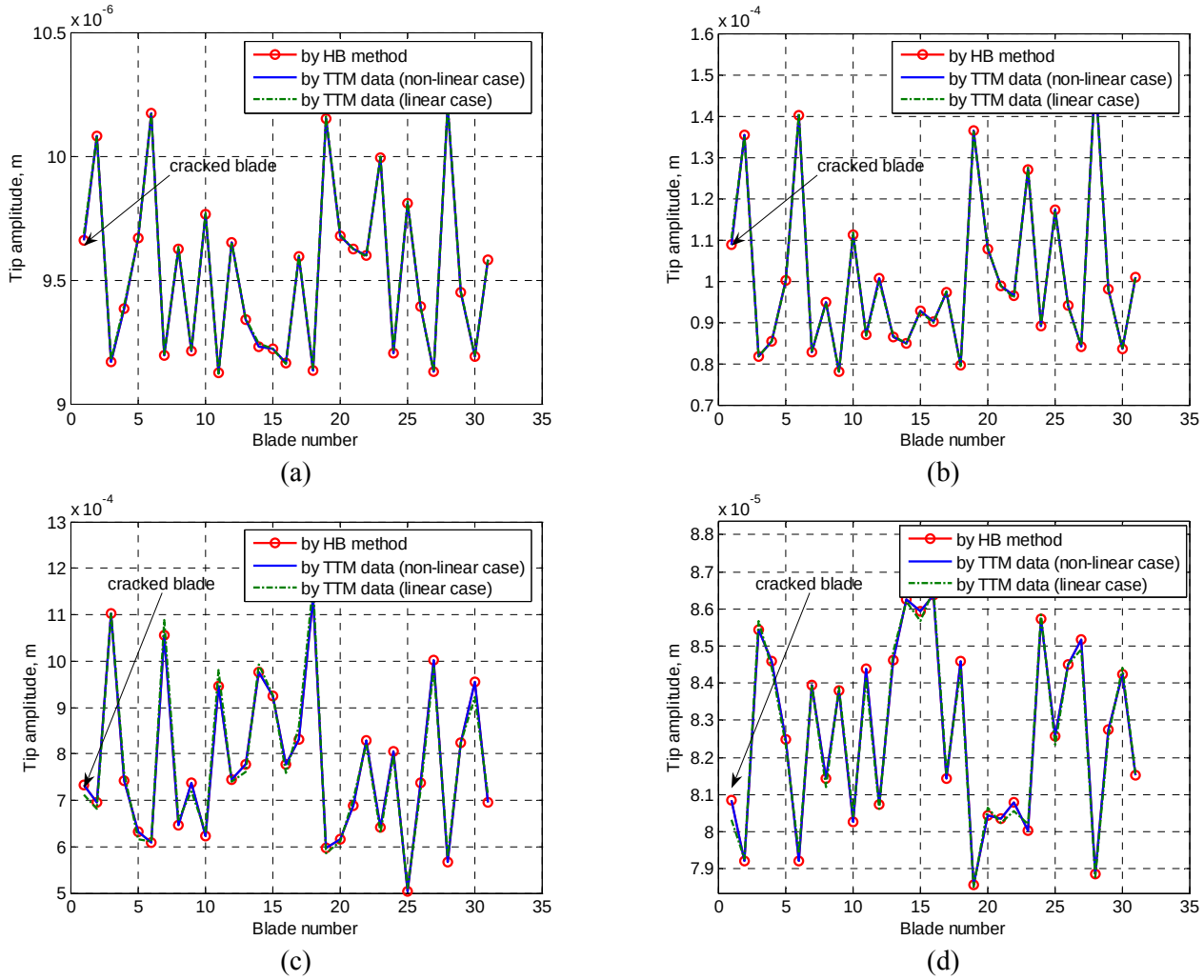

Fig. 4.28. All-blades response in the measurement point (0.5% of mistuning):
(a) ω=3044.2 rad/sec, (b) ω=3218.1 rad/sec, (c) ω=3273.5 rad/sec, (d) ω=3455.3 rad/sec

Measurement results of blade tip amplitudes in the case of absence of the cracked blade localization (Fig. 4.28) confirm stated above: even very small mistuning (0.5%) induces such spread of blade tip amplitudes, which makes impossible identification of the cracked blade. This proceeds from mistuned all-blades principal response (Fig. 4.27) and from possibility to identify cracked blade only on the base of tip amplitude differences.

4.4 Measurement performances influence on cracked blade detectability

Under measurement performances we understand time resolution of the probes. Simulation of time resolution influence is very important task because it directly influences on accuracy of tip-timing method measurements. Three resolution levels are used in simulations: 10^{-8}, 10^{-7}, 10^{-6} and 10^{-5} sec. It means that arriving time differences less then probe time resolution are thrown out. For all simulation cases bladed disk model with the leading edge crack was accepted (a=4 mm.). Number of

measurements was set to 90. Initial data: engine order – *EO*=28, rotor frequency range – Ω=16…20 Hz, rotor acceleration time – *Tr*=5 sec., rotor radius – *R*=0.38 m., number of probes – *n*=3, mistuning level – 0.5% (σ=0.05). The reference amplitude curve on the comparison graphs supposes infinite resolution ability of the probe (Fig. 4.29–4.33). Measurement points are the same as in subchapter 4.3.

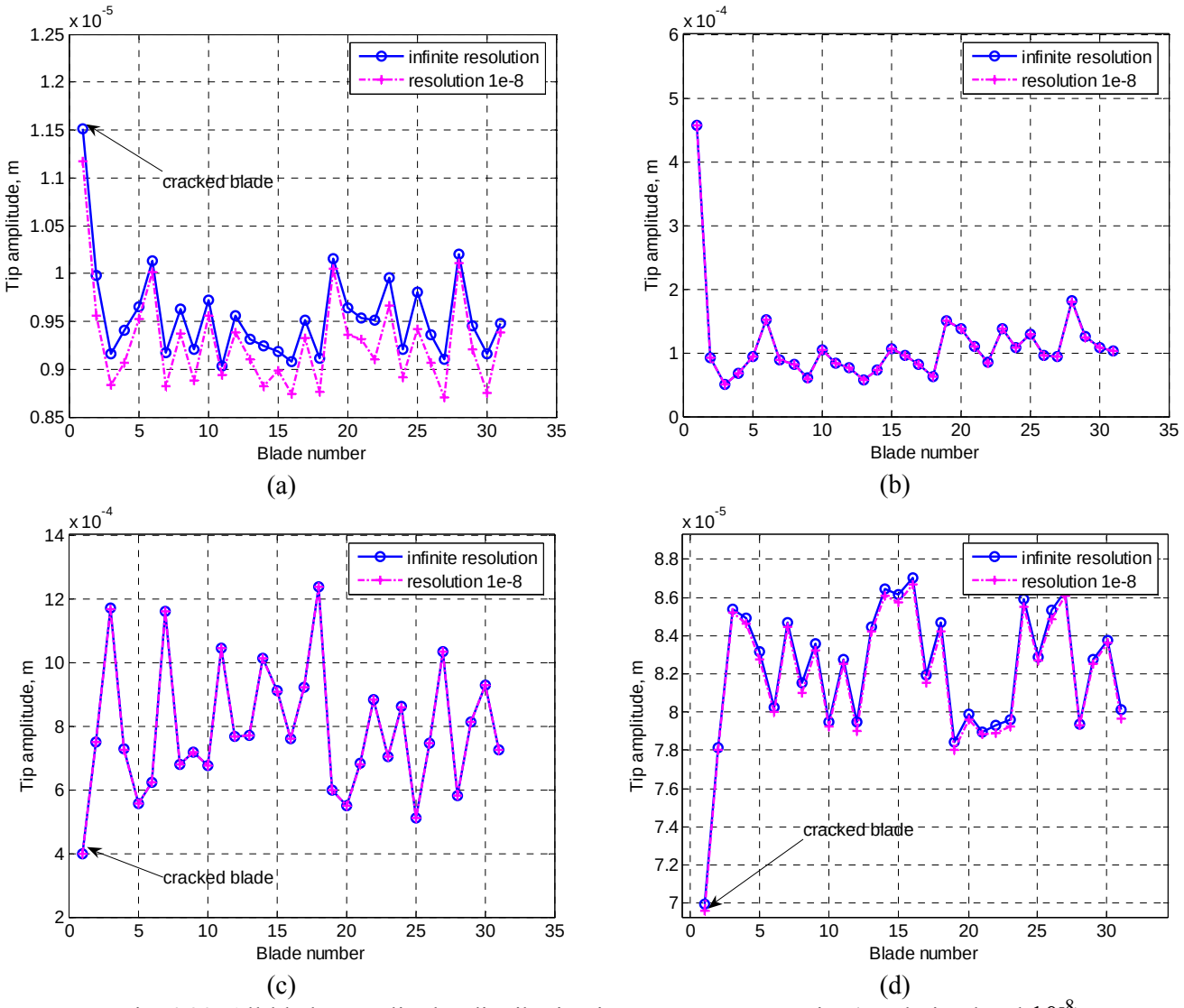

Fig. 4.29. All-blades amplitudes distribution in a measurement point (resolution level 10^{-8}):
(a) ω=3044.2 rad/sec, (b) ω=3218.1 rad/sec, (c) ω=3273.5 rad/sec, (d) ω=3455.3 rad/sec

At the set resolution level of 10^{-8} sec., it is seen from the blade tip amplitudes distribution that all measurement points give us the possibility of accurate amplitudes calculation by measures of tip-timing method. Only some inessential difficulties appear at the frequencies before cracked blade localized response (Fig. 4.29a). They are caused by low level of blade tip amplitudes in these points.

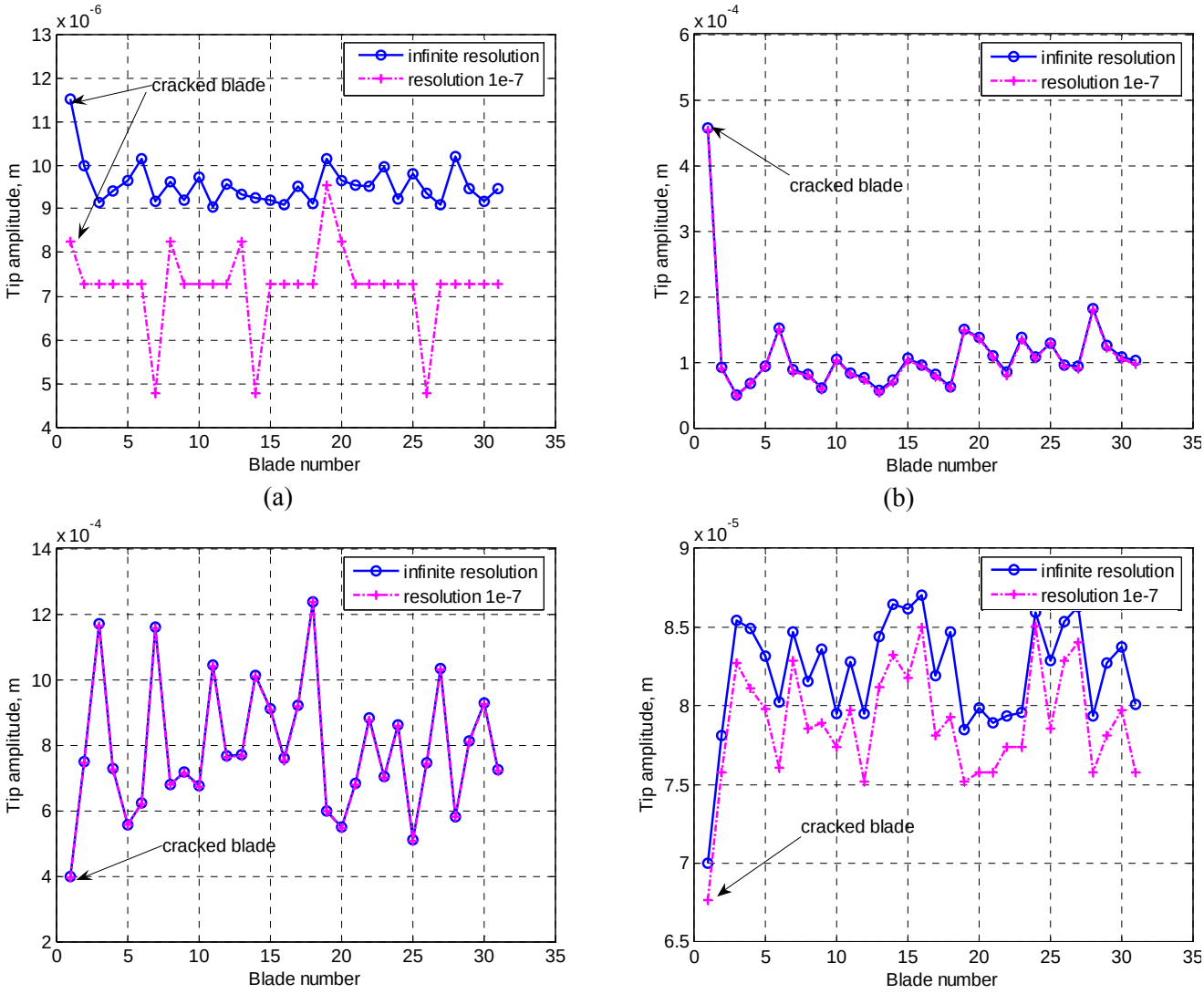

Fig. 4.30. All-blades amplitudes distribution in a measurement point (resolution level 10^{-7}):

(a) ω=3044.2 rad/sec, (b) ω=3218.1 rad/sec, (c) ω=3273.5 rad/sec, (d) ω=3455.3 rad/sec

Decreasing the resolution of the probes the problems of amplitude identification appear. It is in measurement points located far from the resonance frequencies (Fig. 4.30a, 4.30d). But anyway, both of them allow cracked blade identification owing to its higher amplitude response level. It is remained visible, even if some neighbouring blades amplitudes are calculated incorrectly.

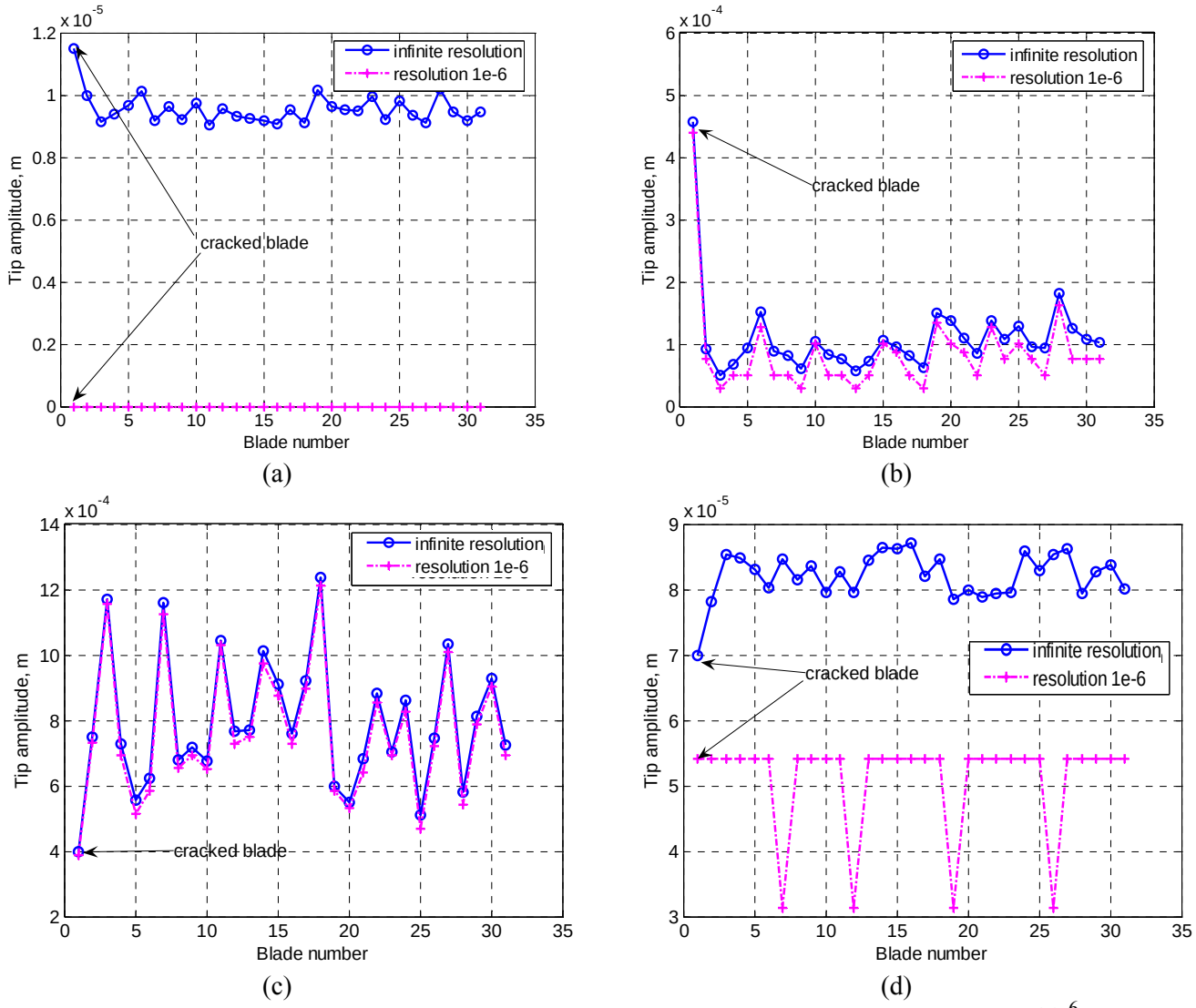

Fig. 4.31. All-blades amplitudes distribution in a measurement point (resolution level 10^{-6}):
(a) ω=3044.2 rad/sec, (b) ω=3218.1 rad/sec, (c) ω=3273.5 rad/sec, (d) ω=3455.3 rad/sec

The resolution level decreased to the value of 10^{-6} sec. can provide blade tip amplitudes calculation only in measurement points, which are located close to the resonance frequency (Fig. 4.31b, 4.31c). Other points make available improper results or sometimes zero amplitudes (Fig. 4.31a). Also they do not allow even cracked blade amplitude separation, whereas it was possible in the previous case.

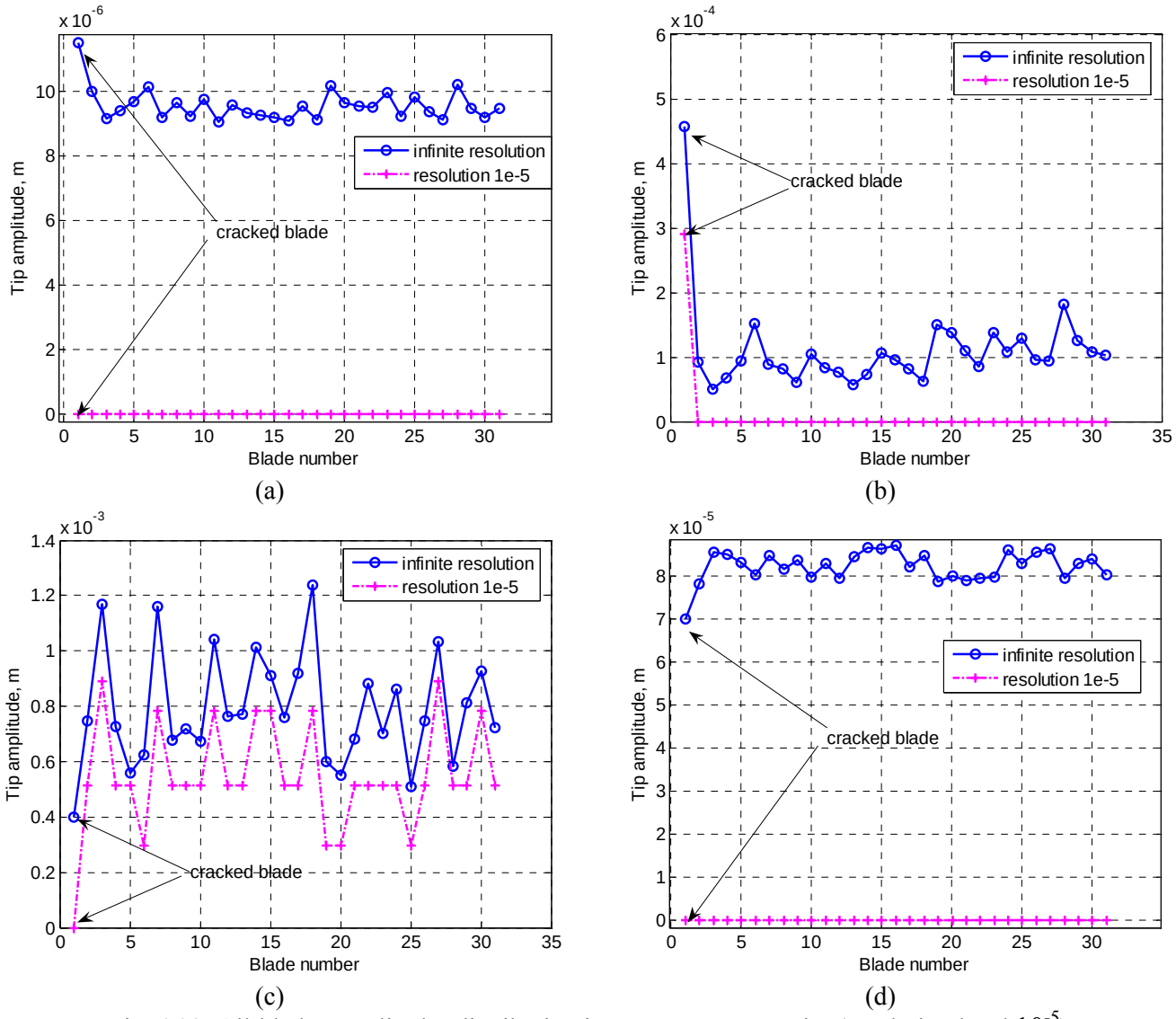

Fig. 4.32. All-blades amplitudes distribution in a measurement point (resolution level 10^{-5}):
(a) ω=3044.2 rad/sec, (b) ω=3218.1 rad/sec, (c) ω=3273.5 rad/sec, (d) ω=3455.3 rad/sec

The resolution level of 10^{-5} sec. is presented only for the reference purposes because it does not permit proper amplitude calculation in any measurement point. It can be used only for the cracked blade presence identification, if the resonance frequency is within the range of tip-timing measurements (Fig. 4.32c). Also such resolution level can be applicable for resonance frequencies calculation.

General conclusions concerning examination of probe time resolution influence on blade tip amplitude reconstruction consist in following. Time resolution applied to our model is sufficient for all measurements points, if it provides ability to capture arriving time differences under 10^{-8} sec. Reducing time resolution, some points will be loosen. Normally, such points are located before or after resonance peaks where blade tip amplitudes are of comparatively low level. At the same time, it is remained possible to calculate blade tip amplitudes near the resonance peaks. The smallest resolution level does

not allow amplitude calculation even around resonances. Only cracked blade presence identification is possible. It is achieved because of higher amplitude response of the cracked blade.

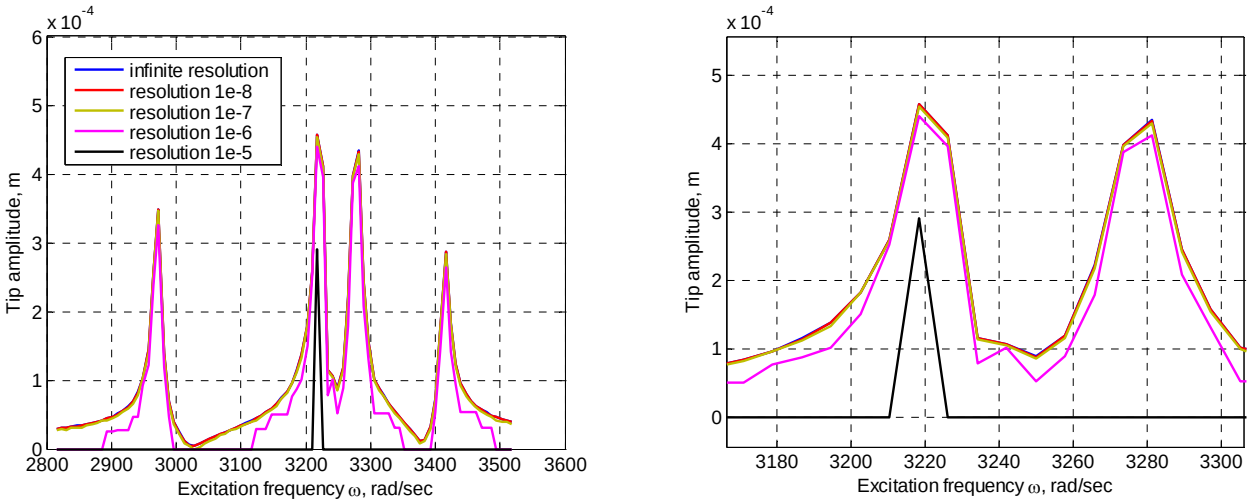

Fig. 4.33. Cracked blade frequency response at different probe resolution levels

Fig. 4.33 presents cracked blade frequency response of bladed disk model at different resolution levels. We can see again the ability to accurately calculate blade tip amplitude only at sufficiently high time resolution of the probe. The smallest, respectively to our model, resolution level is useful only for cracked blade identification, but not for amplitude calculation at particular frequency of excitation (rotor rotation).

The presented above simulations can be used for probes performances specification of the engine health monitoring system based on blade tip-timing method. Generally, probe time resolution abilities can be grouped in three categories:

- probe time resolution allows accurate blade tip amplitudes calculation in all measurement points;
- probe time resolution makes possible amplitudes reconstruction around resonance peaks;
- probe time resolution allows only resonance frequency determination or cracked blade presence identification in the case of its frequency localization.

Conclusions

All dynamic simulation of the bladed disk model was fulfilled within the frameworks of blade tip-timing method application. The benefits of this method are easy formulation and complete control of all blades. The fulfilment of the study concerning implementation of blade-tip timing method permits us to:

- control vibration state of each blade individually and, thus, to have a more complete knowledge about engine dynamic state;
- calculate blade tip amplitudes on the base of data delivered by the probes;
- calculate resonance frequencies;
- detect localized cracked blade in the assembly.

Some problems can arise during implementation of the health monitoring system based on tip-timing method. They can be grouped around low crack presence influence on overall blade dynamic performances. This phenomenon directly depends on crack size, crack location through the blade height and the order of the excited eigenmode. Also the measurement system (probe) time resolution is very important parameter. The higher time resolution will be required with increase of resonance order.

Conclusions and perspectives

It is very often happened with majority of research studies that as many questions are raised as we try to answer on. And the studies presented in this thesis are not the exception. Nevertheless, in the general conclusions to all the work it is intended to estimate the progress made in this work. It was aimed on elaboration of new advanced presentation of the cracked aircraft engine structures dynamics and they behaviour identification in operation.

Within the bounds of the presented doctorate different aspects associated with dynamics of the cracked blade behaviour and its identification in engine operation were studied. In the general way all accomplished studies can be divided into two main phases: theoretical development of the methods of the set problems solution and validation of these method applications by numerical simulation.

General conclusions

The most ambitious objective of the study is to develop the fundamentals of aircraft gas-turbine engine health monitoring system responsible for cracked blade identification in operation. In order to come nearer to this problem solution of two sub-tasks must have been solved:

- cracked blade dynamic model development;
- application of blade tip-timing method to blade tip amplitudes calculation.

Cracked blade dynamic model elaboration dealt with non-linear analysis methods application because it was required to take into account crack induced non-linearity influence on entire structure dynamics.

It is necessary to simulate crack presence in the blade using crack breathing model. It is caused by the fact that during engine operation compressor or turbine blades are subjected to periodically varying loads. Such formulation leads to contact interaction between crack sides. Elements of contact analysis were examined to be able to properly describe such crack behaviour. Frictionless contact elements were applied as it dominates during crack breathing process considering first bending mode.

Elements of fracture mechanics were considered as playing very important role and explaining physics of crack initiation, propagation and final fracture of the cracked structure. The simplified plane models of cracked plates were used, which can be considered as the reference ones for the cracked blade geometry. They allow simple and representative calculation of crack propagation rate, plastic zone development and remained cycles number before failure. The last one

is very important because it can complement our hypothesized health monitoring system with the calculation module responsible for cracked structure service life prognosis.

Having considered elements of contact analysis and fracture mechanics it became possible to directly proceed with elaboration of non-linear cracked blade model. Harmonic balance method was chosen as the tool for non-linear problem formulation. This method gained wide spread in solution of complex engineering problems, which do not allow their analytical formulation. It is known that harmonic balance method is very critical to the problem size. In order to overcome this issue, fixed interface method was applied to reduce system size. Different crack location cases were considered for investigation of the crack influence on forced response of the blade: trailing edge crack, leading edge crack and symmetric cracks. Furthermore the effect of centrifugal forces forming initial gap between crack sides was studied. It was concluded that at certain crack location and frequency of rotation it is useless to apply non-linear formulation of the crack behaviour. All these simulations were accomplished having supposed the cracked blade to be uncoupled.

Then the bladed disk model was created on the base of finite element model of the sector containing cracked blade. Reduction procedure was applied for a second time to be able to proceed with its non-linear analysis. The excitation model of the bladed disk is able to take into account external forces phase lag caused by difference between number of rotor and stator blades. After this the mistuning model based on the blade structural properties variation was added. It can directly affect cracked blade detectability. Cracked blade frequency localization plays here very important role. At certain level of mistuning it seems to be impossible to identify the cracked blade presence even in the case of its frequency localization.

Finally, the simulation of blade tip amplitudes measurement by tip-timing method was performed utilizing the developed disk model. It gives the possibility to measure amplitudes on the base of arriving times of the blades experiencing vibration. Depending on the level of vibration the arriving time will change and this will give the possibility to trace amplitude changes. The proposed approach allows amplitude reconstruction using 3, 5 or 7 probes. The only restriction is that synchronous vibration order (engine order) must not be the integer of probes number. Also some specifications are presented for probes recognition performances specifications. At its certain level it is impossible to accurately calculate blade tip amplitudes in measurement (excitation frequency) points located far from the resonance peak.

All performed studies can be summarized in the form of the main phases:

1. Cracked blade model development.
2. Crack presence non-linear formulation within frameworks of uncoupled cracked blade model.
3. Development of the bladed disk model containing the cracked blade.
4. Fixed interface method application to the bladed disk model.

5. Formulation of the blade tip-timing method and its application to the bladed disk model.
6. Algorithm development of blade tip amplitudes reconstruction using tip-timing measurements.
7. Simulation of the cracked blade identification using blade tip-timing method:
   - generation of blade arriving times;
   - blade tip amplitudes calculation by arriving times.

Perspectives

All perspectives concerning to the presented research can be generally considered in the view of two main directions. They are extension of theoretical developments and experimental validation of the proposed models.

Theoretical developments can be pursued in the field of amelioration of the bladed disk model like that:

- more deep insight to mistuning influence;
- trying to be able to distinguish between responses of mistuned and cracked blades.

Respecting to the theoretical fundamentals of blade tip-timing method some questions must be studied. They are blade installation angles error, problems related with signal under-sampling. Also it will be necessary to consider the possibility to take into account multi-harmonic excitation.

Experimental validation of the developed models is considered as the most important perspective objective. It can be realized using either simplified test bench consisting of the working wheel with probes installed around it. Simulation of the cracked blade presence can be accomplished by stiffness reduction of a blade. Also, at the higher level, such validation can be done using realistic aviation gas-turbine engine of the engine test facility of National Aviation University.

Personal publications

Publications in scientific reviews:

1. Kucher O., Kharyton V. Gas-turbine engine turbine disk deformed state calculation methods comparison. *Visnyk NAU (Scientific review of National Aviation University)*, 4: pp. 43-50, 2005
2. Laine J.-P., Kharyton V. Cracked structure response on external harmonic excitation. *Aerospace technique and technology.* 8(34): 80-52, 2006
3. Kucher O., Kharyton V. GTE blade vibration characteristics determination by non-contact method. *Visnyk NAU (Scientific review of National Aviation University),* 1(31): 134-138, 2007
4. Kucher O., Kharyton V., Laine J.-P., Thouverez F. Harmonic balance method implementation for crack breathing process simulation. *Aerospace technique and technology*, 8(44): 150-156, 2007
5. Kulyk M., Kucher O., Kharyton V., Laine J.-P., Thouverez F. Non-linear analysis of the cracked blade in dynamics. *Aviation*, 12(3): 66-79, 2008

Conferences:

1. Kucher O., Kharyton V. Cracked structure dynamic analysis: Two approaches to system stiffness and mass matrices reduction. *Proceedings of the international scientific conference AVIA-2006*, 25-27 September 2006, Kiev, Ukraine
2. Kucher O., Kharyton V., Laine J.-P., Thouverez F. Vibrational diagnosing of GTE working wheel blades by blade tip-timing method. *Proceedings of the international scientific conference AVIA-2007*, 25-27 April 2007, Kiev, Ukraine
3. Kucher O., Kharyton V., Laine J.-P., Thouverez F. Cracked blade presence influence on bladed disk dynamic response. *Proceedings of the international scientific congress "Aviation in XXI century"*, 22-24 September 2008, Kiev, Ukraine
4. Kharyton V., Laine J.-P., Thouverez F., Kucher O. Cracked blade detection from bladed disk dynamic response. *Proceedings of ASME conference "Turboexpo 2009"*, 8-12 June 2009, Orlando, FL USA

References

1. Abraham O.and Brandon J. Modelling of the opening and closure of a crack. *Journal of vibration and Acoustics,* 117: 370–377, 1995
2. Ahmedzianov A., Dubravskiy N., Tunakov A. *Diagnostics of air-jet engine condition by parameters*. Moscow, 1983
3. Archard J.F. Elastic deformation and the law of friction. *In Proceedings of the Royal Society of London, Series A: Mathematical and Physical Sciences,* 243: 190–205, 1957
4. Babak V. and all *Aviation safety*. Kiev, 2004
5. Beauseroy P., Lengelle R. Nonintrusive turbomachine blade vibration measurement system. *Mechanical Systems and Signal Processing,* 21: 1717–1738, 2007
6. Benfield W. and Hruda R. Vibration analysis of structures by component mode substitution *AIAA Journal,* 9(7) : 1255–1261, 1971
7. Bhat M., Ramamurti V., Sujath C. Studies on the determination of natural frequencies of industrial turbine blades. *Journal of Sound and vibration,* 196 (5): 681–703, 1996
8. Birger I. *Technical diagnostics*. Moscow, 1989
9. Bladh R., Castanier M., Pierre C. Component-Mode-Based Reduced Order Modeling Techniques for Mistuned Bladed DisksPart I: Theoretical models. *ASME Journal of Engineering for Gas Turbines and Power,* 123(1): 100–108, 2001
10. Borodachev N. *Calculation of cracked structural elements*. Mashinostroenie, 1992.
11. Bowie O. and Neal D. Single edge crack in rectangular tensile sheet. *ASME journal of applied mechanics,* 32(3): 708–709, 1965
12. Bowie O. Rectangular tensile sheet with symmetric edge cracks. *ASME journal of applied mechanics,* 31(2): 208–212, 1964
13. Bueckner H. A Novel Principle for the Computation of Stress Intensity Factors. *Zeitschrift für Angewandte Mathematik und Mechanik,* 50: 529–546, 1970
14. Cacciola P. and Muscolino G. Dynamic response of a rectangular beam with a known non-propagating crack of certain or uncertain depth. *Computers and Structures,* 80: 2382–2387, 2002
15. Cacciola P., Impollonia N., Muscolino G. Crack detection and location in a damaged beam vibrating under white noise. *Computers and Structures,* 81: 173–172, 2003
16. Castanier M. and Pierre C. Lyapunov exponents and localization phenomena in multi-coupled nearly periodic systems. *Journal of Sound and Vibration,* 183(3): 493–515, 1995

17. Charleux D. Etude des effets de la friction en pied d'aube sur la dynamique des roues aubagées. PhD thesis, Ecole Centrale de Lyon, 2006.
18. Cheng S., Wu X., Wallace W., Swamidas A. Vibrational response of a beam with a breathing crack. *Journal of Sound and Vibration*, 225: 201–208, 1999
19. Chengwu Duan and Rajendra Singh. Dynamic analysis of preload nonlinearity in a mechanical oscillator. *Journal of Sound and Vibration.* 301: 963–978, 2007
20. Craig R. and Bampton M. Coupling of substructures for dynamic analysis. *AIAA Journal*, 6(7). 1313–1319,1968
21. Diekmann R., Hungershofer J., Lux M. and all. Efficient contact search for finite element analysis, *European Congress on Computational Methods in Applied Sciences and Engineering ECCOMAS 2000*, Barcelona, September 2002
22. Dimitriadis G. and Carrington I. Blade-tip timing measurement of synchronous vibrations of rotating bladed assemblies. *Mechanical Systems and Signal Processing*. 16(4): 599–622, 2002
23. Elber W. Fatigue crack closure under cyclic tension. *Engineering Fracture Mechanics*, 2: 37–45, 1970
24. Fang X., Tang J., Jordan E., Murphy K. Crack induced vibration localization in simplified bladed-disk structures. *Journal of Sound and Vibration*, 291(1–2):395–418, 2006
25. Fatemi A. and Yangt L. Cumulative fatigue damage and life prediction theories: a survey of the state of the art for homogeneous materials. *International journal of fatigue*, 20(1): 9–34, 1998
26. Flotow A. and Drumm M.-.J. Blade-tip monitoring with through-the-case eddy current sensors. *Sensors online*, 6: 21-31, 2004
27. Flotow A. Health Monitoring and Prognosis of Blades and Disks with Blade Tip Sensors. *High Cycle Fatigue Conference*, March 2005
28. Forman R., Kearney V., Engle R. Numerical analysis of crack propagation in cyclic-loaded structures. *ASME Journal of Basic Engineering*, 89:459–464, 1967
29. Gelman L. and Gorpinich S. Non-linear vibroacoustical free oscillation method for crack detection and evaluation. *Mechanical Systems and Signal Processing*, 14(3): 343–351, 2000
30. Geradin M., Rixen D. *Theorie des vibrations.* Masson, 1993
31. Ghoshal A., Sundaresan M., Schulz M., Pai P. Structural health monitoring techniques for wind turbine blades. *Journal of Wind Engineering and Industrial Aerodynamics*, 85: 309–324, 2000
32. Gmur T. *Dynamique des structure*. Presses polytechniques et universitaires romandes, 1997

33. Goldstein H. *Classical Mechanics.* Addison Wesley, 1980
34. Greenwood J.A. and Williamson J.B.P. Contact of nominally flat surfaces. *In Proceedings of the Royal Society of London, Series A: Mathematical and Physical Sciences,* 295: 300–319, 1966
35. Griffiths A. *The theory of rupture and flow in solids*. Phil.Trans.Roy.Soc.Lond, 1920
36. Groll von G. and Ewins D. The harmonic balance method with arc-length continuation in rotor/stator contact problems. *Journal of Sound and Vibration*, 241(2): 221–233, 2001
37. Happawana G., Nwokah O., Bajaj A., Azene M. Free and forced response of mistuned linear cyclic systems: a singular perturbation approach. *Journal of Sound and vibration,* 211(5): 761–789, 1998
38. Heath S. and Imregun M. An improved single-parameter tip-timing method for turbomachinery blade vibration measurements using optical laser probes. *International Journal of Mechanical Sciences,* 38 (10): 1047–1058, 1996
39. Hjelmstad K. and Shin S. Crack identification in a cantilever beam from modal response. *Journal of Sound and vibration*, 198(5): 527–545, 1998
40. Hou J., Wicks B., Antoniou R. An investigation of fatigue failures of turbine blades in a gas turbine engine by mechanical analysis, *Engineering Failure Analysis,* 9: 201–211, 2002
41. Huang B.-W. Effect of number of blades and distribution of cracks on vibration localization in a cracked pre-twisted blade system. *International Journal of Mechanical Sciences,* 48: 1–10, 2005
42. Hwanga H. and Kim C. Damage detection in structures using a few frequency response measurements. *Journal of Sound and vibration,* 270: 1–14, 2004
43. Irwin G. Analysis of stresses and strain near the end of a crack transversing a plate. ASME *journal of applied mechanics,* 24 (3): 361–365, 1957.
44. Isida M. Analysis of stress intensity factors of a centrally cracked strip with stiffened edges. *Engineering fracture mechanics,* 3 (3): 347–365, 1973.
45. Jetteur P. Contact between two bodies in non-linear analysis using Lagrange multipliers. *Proceedings of FENET,* Copenhagen, February 2002
46. Karpov N., Kucher A., Lavruhin S. Remained service life of aviation engine and additional parameters calculation by flight data. *Aviation technique maintenance (Scientific review of Kiev Institute of Engineers of Civil Aviation)*, 1: 75–80, 1980
47. Kikuchi N. and Olden J. Contact problems in elasticity : A study of variational inequalities and finite-elements method. *SIAM, Philadelphia*, 1988
48. Kim J.-T. and Stubbs N. Crack detection in beam-type structures using frequency data. *Journal of Sound and vibration,* 259(1): 145–160, 2003

49. Kisa M. and Bradson J. The effect of closure of cracks on the dynamic of cracked cantilever beams. *Journal of Sound and Vibration,* 238(1): 1–18, 2000
50. Krawczuk M. and Ostachowicz W. Forced vibrations of a cantilever Timoshenko beam with a closing crack. *ISMA,* 19: 1067–1078, 1994
51. Krsanikov A. and Chernenko Zh. Estimate and prognosis of airplane Il-86 technical condition by flight information. *Automation of airplane functional systems diagnostics (Scientific review of Riga Institute of Engineers of Civil Aviation),* 1: 3–11, 1981
52. Kucher O., Dmitriev S., Popov A. Gas-turbine engine technical condition definition by experimental data using neural networks and theory of images recognition. *Aerospace technique and technology*, 10(46): 143–154, 2007
53. Kucher O., Kharyton V. GTE blade vibration characteristics determination by non-contact method. *Visnyk NAU (Scientific review of National Aviation University)*, 1(31): 134–138, 2007
54. Kucher O., Kharyton V., Laine J.-P., Thouverez F. Harmonic balance method implementation for crack breathing process simulation. *Aerospace technique and technology,* 8(44): 150–156, 2007
55. Kucher O., Kharyton V., Laine J.-P., Thouverez F. Vibrational diagnosing of GTE working wheel blades by blade tip-timing method. *Proceedings of the international scientific conference AVIA-2007,* 25-27 April 2007, Kiev, Ukraine
56. Kumar S., Roy N., Ganguli R. Monitoring low cycle fatigue damage in turbine blade using vibration characteristics. *Mechanical Systems and Signal Processing,* 21: 480–501, 2007
57. Laine J.-P. and Kharyton V. Cracked structure response on external harmonic excitation. *Aerospace technics and technology*, 61: 1057–1074, 2006
58. Laursen T. and Maker B. An augmented lagrangian quasi-Newton solver for constrained nonlinear finite-elements application. *International journal for numerical methods in engineering,* 38: 3571–3590, 1955
59. Law S. and Lu Z. Crack identification in beam from dynamic responses. *Journal of Sound and vibration*, 285: 967-987, 2005
60. Lawson C. and Ivey P. Tubomachinery blade vibration amplitude measurement through tip timing with capacitance tip clearance probes. *Sensors and Actuators*, 118: 14-24, 2005
61. Lee L. and Chung M. A study on crack detection using eigenfrequency test data. *Computers and Structures*, 77: 327–342, 2000
62. Lin C. and Mignolet M. An Adaptive Perturbation Scheme for the Analysis of Mistuned Bladed Disks. *ASME Journal of Engineering of Gas Turbines and Power,* 119: 153–160, 1997

63. Lina R., Leeb S.-Y., Wanga W.-R. Dynamic analysis of rotating damped beams with an elastically restrained root. *International Journal of Mechanical Sciences,* 46: 673–693, 2004
64. Liu L., Thomas J., Dowell E., Attar P., Hall K. A comparison of classical and high dimensional harmonic balance approaches for a Duffing oscillator. *Journal of Computational Physics,* 215: 298–320, 2006
65. Loya J., Rubio L., Fernandez-Saez J. Natural frequencies for bending vibrations of Timoshenko cracked beams. *Journal of Sound and vibration*, 290: 640–653, 2006
66. Lozitskiy L. *Aviation engines design.* Vozdushnyy transport, 1992.
67. Luzatto E. Approximate computation of non-linear effects in a vibrating cracked beam. *Journal of Sound and vibration*, 745: 245–763, 2003
68. Mac Neal R. A hybrid method of component mode synthesis. *Computers & Structures*, 1: 581–601, 1971
69. Mignolet M., Hu W., Jadic I. On the Forced Response of Harmonically and Partially Mistuned Bladed Disks. Part II: Partial Mistuning and Applications. *International Journal of Rotating Machinery,* 6(1): 43–56, 2000
70. Miner M. Cumulative Damage in Fatigue. *Journal Applied Mechanics*, 12: 159–164, 1945
71. Murakami Y. *Stress intensity factors handbook*. Pergamon Press, 1987
72. Naeem M., Singh R., Probert D. Implications of engine deterioration for a high-pressure turbine blade's low-cycle fatigue (LCF) life-consumption. *International journal of fatigue*, 21: 831–847, 1999
73. Nayfeh A. and Mook D. *Nonlinear oscillations*. John Wiley, 1979.
74. Neogy S. and Ramamurti V. Effect of partial depth cracks on the natural frequency of twisted blades: A 3-d finite element analysis. *Journal of Sound and vibration,* 205(1): 33–55, 1997
75. Oden J. and Martins J. Models and computational methods for dynamic friction phenomena. *Computer Methods in Applied Mechanics and Engineering,* 52: 527–634, 1985
76. Ottarsson G. and Pierre C. A transfer matrix approach to free vibration localization in mistuned blade assemblies. *Journal of Sound and Vibration*, 197(5): 589–615, 1996
77. Padmanabhan C. and Singh R. Analysis of periodically excited non-linear systems by a parametric continuation technique. *Journal of Sound and Vibration*, 184(1):35–58, 1995.
78. Panasuk V. *Fracture mechanics and strength of materials.* Naukova dumka, 1988
79. Panasuk V. *Mechanics of quasi-brittle fracture of materials*. Naukova dumka, 1991.
80. Paris P. and Erdogan F. A critical analysis of crack propagation laws. *ASME Journal of Basic Engineering,* 85: 528–534, 1963

81. Park M., Hwang Y.-H., Choi Y.-S, Kim T.-G. Analysis of a J69-T-25 engine turbine blade fracture. *Engineering Failure Analysis,* 9: 593–601, 2002
82. Petrov E., Sanliturk E., Ewins D., Elliott R. Quantitative Prediction of the Effects of Mistuning Arrangement on Resonant Response of a Practical Turbine Bladed Disc. 5-*th National Turbine Engine High Cycle Fatigue Conference*, Chandler, 7-9 March, 2000
83. Pronikov A. *Machines reliability*. Moscow, 1978
84. Pugno N. and Surace C. Evaluation of the non-linear dynamic response to harmonic excitation of a beam with several breathing cracks. *Journal of Sound and vibration,* 235(5): 749–762, 2000
85. Rabinowicz E. *Friction and wear of materials*. John Wiley & Sons, 1965.
86. Ranganathan N. A note on finite width correction for a double-edge cracked plate in tension. *Engineering fracture mechanics*, 3 (3): 347–365, 1973
87. Rivas-Guerra J. and Mignolet M. P. Local/Global effects of mistuning on the forced response of bladed disks. *ASME Journal of Engineering for Gas Turbines and Power*, 126: 131–141, 2004
88. Rixen D. A dual Craig–Bampton method for dynamic substructuring. *Journal of Computational and Applied Mathematics*, 168: 383–391, 2004
89. Roy N., Ganguli R. Helicopter rotor blade frequency evolution with damage growth and signal processing. *Journal of Sound and vibration*, 283: 821–851, 2005
90. Ruotolo R. and Surace C. Harmonic analysis of the vibrations of a cantilevered beam with a closing crack. *Journal of Sound and vibration,* 206(4): 566–588, 1997
91. Ruotolo R., Surace C., Crespo P., Storer D. Harmonic analysis of the vibrations of a cantilevered beam with a closing crack. *Computers and Structures,* 61: 1057–1074, 1996
92. Sahli B. Identification du désaccordage et des couplages aéroélastiques dans les roues de turbines. PhD thesis, Université de Franche-Comté, 2008.
93. Serensen S. *Material strength to brittle and fatigue failure*. Naukova dumka, 1975
94. Shifrin E. and Ruotolo R. Natural frequencies of a beam with an arbitrary number of cracks. *Journal of Sound and vibration,* 206(4): 566–588, 1997
95. Slavic J., Cermelj P., Babnik A. and all. Measurement of the bending vibration frequencies of a rotating turbo wheel using an optical fibre reflective sensor. *Measurements Science and Technology*, 13: 477–482, 2002
96. Tada H. A note on the finite width corrections to the stress intensity factor. *Engineering fracture mechanics,* 3: 345–347,1971
97. Tsyfansky S. and Beresnevich V. Detection of fatigue cracks in flexible geometrically non-linear bars by vibration monitoring. *Journal of Sound and vibration,* 213(1): 159–168, 1998

98. Vasiliev V., Gusev Yu., Ivanov A. and all *Automated monitoring and diagnostics of aircrafts power plants control systems*. Moscow, 1989
99. Vetrov A. and Kucher O. Probabilistic methods of gas-turbine engine structural elements service life calculation in operation. *Strength of materials,* 8: 70–76, 1989
100. Vetrov A. and Kucher O. Remained service life estimation of gas-turbine engine working blades by accumulated creep deformations. *Strength of materials,* 1: 50–57, 1993
101. Vetrov A., Kucher O., Koveshnikov A. Probabilistic-parametric models of aviation gas-turbine engine materials long-term strength. *Strength of materials,* 4: 14-17, 1989
102. Vorobyev V., Gluhov V., Kozlov Yu. and all *Estimate and prognosis of airplane's equipment technical condition*. Moscow, 1984
103. Wang J.H. and Shieh L. The influence of variable friction coefficient on the dynamic behaviour of a blade with a friction damper. *Journal of Sound and Vibration,* 149(1): 137–145.
104. Wildheim S. Excitation of rotationally periodic structures. *Transaction of ASME,* 46: 878–883, 1979
105. Wolf J., Swift H., Swinney L., Vastano J. A. Determining Lyapunov exponents from a time series. *Physica,* 16: 174–206, 1965.
106. Ying R. The analysis and identification of friction joint parameters in the dynamic response of structures. PhD thesis, Imperial College of London, 1992
107. Zablotsky Y. and Korostelev Y. Measurement of resonance vibrations of turbine blades with the ELURA device. *Energomashinostroneniy,* 2: 36–39, 1970
108. Zhang J., Xu M., Song L. The balance of the air flow noise in extracting acoustic signals of the cracked blade. *Journal of Sound and vibration,* 245(5): 915–922, 2005
109. Zielinski M. and Ziller G. Noncontact blade vibration measurement system for aero engine application. *International Symposium of Air Breathing Engines,* ISABE-2005
110. Zielinski M. and Ziller G. Noncontact crack detection on compressor rotor blades to prevent further damage after HCF-failure. *NATO/PFP (RTO-MP-AVT-121),* 19: 1–10, 2005
111. Zielinski M. and Ziller G. Noncontact vibration measurements on compressor rotor blades. *Measurements Science and Technology*, 11: 847–856, 2000

Nomenclature

$\mathbf{A}$ – structural matrix of linear system state

$\mathbf{A}_c$ – matrix of contact stresses

$\mathbf{B}$ – transformation matrix

$\mathbf{C}_\xi$ – structural damping matrix

$\mathbf{E}$ – elasticity matrix

$\tilde{\mathbf{F}}$ – externat excitation forces vector in harmonic representation

$\mathbf{F}_c$ – vector of contact forces

$\mathbf{F}_{ext}$ – externat excitation forces vector

$\mathbf{G}$ – vector of initial separation distances between contact elements (chapter 2)

$\mathbf{G}$ – static modes (chapter 3, reduced order modelling methods)

$\mathbf{H}$ – impedance matrix

$\mathbf{I}$ – unity matrix

$\mathbf{J}$ – Jacobian matrix

$\mathbf{K}$ – stiffness matrix

$\mathbf{M}$ – mass matrix

$\mathbf{N}$ – centrifugal matrix

$\mathbf{P}$ – gyroscopic matrix

$\mathbf{R}$ – rotational matrix

$\mathbf{T}$ – transfer matrix

$\mathbf{W}$ – global wave transfer matrix

$\mathbf{\Phi}$ – matrix containing base of truncated eigenmodes

$\mathbf{b}$ – non-linear forces vector

$\mathbf{q}$ – generalized displacements vector

$\mathbf{r}$ – radius–vector

$\mathbf{s}$ – translation vector between fixed and rotated coordinates system

$\mathbf{u}$ – displacements vector

$\tilde{\mathbf{u}}$ – vector of Fourier series coefficients

$\mathbf{v}$ – waves amplitudes vector

$\mathbf{w}$ – nonconservative forces vector

A – amplitude of the complex frequency response

D – damage estimation parameter

E – modulus of elasticity

E_d – energy of deformation (chapter 3)

E_c – kinetic energy

E_p – potential energy

EO – engine order

F_d – dissipation function of Rayleigh

F_{nl} – non-linear force

K – admissible displacements field

K_1 – stress intensity coefficient

K_{1C} – critical stress intensity coefficient

L – lagrangian of the system

N_{dof} – number of degree of freedoms

N_b – base number of cycles

N^1 – number of cycles before crack origination

N_P – number of performed cycles during crack development

N_f – full number of cycles before fracture

N_k – number of cycles at the moment of fracture

P – fracture probability of structure

R – reliability of structure (chapter 2)

R – rotor radius (chapters 3–4)

T – solution period

Tr – rotor acceleration time

V – displacements field

W_i – i–th modal strain energy

a – crack length

a_p^i – i–th blade tip amplitude captured by p–th probe

c – angular distance passed by blade to probe

d – distance between contact surfaces

d_r – distance passed by blade due to rotation

d_v – distance passed by blade due to vibration

f_n – normal contact friction force

f_t – tangential contact friction force

i – imaginary unit

k_c – stress cycle performance

k – spring stiffness

k_{nl} – penalty stiffness coefficient

n^l – normal to the body l.

n_c – safety factor in fracture mechanics

n – number of probes

p – pressure loading

r – cycle ratio

r_y – plastic zone size

t – time variable

u – normal displacement

u_{nl} – non-linear displacement

v – tangential displacement (chapter 2)

v_c – crack growth rate

x,
y, – coordinates in stationary reference frame or fixed coordinates system
z

x_1,
y_1, – coordinates in rotated coordinates system
z_1

σ – normal stress

σ – standard deviation of normal distribution (chapter 3)

σ_c – mean stress of cycle

σ_a – stress cycle amplitude

σ_{-1} – fatigue limit at symmetrical stress cycle

σ_k – critical stress

$\sigma_{0,2}$ – conventional yield strength of material

ξ – structural damping coefficient

Ω – rotor frequency

ε – deformation (chapter 1)

ε – blade installation angle (chapter 4)

ϕ – probe installation angle

ψ – phase of the complex frequency response(chapter 4)

φ – phase angle

$.\varphi_h$ – interblade phase angle

λ_i – *i*–th eigenvalue

λ – multiplier of Lagrange (chapter 2)

γ_k – *i*–th Lyapunov exponent

Λ_j – *j*–th modal stiffness

ω – excitation frequency

ω_i – *i*–th natural frequency

τ – tangential stress

μ – friction coefficient

μ_d – dynamic friction coefficient

δ – mistuning parameter

δ – penalty coefficient (chapter 2)

∇ – differentiation operator

$\langle \cdot,\cdot \rangle$ – denotes inner product

$\otimes$ – denotes Kronecker product

$\dot{x}$ – denotes time derivative of variable *x*

$\mathbf{X}^T$ – operator of matrix or vector transposing

$\mathbf{X}^{-1}$ – operator of matrix inversing

List of figures

Chapter 1

1.1	Aviation turbofan engine	6
1.2	(a) typical turbine blade design, (b) turbine blade profiling	7
1.3	Schematic presentation of deformable solid body	13
1.4	Natural modes spectrum structure of an individual blade	16
1.5	Natural modes of typical turbine blade: (a)flexural, (b) torsional	16
1.6	Structure subjected to stress stiffening effect	17
1.7	Cyclic structure analysis components	18
1.8	Campbell diagram example	20
1.9	Zig-zag diagram presentation	22
1.10	Fundamental presentation of the mistuning problem in bladed disks	23
1.11	A schematic diagram of nearly periodic system	27
1.12	Schematic load-displacement curve for breathing crack behavior case	32
1.13	Contact approach for crack behavior simulation: (a) contact between two bodies, (b) load-displacement curve (normal force)	33

Chapter 2

2.1	Two solid bodies contact interaction	38
2.2	Schematic presentation of loading of metallic contact surface with roughness presence	38
2.3	Schematic presentation of film covering metal surface	39
2.4	Schematic presentation contact element (a) and force-displacement curve of Coulomb's model (b)	39
2.5	Schematic presentation of bilinear model (a) and force-displacement curve of bilinear model (b)	40
2.6	Schematic presentation of contact models hysteretic properties: (a) Coulomb's law, (b) bilinear model	41
2.7	Schematic presentation of contact interaction between two solids	41
2.8	Cycle of alternating stresses	52
2.9	Symmetrical loading cycle	53
2.10	Asymmetrical loading cycle	53
2.11	Fatigue curve	54

2.12	True limit stresses diagram	55
2.13	Schematised limit stresses diagram	55
2.14	Curves of cyclical durability distribution for different σ_{max}	56
2.15	Curves of equal probability of fatigue failure	57
2.16	Fatigue curve for durability estimation	57
2.17	Crack in elastic body	59
2.18	Idea of Bueckner's method: (a) initial plate with crack, (b) same plate without crack and σ_y diagram, (c) calculated plate with crack and σy diagram	61
2.19	Crack location cases: (a) plane with crack, (b) plate with central crack, (c) plate with eccentrically shifted crack, (d) plate with edge cracks	62
2.20	Upper part of the plate with crack	63
2.21	Correction facture F1: curve 1 – the exact solution; curve 2 – approximate solution	64
2.22	Infinite plate with crack	65
2.23	Fracture of plate sample with crack	66
2.24	Plastic zone at crack tip	67
2.25	Safety factor *n* plot	68
2.26	Relation of function F_1 (α) from α	69
2.27	Dependence of stress intensity coefficient K_1 (MPa·m$^{1/2}$) on crack length *a*	70
2.28	Plastic zone representation for the case of the plate with central crack	71
2.29	Plastic zone size dependence on crack length	71
2.30	Dependence of critical stress σ_k on crack length *a*	72
2.31	Dependence of safety factor *n* on crack length *a*	73
2.32	Diagram of fatigue failure	74
2.33	Dependence of crack growth rate on initial crack length	78
2.34	Dependence of remained cycles number on initial crack length	79
	Chapter 3	
3.1	Blade finite-elements model: (a) realistic model, (b) simplified cracked blade model; (c) crack location zone (zoom)	82
3.2	Cracked blade model subjected to forced response analysis	93
3.3	Crack location variants: (a) crack on trailing edge, (b) crack on leading edge, (c) symmetric cracks	93
3.4	Cracked blade model sub-structuring	95
3.5	Relative displacements between contact nodes	95
3.6	Nonlinear force smoothing representation: (a) at different values of *s* coefficient and	97

fixed k_{nl} =1e10N/m, (b) at different values of penalty stiffness k_{nl} and fixed s=1e10

3.7 System response in the time domain in “crack point” (*trailing edge crack*, ω = 3550 rad/sec): (a) a=2 mm, (b) a=4 mm 99

3.8 System response in the time domain in “tip point” (*trailing edge crack*, ω = 3550 rad/sec): (a) a=2 mm, (b) a=4 mm 99

3.9 System response in the time domain in “tip point” (*leading edge crack*, ω = 3550 rad/sec): (a) a=2 mm, (b) a=4 mm 100

3.10 System response in time domain int “tip” point (a=4 mm, ω=3550rad/sec): (a) trailing edge crack, (b) leading edge crack 100

3.11 System response with symmetric cracks in time domain int “crack” point (a=2 mm, ω=3550rad/sec): (a) crack located on trailing edge, (b) crack located on leading edge 101

3.12 System response with symmetric cracks in time domain in “crack” point (a=4 mm, ω=3550rad/sec): (a) crack located on trailing edge, (b) crack located on leading edge 101

3.13 System response with symmetric cracks in time domain in “tip” point (ω=3550rad/sec): (a) a=2 mm, (b) a=4 mm 101

3.14 (a) Simplified two-dimensional model of the cracked structure, (b) Time-history of the relative vertical displacement between crack tips in ANSYS 103

3.15 Nonlinear solution by HB method and direct integration approach: (a) in the “crack point” and (b) in the “tip point” 105

3.16 Cracked blade frequency response function (a=2 mm): (a) trailing edge crack, (b) leading edge crack 105

3.17 Cracked blade response phase change (a=2 mm): (a) trailing edge crack, (b) leading edge crack 105

3.18 Cracked blade frequency response function (a=4 mm): (a) trailing edge crack, (b) leading edge crack 106

3.19 Cracked blade response phase change (a=4 mm): (a) trailing edge crack, (b) leading edge crack 107

3.20 Cracked blade frequency response function (symmetric crack, a=2 mm) 107

3.21 Cracked blade frequency response function (symmetric crack, a=4 mm) 108

3.22 Cracked blade response phase change (symmetric crack): (a) a=2 mm, (b) a=2 mm 108

3.23 Initial crack opening due to centrifugal forces effect: (a) trailing edge crack, (b) leading edge crack 109

3.24 Nonlinear solution by HB method at initial crack opening (Ω=10 Hz): (a) trailing edge crack, (b) leading edge crack 110

3.25 Nonlinear solution by HB method at initial crack opening (Ω=20 Hz): 111

(a) trailing edge crack, (b) leading edge crack

3.26 Nonlinear solution by HB method at initial crack opening (Ω=30 Hz): (a) trailing edge crack, (b) leading edge crack 111

3.27 Nonlinear solution by HB method at initial crack opening (Ω=50 Hz): (a) trailing edge crack, (b) leading edge crack 111

3.28 Nonlinear solution by HB method at initial crack opening (Ω=60 Hz): (a) trailing edge crack, (b) leading edge crack 112

3.29 Brick-type cracked blade model subjected to durability analysis: (a) finite elements model, (b) stress deformed state around crack tip 113

3.30 Cracked blade durability parameters dependence on initial crack length: (a) stress intensity coefficient K (Pa·m$^{1/2}$), (b) remained cycles number dN 113

3.31 Bladed disk assembling 116

3.32 Bladed disk finite-elements model: (a) sector with cracked blade, (b) assembled disk with applied external forces 116

3.33 Bladed disk model sub-structuring: (a) on the base of the full assembled system, (b) on the base of the disk sector 117

3.34 Eigenfrequencies distribution at the different number of retained modes 118

3.35 Full (a) and reduced (b) bladed disk models frequency responses 118

3.36 Nonlinear solution by HB method for different harmonics numbers: (a) “crack point”, (b) “tip point”, (c) “tip point” (zoom), (d) frequency response function at “tip point” (dashed lin(e) linear solution of the cracked blade) 118

3.37 Effect of the phase lag of excitation forces: (a) n_s=28, (b) n_s=25, (c) n_s=23, (d) n_s=20 120

3.38 A bladed disk natural mode: (a) a case of cracked blade frequency localization, (b) a case of absence of the cracked blade frequency localization 123

3.39 Effect of mistuning on the bladed disk forced response (n_s=28): (a) σ=0.01, (b) σ=0.02, (c) σ=0.01 (zoom), (d) σ=0.02 (zoom) 124

3.40 Effect of mistuning on the bladed disk forced response (n_s=23): (a) σ=0.01, (b) σ=0.02, (c) σ=0.01 (zoom), (d) σ=0.02 (zoom) 125

3.41 Effect of mistuning on the bladed disk forced response (n_s=28): (a) no mistuning, (b) σ=0.005, (c) no mistuning (zoom), (d) σ=0.005 (zoom) 126

3.42 Time-history of bladed disk forced response (n_s=28, no mistuning): (a) full 3D view, (b) view in 2D 127

3.43 Time-history of bladed disk forced response (n_s=28, no mistuning): (a) through the time period, (b) at time t=0 128

3.44 Time-history of bladed disk forced response (n_s=28, σ=0.01): (a) through the time period, (b) at time t=0 128

3.45 Time-history of bladed disk forced response (n_s=28, σ=0.02): (a) through the time period, (b) at time t=0 129

3.46 Time-history of bladed disk forced response (n_s=31, no mistuning) 129

3.47 Time-history of bladed disk forced response (n_s=34, σ=0.02): (a) through the time period, (b) at time t=0 130

Chapter 4

4.1 Blade tip timing method presentation: (a) blade behavior as the subject for BTTM procedure, (b) blade positioning 135

4.2 Tip-timing measurements presentation: (a) amplitude of blade tip measurement by three probes, (b) zoom around first probe measurement 137

4.3 Disability of uniformly spaced probes to capture amplitude of blade tip at EO, which is multiple of probes number: (a) EO=6, (b) EO=9 139

4.4 Simulation of blade tip-timing procedure 139

4.5 The research structural scheme 140

4.6 All-blades response in the measurement point: trailing edge crack, a=2 mm 142

4.7 Trailing edge crack (a=2 mm): (a) frequency response of all-blades by tip-timing method data, (b) arriving time differences of all-blades captured by probes 143

4.8 All-blades response in the measurement point: trailing edge crack, a=4 mm 144

4.9 Trailing edge crack (a=4 mm): (a) frequency response of all-blades by tip-timing method data, (b) arriving time differences of all-blades captured by probes 145

4.10 All-blades response in the measurement point: leading edge crack, a=2 mm 146

4.11 Leading edge crack (a=2 mm): (a) frequency response of all-blades by tip-timing method data, (b) arriving time differences of all-blades captured by probes 147

4.12 All-blades response in the measurement point: leading edge crack, a=4 mm 148

4.13 Leading edge crack (a=4 mm): (a) frequency response of all-blades by tip-timing method data, (b) arriving time differences of all-blades captured by probes 149

4.14 All-blades response in the measurement point: symmetric cracks, a=2 mm 150

4.15 Frequency response function (symmetric cracks, a=2 mm): (a) frequency response of all-blades by tip-timing method data, (b) arriving time differences of all-blades captured by probes 151

4.16 All-blades response in the measurement point: symmetric cracks, a=4 mm 152

4.17 Frequency response function (symmetric cracks, *a*=4 mm): (a) frequency response of all-blades by tip-timing method data, (b) arriving time differences of all-blades captured by probes 153

4.18 Cracked blade frequency response of bladed disk dynamic model (trailing edge crack): (a) *a*=2 mm, (b) *a*=4 mm 154

4.19 Cracked blade frequency response of bladed disk dynamic model (leading edge crack): (a) *a*=2 mm, (b) *a*=4 mm 154

4.20 Cracked blade frequency response of bladed disk dynamic model (symmetric cracks): (a) *a*=2 mm, (b) *a*=4 mm 155

4.21 Blade tip timing method application results (0.5% of mistuning): (a) arriving time differences seen on the probes, (b) amplitude forced response by TTM data 156

4.22 Blade tip timing method application results (1% of mistuning): (a) arriving time differences seen on the probes, (b) amplitude forced response by TTM data 157

4.23 Blade tip timing method application results (2% of mistuning): (a) arriving time differences seen on the probes, (b) amplitude forced response by TTM data 157

4.24 All-blades response in the measurement point (1% of mistuning): (a) ω=3044.2 rad/sec, (b) ω=3218.1 rad/sec, (c) ω=3273.5 rad/sec, (d) ω=3455.3 rad/sec 158

4.25 All-blades response in the measurement point (2% of mistuning): (a) ω=3044.2 rad/sec, (b) ω=3218.1 rad/sec, (c) ω=3273.5 rad/sec, (d) ω=3455.3 rad/sec 159

4.26 Blade tip timing method application results (no mistuning): (a) arriving time differences seen on the probes, (b) amplitude forced response by TTM data 160

4.27 Blade tip timing method application results (0.5% of mistuning): (a) arriving time differences seen on the probes, (b) amplitude forced response by TTM data 160

4.28 All-blades response in the measurement point (0.5% of mistuning): (a) ω=3044.2 rad/sec, (b) ω=3218.1 rad/sec, (c) ω=3273.5 rad/sec, (d) ω=3455.3 rad/sec 161

4.29 All-blades amplitudes distribution on a measurement point (resolution level 1e-8): (a) ω=3044.2 rad/sec, (b) ω=3218.1 rad/sec, (c) ω=3273.5 rad/sec, (d) ω=3455.3 rad/sec 162

4.30 All-blades amplitudes distribution on a measurement point (resolution level 1e-7): (a) ω=3044.2 rad/sec, (b) ω=3218.1 rad/sec, (c) ω=3273.5 rad/sec, (d) ω=3455.3 rad/sec 163

4.31 All-blades amplitudes distribution on a measurement point (resolution level 1e-6): (a) ω=3044.2 rad/sec, (b) ω=3218.1 rad/sec, (c) ω=3273.5 rad/sec, (d) ω=3455.3 rad/sec 164

4.32 All-blades amplitudes distribution on a measurement point (resolution level 1e-5): (a) ω=3044.2 rad/sec, (b) ω=3218.1 rad/sec, (c) ω=3273.5 rad/sec, (d) ω=3455.3 rad/sec 165

4.33 Cracked blade frequency response at different probe resolution levels 166

List of tables

3.1	Change of cracked blade eigenfrequencies due to crack presence	94
3.2	Cracked blade model eigenfrequencies (in Hz): crack on trailing edge	96
3.3	Cracked blade model eigenfrequencies (in Hz): crack on leading edge	96
3.4	Crack initial opening at different rotor frequency	110
3.5	Bladed disk model eigenfrequencies (in Hz)	119
4.1	Comparison of the different probes types features	134
4.2	Measurement points at blade tip-timing method simulation	141

Annex 1

Methods of non-linear problems solution

Any non-linear system in its simplified description can be presented by expression subjected to optimization procedure:

$$F(U) = 0\,, \tag{a1.1}$$

where F is non-linear function of U. Equation (a1.1) represents by itself the system of non-linear equation of dimension equal to the system size.

One of the methods of non-linear equations solution is **the method of simple iteration**. The system of non-linear equations can be represented as:

$$\begin{cases} F_1(x, y, ..., w) = 0 \\ F_2(x, y, ..., w) = 0 \\ ..... \\ F_n(x, y, ..., w) = 0 \end{cases} \text{ or } \begin{cases} x = f_1(x, y, ..., w) \\ y = f_2(x, y, ..., w) \\ ..... \\ w = f_n(x, y, ..., w) \end{cases} \tag{a1.2}$$

The system is considered to be solved, if each equation for the given variables x, y, …, w turns to identity. Generally, the system of equations can have 0; 1; 2;... radicals. To solve this problem numerical, analytical or graphical methods are used. Numerical methods allow determination of one radical of non-linear equations system by means of iterations starting from the point $x_0, y_0, \ldots, w_0, \ldots$

In the **method of iterations of Zeidel** the solution is searched in the form of

$$\begin{cases} x_{k+1} = f_1(x_k, y_k, z_k, ..., w_k); \\ y_{k+1} = f_2(x_{k+1}, y_k, z_k, ..., w_k); \\ z_{k+1} = f_3(x_{k+1}, y_{k+1}, z_k, ..., w_k); \quad k=0,1,2, \ldots (2...4) \\ ..... \\ w_{k+1} = f_n(x_{k+1}, y_{k+1}, z_{k+1,...,} w_k), \end{cases} \tag{a1.3}$$

where, unlike the first method, on each iteration in the second equation of system value of variable x_{k+1} is calculated by first equation of the same iteration, in the third – variables x_{k+1}, y_{k+1} are computed by first two equations, etc. And in the last equation all variables, except w, are computed by previous equations of the same iteration.

Non-linear equations system solution by **Newton method** we shall consider on the example of the second order system:

$$\begin{cases} u = f_1(x, y) \\ v = f_2(x, y) \end{cases} \tag{a1.4}$$

which could be considered as transformation of the plane xOy into the plane uOv. We are interested in the reversion of this transformation near the point (x_0, y_0), which image is the point (u_0, v_0). If two functions have the continuous partial derivatives, so using the differential, it is possible to note the system of the linear approximations

$$\begin{cases} u - u_0 = \dfrac{\partial}{\partial x} f_1(x_0, y_0)(x - x_0) + \dfrac{\partial}{\partial y} f_1(x_0, y_0)(y - y_0), \\ v - v_0 = \dfrac{\partial}{\partial x} f_2(x_0, y_0)(x - x_0) + \dfrac{\partial}{\partial y} f_2(x_0, y_0)(y - y_0) \end{cases}. \tag{a1.5}$$

This system is the local linear transformation which relates small changes of independent variables with small changes of dependent variables.

If to take advantage of Jacobian matrix $J(x_0, y_0)$, these relations can be rewritten easily in the form of:

$$\begin{bmatrix} u - u_0 \\ v - v_0 \end{bmatrix} = \begin{vmatrix} \dfrac{\partial}{\partial x} f_1(x_0, y_0) & \dfrac{\partial}{\partial y} f_1(x_0, y_1) \\ \dfrac{\partial}{\partial x} f_2(x_0, y_0) & \dfrac{\partial}{\partial y} f_2(x_0, y_0) \end{vmatrix} \begin{vmatrix} x - x_0 \\ y - y_0 \end{vmatrix},$$

or

$$\Delta F \approx J(x_0, y_0)\Delta X. \tag{a1.6}$$

To solve the system of the non-linear equations it is necessary to consider small deviations of the function near the point (x_0, y_0). Let's have:

$$\begin{aligned} \Delta x &= x - x_0, \\ \Delta y &= y - y_0. \end{aligned} \tag{a1.7}$$

Using these equations for definition of the argument increments, it is possible to gain linear transformation:

$$\begin{vmatrix} \dfrac{\partial}{\partial x} f_1(x_0, y_0) & \dfrac{\partial}{\partial y} f_1(x_0, y_0) \\ \dfrac{\partial}{\partial x} f_2(x_0, y_0) & \dfrac{\partial}{\partial y} f_2(x_0, y_0) \end{vmatrix} \begin{vmatrix} \Delta x \\ \Delta y \end{vmatrix} = \begin{vmatrix} f_1(x_0, y_0) \\ f_2(x_0, y_0) \end{vmatrix}. \tag{a1.8}$$

If Jacobian is non-singular, the system solution can be noted in the form of:

$$\Delta X \approx -J(x_0, y_0)^{-1} F(x_0, y_0), \tag{a1.9}$$

where $[\Delta x, \Delta y]^T = [x, y]^T - [x_0, y_0]^T$.

The first approximation X_1 to X_0 looks like

$$X_1 = X_0 + \Delta X = X_0 - J(x_0, y_0)^{-1} F(x_0, y_0), \tag{a1.10}$$

and k–th approximation

$$X_k = X_{k-1} + \Delta X = X_{k-1} - J(x_{k-1}, y_{k-1})^{-1} F(x_{k-1}, y_{k-1}), \tag{a1.11}$$